From fast to slow rotation in the open clusters NGC 2516 and NGC 3532

Dario Jasper Fritzewski
Leibniz-Institut für Astrophysik Potsdam (AIP)

Kumulative Dissertation
zur Erlangung des akademischen Grades
„doctor rerum naturalium“
(Dr. rer. nat.)
in der Wissenschaftsdisziplin „Astrophysik “

eingereicht an der
Mathematisch-Naturwissenschaftlichen Fakultät
Institut für Physik und Astronomie
der Universität Potsdam
und dem
Leibniz-Institut für Astrophysik Potsdam (AIP)

Potsdam, 26. Mai 2021
Disputation: 28. Oktober 2021

Betreuer: Prof. Dr. Klaus G. Strassmeier
Dr. Sydney A. Barnes
PD Dr. Axel Schwope
1. Gutachter: Prof. Dr. Klaus G. Strassmeier
2. Gutachter: Prof. Dr. Gibor Basri (UC Berkeley)
3. Gutachter: Prof. Dr. Brian C. Chaboyer (Dartmouth College)

Published online on the
Publication Server of the University of Potsdam:
https://doi.org/10.25932/publishup-53135
https://nbn-resolving.org/urn:nbn:de:kobv:517-opus4-531356

Abstract

Angular momentum is a particularly sensitive probe into stellar evolution because it changes significantly over the main sequence life of a star. In this thesis, I focus on young main sequence stars of which some feature a rapid evolution in their rotation rates. This transition from fast to slow rotation is inadequately explored observationally and this work aims to provide insights into the properties and time scales but also investigates stellar rotation in young open clusters in general.

I focus on the two open clusters NGC 2516 and NGC 3532 which are ~150 Myr (zero-age main sequence age) and ~300 Myr old, respectively. From 42 d-long time series photometry obtained at the Cerro Tololo Inter-American Observatory, I determine stellar rotation periods in both clusters. With accompanying low resolution spectroscopy, I measure radial velocities and chromospheric emission for NGC 3532, the former to establish a clean membership and the latter to probe the rotation-activity connection.

The rotation period distribution derived for NGC 2516 is identical to that of four other coeval open clusters, including the Pleiades, which shows the universality of stellar rotation at the zero-age main sequence. Among the similarities (with the Pleiades) the "extended slow rotator sequence" is a new, universal, yet sparse, feature in the colour-period diagrams of open clusters. From a membership study, I find NGC 3532 to be one of the richest nearby open clusters with 660 confirmed radial velocity members and to be slightly sub-solar in metallicity. The stellar rotation periods for NGC 3532 are the first published for a 300 Myr-old open cluster, a key age to understand the transition from fast to slow rotation. The fast rotators at this age have significantly evolved beyond what is observed in NGC 2516 which allows to estimate the spin-down timescale and to explore the issues that angular momentum models have in describing this transition. The transitional sequence is also clearly identified in a colour-activity diagram of stars in NGC 3532. The synergies of the chromospheric activity and the rotation periods allow to understand the colour-activity-rotation connection for NGC 3532 in unprecedented detail and to estimate additional rotation periods for members of NGC 3532, including stars on the "extended slow rotator sequence".

In conclusion, this thesis probes the transition from fast to slow rotation but has also more general implications for the angular momentum evolution of young open clusters.

Zusammenfassung

Entgegen anderer Parameter ändert sich der Drehimpuls von kühlen Hauptreihensternen stark und eignet sich daher gut zur Untersuchung der Sternentwicklung. In dieser Arbeit fokussiere ich mich auf junge Hauptreihensterne, von denen einige einen ausgeprägten Übergang in ihren Rotationsperioden aufweisen. Dieser Übergang von schneller zu langsamer Rotation ist empirisch nur unzureichend erforscht und diese Arbeit zielt darauf ab, Einblicke in seine Eigenschaften und Zeitskalen zu geben, sie untersucht aber auch die stellare Rotation in jungen offenen Sternhaufen im Allgemeinen.

Ich konzentriere mich auf die beiden offenen Sternhaufen NGC 2516 und NGC 3532, die ~150 Myr (Nullalter-Hauptreihe) bzw. ~300 Myr alt sind. Aus einer 42 Tage langen photometrischen Zeitreihe, die am Cerro Tololo Inter-American Observatory gewonnen wurde, bestimme ich Rotationsperioden in beiden Sternhaufen. Darüber hinaus messe ich mit niedrig auflösender Spektroskopie Radialgeschwindigkeiten und die chromosphärische Emission für Sterne in NGC 3532, erstere um eine sichere Mitgliedschaft zu etablieren und letztere um den Zusammenhang zwischen Rotation und Aktivität zu untersuchen.

Die für NGC 2516 abgeleitete Rotationsperiodenverteilung ist identisch mit der von vier anderen gleichaltrigen offenen Sternhaufen, einschließlich der Plejaden, was die Gleichheit und Grundsätzlichkeit der Sternrotation auf der Nullalter-Hauptreihe zeigt. Neben den Ähnlichkeiten (mit den Plejaden) ist die „extended slow rotator sequence“ ein neues, universelles, aber seltenes Merkmal in den Farben-Perioden-Diagrammen offener Sternhaufen.

Aus einer Mitgliedschaftsstudie geht hervor, dass NGC 3532 mit 660 bestätigten Radialgeschwindigkeitsmitgliedern einer der größten nahen offenen Sternhaufen ist. Zudem weist er eine leicht sub-solare Metallizität auf. Die Rotationsperioden für NGC 3532 sind die ersten, die für einen 300 Myr alten offenen Sternhaufen veröffentlicht wurden, ein wichtiges Alter, um den Übergang von schneller zu langsamer Rotation zu verstehen. Die schnellen Rotatoren in diesem Alter sind deutlich weiter entwickelt als in NGC 2516 beobachtet, was es erlaubt, die Zeitskala für den Drehimpulsverlust abzuschätzen und die Probleme zu untersuchen, die Drehimpulsmodelle bei der Beschreibung dieses Übergangs haben. Die Übergangssequenz ist auch in einem Farben-Aktivitäts-Diagramm von Sternen in NGC 3532 deutlich zu erkennen. Die Synergien zwischen der chromosphärischen Aktivität und den Rotationsperioden erlauben es, den Zusammenhang zwischen intrinsischer Farbe, Aktivität und Rotation für NGC 3532 in einzigartigem Detail zu verstehen und zusätzliche Rotationsperioden für Mitglieder von NGC 3532 abzuschätzen, einschließlich der Sterne auf der „extended slow rotator sequence“.

Zusammenfassend untersucht diese Arbeit den Übergang von schneller zu langsamer Rotation, hat aber auch allgemeinere Implikationen für die Drehimpulsentwicklung von jungen offenen Sternhaufen.

Contents

1 Introduction

During the longest phase of stellar evolution, the main sequence stage, stars appear relatively stable to us as observers. They are fusing hydrogen to helium and observables like the luminosity stay mostly constant. However, one property of cool stars changes dramatically during their main sequence life: angular momentum. Cool solar-like stars lose a significant fraction of their angular momentum and spin down amid the otherwise most stable phase of stellar evolution (Skumanich 1972; Barnes 2003, 2010). In this thesis, I focus on a phase of strong change in the stellar angular momentum content: the transition from fast to slow rotation. Over the course of this event, some main sequence stars spin down dramatically over a short period of time. Yet, the mechanisms and time scales of this transition are uncertain.

Although angular momentum is a physical property of the stars, it cannot be measured directly. However, the rotation rate is accessible and, because the internal stellar structure evolves slowly, the stellar moment of inertia can be considered constant. Hence, the measured rotation period is proportional to the angular momentum. The period can be measured through starspot-modulated photometric time series (Kron 1947; Strassmeier 2009), enabling detailed investigations of stellar angular momentum.

This thesis is structured as follows. In the introduction (Chapter 1), I first give an overview of the theoretical and observational knowledge of the angular momentum evolution and present the central research question of this thesis. Further, I summarize the observational methods to measure stellar rotation periods and introduce the two open clusters in which rotation periods are measured for this work. Finally, I outline the peer-reviewed papers on which this thesis is based and describe the contributions of the individual authors. The publications are reprinted in the Chapters 2–5. The discussion in Chapter 6 combines the individual results and places them into the context of current research. In the final Chapter 7, I conclude with respect to the research question.

1.1 Stellar dynamo and angular momentum loss

Young stars contain large amounts of angular momentum which they inherit from the molecular cloud wherein they and their surroundings (i.e. planetary systems) form. However, angular momentum is removed from the star efficiently already in the first million years. Otherwise, the star would spin-up beyond the break-up velocity during the pre-main sequence contraction[1] (Mestel 1965). After the first tens of millions of years, and during its entire main sequence lifetime, angular momentum is removed from the star through the interaction between its magnetic field and the stellar wind (Parker 1958; Schatzman 1962; Weber & Davis 1967). The magnetic field does not only influence the stellar rotation but stellar rotation is a key component in the creation of the magnetic field, too.

The stellar spin-down considered in this work is a feature of solar-like cool stars, i.e. dwarfs of the spectral types FGK and early M. Their interiors are structured into an outer convection zone and an inner radiative core, just like our Sun. Yet, the sizes of these zones depend on the stellar mass. The lower the mass, the deeper the convection zone is, relative to the stellar radius, which means that the lowest-mass stars ($M_\star \lesssim 0.35\,\mathrm{M}_\odot$, later than spectral type M3, Jao et al. 2018) become fully convective and are no longer considered

[1] The mechanisms for angular momentum removal in young T-Tauri stars are discussed below in Sect. 1.2.

solar-like. However, their observed stellar activity has many similarities (e.g. Wright & Drake 2016, Newton et al. 2017) to solar-like stars.

An active dynamo is present[2] in solar-like stars. It acts in the convection zone and can be explained by the mean-field theory as an α-Ω dynamo[3] (Steenbeck & Krause 1969), schematically shown in Fig. 1.1.

At the initial stage (top left), a poloidal field is embedded in the plasma of the convection zone. The field lines are dragged along with the plasma as the star rotates. Because of the differential rotation, they are not carried uniformly but at varying speeds depending on the latitude (top centre) which twists the magnetic field around the axis of rotation and creates a toroidal magnetic field in the convection zone (top right). This mechanism is driven by the rotation and therefore called Ω-effect.

The second component in the stellar dynamo is driven by the convection and called α-effect. Convective cells rise radially outwards and drag along the poloidal field upwards, twisting the field lines perpendicular to the poloidal field (bottom left). Due to the Coriolis force, the toroidal field lines are twisted such that the created loops[4] in both hemispheres have the same polarity (bottom centre). Hence, the loops do not cancel-out but can form a large-scale poloidal field (Parker 1955a) which has the opposite polarity of the initial field (bottom right). The field reversion, accompanied with other phenomena, is (for the Sun) the well-known Solar cycle (Babcock 1961; Leighton 1969).

This mechanism of creation and transformation of the magnetic field emphasizes stellar rotation (along with the convection) as a key ingredient in the dynamo process. Slower rotation leads to a weaker magnetic field because the Coriolis force is weaker, too. Yet, it is the magnetic field itself which causes the spin-down of the star.

The angular momentum-loss of a star is driven by its magnetized stellar wind. Charged wind particles move along the field lines and co-rotate with the stellar surface out to the Alfvén-radius r_A of the star. From thereon, they can continue freely without the influence of the stellar magnetic field (Mestel 1984). However, the co-rotation creates a lever arm of length r_A which counter-acts the stellar rotation. Therefore, the torque applied to the star is proportional to the mass-loss rate through the wind, the Alfvén-radius squared (r_A^2), and the angular velocity (Kawaler 1988). The Alfvén-radius itself depends, among other stellar properties, on the magnetic field strength. Hence, a weaker field leads to smaller torque. In summary, the stellar rotation drives the dynamo process which maintains the stellar magnetic field. However, a strong magnetic field applies a torque to the star, braking the star. Consequently, the star is spun down and the magnetic field becomes weaker. This demonstrates the very important interplay between magnetism and rotation.

Besides the angular momentum loss, the magnetic field also creates a wide array of phenomena throughout the whole upper stellar atmosphere. In the photosphere, this magnetic (or stellar) activity is observed as starspots. Their abundance and size is a direct probe of the magnetic field strength. Higher up in the stellar atmosphere, in the chromosphere, a much hotter, albeit thinner, plasma is present. However, it is still an open question how the chromosphere is heated and the leading ideas consider nano-flares and magneto-acoustic waves (Osterbrock 1961; Parker 1988; Cranmer et al. 2015). The non-radiative equilibrium conditions in the chromosphere lead to line emission of certain

[2] Although large-scale magnetic fields are also observed in massive O and B stars (Hubrig et al. 2008), their creation mechanism is an open question (Shultz et al. 2019).

[3] Other more sophisticated mechanisms are proposed (reviewed in Ossendrijver 2003 and Charbonneau 2014) but are not directly relevant for the purpose of this thesis.

[4] When a magnetic loop rises to the stellar surface, the enhanced magnetic field creates a cooler, darker area in the photosphere known as a starspot (Parker 1955b).

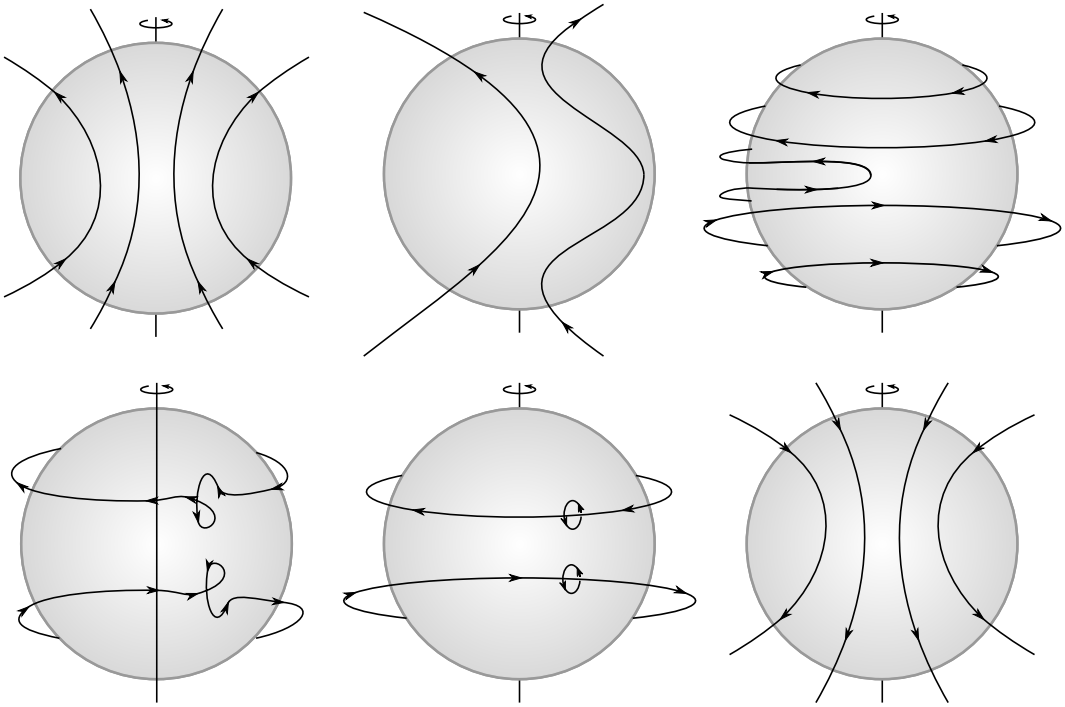

Figure 1.1: Sketch of the α-Ω-dynamo. *Top row:* The Ω-effect turns the poloidal field (top left) into an toroidal field. *Bottom row:* The α-effect creates magnetic loops which establish a global poloidal field of opposite polarity. See text for a detailed description.

elements. Most notable are the H & K and infra-red triplet lines of Ca II and the Hα fill-ins of the spectral lines and even line emissions[5] observed in stellar spectra. Chromospheric activity, as observed through the reversal of the Ca II H & K lines, has been known for the Sun (Young 1872; Hale 1892) and other cool stars (Eberhard & Schwarzschild 1913) for more than a century. Long-term observations from the Mount Wilson Observatory showed activity cycles, like that on the Sun, to be present also on other stars (Wilson 1978; Baliunas et al. 1995). Above the chromosphere, in the stellar corona, further magnetic activity can be observed (Güdel 2004). Because the corona is even hotter, the coronal emission is mainly observed in soft X-rays. Yet the (proposed) heating and emission mechanisms are identical to the chromosphere.

Similar to these activity phenomena, the magnetized stellar wind was first studied for the Sun, demonstrating the importance of the Solar-stellar connection. Weber & Davis (1967) proposed a model of the Solar wind and estimated for the first time the amount of angular momentum it carries away. At the same time of the theoretical calculations, Kraft (1967) observed that older stars show smaller rotational velocities. He compared stars with different levels of Ca II emission and concluded that the stars with the highest emission, which are the younger stars, have the highest rotational velocities. Based on these (and other) observations Skumanich (1972) first quantified the spin-down of cool stars with $v_{\rm rot} \propto t^{-0.5}$, where $v_{\rm rot}$ is the rotational velocity and t the stellar age.

[5] Hence, the name chromosphere which describes the coloured layer observable during a solar eclipse. This reddish glow is the Hα line emission.

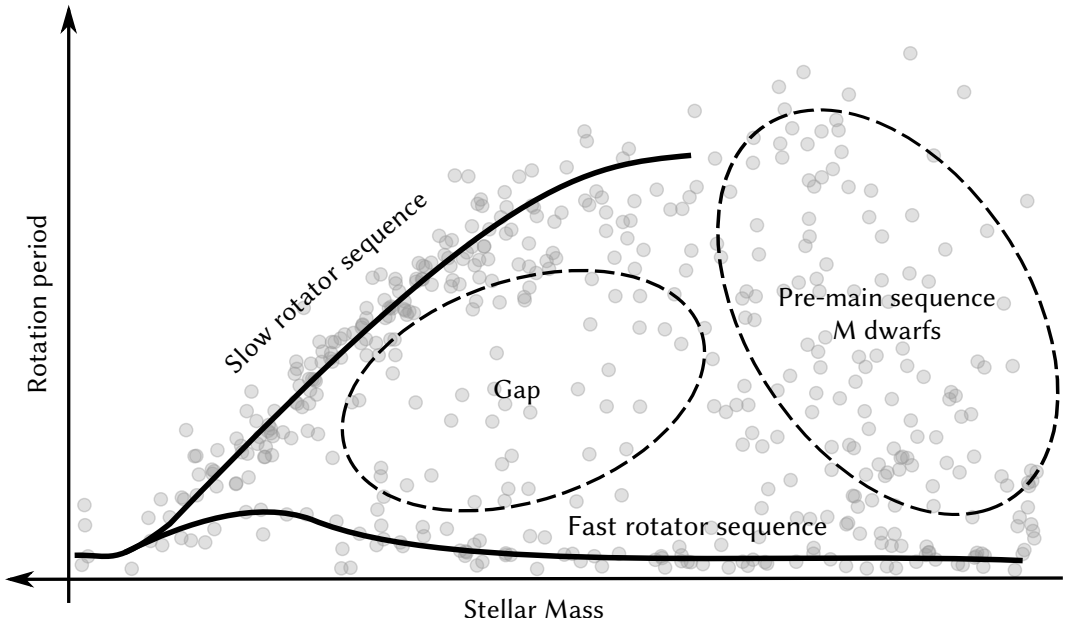

Figure 1.2: Simplified presentation of the fast and slow rotator sequences in young open clusters (solid lines). The left dashed ellipses marks the gap between the fast and slow rotator sequence while the right marks the pre-main sequence M dwarfs which do not follow any sequence yet. The upwards shift of the highest-mass fast rotators indicates that the evolution from fast to slow rotation already progresses for these stars. Grey data points in the background are from NGC 2516 (Fritzewski et al. 2020) and the Pleiades (Rebull et al. 2016).

1.2 Age-dependence of stellar rotation and activity from observations

This "Skumanich-like" spin-down can be observed for slow rotators to which the majority of solar-like stars belong. However, young stars which just reached the main sequence (zero-age main sequence, ZAMS) populate two groups of rotators. In coeval stellar associations, we observe at the same mass (or colour) slow rotators, with rotation periods on the order of a few days, as well as fast rotators, with rotation periods near or less than one day. Between the two populations, a distinct gap exists (Barnes 2003). Fig. 1.2 shows data from the two ZAMS open clusters NGC 2516 and Pleiades. Overlaid are the two sequences and the rotational gap is marked.

It is not yet fully understood what causes those two distinct populations, but a common explanation is the interaction between the stellar magnetic field and circum-stellar material (i.e. proto-planetary disc) in the first few million years of the stellar life (Edwards & Snell 1982; Barnes et al. 2001). In this disc-breaking mechanism, stars which lose their disc faster can spin up due to contraction on the pre-main sequence and become fast rotators. In contrast, stars that keep their disc longer cannot spin-up while they contract, because the magnetic interaction with the disc removes angular momentum from the star, i.e. disc braking (Koenigl 1991)[6]. For this thesis and the angular momentum evolution on the main

[6] See Orcajo et al. (2019) for a recent overview on the observational evidence against and in favour of disc braking.

sequence, the exact mechanisms are of lesser interest than the existence of two populations (fast and slow rotators), a given observational fact.

The two classes can only be observed simultaneously in young coeval groups of stars. To our advantage, star formation happens in molecular clouds and the newly-born stars are locally concentrated. While some associations are loosely linked and disperse quickly, some stay gravitationally bound and form open clusters, which disperse only on the time-scale of a billion years. Since these clusters formed in a single star-forming event (over several million years) their members share the chemical compositions and age. Additionally, they inherit the space motion of their birth cloud and move as a gravitationally bound cluster in the Milky Way, enabling the observer to separate them from the background population. Main sequence stars of most masses[7] are present in an open cluster and form a sequence in the colour-magnitude space, the cluster main-sequence. This allows an accurate age determination through isochrone fitting. Combined, all of these properties make open clusters the ideal laboratories for stellar astrophysics. Clusters of different age can be arranged in a succession tracing stellar evolution[8]. Among the several properties which change during the stellar life and that can be traced with open clusters are the angular momentum content and the stellar activity.

The rotation period as a proxy for the angular momentum content can easily be measured for many stars in an open cluster (see Section 1.5) and these observations are usually displayed in colour-period diagrams (CPD). Here, the colour is an observational proxy for the stellar mass. Using two observational properties enables empirical comparisons between open clusters. Fig. 1.3 shows a colour-period diagram with data from several exemplary open clusters of different ages.

The direct comparison in this figure demonstrates the spin-down of the slow rotators. The youngest open cluster shown is the Pleiades (Rebull et al. 2016) which is about 130 Myr old. The solar-like stars in this cluster are mostly at the ZAMS and its slow rotators have periods of a few days (depending on the mass). By the age of Praesepe (~790 Myr, Rebull et al. 2017) the stars have spun-down to periods nearly twice as long as in the Pleiades. Praesepe and the next older example, NGC 6819 (Meibom et al. 2015), have a large age difference. At the stellar age of 2.5 Gyr in NGC 6819, the periods have doubled again for most stars. The oldest open cluster with measured rotation periods to date is M 67 (Barnes et al. 2016) at ~4 Gyr. The rotation periods in M 67 are comparable to the Solar value (also marked in Fig. 1.3).

In addition to the general stellar spin-down, indicated by the upward movement of the slow rotator sequence, the mass dependence of the spindown can be inferred from the measurements. For example the higher-mass stars in Praesepe and NGC 6819 rotate with similar rotation periods, hence they have barely spun down. In contrast, the lower-mass stars spin down with a factor of two in between the ages of these two clusters. Lower-mass stars with deeper convection zones experience a much stronger spindown.

The comparison of different open clusters illustrates not only the spindown itself but shows in particular the rapid evolution at young ages. It is among the youngest stars that fast rotators are observed in addition to the slow rotators. In the open clusters shown in Fig. 1.3, the fast rotators belong mostly to the Pleiades. By the ages of Praesepe most of these stars have already spun down to slow rotators[9].

[7] The highest-mass stars might have already evolved off the main sequence, depending on the age.

[8] Of course, one has to assume that stellar astrophysics is universal (at least in the local universe). Indeed, no observation yet has shown fundamental differences between stars in different parts of our Galaxy.

[9] Very few stars remain on the fast rotator sequence. However, they might be tidally locked, close binaries (Rebull et al. 2017).

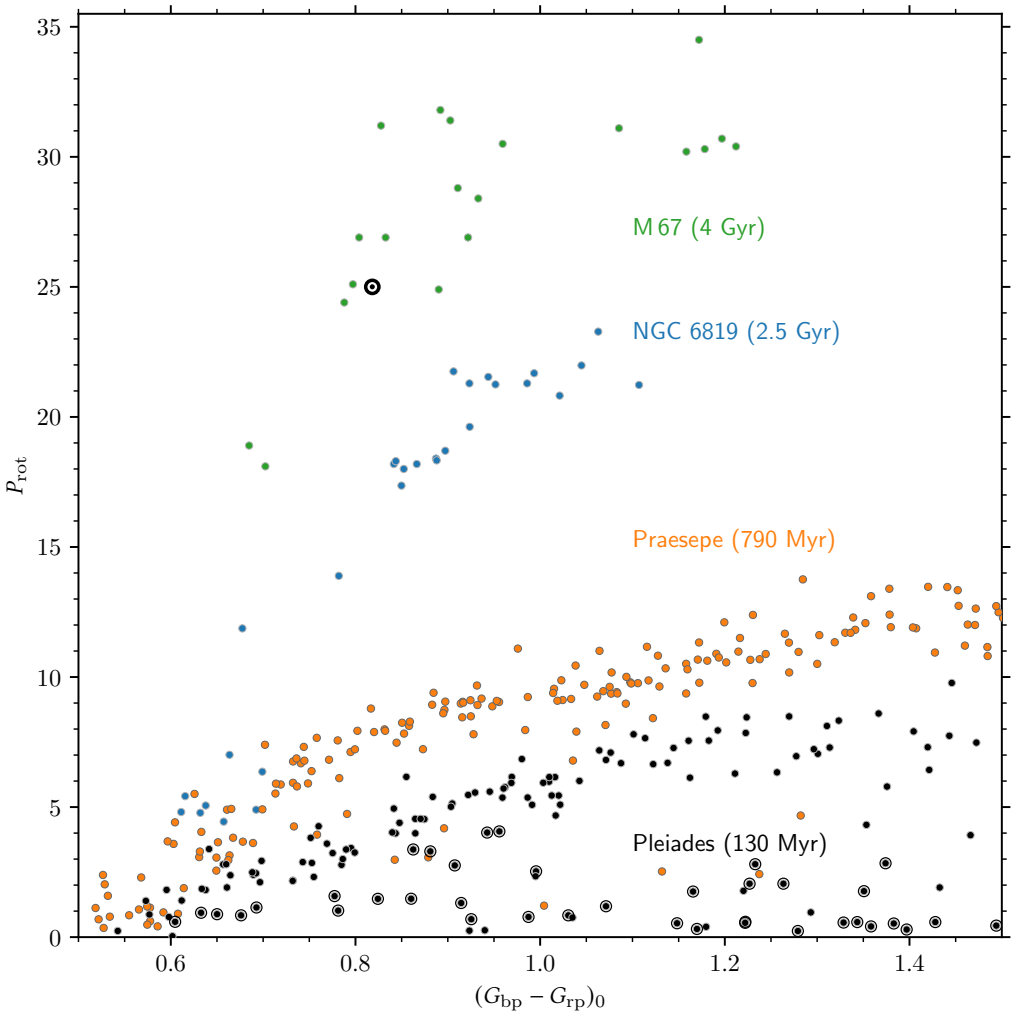

Figure 1.3: Colour-period diagram for several open clusters of different ages, illustrating the spindown with age. The older the stars are, the higher they are found in this diagram. The warmer stars do not spin down as strongly as the cooler stars, due to the shallower convection zones of the former. Hence, the slope of the slow rotator sequence is larger for older open clusters. The data are from the open clusters (bottom to top) Pleiades (black, Rebull et al. 2016), Praesepe (orange, Rebull et al. 2017), NGC 6819 (blue, Meibom et al. 2015), and M 67 (green, Barnes et al. 2016). The fast rotators in the Pleiades (black) are encircled. The Sun's position (among the stars of M 67) in this diagram is marked with the Sun symbol (⊙) for reference.

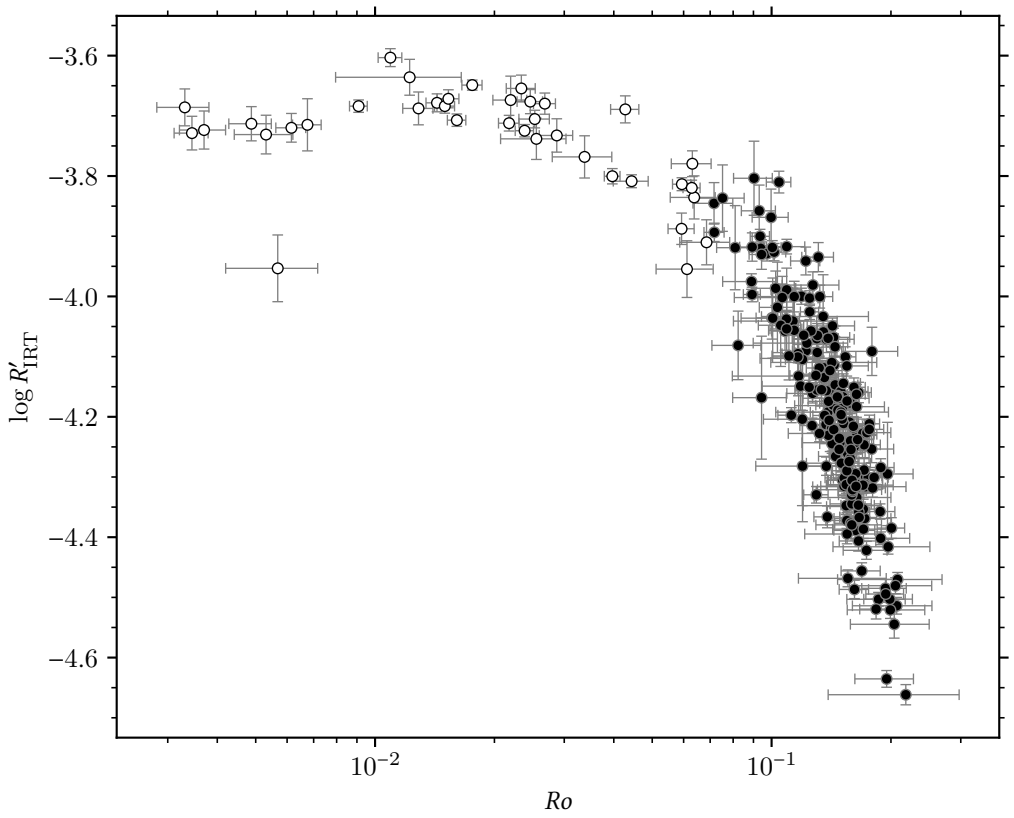

Figure 1.4: Rotation-activity diagram for NGC 3532. In the flat saturated regime (open symbols), the chromospheric activity $\log R'_{\mathrm{IRT}}$ is independent of the Rossby number *Ro*. For slower rotators (filled symbols) with larger Rossby numbers the activity is correlated with the rotation and can be used to estimate the period. Data from Fritzewski et al. 2021a. Similar relationships can be observed for Ca II H & K (e. g. Mamajek & Hillenbrand 2008) and X-rays (e. g. Patten & Simon 1996, Pizzolato et al. 2003, Wright et al. 2011)

In similarity with rotation, stellar activity can also be traced along the stellar evolution. However, the typical analysis emphasises the connection with stellar rotation. Going back to Noyes et al. (1984), the Rossby number, rather than the colour or the rotation period, is used to compare the stellar activity between different stars. The Rossby number is defined as $Ro = P_{\mathrm{rot}}/\tau_c$ with τ_c being the mass-dependent convective turn-over time. This mass-normalization of the rotation period expresses the rotational state of the star rather than the actual rotational speed. Hence, coeval stars on the slow rotator sequence have a similar Rossby number.

Displayed against Rossby number, stellar activity can be divided broadly into two regimes. As seen in Fig. 1.4, stars with small Rossby numbers show a flat distribution, while stars with $Ro \gtrsim 0.07$ follow a trend with smaller activity for larger Rossby numbers. The former regime is called saturated, and the latter unsaturated. Similar distributions are not only found for photospheric (Fritzewski et al. 2021a), chromospheric (Fritzewski et al. 2021a), and coronal activity (Fritzewski et al. 2020), but also for the magnetic field strength (See et al. 2019b) which is the underlying cause for all the other phenomena. With age, the Rossby number increases as the star spins down and initial fast rotators desaturate.

The fast rotators and their evolution to slow rotation can only be observed in young open clusters. Hence, this thesis focuses on these clusters to study the spin-down.

1.3 The transition from fast to slow rotation in open clusters

The first fast rotators were discovered in the Pleiades by Alphenaar & van Leeuwen (1981) through time-series photometry and confirmed with spectroscopy (van Leeuwen & Alphenaar 1982; van Leeuwen et al. 1987). Their existence in the ZAMS open cluster Pleiades was surprising and raised questions about their evolution. Stauffer & Hartmann (1987) confirmed the fast rotators with additional observations and found that they cannot spin down in the same manner as the slow rotators, because a Skumanich-like spin-down would remove the angular momentum from the fast rotators too effectively. This would turn them into slow rotators on time scales much shorter than the main sequence age of the fast rotators in the Pleiades. Hence, fast rotators would not be observable in the Pleiades. Thus, it was clear from early on that the angular momentum loss of fast rotators cannot have a strong dependence on the rotation rate and is therefore intrinsically different from the slow rotators.

Following the idea of a weaker dependence on the rotation rate, MacGregor & Brenner (1991) proposed the magnetic field strength of the fast rotators to be mostly independent of the rotational velocity, too. They postulated that the magnetic field strength saturates above a certain angular velocity. Consequently, the spin-down rate does not have the same strong dependence on the rotation. Their model was able to explain the observed fast rotators of solar-mass in the Pleiades, as well as the lack thereof in the Hyades.

Soderblom et al. (1993) proposed additionally the internal (radial) differential rotation. In this picture, the core spins with a higher rotation rate than the outer envelope. Angular momentum can be transferred from the core to the convection zone and increase the surface rotation. The slow rotators still spin down but not as fast as in a solid body scenario. Fast rotators with a saturated magnetic field, which suppresses the angular momentum loss, can keep their surface rotation rate mostly constant and stay therefore on the fast rotator branch while the slow rotators spin down.

In order to fit the weaker angular momentum loss into the existing framework, Chaboyer et al. (1995) modified the Kawaler (1988) wind-breaking law, leading to a split relation for the angular momentum loss rate $\left(\frac{\mathrm{d}J}{\mathrm{d}t}\right)$ (see also Barnes & Sofia 1996, Bouvier et al. 1997):

$$\frac{\mathrm{d}J}{\mathrm{d}t} = -K_\mathrm{w}\Omega^3 \left(\frac{R}{R_\odot}\right)^{\frac{1}{2}} \left(\frac{M}{M_\odot}\right)^{-\frac{1}{2}} \qquad (\Omega < \omega_\mathrm{sat}) \tag{1.1}$$

$$\frac{\mathrm{d}J}{\mathrm{d}t} = -K_\mathrm{w}\Omega\omega_\mathrm{sat}^2 \left(\frac{R}{R_\odot}\right)^{\frac{1}{2}} \left(\frac{M}{M_\odot}\right)^{-\frac{1}{2}} \qquad (\Omega \geq \omega_\mathrm{sat}) \tag{1.2}$$

Here, K_w is the wind constant and R ($R_\odot$) and M ($M_\odot$) the stellar (Solar) radius and mass, respectively. Ω is the angular velocity and ω_sat the angular velocity above which the magnetic field saturates. This wind-breaking law can explain the persistence of the fast rotators beyond the zero-age main sequence. However, it does not contain any physical interpretation of the saturation of the magnetic field at high angular velocities.

When data of intermediately-aged open clusters became available, Barnes (2003) expanded the thoughts of the previous works and laid the foundation of gyrochronology. In this framework, slow rotators have an interface dynamo which produces the magnetic field

at the tachocline, the boundary between the convective and radiative zone. Fast rotators in contrast have a convective dynamo because their convection zones are weakly coupled to the core and the dynamo is exclusively driven by the convection. As a result, different magnetic field properties arise. The convective dynamo creates a weaker, small-scale magnetic field, which results in the observed less efficient spin-down. As the fast rotators become older the shear between the convection zone and the core creates the interface dynamo. Once established, the star quickly spins down to the slow rotator sequence. In this scenario no saturation of the magnetic field is needed. However, recent observations suggest that the evolution from fast to slow rotation is not a dynamo transition because the magnetic field topology changes slowly with rotation period (Folsom et al. 2016). In addition, See et al. (2019b) observe a saturation of the magnetic field strength for fast rotators.

To explain the evolution from fast to slow rotators, Brown (2014) proposed the metastable dynamo model (MDM) which renders the transition into a stochastic event. In contrast, the evolved fast rotator sequences presented in Barnes (2003) are smooth, which indicates a deterministic spin-down for most of the fast rotators.

Inspired by the MDM, Garraffo et al. (2018) propose that the magnetic field complexity decides on the spin-down strength and that fast rotators have a higher-order magnetic field, which cannot contribute effectively to the spin-down. Accordingly, See et al. (2019a) find that high-order magnetic fields can only contribute to the spin-down if the mass-loss rate is high enough. However, they find high mass-loss rates only for slow rotators. Hence, the high-order magnetic field components do not spin down the fast rotators. Furthermore, See et al. (2019a) always find a significant dipolar component of the magnetic field, even for the fastest rotators.

Despite the vast improvements over the past decades, the evolution from fast to slow rotation is not understood yet. The magnetic field configuration and strength are important parameters but hard to measure because one needs either high-resolution spectroscopy to measure the magnetic effects on the spectral lines, or polarimetric observations. Both techniques require bright targets and/or large telescopes and are therefore limited to the application of a few stars. In contrast, detailed observations of the rotation periods are accessible with small telescopes and can support and constrain the models and theories. For the earliest models large uncertainties on the evolutionary time scales arose because the knowledge of stellar rotation was limited to the Pleiades and the much older Hyades, in which only a few (M dwarf) fast rotators are observed. Observations in intermediately-aged open clusters provide evidence on the transition time scales.

One such open cluster is the 180 Myr-old M 35 for which Meibom et al. (2009) estimated the time scales of the spin-down for different spectral types from its colour-period diagram. They found that G dwarfs evolve off the fast rotator sequence within 100 – 150 Myr, while K dwarfs spin down to slow rotators in 150 – 300 Myr. These time scales were confirmed by observations of the 220 Myr-old open cluster M 34 (Meibom et al. 2011).

In M 34, the fast rotator sequence is well-populated for K stars. Hence, only observations of an older open cluster can constrain their exact spin-down time scales. In this thesis, I observe the two open clusters NGC 2516 and NGC 3532 to estimate those time scales and test the predictions of angular momentum models at the intermediate age. The work is empirical and aims to answer how the rotation periods of fast rotators evolve between the ZAMS (NGC 2516) and 300 Myr (NGC 3532). Further, I will probe the mass-dependence of the evolutionary time scales.

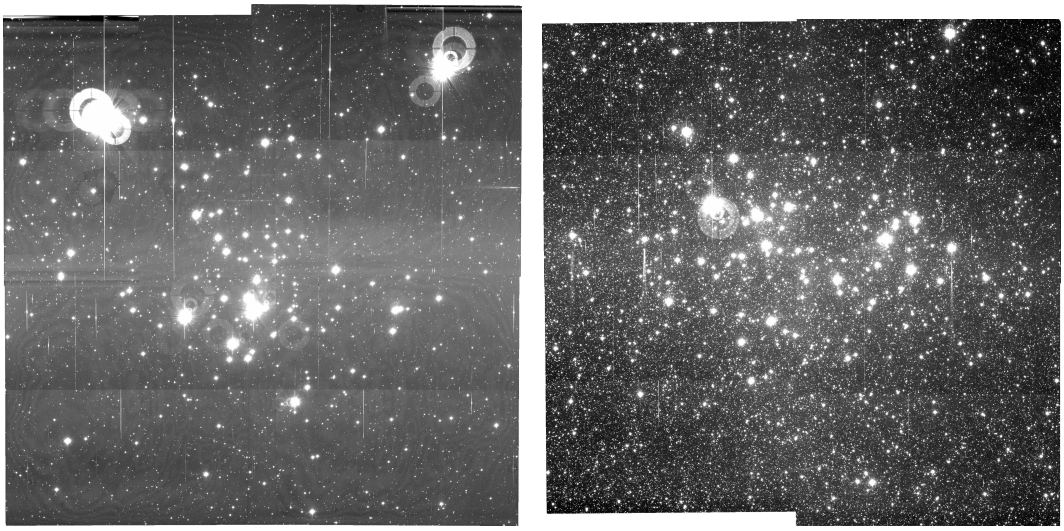

Figure 1.5: Mosaic images of NGC 2516 (left) and NGC 3532 (right) from the CTIO observations. Both images consist of the inner four fields observed in the I_c filter (60 s exposure time) and are ~38′ on each side. The much larger stellar content of the NGC 3532 field is well visible. Despite its richness, only a minority of the stars belong to the open cluster and the majority are background field stars. North is up, East to the left.

1.4 The open clusters NGC 2516 and NGC 3532

The two Southern open clusters NGC 2516 and NGC 3532 are ideal targets to study the evolution of fast rotators. In general, the age-ranked succession of open clusters gives insight into both the evolution of stars of a particular mass and into the mass-dependence of the spin-down. In particular, NGC 2516 with an age of ~150 Myr and NGC 3532 at ~300 Myr provide on the one hand the initial ZAMS rotational distribution and on the other hand an evolved fast rotator sequence.

Important for a detailed understanding of the transition from fast to slow rotation is a well populated colour-period diagram which can only be constructed for populous open clusters. Both, NGC 2516 and NGC 3532, belong to the richest open clusters in the Solar neighbourhood with $\gtrsim$800 and $\gtrsim$1 000 members, respectively. In addition, both open clusters are located in the Southern constellation Carina, making them accessible for ground-based observations at the same time of the year. Fig. 1.5 displays mosaic images of both open clusters from the observations at the Cerro Tololo Inter-American Observatory (CTIO) (see Fritzewski et al. 2020 for details of the observations).

Even more important for this thesis than their richness are their ages, which span the transition from fast to slow rotation well. At the age of NGC 2516 (150 Myr), fast rotators are observed for all masses and it provides the rotational zero-age main sequence distribution. By the age of NGC 3532 (300 Myr), solar-mass stars have already evolved into slow rotators, while lower-mass stars are either in the transition (mid-K dwarfs) or still on the fast rotator sequence (late-K and M dwarfs). Hence, one can observe all phases of the transition in one open cluster, although for different stellar masses.

NGC 2516 is a well studied open cluster with many photometric and spectroscopic studies over the past decades[10]. However, photometric rotation periods were previously

[10] A detailed overview, beyond the short introduction given here, can be found in Fritzewski et al. (2020).

determined only for late-K and M dwarfs (Irwin et al. 2007), while I am interested in G and K dwarfs mainly. The wealth of literature data, including radial velocities even for M dwarfs, enables a detailed membership analysis for the majority of FGKM stars down to $V = 21$.

The mean cluster distance, based on *Gaia* DR2 parallaxes is 409 pc (Cantat-Gaudin et al. 2018) and the cluster stars are slightly reddened ($E_{B-V} = 0.11$, Sung et al. 2002). One reason why NGC 2516 is well studied is that the cluster was thought to be metal-poor and hence to be very different from other open clusters especially the coeval Pleiades cluster. Jeffries et al. (1997) estimated [Fe/H]= −0.3 but later studies found it to be near the Solar value ([Fe/H]= 0.01, Terndrup et al. 2002). Recently, Bailey et al. (2018) measured [Fe/H]= −0.08 from high-resolution spectroscopy.

NGC 3532 is embedded in the Galactic disc ($b = 1.36^\circ$), which complicates the study of this open cluster. In Fig. 1.5, one can easily see the high stellar density in the sky region of NGC 3532, which is much larger than around NGC 2516. As a consequence of the crowded field, NGC 3532 is barely studied compared to other open clusters, even at comparable distances and in the Southern hemisphere. Some studies on the giant stars and the upper main sequence (which can easily be separated from the background) were conducted in the 1980s (e.g. Fernandez & Salgado 1980, Gieseking 1980, Eggen 1981, Claria & Lapasset 1988) but only 23 years later[11] Clem et al. (2011) published CCD photometry of the open clusters down to $V = 22$. Our membership study (Fritzewski et al. 2019, part of this thesis in Chapter 2) is the first work since then on the overall stellar population of NGC 3532[12].

The *Gaia* DR2 parallaxes place NGC 3532 at a distance of 484 pc (Fritzewski et al. 2019), slightly more distant than NGC 2516. Despite its larger distance the cluster stars are hardly reddened ($E_{B-V} = 0.034$, Fritzewski et al. 2019) which facilitates the construction of the colour-period diagram. In Fritzewski et al. (2019), we measure [Fe/H]= −0.07 for dwarf members of NGC 3532. Given the similarity to NGC 2516, it makes the two open clusters an even better pair to study the evolution of the fast rotators.

1.5 Observations of stellar rotation periods

Despite its great physical importance, angular momentum cannot directly be observed or measured. However, the stellar rotational velocity or its rotation period are accessible with different techniques.

Historically, rotational velocities of stars were measured from spectra through rotationally broadened spectral lines (e.g. Abney 1877, Shajn & Struve 1929). The rotational broadening is easily accessible for fast rotating stars with very broad spectral lines and this method can be applied to stars of all spectral types. An additional advantage is that the rotational velocity can be measured from a single observation. However, the main disadvantage is the dependence on the inclination angle i under which the star is seen, because one can only measure $v \sin i$ and not the true rotational velocity. The inclination of the rotation axis is usually unknown and actual rotation periods are superior to $v \sin i$ data. Additionally, slowly rotating stars have narrow lines and high-resolution spectroscopy is needed to measure their rotational broadening.

A complementary approach is time-series photometry which is applied in this work. It uses the fact that solar-like stars have dark starspots and bright faculae in the upper photosphere which rotate in- and out-of-view for an observer (Kron 1947). To measure the

[11] The otherwise unpublished PhD thesis of Barnes (1997) includes standardized photometry of NGC 3532.
[12] A full historic overview is presented in the introduction of Fritzewski et al. (2019).

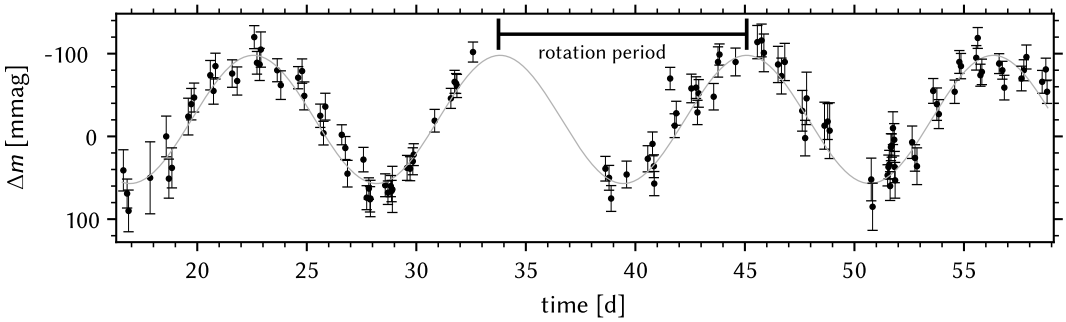

Figure 1.6: Light curve of a rotator in NGC 2516, with the rotation period marked.

rotation period, a star is photometrically monitored and the periodic light variations are interpreted as its rotation period. The photometric time series is called a *light curve* and Fig. 1.6 shows one example with a rotationally induced signal. Although the example shown here is a particularly good case, the data are actual observations of a star in NGC 2516. Due to the interplay between rotation and the magnetic field, younger stars with a stronger magnetic field host larger star spots and are therefore easier to observe. In fact, for stars of solar-age it is very challenging to obtain photometric rotation periods (Barnes et al. 2016).

For centuries, the stellar brightness and variability were estimated by observers looking through a telescope. With the invention of photography, many more stars could be photometrically measured (Miles 2007). However, this technique only allowed the measurement of large variabilities. Yet, only the use of photo-diodes enabled the first detection of stellar rotation periods from photometry (Kron 1947). Despite delivering superior data, photo-electric measurements have the big disadvantage that each star has to be observed individually. Only with the advance of CCD detectors in astronomy, photometric surveys for larger areas on the sky and with high precision became common (e.g. Prosser et al. 1993).

To measure the true astrophysical variability of the stars, one has to adjust the individual observations to each other, such that effects of the airmass and the seeing, as well as the influence of other atmospheric and instrumental changes are removed. With differential photometry, one measures the brightness of the stars in the field relative to each other. To construct light curves, one assumes that, on average, those relative differences are constant. Hence, all changes in the mean value are observational, not astrophysical and can be removed. The true astrophysical photometric signal remains.

Two main methods are used to extract the flux from the CCD images. First, aperture photometry in which the count-rate in a pre-defined area around the stellar position in the image is measured. Second, point-spread function (psf) photometry, which I apply for this thesis. Here, a psf model is fitted to the count rate distribution of each star in the image. The counts enclosed by the model function are converted into the stellar flux for each star. This method is more precise than aperture photometry but computationally more challenging and requires some experience to gain the best results.

From the differential photometry a light curve can be constructed for each source. The light curves are the starting point to measure stellar variability, in particular rotation periods. Unlike the example in Fig.1.6, one can usually not read-off the rotation period easily from the light curve. Hence, several algorithms were developed to search for periodic signals. Broadly speaking, they fall into two categories. Firstly, Fourier-based methods decompose the photometric signal into frequency components with different occurrence rates. Secondly,

phase-folding methods fold the data with different trial periods and measure the smoothness of the phase folded light curve. All methods produce periodograms (frequency spectra) which shows the contribution of each trial period to the overall signal. In the analysis presented in the publications, I use methods from both classes in order to find the correct rotation period. The details of the individual methods are given in Fritzewski et al. (2020).

Although the true rotation periods are best derived from high-quality light curves, stellar activity measurements can help to identify the true rotation periods. Already proposed by Noyes et al. (1984), it is possible to estimate the rotation period from the stellar activity through the rotation-activity diagram. Despite the good relation between the Rossby number and the activity, the uncertainty introduced by the intrinsic scatter of this correlation is large compared to photometric rotation periods. Nevertheless, one can use the stellar activity as a prior in the period search to increase the sensitivity. I apply this method for NGC 3532, where I am able to work off the unique data set with both superb light curves and spectra of the Ca II infra-red triplet.

1.6 Overview on the research papers

Four research papers published in *Astronomy & Astrophysics* form the core of this the thesis. Here, I give a brief overview on the data and analysis while focusing on my contribution in each publication. For all four papers, I am the principal author and I conducted the majority of the data analysis and scientific exploration of the data. A reproduction of the works can be found in the following Chapters 2-5.

1. **Spectroscopic membership for the populous 300 Myr-old open cluster NGC 3532 (A&A 622, A110, 2019)**
   This paper provides a spectroscopic membership analysis of stars in the open cluster NGC 3532. Well-defined membership is crucial for the interpretation of the rotation periods and this work presents the first such membership from spectroscopy for NGC 3532. For this work, we obtained multi-object spectra from the Anglo-Australian Telescope (AAT) in service mode (under proposal S/2017A/02, PI Fritzewski). I reduced the data with the 2dFdr pipeline and measured the radial velocities with IRAF. In addition to those data, Aaron Geller and Søren Meibom obtained multi-epoch spectroscopy of stars in NGC 3532 at the Victor Blanco Telescope. For this publication, I used their measured radial velocities and added them to the analysis. Further radial velocity data were obtained from the literature and public surveys. Beyond the radial velocity analysis, I measured stellar atmospheric parameters for a subset of stars from the AAT observations. The presented membership is based on photometry, radial velocity, proper motions from *Gaia* DR2, and the stellar atmospheric parameters.

   The work described above was conducted by myself with the exception of the radial velocities from Aaron Geller and Søren Meibom. I wrote the initial draft for the publication and gathered feedback from all co-authors.

2. **The rotation period distribution of the rich Pleiades-age Southern open cluster NGC 2516 – Existence of a representative zero-age main sequence distribution (A&A 641, A51, 2020)**
   In this publication, we present the rotation periods for the younger of the two studied open clusters in this thesis (NGC 2516). This work is based on observations carried out by Sydney Barnes and David James with the 1 m SMARTS telescope at the Cerro Tololo Inter-American Observatory from February to April 2008. I used pre-reduced

images from which I measured the stellar flux with psf-photometry. The photometry and the light curve analysis were carried-out by myself with guidance by Sydney Barnes.

In order to fully understand the distribution of rotation periods in NGC 2516, I compiled data from the literature such as photometry, radial velocities, and astrometric measurements and constructed an inclusive membership based on these data. This work is one of the most comprehensive membership studies of NGC 2516 yet and is included in the publication as the foundation of the analysis of the rotation periods.

Beyond the presentation of the rotation periods, I compare their distribution to the Pleiades and other ZAMS open clusters and find no major differences, indicating an environment independent evolution of the rotation periods at young ages, or, as the title states, a representative ZAMS distribution. As for the previous work, I wrote the initial draft and included the comments from the co-authors.

3. **Rotation periods for cool stars in the open cluster NGC 3532 – The transition from fast to slow rotation (A&A 652, A60, 2021)**
   Based on the membership study for NGC 3532, I measure the rotation periods of cluster members and present them in this publication. Since both open clusters were observed contemporaneously in the same observing campaign, the observations and data reduction were carried out by Sydney Barnes and David James, too. The light curve extraction and analysis is identical to NGC 2516 and I used the same software for both data sets.

   The unique age of NGC 3532 makes it an interesting target to study stellar rotation. I evolved the NGC 2516 data forward in time to compare rotational evolution models to the data and find discrepancies which were not reported before. New insights were gained into the evolution and mass-dependence of the transition from fast to slow rotation. Again, I wrote the initial draft and the co-authors contributed with comments and suggestions on the content and its presentation.

4. **A detailed understanding of the rotation-activity relationship using the 300 Myr old open cluster NGC 3532 (A&A 656, A103, 2021)**
   This work uses the synergy of the data sets presented in the other two publications on NGC 3532. From the radial velocity observations, we posses spectra of the Ca II infrared triplet spectral region which is a well-known tracer of the chromospheric activity. The measured stellar activity itself, already provides a picture of the transition from fast to slow rotation. Yet, joining this data set with the photometric rotation periods unlocks the full potential and leads to a detailed and unprecedented understanding of the colour-activity-rotation connection. Additionally, this connection enabled the determination >100 additional photometric rotation periods informed through the chromospheric activity.

   For this work, I developed the main research idea, carried out the data analysis, and wrote the initial draft. The co-authors provided additional ideas, comments, and suggestions to the content of the paper.

2

Spectroscopic membership for the populous 300 Myr-old open cluster NGC 3532

D. J. Fritzewski, S. A. Barnes, D. J. James, A. M. Geller, S. Meibom, and K. G. Strassmeier

Abstract

Context: NGC 3532 is an extremely rich open cluster embedded in the Galactic disc, hitherto lacking a comprehensive, documented membership list.
*Aims:*We provide membership probabilities from new radial velocity observations of solar-type and low-mass stars in NGC 3532, in part as a prelude to a subsequent study of stellar rotation in the cluster. *Methods:* Using extant optical and infra-red photometry we constructed a preliminary photometric membership catalogue, consisting of 2230 dwarf and turn-off stars. We selected 1060 of these for observation with the AAOmega spectrograph at the 3.9 m-Anglo-Australian Telescope and 391 stars for observations with the Hydra-South spectrograph at the 4 m Victor Blanco Telescope, obtaining spectroscopic observations over a decade for 145 stars. We measured radial velocities for our targets through cross-correlation with model spectra and standard stars, and supplemented them with radial velocities for 433 additional stars from the literature. We also measured $\log g$, $T_{\rm eff}$, and [Fe/H] from the AAOmega spectra.
Results: The radial velocity distribution emerging from the observations is centred at $5.43 \pm 0.04\,\mathrm{km\,s^{-1}}$ and has a width (standard deviation) of $1.46\,\mathrm{km\,s^{-1}}$. Together with proper motions from *Gaia* DR2 we find 660 exclusive members, of which five are likely binary members. The members are distributed across the whole cluster sequence, from giant stars to M dwarfs, making NGC 3532 one of the richest Galactic open clusters known to date, on par with the Pleiades. From further spectroscopic analysis of 153 dwarf members we find the metallicity to be marginally sub-solar, with [Fe/H] $= -0.07 \pm 0.10$. We confirm the extremely low reddening of the cluster, $E_{B-V} = 0.034 \pm 0.012$ mag, despite its location near the Galactic plane. Exploiting trigonometric parallax measurements from *Gaia* DR2 we find a distance of 484^{+35}_{-30} pc [$(m - M)_0 = 8.42 \pm 0.14$ mag]. Based on the membership we provide an empirical cluster sequence in multiple photometric passbands. A comparison of the photometry of the measured cluster members with several recent model isochrones enables us to confirm the 300 Myr cluster age. However, all of the models evince departures from the cluster sequence in particular regions, especially in the lower mass range.

This chapter was published in *Astronomy & Astrophysics* 622, A110, 2019, reproduced with permission

2.1 Introduction

In the first recorded description de la Caille (1755) called the southern open cluster NGC 3532 a "prodigious cluster of small stars"[1] and for Herschel (1847) NGC 3532 was "the most brilliant object of the kind I have ever seen". However, NGC 3532 has received little attention in modern times compared with other open clusters in the southern sky. Our radial velocity study confirms Herschel's statement, and this paper is the first in a series that we plan, aimed at transforming NGC 3532 into a canonical young open cluster that can be used by the community for new and detailed astrophysical investigations, e.g. on the rotational dynamo transitions of cool stars (e.g. Barnes 2003).

As regards prior work, an initial photoelectric photometry study was published by Koelbloed (1959), and despite the limited magnitude range of the sample the author was able to derive a distance of 432 pc. Fernandez & Salgado (1980) presented additional photoelectric and photographic photometry for 700 stars in the region of NGC 3532. This was soon followed by a radial velocity study including the Koelbloed sample published by Gieseking (1980, 1981). Further photometric studies in different filters and with additional targets included Johansson (1981), Eggen (1981), Wizinowich & Garrison (1982), Schneider (1987), and Claria & Lapasset (1988). Those studies concentrated on the upper main sequence and the giant branch stars. Surprisingly, no further photometric study of main sequence stars in NGC 3532 was published for 23 years[2] until the recent comprehensive CCD-photometric study of Clem et al. (2011), hereafter referred to as C11. They measured the magnitudes and positions of stars to a depth of $V = 22$ in a 1° field of view.

The distance to NGC 3532 has been estimated using photometry, and also has been directly measured by the Hipparcos mission. The initial reduction, based on eight stars, Robichon et al. (1999), yielded 405^{+76}_{-55} pc. The precision was improved in the new Hipparcos catalogue (van Leeuwen 2009), and found to be essentially the same, 406^{+75}_{-56} pc, based on six stars. In contrast isochrone fitting to the cluster sequence gave a distance of 492^{+12}_{-11} pc (C11). From parallax measurements included in the second *Gaia* data release (*Gaia* DR2, Gaia Collaboration et al. 2018b), Gaia Collaboration et al. (2018a) found 484 pc, reducing the tension considerably.

The age of the open cluster has been estimated by most of the photometric studies. Koelbloed (1959) suggested 100 Myr, based on the absolute magnitude-age relation by Sandage (1957). Both Fernandez & Salgado (1980) and Johansson (1981) estimated 200 Myr, while Eggen (1981) gave 350 Myr. More recent estimates based on isochrone fitting are 300 Myr from C11 and 310 Myr by Mowlavi et al. (2012). Based on white dwarfs in the cluster and mostly independent of the main sequence stars, Dobbie et al. (2012) constrained the age to 300 ± 25 Myr. Modern age estimates for NGC 3532 are all in agreement with 300 Myr and our work will be shown to confirm this.

With the notable exception of the above-mentioned studies by Gieseking (1980, 1981), who obtained objective prism spectra of 84 main sequence stars near the turn-off, most radial velocity studies of the open cluster are from recent times. González & Lapasset (2002) observed 21 of the brightest cluster members and Mermilliod et al. (2008) focused on the cluster giants (8 stars). The latest public spectroscopic surveys RAVE (Steinmetz et al. 2006), *Gaia*-ESO (Gilmore et al. 2012), and *Gaia* (Gaia Collaboration et al. 2016) included some cluster stars but did not specifically investigate the cluster sequence.

The richness of NGC 3532 may also be observed in the number of known cluster white dwarfs. Reimers & Koester (1989) discovered seven white dwarf candidates on photographic plates of which three could be verified spectroscopically (Koester & Reimers 1993). More recently Dobbie et al. (2009, 2012) have confirmed further white dwarfs and Raddi et al. (2016) have discovered an additional candidate. Having seven confirmed white dwarf members makes NGC 3532 a rich source for degenerate objects among Galactic open clusters (Dobbie et al. 2012), further testifying to its value for studies of stellar evolution.

The overall richness of the cluster is apparent in the photometric work by Schneider (1987) and C11, showing NGC 3532 to have a cluster sequence extending deep enough for it to be embedded in the Galactic background field. We aim to identify the cluster members down to its M dwarfs and out to 1° (diameter), in order to construct the corresponding clean cluster sequence.

Finally, we note that with an ecliptic latitude of −56.4° (J2000), NGC 3532 will be in the 54-day observing window of NASA's Transiting Exoplanet Survey Satellite (TESS) mission (Ricker et al. 2015). In the era of exoplanet discovery and characterization, exoplanet hosts in open clusters have particularly high scientific worth because their ages and other properties can be relatively well-determined and ranked (e.g. Sandage 1958, Demarque & Larson 1964, Meynet et al. 1993, Basri et al. 1996, Rebolo et al. 1996, Barnes 2003, Barnes 2007). Knowing the ages of exoplanets and their host stars is of course crucial to better understand their physics and formation history.

This paper is structured as follows. In Sec. 2.2 we construct and present the photometric membership of NGC 3532, enabling the selection of appropriate targets for spectroscopic study. In Sec. 2.3 and Sec. 2.4 we explain our data reduction, leading to the measurement of radial velocities and stellar parameters, respectively. In Sec. 2.6 we present the cluster membership, the cluster sequence it defines, and the comparison with isochrones.

[1] "Amas prodigieux de petites étoiles [...]"

[2] The otherwise unpublished PhD thesis of one of the authors (Barnes 1997) includes standardised and time-series photometry of NGC 3532.

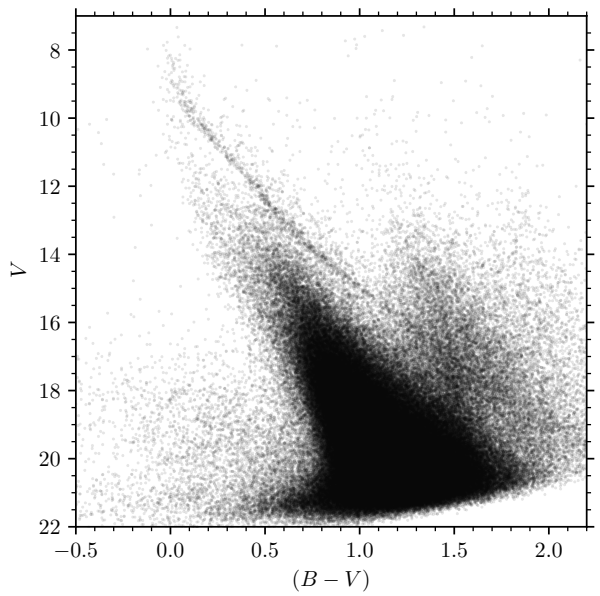

Figure 2.1: The (B, V) colour-magnitude diagram of the NGC 3532 field, based on photometry from C11. A rich and clear cluster sequence is visible against the substantial Galactic disc background field, the latter overpowering it below $V \sim 16$.

2.2 Joint optical and infrared photometric membership

The (B, V) colour-magnitude diagram (CMD) in Fig. 2.1 shows the full stellar content of the probed region, heavily contaminated with background stars. Because a membership list for NGC 3532 is not available in the literature, we constructed a list of joint optical and infrared photometric members. Although we used the photometry of C11 and followed their method for the construction of the single-star photometric cluster sequence, we were careful to also retain the potential photometric binary members.

C11 plotted colour-colour diagrams in $[(V - I_c), (V - J)]$ and $[(V - I_c), (V - K_s)]$, allowing the foreground dwarfs and the background giants to be separated based on the relations of Bessell & Brett (1988) and the appropriate reddening vector. Stars more than 0.5 mag away in colour from the visible cluster sequence were rejected, and after transforming the distance of each star from the sequence into a χ^2-value, they suppressed stars with χ^2 greater than a threshold, and plotted the results in their paper. However, they did not provide the resulting list of candidate members.

We followed the general method of C11, but made certain deviations to suit our purposes, particularly to retain any cluster photometric binaries. We began by matching the $BV(RI)_c$ photometry from C11 with JHK_s photometry from 2MASS (Skrutskie et al. 2006), to construct colour-colour plots in $[(V - I_c), (V - J)]$ and $[(V - I_c), (V - K_s)]$ for all stars common to the two catalogues (see Fig. 2.2). While all stars from C11 were used, we included only those stars from the 2MASS photometry that have a photometric quality flag of A, B, C, or D for all three passbands. With these requirements we retained only the stars with valid detections in all photometric bands. This usage of 2MASS photometry imposes a new brightness limit on our membership, fortunately not adversely impacting our own scientific goals. The cluster sequence in Johnson-Cousins colours can be traced down to at least $V = 21$ but 2MASS is limited to $J = 15.8$, corresponding to $V \approx 19$ (based on the YaPSI isochrones, Spada et al. 2017) for a cluster of NGC 3532's estimated distance and age (492 pc, 300 Myr, C11).

As suggested by C11, we included only stars above both dividing lines

$$(V - J) = \frac{3}{2}(V - I_c) + \frac{2}{5} \tag{2.1}$$

and

$$(V - K_s) = \frac{25}{14}(V - I_c) + \frac{5}{7}, \tag{2.2}$$

separating foreground and background stars (Fig. 2.2). This is possible for NGC 3532 because of the large difference in reddening between the cluster and the field. The cluster itself has low extinction, with $A_V = 0.087$ mag (C11) while the line-of-sight extinction is $A_{V,\mathrm{LOS}} = 3.04$ mag (Schlafly & Finkbeiner 2011). Although, the two sequences of foreground and background stars overlap, most background disc stars can be removed from the sample with this method. Stars in the overlap region of the two sequences could still lie on the cluster sequence in the CMD (especially background giants).

The cluster sequence is clearly visible in the cleaned CMD (discussed below), and can be traced by eye. In contrast to the exclusive selection of C11, we wish to retain the binary cluster members. Therefore, we do not calculate a χ^2-value associated with the distance from the cluster sequence, and instead retain all stars up to 0.1 mag bluer, and up to 1 mag brighter than the hand-traced cluster sequence. As such, our selection includes all potential members from the blue edge of the cluster sequence to the equal-mass binary sequence, the latter situated ~0.75 mag above the cluster sequence. These stars were extracted jointly from both the $[(B - V), V]$ and $[(V - I_c), V]$ CMDs (Fig. 2.3), and are hereafter called *photometric cluster members*. A $[(V - K_s), V]$ CMD (Fig. 2.3, right-most panel) was additionally used to verify that all photometrically-selected cluster members are indeed on the cluster sequence, including in colours not used to extract the members. We observe that this is indeed the case. Within the 1° diameter limit for NGC 3532, we find a total of 2230 stars on the photometric cluster sequence common to both the C11 and 2MASS samples. These are listed in Table 2.1.

The next logical step would normally have been to refine the cluster sequence with the help of the proper motions of the stars on the preliminary (i.e. photometric) cluster sequence. As data from the *Gaia* mission were not

Table 2.1: Photometric dwarf members of NGC 3532 cross-matched with 2MASS and *Gaia* DR2. The proper motion membership is from Sec. 2.5.1.

CLHW	RAJ2000 (°)	DEJ2000 (°)	*Gaia* DR2 ID	2MASS ID	μ_α mas yr^{-1}	μ_δ mas yr^{-1}	PM
85	167.42946	-58.37269	5339436345251570944	11094305-5822217	-10.3164	4.9711	y
206	167.42750	-58.40275	5339430332297021568	11094258-5824099	-5.0697	2.6553	n
451	167.41925	-58.24475	5339438853512774656	11094060-5814411	-10.7149	5.2366	y
485	167.42150	-58.33967	5339436688849023232	11094115-5820228	-4.0350	2.8414	n
530	167.42896	-58.61464	5339403218113480192	11094293-5836527	2.9750	-0.9000	n
...							

Notes. The full table is available at the CDS. *CLHW*: ID from C11; proper motions from *Gaia* DR2; *PM*: proper motion member (y/n).

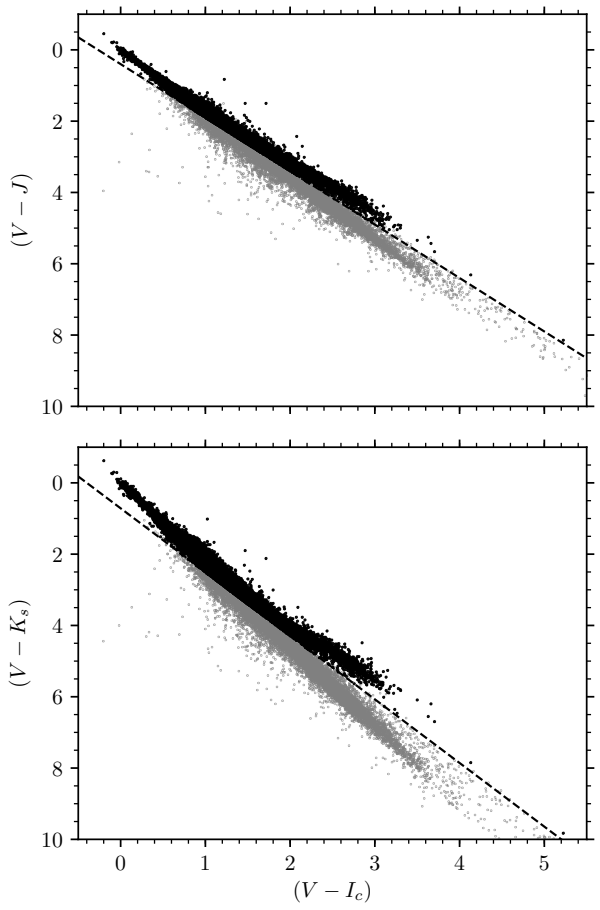

Figure 2.2: Colour-colour diagrams for the NGC 3532 field, showing the lines (see text) separating the retained (above) and suppressed (below) stars. The stars below the indicated lines, are reddened significantly more than the cluster stars and are presumed to be field stars.

readily available at the time of target selection this did not yield any significant additional information because the mean proper motion of the cluster does not differ significantly from the background (c.f. C11 for a detailed analysis). Consequently, we did not include the proper motions and have solely used the photometric membership information to select the targets for the spectroscopic observations. Data from the *Gaia* mission became available after our observing campaigns in the form of UCAC5 (Zacharias et al. 2017) and *Gaia* DR2 (Gaia Collaboration et al. 2018b). We discuss the proper motion of the open cluster later, in Sec. 2.5.1, in the light of those new data and our spectroscopic membership. We also note that initial *Gaia*/TGAS proper motions (Gaia Collaboration et al. 2017) appear to have found bright kinematic cluster members up to 5° from the cluster centre. Lacking dedicated cluster photometry for the outer regions, and with a focus on the inner parts of NGC 3532, we have not included those stars in our sample.

2.3 Radial velocity measurements

We targeted the photometric candidate members in spectroscopic observing campaigns at the Anglo-Australian Telescope and the Victor Blanco Telescope. Here we present the observations, the resultant radial velocity distribution, compare our data to prior work, and include a relatively small number of additional measurements from the literature and public surveys.

2.3.1 Observations

2.3.1.1 AAO

NGC 3532 was observed on 10 and 11 March 2017 in service mode with the AAOmega two-armed spectrograph fed by the 392-fibre 2dF fibre positioner (Lewis et al. 2002) at the 3.9 m Anglo-Australian Telescope at Siding Spring observatory. We used the 1700D grating (R = 10 000) in the red arm, designed for radial velocity studies with the infra-red Ca II triplet (IRT) in the wavelength range from 8340 Å to

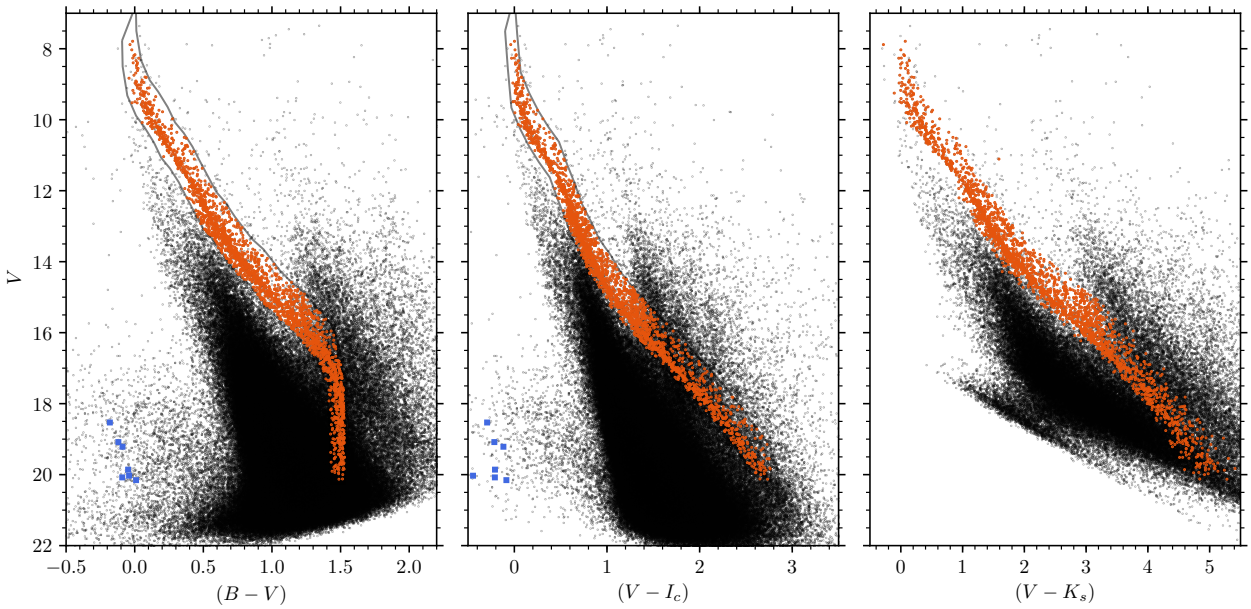

Figure 2.3: Colour-magnitude diagrams for NGC 3532. The left and centre panels include all stars in the C11 catalogue while the right panel shows a CMD in $(V - K_s)$ and V with only the stars common to the 2MASS survey and the C11 sample. The grey stroke outlines the area defined as 0.1 mag bluer and 1 mag brighter than the hand-traced cluster sequence. In orange we show all stars that are both in the defined region, and are part of the dwarf sequence in Fig. 2.2. The seven confirmed white dwarfs in NGC 3532 are also marked (blue squares) in the first two panels.

8940 Å. The blue arm, not useful to us because our targets are too faint for that spectral range, was equipped with the standard grating 580V (R = 1200).

With a field of view of 2°, a large fraction of the cluster could be observed simultaneously, facilitating the target selection. We only targeted the photometric members of NGC 3532 as determined above, and assigned the highest priority to stars for which we have obtained differential photometry time-series[3]. Those stars occupy a somewhat smaller field of view than the photometric study of C11. Correspondingly, lower observing priorities were assigned to stars that lie beyond our photometric monitoring region. However, the guide stars were assigned exclusively from the outer regions to avoid crowding in the inner part where our highest priority targets are situated.

The large field of view allowed us to divide the fibre configurations into two magnitude ranges to avoid fibre crosstalk. In total we observed NGC 3532 with three different fibre configurations, with the cluster centred in the field of view each time (equinox J2000.0, α = 11:05:39, δ = -58:45:12, Wu et al. 2009). From the 392 fibres available 354 (352 in one case) fibres were used for the science targets, 25 were dedicated sky fibres, and 8 (7) fibres were used for the guiding stars. The remaining 13 (16) fibres were not used because they were either broken, or the field was too crowded to position them on a target.

The exposure time was 120 min for the fainter stars (I_c = 15 – 17, which corresponds to V = 16.6 – 19.5) and 30 min each for the two bright configurations (I_c = 12 – 15, corresponding to V = 12.6 – 16.6). Each exposure was split into three sub-exposures to assist in cosmic ray removal. For the bright configurations we were able to achieve signal-to-noise ratios (SNR) per pixel ranging from 20 for the faintest to 160 for the brightest stars. With the longer exposure time for the faint configuration we obtained SNRs between 10 and 80. Calibration files included dark, flat, bias, and arc frames. For the arc frames four lamps containing He, CuAr, FeAr, CuNe were used.

With the time restrictions of service mode we limited our observations to three different fibre configurations. Hence, we were unable to observe all 2230 photometric members determined in Section 2.2, and observed only 1060 stars. The fraction of observed stars from the photometric cluster members is shown in Fig. 2.4 as a function of V. For most magnitude bins we were able to observe approximately half of the photometric members, sufficient for our purpose of constructing a cluster sequence.

2.3.1.2 CTIO

We also include previously-obtained (but hitherto unpublished) multi-epoch multi-object spectroscopy with the fibre-fed Hydra-S spectrograph at the Victor Blanco 4 m Tele-

[3] These data were obtained in order to study the rotation of the cluster's cool stars, and will be published separately (Fritzewski et al. in prep.).

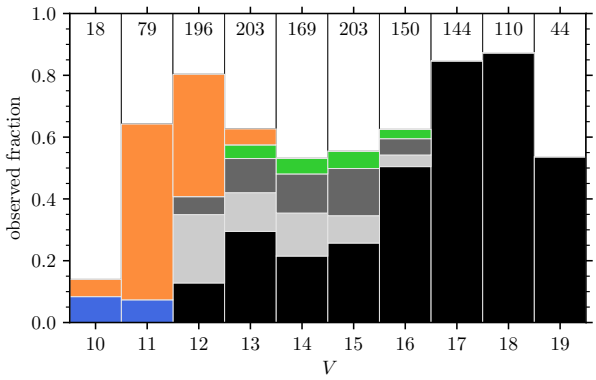

Figure 2.4: Stacked histogram of the fraction of observed photometric cluster members as a function of V. In blue we show the contribution from the RAVE survey (first two bins), in orange from *Gaia* DR2 (V = 10 to 13), and in green from the *Gaia*-ESO survey (V = 12 to 16). The components in black and light grey represent our own observations with only AAOmega and Hydra-S, respectively (V = 12 to 19). In dark grey we show the contribution of stars observed with both instruments (V = 12 to 16). The number in each above each bar indicate the total number of observed stars.

scope at Cerro Tololo Interamerican Observatory (CTIO). The observations were carried out in seven runs over 15 nights from 28 February 2008 to 27 March 2010; an overview of these observations is given in Table 2.2. We used Hydra-S in Echelle-mode with a wavelength-coverage from 5092 Å to 5274 Å (λ_c = 5185 Å, R = 18 500), a dispersion of 0.086 Å px^{-1}, and 1x2 binning. The observing strategy was similar to Geller et al. (2008) and we achieved a single measurement radial velocity precision of 0.8 km s^{-1}.

Fibres were placed on 391 stars selected photometrically from the colour-magnitude diagram in the range from V = 12 to V = 16. This sample has an overlap of 145 stars with the AAO sample. Each Hydra-S field was exposed for 2400 s with up to four exposures in a sequence to remove cosmic rays from the data.

For calibration we obtained nightly ThAr arc frames, dark and bias frames, and flat fields in different configurations. The flat fields were both dome flats and sky flats. For the sky flats the fibres were either arranged in a circle or positioned as on target. We need these multi-configuration flat fields to remove systematics arising from the positioning of the fibres as detailed in Geller et al. (2008).

In total we obtained 1695 radial velocity measurements for 391 individual stars with Hydra-S. Multiple measurements of individual sources also allow us to identify binary stars from their radial velocity variability (see below).

Table 2.2: Observing log for all observations at CTIO and AAO.

Date	Observatory	Fields	Spectra
28 Feb. 2008	CTIO	F1, F2	186
22–24 Mar. 2008	CTIO	F1–F4	337
10/11 Jan. 2009	CTIO	F1, F2	113
30/31 Jan. 2009	CTIO	F3, F4	185
30/31 Jan. 2010	CTIO	F1, F2	184
27/28 Mar. 2010	CTIO	F1–F4	335
25–27 Jan. 2011	CTIO	F1–F4	355
10/11 Mar. 2017	AAO	3 set-ups	1060

2.3.2 Data reduction and radial velocity determination

To reduce and wavelength-calibrate the spectra obtained from AAOmega we used the standard 2dFdr pipeline (AAO Software Team 2015, version 6.28). During pre-processing, the median bias and dark frames were subtracted from each science frame, and cosmic rays were removed. After fitting the image with a scattered light model the spectra were extracted. Those extracted spectra were divided by the fibre flat-fields and wavelength calibrated using ~30 out of 40 available spectral lines in the arc frames. The sky lines were then used for throughput calibration and subsequently removed from the spectra. Finally, the three sub-exposures for each configuration were combined into a single spectrum.

Each combined spectrum was later continuum-normalized with a fifth-order Chebyshev polynomial. The radial velocity shift was measured with the FXCOR routine from IRAF[4] using the PyRAF interface. For the cross-correlation we used seven different template spectra from the synthetic spectral library of Coelho (2014). For the hotter stars the infra-red triplet partly overlaps with lines from the Paschen series, which are not present for cooler stars. On the cool end of our observed sequence, the M dwarfs show TiO and VO bands. We assumed that our sample contains dwarf stars with solar-like metallicity and chose all template spectra to have $\log g$ = 4.5 and [Fe/H] = 0. To achieve a good match between the template spectrum and the observations we divided the data into magnitude bins and assigned a temperature from $T_{\rm eff}$ =[7000, 6000, 5500, 5000, 4750, 4250, 3800] K to each of them. We have not used colour information because the effective temperature is monotonically dependent on the magnitude in the given range. The measured radial velocities were individually corrected for barycentric motion.

The initial uncertainties obtained from IRAF were unrealistic. However, limiting the width of the Gaussian that

[4] IRAF is distributed by the National Optical Astronomy Observatories, which are operated by the Association of Universities for Research in Astronomy, Inc., under cooperative agreement with the National Science Foundation.

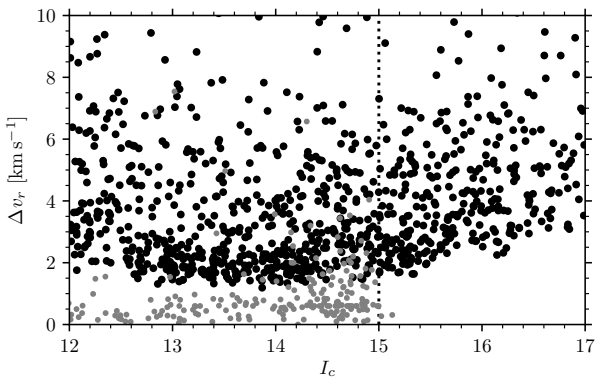

Figure 2.5: Distribution of the radial velocity uncertainties Δv_r against the I_c magnitude of the stars observed with AAOmega (black) and Hydra-S (grey). The dotted line shows the separation between the bright and faint configurations in the AAO campaign.

IRAF uses to fit the cross-correlation peak to 10 pixels helps to achieve a good radial velocity measurement with a reasonable error estimate (Thompson et al. 2016). The lower boundary of the error distribution, shown in Fig. 2.5, is between 1.1 km s^{-1} and 3.2 km s^{-1} depending mostly on the spectral type; we show I_c magnitude as a proxy. As seen from the smooth transition in Fig. 2.5 between the configurations with different exposure times (dotted line) the main contribution to the larger errors for the fainter stars can be attributed to the spectral type, rather than the SNR. Some stars show larger uncertainties because their cross-correlation functions are very wide and the heights are therefore lower. Hence, the height of the cross-correlation peak can be used as a quality indicator and larger radial velocity uncertainties are usually correlated with lower heights.

One reason for poor quality in certain cases could be fast rotation, and therefore broadened spectral lines. We also observe that for the hottest stars in our sample, e.g. those with very strong Paschen lines, the errors are much larger than for stars with weaker Paschen lines. In those cases no good match between the synthetic and the observed spectra could be achieved.

The median error for the (later determined) members of NGC 3532 with a good error estimate ($\Delta v_r < 10$ km s^{-1}) is 2.0 km s^{-1} for the bright sample and 3.8 km s^{-1} for the fainter stars.

The Hydra-S observations were reduced and the radial velocities measured within IRAF. For details we refer the reader to the extensive description and error analysis in Geller et al. (2008). The error distribution of these observations is constant for all magnitudes (see Fig. 2.5) with a median uncertainty of 1.3 km s^{-1}.

2.3.3 Radial velocity distribution

Before joining the two independently-reduced data sets we checked for systematic zero-point offsets. With the overlapping sample of 145 stars we are able to compare the zero-points directly. After removing all known radial velocity variables, 103 stars could be used to calculate the zero-point difference. We found no significant offset, hence we create a joint radial velocity distribution without adjustment.

In addition to our own two data sets we added the radial velocities from the *Gaia*-ESO survey (GES), the RAVE survey DR5 (Kunder et al. 2017) and *Gaia* (Cropper et al. 2018). The GES overlaps only with the AAO observations because the target region of the CTIO observations and the GES are different. We found only a minor zero-point offset ($\Delta v = 0.075 \pm 5.164$ km s^{-1}) which is negligible for the subsequently determined membership probability (because the radial velocity distribution is much wider than the calculated offset). The RAVE data have no stars in common with any other data set because that survey targeted a different magnitude range, not permitting us to test for a zero-point offset. The radial velocities in the RAVE catalogue are similar to the data from all other observations (median 4.4 km s^{-1}) and we can assume that any possible zero-point difference is small.

Although there is overlap between the *Gaia* data and the other data sets, we have not used them to bring the data to a common level because the uncertainties in the Gaia data are much larger than any possible zero-point offset. For this reason we exclude the *Gaia* radial velocities from the fit to the radial velocity distribution, while we include both of the other survey data sets from the surveys. Additionally, for stars with observations from multiple sources we chose ground-based data over *Gaia* radial velocities.

Before fitting the radial velocity distribution with a model we excluded all known radial velocity variable stars (c.f. Sec. 2.3.5) from our combined data set, noting that it could still include binary stars with only one data point. The cleaned sample should give the underlying cluster radial velocity distribution which we fit with a two-component Gaussian mixture model. It combines a strong cluster peak at $v_r = 5.43 \pm 0.04$ km s^{-1} ($\sigma_1 = 1.46$ km s^{-1}) with a low-level, very wide ($v_r = 10.3 \pm 0.9$ km s^{-1}, $\sigma_2 = 26$ km s^{-1}) field component (Fig. 2.6).

The width of the radial velocity distribution is a superposition of the intrinsic dispersion of the cluster, the width resulting from the measurement uncertainties, and some inflation from undetected binaries. Despite the combination of data with differing radial velocity precisions the width is dominated by the largest data set (AAOmega data, 59 per cent of the data points). Combining all data sets increases the width by less than five per cent.

With the obtained model ($\Phi(v_r)$) we calculate the membership probabilities p_{RV} from

$$p_{RV} = \frac{\Phi_{cluster}(v_r)}{\Phi_{cluster}(v_r) + \Phi_{field}(v_r)} \tag{2.3}$$

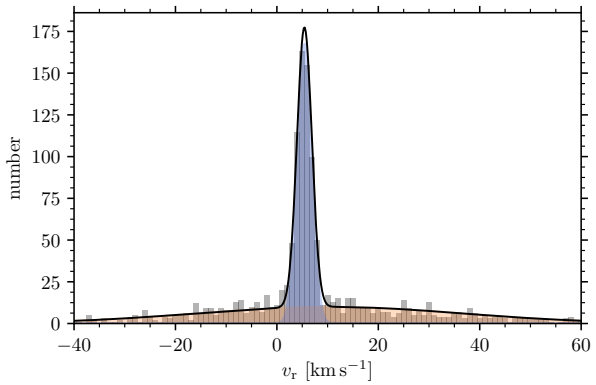

Figure 2.6: Radial velocity distribution of the combined data set. The fitted distribution is a two-component model with a mean cluster radial velocity of $v_r = 5.43\,\mathrm{km\,s^{-1}}$ ($\sigma = 1.46\,\mathrm{km\,s^{-1}}$), and a field component with $v_r = 10.3\,\mathrm{km\,s^{-1}}$ ($\sigma = 26\,\mathrm{km\,s^{-1}}$).

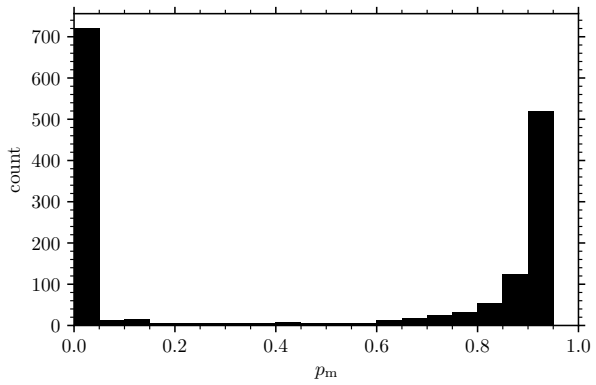

Figure 2.7: Membership probability distribution, p_{RV}, obtained from the model in Fig. 2.6. We include all stars with $p_{RV} > 0.5$ as radial velocity members.

for all stars with measured radial velocities from the data sets mentioned above. The membership probability distribution (Fig. 2.7) is strongly bi-modal. We chose to include all stars with $p_{RV} > 0.5$ as members because the radial velocity members are somewhat spread out at the high probability end, while most of the non-members have membership probabilities near zero. The spread for the radial velocity members is independent of the stellar mass and the radial velocity uncertainties; hence it comes from field star interlopers, the intrinsic cluster dispersion, and undetected binaries. We note that with the chosen threshold some field star non-members are likely included in this sample. We find 819 probable radial velocity member. All membership probabilities together with other data are given in Table 2.3.

2.3.4 Comparison with prior work

Few prior radial velocity measurements are available in the literature. The first study of radial velocities in NGC 3532, based on objective prism spectra, was presented in two papers by Gieseking (1980, 1981). The author measured relative radial velocities for 84 stars and found a mean cluster radial velocity of $4.6\,\mathrm{km\,s^{-1}}$ (relative to a zero point based on the radial velocity of other stars). In the study of González & Lapasset (2002) some of the same stars were observed and the authors estimated the zero point for the Gieseking sample to be $2.4\,\mathrm{km\,s^{-1}}$, and thus a mean cluster radial velocity of $2.2\,\mathrm{km\,s^{-1}}$ relative to the barycentre of the solar system.

Independent of the zero point estimate, González & Lapasset (2002) give a mean cluster velocity of $3.4 \pm 0.3\,\mathrm{km\,s^{-1}}$ from observations of 21 mainly giant stars. The radial velocity study by Mermilliod et al. (2008) targeted eight red giants in NGC 3532 and obtained a mean cluster velocity of $4.3 \pm 0.34\,\mathrm{km\,s^{-1}}$.

First results from the GES were presented in Jacobson et al. (2016). This study included only two stars in NGC 3532 although many more were observed and are provided in the data releases. For the two stars in Jacobson et al. (2016) radial velocities of $3.8\,\mathrm{km\,s^{-1}}$ and $5.8\,\mathrm{km\,s^{-1}}$ were found. The full sample of GES stars was analysed in the joint data set above.

Our mean radial velocity of $v_r = 5.43 \pm 0.04\,\mathrm{km\,s^{-1}}$ is somewhat different from the cluster velocities determined by González & Lapasset (2002) and Mermilliod et al. (2008). Those two studies targeted the massive stars in the cluster, while our sample includes exclusively cooler dwarf stars. Because of the mean velocity differences and the disjunct data sets we have not fitted the whole cluster with a single model. Instead, we refrained from recalculating the membership probability and use the values given by González & Lapasset (2002) and Mermilliod et al. (2008). Additionally, we reanalysed the data of Gieseking (1981) with a two-component Gaussian mixture model. We find the parameters compatible with the widths and positions of the Gaussians estimated by Gieseking (1981) and derive membership probabilities. Later, we define the cluster sequence from the full set of probable members.

2.3.5 Repeated radial velocity observations

The aim of our observing campaign at CTIO was to discern between the single and binary members of NGC 3532. Within three years we obtained up to nine radial velocity data points per star and are able to find candidate single members. Later at AAO, 145 of the CTIO targets were re-observed, extending the time-series to a baseline time-scale of a decade. Single members are easily confirmed and even long-term radial velocity variations may be found in these data.

Table 2.3: Radial velocities and membership probabilities of stars in the NGC 3532 field.

CLHW	RAJ2000 (°)	DEJ2000 (°)	v_r (km s^{-1})	Δv_r (km s^{-1})	$p_{\rm RV}$	PM	M	Class	V (mag)	$(B-V)$ (mag)	$(V-I_c)$ (mag)	$(V-K_s)$ (mag)	Name	Ref.
316006	165.38629	-58.66414	7.30	4.63	0.88	y	m	…	17.43	1.47	1.93	4.06	…	1
316085	165.39042	-58.45367	7.43	2.50	0.87	y	m	…	16.79	1.42	1.62	3.51	…	1
314978	165.39146	-59.01008	5.11	3.67	0.94	y	m	…	18.39	1.46	2.29	4.30	…	1
…														
244323	166.03392	-58.79339	4.08	1.92	0.92	y	m	SM	16.06	1.27	1.41	3.05	ID 203438, CTIO 4_12400	1, 2
244398	166.03617	-58.51553	6.91	2.43	0.91	y	m	U	16.16	1.26	1.43	3.04	ID 102467, CTIO 3_9428	1, 2
244108	166.03654	-58.68747	6.06	1.85	0.94	y	m	SM	16.28	1.33	1.50	3.24	ID 102481, CTIO 3_9384	1, 2
…														
244333	166.03254	-58.91892	27.68	1.97	0.00	n	n	BLN	15.87	1.12	1.21	…	ID 203421, CTIO 4_12409	2
244134	166.03400	-58.91925	12.08	2.54	0.00	n	n	BLN	15.47	1.22	1.30	…	ID 203440, CTIO 4_12376	2
241907	166.05104	-58.85297	4.30	0.43	0.93	y	m	U	16.40	1.45	1.75	3.65	ID 203721, CTIO 4_11972	2
…														
…	164.96744	-59.57667	10.60	…	0.49	…	n	…	8.74	-0.03	…	…	HD 95413, G 2	3
…	164.97040	-58.16675	9.40	…	0.67	…	m	…	8.91	0.05	…	0.25	HD 95412, G 1	3
…	165.03093	-58.34816	2.50	…	0.82	…	m	…	9.37	0.04	…	0.12	HD 95448, G 3	3
…														
315560	165.40133	-58.40169	8.65	11.86	0.59	…	m	…	13.03	0.65	0.60	1.38	…	4
312333	165.42154	-58.99550	-4.95	1.36	0.00	n	n	…	12.60	0.65	0.72	1.58	…	4
313635	165.42483	-58.38972	17.36	2.68	0.00	n	n	…	12.47	0.53	0.59	1.26	…	4
…														
134898	166.71192	-58.68503	4.17	0.37	0.94	y	m	…	15.63	1.15	1.27	…	GES 11065085-5841061	5
123294	166.77296	-58.65750	4.59	0.37	0.95	y	m	…	16.34	1.34	1.51	3.17	GES 11070549-5839270	5
121200	166.78446	-58.74417	5.56	0.37	0.93	y	m	…	15.78	1.19	1.32	2.84	GES 11070825-5844390	5
…														
223513	166.18767	-58.70257	4.60	…	0.98	…	m	BU	8.29	-0.08	0.10	0.03	HD 96213, BDA 155	6
216879	166.22983	-58.74963	3.30	…	0.99	y	m	SM	8.17	0.00	0.02	0.05	HD 96227, BDA 40	6
215077	166.24179	-58.79508	2.00	…	0.97	n	n	SN	8.35	-0.08	0.15	0.23	HD 96246, BDA 50	6
…														
241779	166.05317	-58.72860	-23.05	0.46	0.00	n	n	SN	7.91	0.56	0.79	1.71	HD 96122, BDA 273	7
301535	165.53463	-59.04061	3.64	10.06	0.89	y	m	…	11.97	0.46	0.59	1.25	RAVE J110208.3-590226	8
275139	165.79721	-58.18592	16.07	5.10	0.00	y	n	…	10.87	0.29	0.28	0.67	RAVE J110311.4-581109	8
271266	165.82500	-58.48844	4.45	2.71	0.93	y	m	…	11.33	0.32	0.38	0.82	RAVE J110318.0-582918	8

References. (1) This work, AAO observations; (2) This work, CTIO observations; (3) Gieseking (1981); (4) *Gaia* DR2 (Gaia Collaboration et al. 2018b); (5) *Gaia* ESO Survey DR2; (6) González & Lapasset (2002); (7) Mermilliod et al. (2008); (8) RAVE survey DR5 (Kunder et al. 2017)

Notes. The full table is available at the CDS. *CLHW*: ID from C11; *PM*: proper motions member (y/n); *M*: cluster membership from (mean) radial velocity, spectroscopic analysis, and proper motions (m) member, (n) non-member; *Class*: Membership class for stars with multiple measurements: B: binary, G: background giant, L: likely, M: member, N: non-member, P: photometric (only non-members), S: single, U: unknown multiplicity; V and $(B-V)$ photoelectric magnitudes (Fernandez & Salgado 1980; Wizinowich & Garrison 1982) if available, otherwise from C11, or from Tycho-2 (Høg et al. 2000), I_c: C11; K_s: 2MASS; *Name*: ID: this work, CTIO: this work CTIO observations, G: Gieseking (1981), GES: *Gaia* ESO Survey, BDA: Mermilliod (1992). The *Gaia* DR2 IDs can be found in Table 2.1.

We have obtained more than one observation for 334 of the 372 observed stars and at least three for 276 stars. We analysed the radial velocity time-series by visual inspection and with the e/i-statistic (Geller et al. 2008), where e is the standard deviation of the radial velocities and i the precision. The e/i threshold used is 4. Among the stars with multiple observations we find 41 radial velocity variables, of which 27 can be identified as likely binaries with oscillating radial velocities. The remaining 14 have too few data points to draw firm conclusions. We have not attempted to determine a γ velocity for the likely binaries because the time-series contain too few data points at present to solve the orbits.

We have assigned labels to the data in Table 2.3 on the basis of these time-series. They include B for binary, S for single star and U for unknown variability, the latter the result of having to too few data points[5]. For all stars with multiple measurements we calculated a mean radial velocity which we use for our analysis.

Having obtained only a single observation at AAO we do not know whether stars in this data set have constant radial velocities. Despite this uncertainty we have included all stars with a single measurement from the AAO into the determination of the membership probabilities. Consequently, some of these stars could potentially be binaries, and their observed orbital velocities could disguise their true membership status. Additionally small radial velocity variability could potentially widen the radial velocity distribution.

Assuming the Gaussian two-component model to be correct, we can also deduce membership for the radial velocity variables. For each variable star we calculate the mean radial velocity and apply the trained model to it. We publish the membership probabilities determined through this method as is, but note that they should be used with care[6].

2.4 Additional stellar parameters from the spectra

To obtain information beyond the radial velocities from the AAOmega spectra (see Fig. 2.8 for three examples) we used the software SP_Ace (Stellar Parameter And Chemical abundances Estimator, Boeche & Grebel 2016, version 1.1) which estimates the stellar parameters based on polynomial fits to the equivalent widths of several spectral lines. The parameters for those fits are stored in the General Curve-Of-Growth library (GCOG) which is included in SP_Ace. GCOG is based on calibrated[7] oscillator strengths from the line list of the Vienna Atomic Line Database (VALD, Kupka et al. 1999) and 1D atmospheric models synthesized from ATLAS9 (Castelli et al. 1997) under LTE assumptions.

[5] Labels were only assigned to stars with multiple observations from our own data sets and known binaries from other data sets.

[6] The stars in question have a class label of either B or U.

[7] Boeche & Grebel (2016) use the Sun, Arcturus, Procyon, ϵ Eri, and ϵ Vir for calibration.

The best-fitting grid point from the GCOG library is determined through an iterative Levenberg-Marquardt minimization routine. To find the stellar parameters and abundances the equivalent width of that grid point is used. SP_Ace can also output a synthetic spectrum based on those parameters. One illustrative example is shown in Fig. 2.8 (bottom panel). For this spectrum SP_Ace achieved $\chi^2 = 1.06$. This fit is representative of our analysis where more than 90 per cent of the successful fits have $\chi^2 < 1.2$.

The grid of SP_Ace is restricted to $T_{\rm eff} > 3600$ K, a fact which implies that parameters cannot be estimated for the coolest stars in our sample. In any case, stars in our sample with $T_{\rm eff} < 4000$ K do not have reliable measurements due to their faintness and the low SNRs of their spectra.

The estimated stellar parameters include effective temperature ($T_{\rm eff}$), gravity ($\log g$), and various abundances, particularly the iron abundance ([Fe/H]) relative to the Sun. [Fe/H] can be measured from ~ 60 lines in the spectral range, where the exact number depends on the SNR. The typical uncertainties arising in the analysis of the AAOmega spectra are $\Delta T_{\rm eff} = 100$ K, $\Delta \log g = 0.23$, and Δ[Fe/H] = 0.06. Apart from the figures presented in this work (e.g. Fig. 2.9) we have tested the results of SP_Ace for consistency with additional checks. For example we have checked that $T_{\rm eff}$ plotted against colour shows a clear cluster sequence.

We were able to estimate atmospheric parameters for a total of 355 stars in our sample. The individual values for each star are given in Table 2.4.

2.4.1 Surface gravity and effective temperature

The derived $\log g$ and $T_{\rm eff}$ values are displayed in Fig 2.9, in combination with our derived membership status. We find 93 (out of 233) dwarf stars ($\log g > 4.0$) with obtained surface gravity to be radial velocity non-members. This shows that in the field of NGC 3532 there is a significant field contamination from foreground stars.

The photometric membership list is also contaminated by a population of (background) giant stars which we were unable to remove through the colour-colour diagrams. In the CMDs (Fig. 2.3) a background component crosses the cluster sequence at $(B - V) = 1.3$ which matches the reddened stellar parameters of the giant stars ($T_{\rm eff} \approx 5300$ K and $(B-V)_0 \approx 0.9$). Among the giants we find several radial velocity members which we can now remove from the sample of cluster members in order to obtain a cleaner cluster sequence, reducing the number of probable members to 804. We therefore see that obtaining the additional parameters $\log g$ and $T_{\rm eff}$ from the spectra can help to clean up the sample of cluster members beyond the radial velocity information.

With the additional information about background giant stars we recalculated the radial velocity distribution but found only minor differences from the initial distribution. Hence, we do not update the membership probability

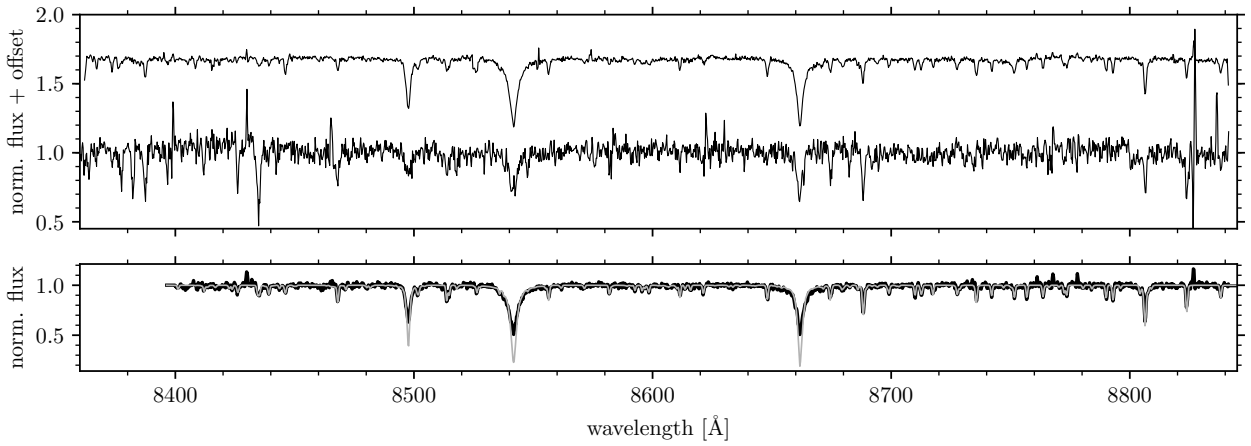

Figure 2.8: Spectra for three stars of our sample observed with AAOmega. *Top:* Examples for a spectrum with a high SNR (SNR~ 150, I_c = 12, upper) and a spectrum with a low SNR (SNR~ 15, I_c = 17, lower). *Bottom:* spectrum of a solar-like radial velocity member (black) with the best fit by SP_Ace shown in light grey.

Table 2.4: Stellar parameters obtained from the spectra using SP_Ace.

CLHW	ID	RAJ2000 (°)	DEJ2000 (°)	p_{RV}	T_{eff} (K)	ΔT_{eff} (K)	log g	Δ log g	[Fe/H]	Δ[Fe/H]
310132	800249	165.44771	-58.87789	0.94	5471	133	4.41	0.23	-0.15	0.07
309783	800325	165.45367	-58.80531	0.74	5264	107	4.72	0.19	-0.26	0.06
300827	802057	165.54779	-58.81253	0.89	4684	127	4.50	0.24	0.02	0.07
299782	802295	165.55558	-58.90439	0.94	5464	164	4.24	0.36	-0.03	0.08
294532	803729	165.61046	-58.64156	0.00	6495	479	3.72	0.67	0.10	0.11
291918	804397	165.62996	-58.85247	0.00	6153	178	4.04	0.33	0.02	0.04
...										

Notes. The full table is available at the CDS. *CLHW*: ID from C11; *ID*: ID this work; *RAJ2000*, *DEJ2000*: from C11.

and continue with the previously calculated values while marking the background giants as non-members.

2.4.2 Abundances of NGC 3532

A number of prior estimates for the metallicity of NGC 3532 are available in the literature. The first photometrically determined metallicity was presented by Claria & Minniti (1988) [Fe/H] = 0.08 ± 0.08 while the first spectroscopic study by Luck (1994) found [Fe/H] = 0.07 ± 0.06 for the cluster giants.

A photometric estimate from DDO photometry by Piatti et al. (1995) gave [Fe/H] = −0.10±0.09, also for red giants. The same data and additional *UBV* photometry were used by Twarog et al. (1997) who reported [Fe/H] = −0.02 ± 0.09 for the same set of stars.

Gratton (2000) recalibrated all the prior studies and found [Fe/H] = 0.02 ± 0.06. Cayrel de Strobel et al. (2001) listed eleven giant stars, of which six are radial velocity members of NGC 3532 with a mean metallicity of [M/H] =

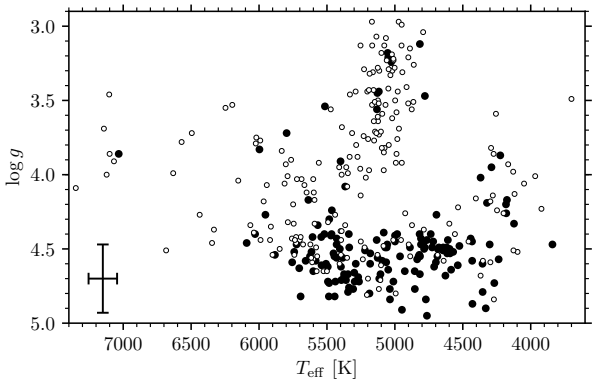

Figure 2.9: Gravity (log g) against effective temperature (T_{eff}) for stars observed spectroscopically with AAOmega. Filled circles are radial velocity members while the unfilled ones are non-members. Some radial velocity members are found among the background giant population. In the lower left we show the typical errors.

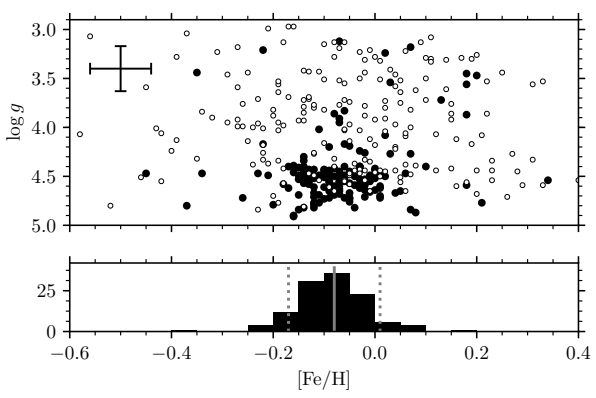

Figure 2.10: *Top:* Gravity ($\log g$) dependence on the iron abundance ([Fe/H]) relative to the Sun for radial velocity members (filled) and non-members (unfilled). The typical individual measurement error is given in the upper left corner. *Bottom:* Histogram of the iron abundance, including only the cluster dwarfs ($\log g > 4$). The median value of the distribution (solid line) is $[\mathrm{Fe/H}]_{\mathrm{cluster}} = -0.07 \pm 0.1$. The dashed lines show the standard deviation.

0.06. Santos et al. (2012) compared different line lists and found a range from [Fe/H] = −0.06 ± 0.07 to [Fe/H] = 0.03 ± 0.03 for giants in NGC 3532.

The RAVE survey was the first to publish metallicities for dwarf stars in NGC 3532. From seven stars Conrad et al. (2014) found [M/H] = −0.021 ± 0.057. From high-quality spectra of four stars Netopil et al. (2016) found [Fe/H] = 0.00 ± 0.07 and a photometric metallicity estimate by Netopil (2017) gave [Fe/H] = 0.0 ± 0.06 for giants stars and [Fe/H] = 0.02 ± 0.12 from 49 dwarfs. The GES data release 2 unfortunately does not have metallicity estimates for NGC 3532.

All of these suggest a cluster with near-solar metallicity value, with an error in the range of 0.1 dex. We note that most prior estimates were made for a small sample of giant members and not the dwarf stars in NGC 3532. With our observations of solar-like stars from NGC 3532 we now have a large sample of dwarf stars at hand.

SP_Ace is capable of measuring several different abundances from the spectra. Because of the relatively low SNR we chose to use only the [Fe/H] values in this study. The mean cluster iron abundance, measured from the 139 radial velocity dwarf members, is [Fe/H] = −0.07 ± 0.10.

The metallicity distributions for both the members and non-members are shown in Fig. 2.10, including a histogram for the cluster dwarf members. Although a solar-like metallicity for the open cluster is within the uncertainties, the determined mean metallicity is slightly sub-solar.

2.5 Astrometric data from *Gaia*

With the information from *Gaia* DR2 (Gaia Collaboration et al. 2018b) becoming available after our observation, we have the possibility of verifying the proposed members with precise astrometric parameters. We first use the proper motions, and analyse whether they are suitable for refining the cluster sequence. Second, we turn to the parallaxes to calculate the cluster distance.

2.5.1 Proper motions of cluster members

Knowing the radial velocity members of NGC 3532, we can extract additional information from the proper motions. From the precise proper motions provided in *Gaia* DR2, with uncertainties $\lesssim 0.1\,\mathrm{mas\,yr^{-1}}$, we can derive clean cluster membership. In Fig.2.11 we plot in the left panel all stars in the field. The open cluster and the field are inseparable, due to the large number of stars in the area. Even in a density plot the separation is not easy to achieve. We show in the right panel only the proper motions of the photometric cluster members for which we have obtained radial velocities. From the analysis of the spectra we can split these stars into three groups: radial velocity members, non-members and background giant non-members.

The most obvious feature is the tight clustering of radial velocity members around $\mu_\alpha = -10.37 \pm 0.16\,\mathrm{mas\,yr^{-1}}$, $\mu_\delta = 5.18 \pm 0.08\,\mathrm{mas\,yr^{-1}}$ marked in Fig. 2.11 with dashed lines. This centre is the mean proper motion of the radial velocity members in this clustering with the uncertainty given by the standard deviation. The proper motion found for NGC 3532 is marginally in agreement for μ_α with the published proper motion from both Hipparcos ($\mu_\alpha = -10.84 \pm 0.38\,\mathrm{mas\,yr^{-1}}$, $\mu_\delta = 5.26 \pm 0.37$ Robichon et al. 1999) and *Gaia*/TGAS ($\mu_\alpha = -10.54 \pm 0.03\,\mathrm{mas\,yr^{-1}}$, $\mu_\delta = 5.19 \pm 0.04\,\mathrm{mas\,yr^{-1}}$, Gaia Collaboration et al. 2017). Our value though is (unsurprisingly) confirmed by Gaia Collaboration et al. (2018a), who found a very similar proper motion for NGC 3532 ($\mu_\alpha = -10.3790 \pm 0.0079\,\mathrm{mas\,yr^{-1}}$, $\mu_\delta = 5.1958 \pm 0.0079\,\mathrm{mas\,yr^{-1}}$) also from *Gaia* DR2.

Although the centre of the cluster proper motions is well-defined, some radial velocity members are scattered over the whole proper motion plane. We chose to include all stars within a radius of $1.3\,\mathrm{mas\,yr^{-1}}$ around the cluster centre in proper motion space as proper motion members (circle in Fig. 2.11) because out to this radius the number of proper motion members increases non-linearly with radius. For larger radii the linear increase of proper motion members observed can be attributed to field stars, while the non-linear increase is due to the clustering of stars. The radial velocity members follow the same pattern, a fact which gives us confidence about the chosen cut-off value. Among the included stars we find 58 radial velocity non-members, each of which could potentially a be binary (because we have only obtained a single radial velocity measurement for these stars). However, at least six of the proper motion members have multiple radial velocity observations and are

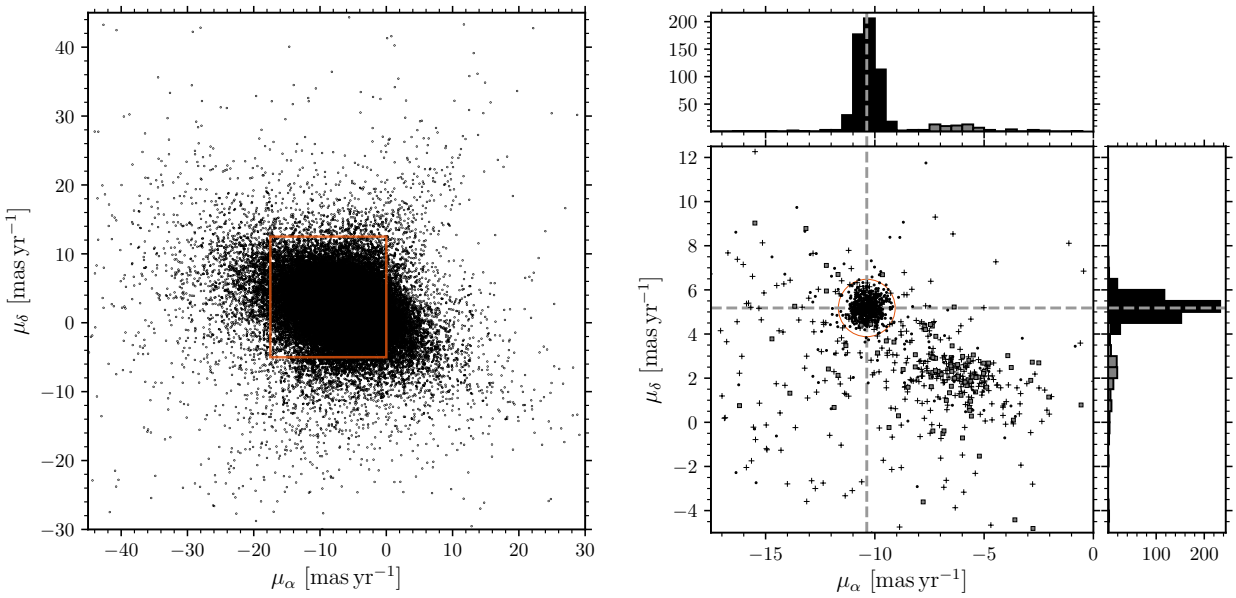

Figure 2.11: Proper motion diagram of the NGC 3532 field. *Left:* All stars common to the catalogues of C11 and Gaia DR2. In this plot no difference between the proper motions of the field and cluster stars is visible. *Right:* Same as left but zooming in on the region outlined on the left, with the sample limited to the spectroscopically observed stars. Here the cluster (black dots) is distinguishable from the field (crosses and grey squares). We have separated the field into the background giant component (grey squares) and the foreground component(crosses). The histograms show the distribution of radial velocity members (black) and background giant stars (grey). The dashed lines give the centre of the distribution of the members ($\mu_\alpha = -10.37 \pm 0.16$ mas yr^{-1}, $\mu_\delta = 5.18 \pm 0.08$ mas yr^{-1}) and the circle defines the region of proper motion members.

classified as single non-members, a fact which demonstrates that background contamination remains in the proper motion membership. After all proper motion membership, like that from radial velocities, is probabilistic. The proper motion membership is given in a column in Tables 2.1 and 2.3. By jointly demanding both radial velocity and proper motion membership, we define an exclusive set of bona fide cluster members which are listed as *m* in the joint membership column (*M*) in Table 2.3.

In Fig.2.11 we also highlight the background giant stars from our photometric membership. Those stars might be assumed to define the "field". Their proper motion is centred on $\mu_\alpha \approx -5$ mas yr^{-1}, $\mu_\delta \approx 5$ mas yr^{-1}. In the absence of better information C11 assumed $\mu_\alpha = 0$ mas yr^{-1}, $\mu_\delta = 0$ mas yr^{-1}. The giant stars show a wider distribution in the proper motion plane than the compact cluster. Noticeable in this context are the stars identified as radial velocity members but with a low log *g*. Among those giants with the same radial velocity as the open cluster we find some which even have very similar proper motions. This is a consequence of the low proper motion of NGC 3532 combined with the wide distribution of proper motions of field stars. This validates our cautious approach to assignment of cluster membership based on photometry, radial velocity, or proper motion alone. Sometimes spectral analysis is the only way to uncover false-positives.

2.5.2 Astrometric distance to NGC 3532

Gaia DR2 has provided parallaxes for most of the stars in our sample of cluster stars. We have included all sources with positive parallaxes and relative uncertainties less than 10 per cent. In our case we use the provided parallaxes regardless of the known correlations on small scales because we use a simple mean to estimate the distance (Bailer-Jones et al. 2018). Other known systematics of the *Gaia* DR2 include a small zero-point offset of the parallaxes which is dependent on the sky position, and dependencies of the parallax measurements on colour and magnitude (Lindegren et al. 2018). All effects are superseded by the uncertainties and the spread of parallaxes in the cluster. Additional, presently unknown, global and local systematics might be included in the data but should not be relevant to our aim of determining the distance to the open cluster.

In order to compute the mean parallax of the cluster we chose to use only the stars which are proper motion and radial velocity members. From this set of stars we find $\varpi = 2.068 \pm 0.139$ mas (484^{+35}_{-30} pc), a value which is beyond that from the Hipparcos results (406^{+76}_{-56} pc). Our distance agrees with the 484 pc from the Gaia Collaboration et al. (2018a). We note that this distance is simply the mean distance of

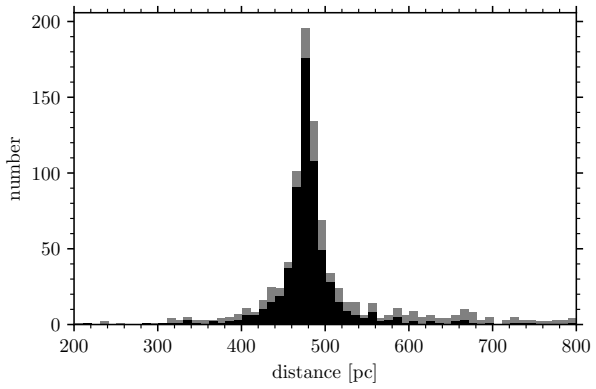

Figure 2.12: Distribution of Gaia distances for stars with measured radial velocities. The distribution of radial velocity members is shown in black, while the background (grey) includes all stars. The mean cluster distance (inferred from the parallaxes) is 484^{+35}_{-30} pc. We only show a distance range near the open cluster.

the members and not the centre of mass distance. This value certainly agrees with the isochrone fitting distance of C11 (492^{+12}_{-11} pc), reducing the tension between the prior astrometric distance and theoretical models.

In Fig. 2.12 we show the distribution of distances to illustrate the size of NGC 3532. For this figure we use the individual distances provided by Bailer-Jones et al. (2018). The peak indicating the cluster position is prominent, but the distribution is very wide for an open cluster. We find a number of radial velocity members which are 80 pc closer or more distant to the Sun than the cluster centre in this distribution. Those stars are not only radial velocity–but also *Gaia* DR2 proper motion members. The Pleiades for comparison have a radius of ~ 10 pc, using the members from Gaia Collaboration et al. (2018a). NGC 3532 is probably intrinsically more extended or has tidal tails like the Hyades (Meingast & Alves 2019; Röser et al. 2018). In view of this issue we do not use the distance as a membership criterion.

2.6 Final Membership, cluster sequence, and isochrones

With the above-presented analysis of the radial velocities, stellar parameters, and proper motions we have found an exclusive and final set of 660 cluster members among 1613 spectroscopically observed photometric members[8]. By *exclusive* we mean that all relevant criteria (photometry, radial velocity, and proper motion) are fulfilled without exceptions, creating a high quality data set for further studies of NGC 3532. These are the members shown in the following CMDs in this paper.

[8] This number includes all observations of unique stars presented in this work and the data from the literature.

We present the exclusive members under column *M* in Table 2.3, together with all other radial velocity data, including both data from this study and the literature. We give the position of the star, its radial velocity, membership probability, the proper motion membership, the V magnitude, and colours in $(B-V)$, $(V-I_c)$, and $(V-K_s)$. The V magnitude and the $(B-V)$ colour are photoelectric measurements from Fernandez & Salgado (1980) and Wizinowich & Garrison (1982) where available, and CCD photometry from C11 otherwise. The column *Ref.* gives the original publications for the radial velocity data. Furthermore, we included the identifiers from C11 for all stars that were observed in that study. Additionally, we give the identifiers assigned to the stars by the various studies including our own numbers and the labels for stars with multiple observations from Sec 2.3.5.

In the rest of this paper we will work with this set of 660 exclusive members. First, we construct an empirical cluster sequence, tracing the locus of the open cluster in several colour-magnitude diagrams. Next, we compare various isochrone models to the observed cluster stars and finally, we estimate the total number of stars in this open cluster.

2.6.1 Empirical cluster sequence

A defining characteristic of an open cluster is the single-star main sequence along which almost all the members are distributed. With the set of exclusive members we can trace this main sequence in a CMD and construct a cluster sequence from the locus of the stars.

In order to accomplish this we plot CMDs in $(B-V)$, $(V-R_c)$, $(V-I_c)$, and $(V-K_s)$ against V. In addition we make use of the excellent photometry provided by *Gaia* DR2. The $[(B_p-R_p), G]$ CMD is shown in Fig. 2.13. In each of these CMDs we trace the cluster sequence manually and tabulate the colours for fixed magnitudes. In order to improve the accuracy we use colour-colour diagrams and corrected small deviations. A magnitude-magnitude diagram helped us to find a smooth transformation between V and G. In Fig. 2.13 we present this final cluster sequence in the *Gaia* photometric system. We display the data (exclusive cluster members) on top of the cluster sequence to emphasise the good match.

In Table 2.5 we present the data for the cluster sequence in two photometric passbands and five different photometric colours. For the two photometric passbands we converted the magnitudes to absolute values using the *Gaia* distance. All data were de-reddened. We use the coefficients from Johnson (1968) and for the *Gaia* photometry we applied the relations from Jordi et al. (2010).

This cluster sequence can be used in future for comparison with other open clusters. Our sequence reaches down to ~ 0.35 $M_\odot$, equivalent to a spectral type of M3V. We placed the brighter end of our sequence near the turn-off which, for NGC 3532 is populated by A0V stars with M ~ 2.6 $M_\odot$.

Table 2.5: Empirical cluster sequence of NGC 3532 with M_V and M_G as well as several photometric colours. All data was de-reddened and shifted with the *Gaia* distance.

M_V	M_G	$(B-V)_0$	$(V-R_c)_0$	$(B_p-R_p)_0$	$(V-I_c)_0$	$(V-K_s)_0$
0.48	0.48	-0.014	0.008	0.001	-0.005	0.01
0.98	0.98	0.046	0.009	0.021	0.025	0.11
1.48	1.46	0.106	0.038	0.101	0.065	0.22
1.98	1.98	0.171	0.083	0.171	0.165	0.37
2.48	2.44	0.246	0.143	0.331	0.260	0.55
2.98	2.90	0.336	0.198	0.471	0.365	0.77
3.48	3.38	0.416	0.243	0.581	0.470	1.01
3.98	3.91	0.486	0.278	0.651	0.545	1.16
4.48	4.33	0.566	0.323	0.731	0.630	1.34
4.98	4.84	0.646	0.363	0.821	0.685	1.51
5.48	5.28	0.751	0.418	0.931	0.770	1.72
5.98	5.78	0.851	0.473	1.051	0.865	2.06
6.48	6.23	0.966	0.533	1.161	0.995	2.30
6.98	6.68	1.086	0.638	1.311	1.155	2.55
7.48	7.03	1.206	0.718	1.451	1.335	2.87
7.98	7.48	1.336	0.783	1.611	1.495	3.20
8.48	7.85	1.406	0.863	1.761	1.665	3.51
8.98	8.23	1.446	0.918	1.881	1.845	3.73
9.48	8.65	1.466	0.973	2.031	2.045	4.01
9.98	9.01	1.476	1.023	2.181	2.225	4.31
10.48	9.46	1.486	1.073	2.301	2.345	4.53
10.98	9.78	1.496	1.113	2.381	2.465	4.81

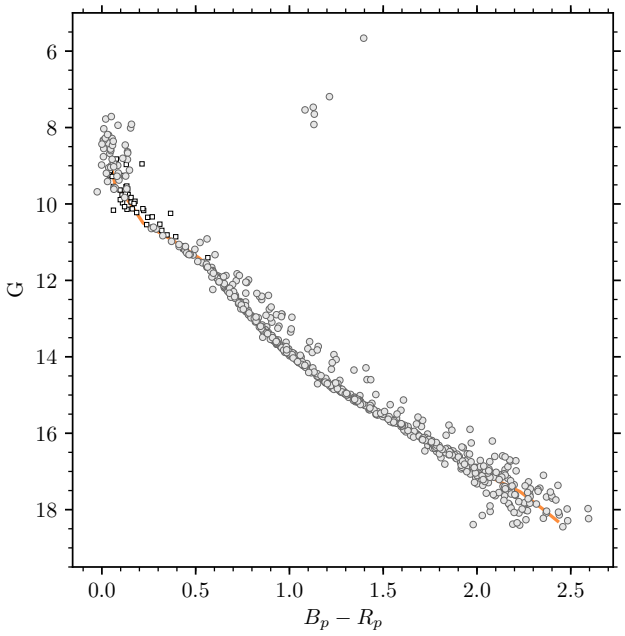

Figure 2.13: Colour-magnitude diagram of the exclusive set of members from *Gaia* photometry. In the background we show our empirical cluster sequence (see. Table 2.5).

2.6.2 Comparison with isochrones

The large number of cluster members identified enables us to compare the observations in detail to theoretical isochrones. In Fig. 2.14 we show the cluster members from the giant branch through the turn-off down to the low-mass stars. The membership is nearly complete for the inner 1°region of NGC 3532 from the brightest stars in NGC 3532 down to $V = 10$. In Fig. 2.14 a sparsely populated region of radial velocity members between $V = 10$ and $V = 13$ is visible. In this region the only data available come from the RAVE survey. To fill the gap we include in Fig. 2.14 and 2.16, for the inner 1°of NGC 3532, the members from the *Gaia*/TGAS proper motions (Gaia Collaboration et al. 2017). Due to the paucity of radial velocity members in this region it would be of interest for later studies to complete the radial velocity cluster sequence. Both the GES and the present study concentrate on the fainter regions of the CMD and have preferentially probed the cool stars.

For the comparison with isochrones in this subsection we use the already measured metallicity (Sec 2.4.2) and distance (Sec. 2.5.2) and will determine the age and the reddening towards NGC 3532.

We have not fitted an isochrone automatically to the data for several reasons. First, there is a well known, but not yet fully understood, deviation of the isochrones for

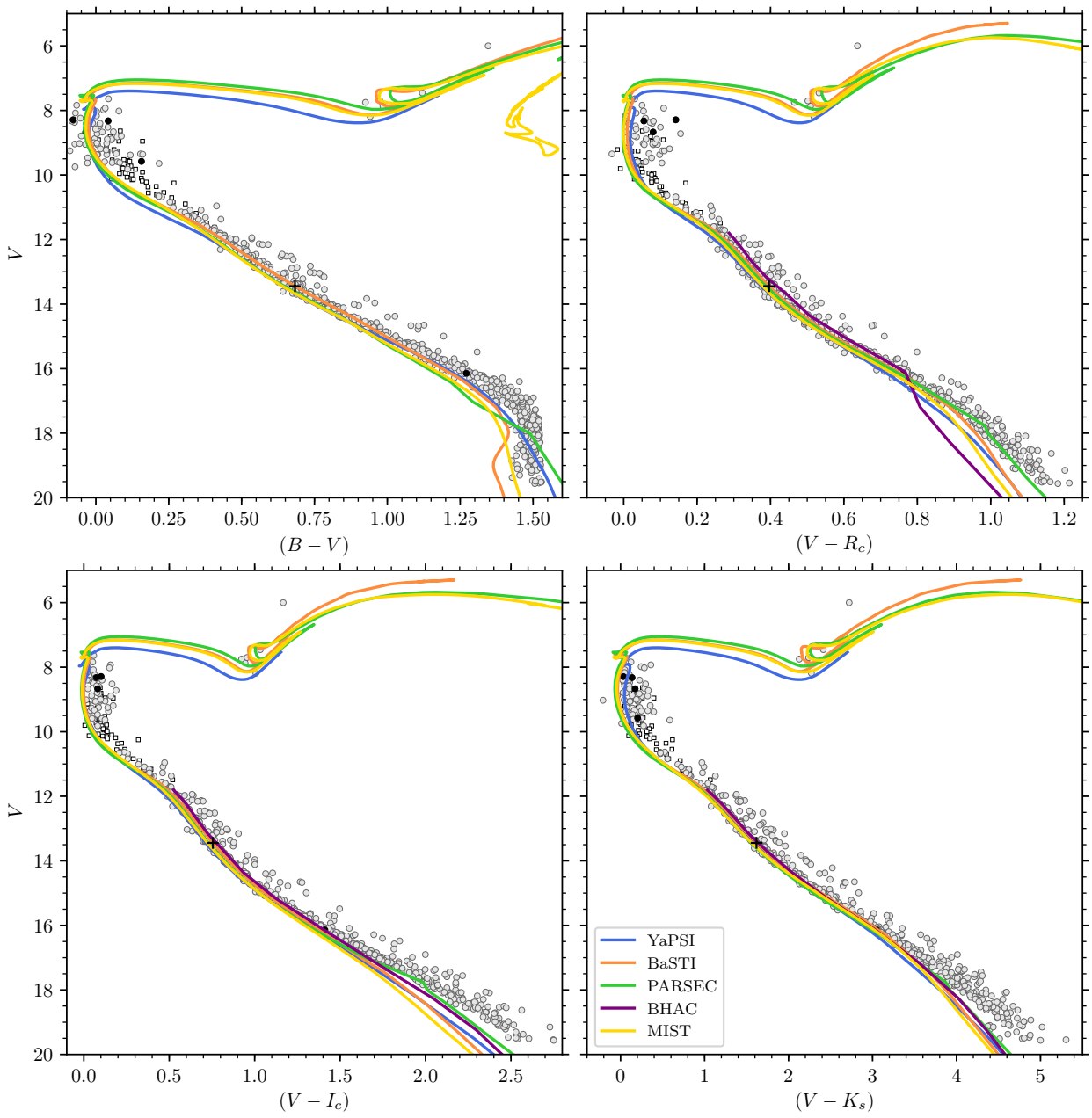

Figure 2.14: Radial velocity single cluster members (grey circles), (likely) binary members (black circles) and additional Gaia/TGAS proper motion members (white squares) of NGC 3532 in four colour-magnitude diagrams. For comparison with each other and the data we show the YaPSI (blue), PARSEC (green), BaSTI (orange), MIST (yellow), and BHAC (purple, not available in $(B-V)$) models. The solar-mass model for 300 Myr is marked with a black plus sign.

the lowest-mass stars which is mainly an effect of the transformations between stellar model parameters and intrinsic colour used in the isochrones (Baraffe et al. 2015; Spada et al. 2017). Second, we lack radial velocity members in the range V = 10 to 11. This can be filled in with the proper motion members from Gaia Collaboration et al. (2017) but a third problem arises in the same range of the isochrones. The colour of the isochrone models differ a little from the observed colour. Finally, the aim this work is to present the cluster sequence rather than a detailed fit of the the best isochrone model.

The reddening towards NGC 3532 is known to be very small, despite its location in the Galactic disc. Previous estimates of the reddening include Fernandez & Salgado (1980) (E_{B-V} = 0.042 ± 0.016 mag), Johansson (1981) (E_{B-V} = 0.1 ± 0.04 mag), Claria & Lapasset (1988) (E_{B-V} = 0.07 ± 0.02 mag), and C11 (E_{B-V} = 0.028 ± 0.006 mag).

In order to derive a reddening independently we used the obtained stellar parameters from the AAOmega spectra and compared them to the photometric measurements. We first calculated the intrinsic colours from the measured effective temperatures of the members of NGC 3532 by applying the $T_{\rm eff}$-colour relations of Ramírez & Meléndez (2005) which are implemented in the software package PyAstronomy. We made use of the multi-colour photometry and calculated $(B-V)_0$, $(V-R_c)_0$, $(V-I_c)_0$, and $(V-K_s)_0$. With those values we were able to calculate the reddening $E_{\rm colour}$ as presented in Fig. 2.15. We used the coefficients from Johnson (1968), transformed all reddening values to E_{B-V}, and averaged them per colour.

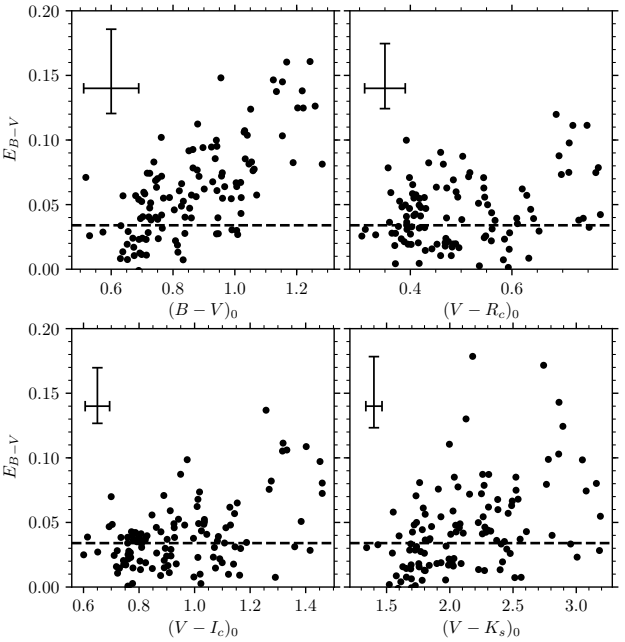

Figure 2.15: Reddening estimate calculated from the effective temperatures and the measured colours. For each intrinsic colour the reddening was calculated and converted to E_{B-V} with the coefficients from Johnson (1968). The dashed line marks the finally adopted reddening E_{B-V} = 0.034 mag. In the upper left of each panel we show the typical uncertainties.

Except for $(B-V)$, all other colours give a consistent extinction towards the members of NGC 3532 of E_{B-V} = 0.034 ± 0.012 mag. In $(B-V)$ the reddening is correlated with the intrinsic colour, a fact likely due to the colour transformations. In this colour we used only stars with $(B-V)_0 < 1.1$ to calculate the median reddening because those stars are less affected. The quoted reddening is the mean of the reddening values obtained from the different filter combinations, with the standard deviation as the uncertainty. The uncertainties of the determined individual colours from $T_{\rm eff}$ are about the same size as the calculated reddening (see Fig. 2.15) because of the average uncertainty on the effective temperature $\Delta T_{\rm eff}$ = 100 K. This reddening estimate agrees with Fernandez & Salgado (1980), Claria & Lapasset (1988), and C11; hence we use the determined value hereafter.

With the reddening, metallicity, and distance fixed, the only missing parameter to find the correct isochrone is the age. NGC 3532 is usually assumed to be 300 Myr old (C11), hence we will use this value as a starting point. The known white dwarfs in NGC 3532 also constrain the age and (Dobbie et al. 2012) estimated 300 ± 25 Myr. We also note that all parameters presented in Table 2.6 are consistent with the values estimated by C11 and Mowlavi et al. (2012) who found similar parameters to C11 from an isochrone fit of NGC 3532. However, Mowlavi et al. (2012) did not fit either the low-mass stars or the whole giant branch.

In order to verify the isochronal age for NGC 3532 we decided to overlay multiple model isochrones with the data to find a model which best represents the data. Later we compare the data to isochrones of different ages from one particular model. For this exercise we use the low-mass isochrones from Baraffe et al. (2015) (hereafter BHAC), the BaSTI models (Hidalgo et al. 2018), the MIST isochrones (Choi et al. 2016, Dotter 2016), the PARSEC isochrones (Marigo et al. 2017), and the YaPSI models (Spada et al. 2017). We used isochrones with [Fe/H]= −0.1 for all models except for BHAC, for which we had to use the solar metallicity models. All magnitudes are transformed to Johnson-Cousins and the 2MASS system (Carpenter 2001)[9] as needed.

All of the tested models are very similar and follow the observed cluster sequence reasonably. Variations can be found on the detailed level and we note differences in order to find a model that represents the data best, moving from high to low-mass stars. The giants of NGC 3532 are represented[10] by all models equally well, although it seems as if the YaPSI models are somewhat fainter. The same can be observed at the turn-off where the YaPSI models are ~ 0.2 mag fainter than the other models. Moving along the

[9] In fact we used the updated coefficients from http://www.astro.caltech.edu/~jmc/2mass/v3/transformations/.

[10] Except BHAC, which does not include stars of high mass.

Table 2.6: Properties estimated for NGC 3532.

Property	Symbol	Value
Age	t	300± ~ 50 Myr
Distance modulus	$(m - M)_0$	8.42 ± 0.14 mag
Distance	d	484^{+35}_{-30} pc
Reddening	$E_{(B-V)}$	0.034 ± 0.012 mag
Metallicity	[Fe/H]	−0.07 ± 0.1

main-sequence we focus on the solar-like stars. Each CMD in Fig. 2.14 has the solar model (BaSTI) marked. We see that in $(B - V)$ the BaSTI model matches the position of the main-sequence somewhat better than the others under the assumption that the *Gaia* distance is correct. The other models are slightly too faint. In the other three colours the isochrones differ a little from one other but seem to follow the cluster sequence well for solar-like stars. At the faint end of our observations none of the model isochrones describe the observations well. Part of the reasons for deviations from the empirical cluster sequence are the above-mentioned colour transformation issues. We suspect that the better match of the BaSTI models originates in their semi-empirical nature of their colour transformations. Regardless, we adopted the BaSTI model to discuss the age considerations because it best represents the solar-like stars under the assumption of the *Gaia* distance.

In the previous analysis we have fixed the age of NGC 3532 to 300 Myr based on Dobbie et al. (2012). To illustrate the differences between younger and older cluster models we show in Fig. 2.16 the BaSTI isochrones for the age of 200, 300, and 400 Myr ([Fe/H]= −0.1). All isochrones are shifted with the same distance modulus and reddened the same amount. The three models differ only in the turn-off region and for giant stars. For a younger cluster the turn-off is of course bluer and at higher mass stars while for an older model the it moves to redder, lower mass stars. The 300 Myr isochrone matches the turn-off the best. For the giants the 200 Myr model is too bright, the 300 Myr model describes the data well, and the 400 Myr model is too faint. In conclusion, 300 Myr is a good fit to the cluster sequence of NGC 3532 and we can agree that its age is 300 Myr within a margin of, say, 50 Myr.

2.6.3 Membership count

To infer the total number of possible cluster members we use the observed stars and their membership fraction. The distributions of photometric members observed in this work, the GES and RAVE surveys, and *Gaia* DR2 were previously displayed in Fig. 2.4. In the magnitude bins between $V = 11$ and $V = 19$ fifty per cent or more of those stars have been observed spectroscopically, with the most complete bins being those for $V = 17$ and $V = 18$. For $V = 10$ the fraction of observed stars is lower, with only a few stars included in RAVE and *Gaia*.

Among the observed stars we find that about half are members. Although one might expect that it is easier, and therefore more likely, to find the members among the brighter stars, the fraction of non-members is nearly constant for all observed magnitude bins, as shown in Fig. 2.17.

From both the fraction of observed stars and the fraction of exclusive cluster members among those, we estimate the total number of expected cluster members. Not having complete coverage of the cluster we have had to rely on two assumptions. First, the fraction of radial velocity members among the unobserved photometric members is the same as that for the observed members. Since we selected our targets randomly from the photometric members the unobserved stars are expected to have the same distribution. Second, the membership for stars brighter than $V = 10$ is complete. With the wealth of radial velocity studies at the bright end of the cluster sequence, especially the one by Gieseking (1981) and the recent astrometric analysis with the TGAS data (Gaia Collaboration et al. 2017), we believe that this holds true for the inner 1° of the cluster.

We extrapolate the number of members based on those assumptions. This yields an estimated number of ~1000 cluster members for NGC 3532 in the studied region, an impressive number for any open cluster (c.f. Trumpler 1930). The photometry by C11 and our radial velocity study include only the inner 1 deg^2 of NGC 3532; we actually expect the cluster to reach out much further (up to 5°, equivalent to 15 pc) as the first *Gaia* results (Gaia Collaboration et al. 2017) suggested. Many additional cluster members will likely be found outside our currently studied region. Furthermore, the *Gaia* DR2 data themselves suggest 1879 cluster members within 2.31°(Gaia Collaboration et al. 2018a), making NGC 3532 one of the richest open clusters in that study.

In order to compare the stellar content of NGC 3532 with the well-studied and very rich Pleiades cluster we constructed a luminosity function in M_{K_s} for both NGC 3532 and the Pleiades. (In the latest Pleiades membership by Bouy et al. (2015) K_s is the only passband available for all stars.) We display the luminosity functions obtained in Fig. 2.18. Three lines are displayed: first the luminosity function from the current observations of NGC 3532 (solid); second our estimate of the total NGC 3532 luminosity function based on the membership fraction of the observed stars (dashed); and third the Pleiades luminosity function (dotted).

As expected, the observed luminosity function shows features that hint at biases in the data. There are fewer stars than one would expect in the $M_{K_s} = 1$ bin. This bin corresponds to the poorly observed range between $V = 10$ and $V = 12$, and the dip is to be expected. In the estimated luminosity function this bias is corrected, although the membership fraction is based only on a few stars. At the faint end of our observed luminosity function the number of stars drops significantly, although it is expected to rise further. Based on the comparison with the Pleiades in Fig. 2.18 we would expect ~ 400 members for $M_{K_s} = 5$ but

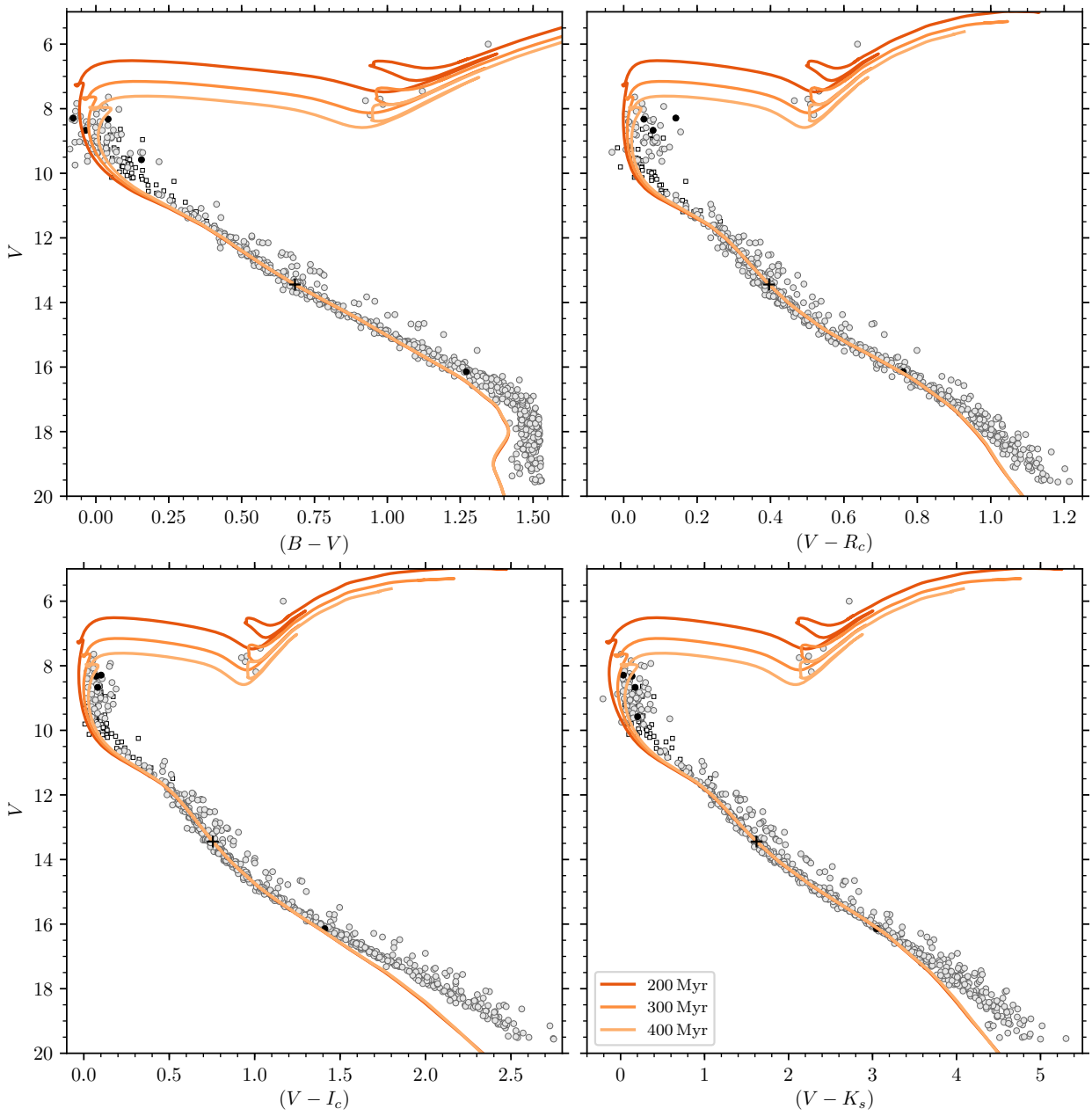

Figure 2.16: Same as Fig 2.14 but a single model of different age. The BaSTI isochrones for 200, 300, and 400 Myr (dark to light orange) are shown and shifted by the distance modulus determined with *Gaia* DR2 ($(m-M)_0$ = 8.42 mag). The solar-mass model for 300 Myr is marked with a black plus sign.

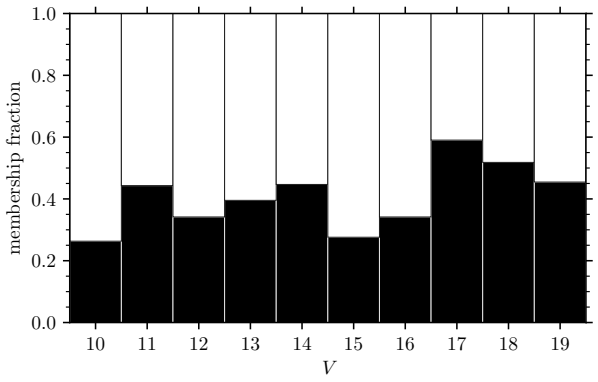

Figure 2.17: Membership fraction for the spectroscopically observed stars as a function of V magnitude.

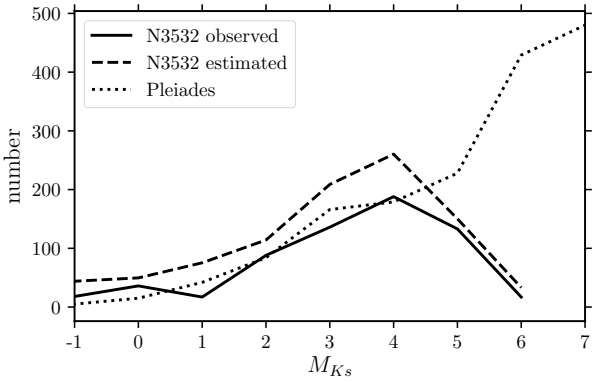

Figure 2.18: Luminosity functions for NGC 3532 and the Pleiades. For NGC 3532 we show the empirical luminosity function (solid line) based on our radial velocity observations and an estimate for the inner 1° of the cluster (dashed line) based on the photometric membership. The Pleiades luminosity function (dotted line) is based on Bouy et al. (2015).

find only 135.

Our photometric membership information is incomplete at the faint end for two reasons. First, we included only stars common to the 2MASS survey and the photometry of C11, leading to a theoretical brightness limit of $V = 19.1$, derived from the brightness limit of 2MASS. Additionally we filtered the 2MASS data to only include photometry that is good in all passbands; hence the rejection rate near the faint end is higher. Second, we used a fixed criterion to define the photometric cluster members and selected only stars up to 0.1 mag bluer and 1 mag brighter than the manually traced cluster sequence. As seen from Fig. 2.3, the cluster sequence in $[(B - V), V]$ runs nearly vertically in the CMD, binding the region of selection tightly to the manually traced cluster sequence. This may leave potential cluster members classified as photometric non-members.

Based on our estimate we conclude that NGC 3532 is likely as rich as the Pleiades, if not even richer. Seen in this context it is even more surprising that NGC 3532 was hitherto poorly studied in the astronomical literature. This open cluster is a very interesting test bed for further studies of stellar evolution especially when compared to the Pleiades. With an age of 300 Myr it is over twice as old as the Pleiades and has only half the age of the Hyades cluster. This age range in-between the two well-studied open clusters is a critical one for studies of stellar rotation and for dynamo transitions in cool stars (e.g. Barnes 2003).

2.7 Conclusions

We have presented a spectroscopic study of stars in the field of NGC 3532, an open cluster embedded in the crowded field of the Galactic disc. We construct a membership list for the open cluster from our radial velocity study and *Gaia* proper motions.

To select the targets for spectroscopy we constructed a photometric cluster membership list containing 2230 stars within a 1° field centred on NGC 3532. For about half of those photometric members we obtained spectra from the AAO with the fibre-fed AAOmega spectrograph and from CTIO with the Hydra-S spectrograph, and measured their radial velocities.

Combining our radial velocity measurements with data from the literature and the *Gaia*-ESO and RAVE surveys we construct a radial velocity membership of NGC 3532. With the precise proper motions from *Gaia* DR2 we were able to improve on that list and find 660 stars to be also proper motion members, defining a joint and exclusive membership list of these stars. Based on the fraction of observed stars and the confirmed radial velocity members we expect NGC 3532 to contain at least 1000 members within 1°, making it one of the richest clusters within 500 pc, on par with the well-studied Pleiades. Despite the large number of cluster members presented in this work the cluster sequence is not yet complete. This may be addressed by further ground-based radial velocity observations and additional astrometry from the *Gaia* mission.

We provide in Table 2.3 all observed radial velocities together with our computed membership probability. For use in the wider open cluster community we created a cluster sequence for NGC 3532 (Table 2.5) in various photometric colours, including the passbands of the *Gaia* photometric system.

From our spectroscopic observations of NGC 3532 we find the cluster to be slightly metal-poor, with [Fe/H] = −0.07 ± 0.10. In comparison, most other studies, which focused on the giant stars, found [Fe/H] = 0 to 0.1. For a definitive statement a homogeneous analysis of giants and dwarfs with reduced uncertainties would be necessary.

In addition to abundances, we measured effective temperatures and surface gravities from the spectra. This

helped to remove false-positive background giants from the sample. Furthermore, we used the effective temperature to estimate the reddening towards NGC 3532 and found $E_{B-V} = 0.034 \pm 0.012$ mag, in good agreement with previously estimated values.

The precise astrometric measurements from *Gaia* DR2 enabled us not only to determine an exclusive membership based on proper motions and radial velocities but also to determine the distance to NGC 3532 independently of isochrone models. Based on the parallaxes we find a distance of 484^{+35}_{-30} pc ($(m - M)_0 = 8.42 \pm 0.14$ mag).

With the metallicity, reddening, and distance known, we compared different model isochrones to the obtained cluster sequence. We showed that most modern isochrones follow the sequence well but find small differences between the models. From the BaSTI models for different ages we infer that NGC 3532 has an age of 300± ~ 50 Myr.

Echoing the words of Herschel, we conclude that NGC 3532 is truly an outstanding open cluster with a very rich stellar population.

Acknowledgements. We thank Frederico Spada for providing the interpolated YaPSI isochrones and for useful discussions. We thank Corrado Boeche for useful discussions about SP_Ace. We thank the anonymous referee for the very helpful comments which led to improvements of the paper. We thank D. Zucker and C. Lidman from AAO for performing the radial velocity observations. Based in part on observations at Cerro Tololo Inter-American Observatory, National Optical Astronomy Observatory (2008A-0476; S. Barnes, SMARTS consortium through Vanderbilt University; D. James, 2008A-0512, 2008B-0248, 2010A-0281, 2010B-0492; S. Meibom, 2011B-0322; A. Geller), which is operated by the Association of Universities for Research in Astronomy (AURA) under a cooperative agreement with the National Science Foundation. DJJ gratefully acknowledges support from National Science Foundation award NSF-1440254. This research has made use of NASA's Astrophysics Data System Bibliographic Services. This research has made use of the SIMBAD database and the VizieR catalogue access tool, operated at CDS, Strasbourg, France. This publication makes use of data products from the Two Micron All Sky Survey, which is a joint project of the University of Massachusetts and the Infrared Processing and Analysis Center/California Institute of Technology, funded by the National Aeronautics and Space Administration and the National Science Foundation. This publication makes use of the RAVE survey. Funding for RAVE has been provided by: the Australian Astronomical Observatory; the Leibniz-Institut für Astrophysik Potsdam (AIP); the Australian National University; the Australian Research Council; the French National Research Agency; the German Research Foundation (SPP 1177 and SFB 881); the European Research Council (ERC-StG 240271 Galactica); the Istituto Nazionale di Astrofisica at Padova; The Johns Hopkins University; the National Science Foundation of the USA (AST-0908326); the W. M. Keck foundation; the Macquarie University; the Netherlands Research School for Astronomy; the Natural Sciences and Engineering Research Council of Canada; the Slovenian Research Agency; the Swiss National Science Foundation; the Science & Technology Facilities Council of the UK; Opticon; Strasbourg Observatory; and the Universities of Groningen, Heidelberg and Sydney. The RAVE web site is at https://www.rave-survey.org. Based on observations made with ESO Telescopes at the Paranal Observatories under programme ID 188.B-3002 (*Gaia*-Eso survey). This work has made use of data from the European Space Agency (ESA) mission *Gaia* (`https://www.cosmos.esa.int/gaia`), processed by the *Gaia* Data Processing and Analysis Consortium (DPAC, `https://www.cosmos.esa.int/web/gaia/dpac/consortium`). Funding for the DPAC has been provided by national institutions, in particular the institutions participating in the *Gaia* Multilateral Agreement.
Software: PyRAF is a product of the Space Telescope Science Institute, which is operated by AURA for NASA. This research made use of Astropy, a community-developed core Python package for Astronomy (Astropy Collaboration et al. 2013). This work has made use of the SP_Ace spectral analysis tool version 1.1. This work has made of Topcat (Taylor 2005). This research made use of the following Python packages: Pandas (McKinney 2010); NumPy (Walt et al. 2011); MatPlotLib (Hunter 2007); IPython: (Pérez & Granger 2007); SciKit-learn: (Pedregosa et al. 2011); Seaborn: (Waskom et al. 2017). This work made use of PyAstronomy and Speclite.

References

AAO Software Team 2015, Astrophysics Source Code Library
Astropy Collaboration et al. 2013, A&A 558, A33
Bailer-Jones, C. A. L., Rybizki, J., Fouesneau, M., Mantelet, G., & Andrae, R. 2018, AJ 156, 58
Baraffe, I., Homeier, D., Allard, F., & Chabrier, G. 2015, A&A 577, A42
Barnes, S. A. 2003, ApJ 586, 464
— 2007, ApJ 669, 1167
Barnes, S. A. 1997, PhD thesis (Yale University)
Basri, G., Marcy, G. W., & Graham, J. R. 1996, ApJ 458, 600
Bessell, M. S., & Brett, J. M. 1988, PASP 100, 1134
Boeche, C., & Grebel, E. K. 2016, A&A 587, A2
Bouy, H. et al. 2015, A&A 577, A148
Carpenter, J. M. 2001, AJ 121, 2851
Castelli, F., Gratton, R. G., & Kurucz, R. L. 1997, A&A 318, 841
Cayrel de Strobel, G., Soubiran, C., & Ralite, N. 2001, A&A 373, 159
Choi, J. et al. 2016, ApJ 823, 102
Claria, J. J., & Lapasset, E. 1988, MNRAS 235, 1129
Claria, J. J., & Minniti, D. 1988, The Observatory 108, 218
Clem, J. L., Landolt, A. U., Hoard, D. W., & Wachter, S. 2011, AJ 141, 115
Coelho, P. R. T. 2014, MNRAS 440, 1027
Conrad, C. et al. 2014, A&A 562, A54
Cropper, M. et al. 2018, A&A 616, A5
de la Caille, A. N. L. 1755, in: Mémoires de mathématique et de physique, ed. by Académie des sciences (France) (Paris: Panckoucke), 194
Demarque, P. R., & Larson, R. B. 1964, ApJ 140, 544
Dobbie, P. D. et al. 2009, MNRAS 395, 2248
Dobbie, P. D. et al. 2012, MNRAS 423, 2815
Dotter, A. 2016, ApJS 222, 8
Eggen, O. J. 1981, ApJ 246, 817
Fernandez, J. A., & Salgado, C. W. 1980, A&AS 39, 11
Gaia Collaboration et al. 2016, A&A 595
Gaia Collaboration et al. 2017, A&A 601, A19
Gaia Collaboration et al. 2018a, A&A 616, A10
Gaia Collaboration et al. 2018b, A&A 616, A1
Geller, A. M., Mathieu, R. D., Harris, H. C., & McClure, R. D. 2008, AJ 135, 2264

Gieseking, F. 1980, A&AS 41, 245
— 1981, A&A 99, 155
Gilmore, G. et al. 2012, The Messenger 147, 25
González, J. F., & Lapasset, E. 2002, AJ 123, 3318
Gratton, R. 2000, in: Stellar Clusters and Associations: Convection, Rotation, and Dynamos, ed. by R. Pallavicini, G. Micela, & S. Sciortino, vol. 198, Astronomical Society of the Pacific Conference Series, 225
Herschel, J. 1847, Results of astronomical observations made during the years 1834, 1835, 1836, 1837, 1838, at the Cape of Good Hope; being the completion of a telescopic survey of the whole surface of the visible heavens, commenced in 1825 (Smith, Elder and Co.)
Hidalgo, S. L. et al. 2018, ApJ 856, 125
Høg, E. et al. 2000, A&A 355, L27
Hunter, J. D. 2007, Computing in Science & Engineering 9, 90
Jacobson, H. R. et al. 2016, A&A 591, A37
Johansson, K. L. V. 1981, A&AS 43, 421
Johnson, H. L. 1968, in: Nebulae and Interstellar Matter, ed. by B. M. Middlehurst, & L. H. Aller (the University of Chicago Press), 167
Jordi, C. et al. 2010, A&A 523, A48
Koelbloed, D. 1959, Bull. Astron. Inst. Netherlands 14, 265
Koester, D., & Reimers, D. 1993, A&A 275, 479
Kunder, A. et al. 2017, AJ 153, 75
Kupka, F., Piskunov, N., Ryabchikova, T. A., Stempels, H. C., & Weiss, W. W. 1999, A&AS 138, 119
Lewis, I. J. et al. 2002, MNRAS 333, 279
Lindegren, L. et al. 2018, A&A 616, A2
Luck, R. E. 1994, ApJS 91, 309
Marigo, P. et al. 2017, ApJ 835, 77
McKinney, W. 2010, in: Proceedings of the 9th Python in Science Conference, ed. by S. van der Walt, & J. Millman, 51
Meingast, S., & Alves, J. 2019, A&A 621, L3
Mermilliod, J. C., Mayor, M., & Udry, S. 2008, A&A 485, 303
Mermilliod, J.-C. 1992, Bulletin d'Information du Centre de Donnees Stellaires 40, 115
Meynet, G., Mermilliod, J. .-., & Maeder, A. 1993, Astronomy and Astrophysics Supplement Series 98, 477
Mowlavi, N. et al. 2012, A&A 541, A41
Netopil, M., Paunzen, E., Heiter, U., & Soubiran, C. 2016, A&A 585, A150
Netopil, M. 2017, MNRAS 469, 3042
Pedregosa, F. et al. 2011, English, Journal of Machine Learning Research, 2825
Pérez, F., & Granger, B. E. 2007, Computing in Science & Engineering 9, 21
Piatti, A. E., Claria, J. J., & Abadi, M. G. 1995, AJ 110, 2813
Raddi, R. et al. 2016, MNRAS 457, 1988
Ramírez, I., & Meléndez, J. 2005, ApJ 626, 465
Rebolo, R., Martin, E. L., Basri, G., Marcy, G. W., & Zapatero-Osorio, M. R. 1996, ApJ 469, L53
Reimers, D., & Koester, D. 1989, A&A 218, 118
Ricker, G. R. et al. 2015, Journal of Astronomical Telescopes, Instruments, and Systems 1, 014003
Robichon, N., Arenou, F., Mermilliod, J.-C., & Turon, C. 1999, A&A 345, 471
Röser, S., Schilbach, E., & Goldman, B. 2018, ArXiv e-prints, arXiv:1811.03845
Sandage, A. 1958, Ricerche Astronomiche 5, 41
Sandage, A. 1957, ApJ 125, 435
Santos, N. C. et al. 2012, A&A 538, A151
Schlafly, E. F., & Finkbeiner, D. P. 2011, ApJ 737, 103
Schneider, H. 1987, A&AS 71, 147
Skrutskie, M. F. et al. 2006, AJ 131, 1163
Spada, F., Demarque, P., Kim, Y.-C., Boyajian, T. S., & Brewer, J. M. 2017, ApJ 838, 161
Steinmetz, M. et al. 2006, AJ 132, 1645
Taylor, M. B. 2005, in: Astronomical Data Analysis Software and Systems XIV, ed. by P. Shopbell, M. Britton, & R. Ebert, vol. 347, Astronomical Society of the Pacific Conference Series, 29
Thompson, G. P., Ryan, S. G., & Sibbons, L. F. 2016, MNRAS 462, 3376
Trumpler, R. J. 1930, Lick Observatory Bulletin 420, 154
Twarog, B. A., Ashman, K. M., & Anthony-Twarog, B. J. 1997, AJ 114, 2556
van Leeuwen, F. 2009, A&A 497, 209
Walt, S. van der, Colbert, S. C., & Varoquaux, G. 2011, Computing in Science & Engineering 13, 22
Waskom, M. et al. 2017
Wizinowich, P., & Garrison, R. F. 1982, AJ 87, 1390
Wu, Z.-Y., Zhou, X., Ma, J., & Du, C.-H. 2009, MNRAS 399, 2146
Zacharias, N., Finch, C., & Frouard, J. 2017, AJ 153, 166

3

The rotation period distribution of the rich Pleiades-age Southern open cluster NGC 2516

Existence of a representative zero-age main sequence distribution

D. J. Fritzewski, S. A. Barnes, D. J. James, K. G. Strassmeier

Abstract

Aims: We wish to measure the cool star rotation period distribution for the Pleiades-age rich open cluster NGC 2516 and use it to determine whether cluster-to-cluster variations exist in otherwise identical open clusters.
Methods: We obtained 42 d-long time-series CCD photometry of NGC 2516 in the V and I_c filters using the Yale 1 m telescope at CTIO and performed a number of related analyses, including PSF-based time-series photometry. Our data are complemented with additional information from several photometric datasets, literature radial velocities, and *Gaia* DR2 astrometry. All available data are used to construct an integrated membership list for NGC 2516, containing 844 stars in our $\approx 1^\circ$ field of view.
Results: We derived 308 rotation periods for late-F to mid-M cluster members from our photometry. We identified an additional 247 periodic M dwarf stars from a prior study as cluster members, and used these to construct a 555-star rotation period distribution for NGC 2516. The colour-period diagram (in multiple colours) has almost no outliers and exhibits the anticipated triangular shape, with a diagonal slow rotator sequence that is preferentially occupied by the warmer stars along with a flat fast rotator sequence that is preferentially populated by the cooler cluster members. We also find a group of extremely slowly rotating M dwarfs ($10\,\mathrm{d} \lesssim P_{\mathrm{rot}} \lesssim 23\,\mathrm{d}$), forming a branch in the colour-period diagram which we call the 'extended slow rotator sequence'. This, and other features of the rotational distribution can also be found in the Pleiades, making the colour-period diagrams of the two clusters nearly indistinguishable. A comparison with the well-studied (and similarly aged) open cluster M 35 indicates that the cluster's rotational distribution is also similarly indistinguishable from that of NGC 2516. Those for the open clusters M 50 and Blanco 1 are similar, but data issues for those clusters make the comparisons somewhat more ambiguous. Nevertheless, we demonstrate the existence of a representative zero-age main sequence (ZAMS) rotational distribution and provide a simple colour-independent way to represent it. We perform a detailed comparison of the NGC 2516 rotation period data with a number of recent rotational evolution models. Using X-ray data from the literature, we also construct the first rotation-activity diagram for solar-type stars in NGC 2516, one that we find is essentially indistinguishable from those for the Pleiades and Blanco 1.
Conclusions: The two clusters NGC 2516 and Pleiades can be considered twins in terms of stellar rotation and related properties (and M 35, M 50, and Blanco 1 are similar), suggesting that otherwise identical open clusters also have intrinsically similar cool star rotation and activity distributions.

This chapter was published in *Astronomy & Astrophysics* 641, A51, 2020, reproduced with permission

3.1 Introduction

Coeval stellar populations within open clusters are widely used to provide snapshots of stellar evolution, fitting them into an age-ranked succession to allow an empirical understanding of the underlying phenomena. However, very few clusters share an identical age and it is debatable whether cluster-to-cluster variations beyond the compositional one exist.

One particularly sensitive way to probe the existence of any cluster-to-cluster variations between otherwise coeval systems is to measure and compare the rotation rates (preferably periods) of the corresponding late-type stars in the relevant clusters. The dual reasons for this are that rotation periods can be measured with great precision (routinely better than 1 %) and that cool star rotation periods themselves change by up to an order of magnitude over a timescale comparable to young open cluster ages (Skumanich 1972; Barnes 2003b).

The stellar rotation period is measured by following the light modulation caused by cool starspots rotating into and out of view (Kron 1947, van Leeuwen et al. 1987, Strassmeier 2009). Although the number of measured rotation periods in open clusters has increased significantly over the past years (see references in e. g. Barnes 2003b, Barnes 2007 and Bouvier et al. 2014), their number is still small in comparison with the general open cluster population, even when restricted to that within 1 kpc. Hence, limited work is available when directly comparing two open clusters of similar age.

Irwin et al. (2009) have directly compared the rotation periods of low-mass (mostly M) stars in NGC 2516 and the similarly-aged M 50 cluster, and found no dependence on the cluster environment. We confirm and extend their basic conclusion, while noting two issues: 1. their observational baseline was limited, resulting in a number of period aliases, and 2. subsequent membership information also shows that a certain number of their stars are non-members, making detailed comparisons ambiguous. We sort out these issues, and append the corresponding cleaned sample to our own below.

Cargile et al. (2014) compared their 33-star KELT-South-based rotation period distribution for Blanco 1 with the HATNET-based period distribution for the Pleiades (Hartman et al. 2010), interpreting the measured difference as a small (146 Myr vs 134 Myr) age difference between the clusters. Both Delorme et al. (2011) and Douglas et al. (2019) have compared Praesepe with the Hyades and found measurable differences between their rotational distributions. In fact, they have also interpreted the difference between the rotational distributions as an age difference of 47 Myr and 57 Myr respectively between the two open clusters. Both studies used the stellar rotation period as an age estimator via gyrochronology (Barnes 2003b, 2010), which itself makes use of the fact that cool stars steadily lose angular momentum in a mass-dependent way as they age, a consequence of their winds (Parker 1958; Weber & Davis 1967), resulting in the well-known relationship between the equatorial rotation velocity and age, t: $V_{\rm eq} \sim t^{-0.5}$, first identified by Skumanich (1972) for solar-type stars[1]. We now know that the relationship can be generalized to rotation periods P, as a function of stellar mass, m: $P(m) \propto t^{0.5}$, a relationship believed to be roughly true for FGK stars (e.g. Barnes (2003b)), and often used as a simple approximate implementation of gyrochronology.

The focus of recent studies has been mostly on the slow rotators whose general spin-down is empirically well-delineated and can be applied to the open clusters of relatively advanced age, as witnessed by results in the 2.5 Gyr NGC 6819 (Meibom et al. 2015) and the 4 Gyr-old M 67 (Barnes et al. 2016b) open clusters. However, many details of the evolution in young open clusters are unclear, and arguably are more important in understanding the transitions between rapid and slow rotators which observations have shown to exist within the same open cluster. Hence, the best way to test for any possible cluster-to-cluster variations is to compare two (or more) coeval young open clusters, preferably of the same composition.

Here we present new rotation period measurements for the zero-age main sequence (ZAMS) open cluster NGC 2516, which is in many ways comparable to the Pleiades. It has a similar age and richness[2], although it is somewhat more distant (409 pc vs. 136 pc, Cantat-Gaudin et al. 2018), the last fact making it less prominent in the night sky. Given the similarities, NGC 2516 and the Pleiades are an ideal pair to search for cluster-to-cluster variations in astrophysical properties, in particular stellar rotation. Rich cluster pairs are crucial because if any such variations exist, we would expect to find them at the level of detail which can only be probed with large numbers of stars spanning the whole mass range.

The Pleiades is probably the best-studied open cluster because of its proximity, richness, and northern location. Several studies have measured rotation periods therein, beginning with van Leeuwen et al. (1987). In fact, that work represents the first time rotation periods were derived in any open cluster. It also demonstrated the existence of both slow and fast rotators (including some near break-up speed) in the same open cluster (see also van Leeuwen & Alphenaar 1982). This was followed by other ground-based work on the cluster, including $v \sin i$ work by Stauffer et al. (1987), and more recently, rotation period work by Hartman et al. (2010). These ground-based efforts have now been superseded by an even more recent large space-based study using Kepler/K2 satellite data (Rebull et al. 2016), which

[1] See Barnes et al. (2016a) for a modern equivalent of the Skumanich (1972) relationship using rotation periods in open cluster stars.

[2] Cantat-Gaudin et al. (2018) list 798 members for NGC 2516 vs. 992 members for the Pleiades.

now has become our principal source for comparison with NGC 2516.

The age of NGC 2516 is believed to be ~150 ± 35 Myr (Meynet et al. 1993; Sung et al. 2002). The age of the Pleiades has been determined by various authors, with a recent estimate being ~110 – 160 Myr (Gossage et al. 2018), in agreement with the lithium depletion age of 125 – 130 Myr (Stauffer et al. 1998). The uncertainties in classical isochrone fitting results, especially for young clusters, are large enough for the two clusters to be considered essentially coeval.

The metallicity of NGC 2516 has been disputed in the past, with photometric estimates finding values as low as [Fe/H]= −0.3 (Jeffries et al. 1997). In contrast, spectroscopic observations have found near-solar values of [Fe/H]= 0.01 ± 0.03 (Terndrup et al. 2002) and [Fe/H]= −0.08±0.01 (Bailey et al. 2018). Terndrup et al. (2002) have directly inter-compared equivalent stars in both clusters and found NGC 2516 to have Δ[Fe/H] = +0.04 ± 0.07 with respect to the Pleiades, which itself has a measured value of [Fe/H]= +0.075 ± 0.011 (Soderblom et al. 2009). The near-agreement between the spectroscopic metallicity determinations of both clusters makes the Pleiades and NGC 2516 even more similar.

There are three other comparable open clusters, M 35, M 50, and Blanco 1, which have been studied respectively by Meibom et al. (2009), Irwin et al. (2009), and Gillen et al. (2020). For various reasons, the relevant data are not as comparable with NGC 2516 as those for the Pleiades. Nevertheless, we perform the relevant analyses and comparisons below.

A prior rotation period study of NGC 2516 has been presented by Irwin et al. (2007), as mentioned earlier. That study focused on the lower-mass, and consequently, pre-main sequence late-K and M-type stars ($0.15 \lesssim M/M_{\odot} \lesssim 0.7$), but did not measure the F, G, and early K stars. We complete the picture here by measuring the important higher-mass range of solar-like stars, including stars from late-F to mid-M (with enough overlap among the M stars to compare the results). In fact, we subsequently supplement our sample with additional rotators from their sample that satisfy our membership criteria to present the most complete picture possible of stellar rotation in NGC 2516. Finally, it should be noted that this work subsumes prior work on rotation of NGC 2516 cool stars in the otherwise unpublished PhD thesis of Barnes (1997).

This paper is structured as follows. In Section 3.2 we present our observations and the photometric reductions. In Sect. 3.3 we determine the cluster members among our observed stars. Sect. 3.4 describes our time-series analysis. We present the colour-period diagram for NGC 2516 and related analysis in Sect. 3.5. In Sect. 3.6 we compare the observed rotation periods to angular momentum models from the literature and in Sect. 3.7 we compare the stellar rotation periods of NGC 2516 with those of the Pleiades and other open clusters. Finally, in Sect. 3.8, we construct and present the first rotation-X-ray activity diagram for FGKM stars in NGC 2516, followed by our conclusions.

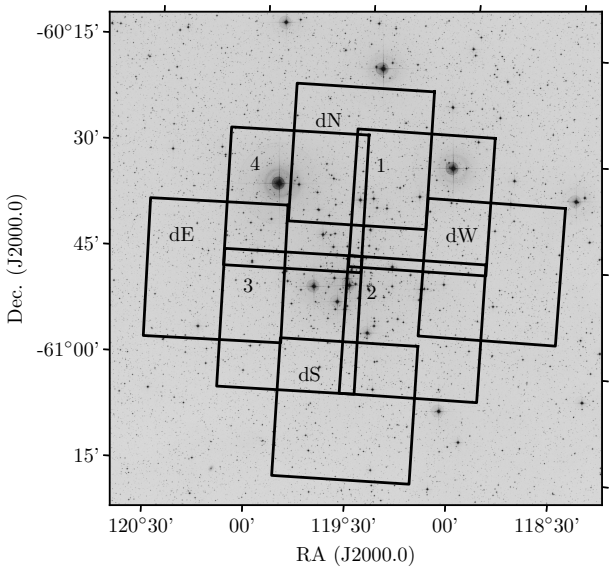

Figure 3.1: Field of NGC 2516 from the Digitized Sky Survey 2 (red filter), with our time-series observing fields overlaid in black contours. Individual fields are square, with each labelled in the North-East corner. The inner fields (1 through 4) were observed with exposure times of 60 s in V and 120 s in I_c filters, while the outer (deep) fields received 600 s in the I_c filter. Apart from a small overlap with our outer fields, the region covered by Irwin et al. (2007) lies beyond that of this study, extending the total area covered by time-series observations to >1 sq. degree.

3.2 Observations and photometry

We observed the southern Galactic open cluster NGC 2516 between 19 February 2008 and 1 April 2008 from the Cerro Tololo Inter-American Observatory (CTIO) with the Yale 1 m telescope operated by the SMARTS consortium. Within those 42 d only a 4 d scheduling gap from 8 March 2008 to 11 March 2008 interrupted the time-series observations, leading to a well-sampled photometric time-series. All observing nights had superb seeing conditions, typically better than ~1.3″.

The CTIO Yale 1 m telescope was equipped with the *Y4KCam* camera, based on a 4064 px × 4064 px STA CCD detector and with a field of view (FoV) of 19.3′ × 19.3′ and a 0.″289 px^{-1} image scale. The average detector read noise was 4.8 e^{-} px^{-1}.

With an extent of more than 1 deg^2 on the sky, NGC 2516 is too large to fit into a single FoV. Therefore, we covered the open cluster with eight different fields, as shown in Fig. 3.1. We cycled through these fields to obtain a homogeneous time-series. The centre of our observing programme is α = 7:58:05, δ = -60:48:47 (J2000.0), near the cluster giant CPD-60 980.

In order to provide greater reliability, the four inner fields (numbered F1 to F4) were observed both in the John-

Table 3.1: Number of exposures in the different fields and filters.

Field name	Filter	Exposure time (s)	Number of visits
F1	I_c	60	106
	V	120	108
F2	I_c	60	104
	V	120	104
F3	I_c	60	106
	V	120	105
F4	I_c	60	105
	V	120	103
deepN	I_c	600	86
deepE	I_c	600	88
deepS	I_c	600	88
deepW	I_c	600	82

son-Kron-Cousins V and I_c band, with exposure times of 120 s and 60 s, respectively. In addition, we observed four outer fields (called deepN/E/S/W). These outer fields partially overlap with the inner fields, allowing consistency checks, but for these we optimized the exposure for the fainter M dwarf members with an exposure time of 600 s in I_c.

In total, we obtained between 82 and 108 observations for each field with up to ten visits (median four) per field per night. A summary of the observations is provided in Table 3.1.

3.2.1 Data reduction and photometry

Supplementary to the science data, zero-second bias images and per-filter sky-flat fields were acquired each night. Using IRAF[3], a median bias frame was subtracted from all calibration and science images, and the science data in each filter were corrected for pixel-to-pixel sensitivity differences using a per-filter balance frame. The dark current of the *Y4Kcam* is sufficiently low (21 e^- px^{-1} h^{-1}) that dark current correction was not applied to the images.

In order to construct the best possible light curves, we used point spread function (PSF) photometry and the DaoPhot II Software (Stetson 1987, 1994; Stetson et al. 2003). The key to good PSF subtraction of each star from the obtained images is a clean model PSF that includes as many properties of the data as possible. To construct such a model PSF, we examined (for each field) the frames with the best seeing[4] to identify suitable stars.

After several experiments with the data and different set-ups for the PSF, we settled on four criteria for our PSF stars. Our PSF stars are required (1) to have a count number in the middle of the dynamic range of the CCD and (2) each is required to be the only source within at least 25 px of its centre of light (≈15″ in diameter). Furthermore, those stars (3) should have a regular shape on visual inspection, in other words the shape should not differ from nearby stars. Intending to use the same PSF stars for each exposure of a given field, (4) we also avoid stars close to bad columns of the CCD because in some frames these stars could potentially fall onto those columns in cases where the pointing is slightly different. Bad pixels within the fitting area of the PSF would lead to removal of that particular star from the list of PSF stars, lowering the number of available PSF stars for that frame.

For each field, we chose roughly 350 stars to construct the model PSF. Our aim is to exclude as much non-astrophysical variability as possible from the final light curves. Therefore, we used the same PSF stars for all exposures of a given field. Each image was matched to the reference image with DaoPhot II. This enabled us to translate the ID numbers of the PSF stars in the reference frame to the ID numbers of the working frame and to construct the list of PSF stars for the frame, including only stars with valid data, in particular unsaturated ones.

The workflow in DaoPhot II starts with source finding, which assigns an ID to each possible point source in the image. Afterwards, aperture photometry is carried out to estimate the brightness of the sources. Those magnitudes are used as an input to create the second-order spatially-varying model PSF, which is obtained by fitting the selected sources with the "Penny" function[5]. Subsequently, the actual PSF fitting of all stars is performed in AllStar and delivers the final instrumental magnitude of the sources in the frame.

After performing the PSF photometry with DaoPhot II, we used the software DaoMaster to match the images to within 0.3 px to obtain accurate positions of the stars for the creation of the light curves. In the next step, DaoMaster adjusts the instrumental magnitudes of the individual frames to a common system and combines all data points of a star into a light curve. We chose to construct light curves only for stars for which at least 60 data points remained (~50 percent of the available frames). In total DaoMaster created ~24 000 light curves which correspond, due to the overlap of the normal and the deep frames and the usage of two filters, to ~14 000 distinct sources.

In the following, we use the IDs assigned by DaoPhot II preceded by the field as the main identifiers in the text. In the tables we additionally give the global identifier from *Gaia* DR2. For example, a star from field F2 in I_c has the name *2i516* while a star from the deep I_c south field is named *dS2516*.

[3] IRAF is distributed by the National Optical Astronomy Observatories, which are operated by the Association of Universities for Research in Astronomy, Inc., under cooperative agreement with the National Science Foundation.

[4] These fiducial images were chosen from the night of UT20080319, with a seeing of 0.9″ to 1.2″ for the eight different fields

[5] DaoPhot II settings: ANALYTIC MODEL PSF = 5.00, VARIABLE PSF = 2.0

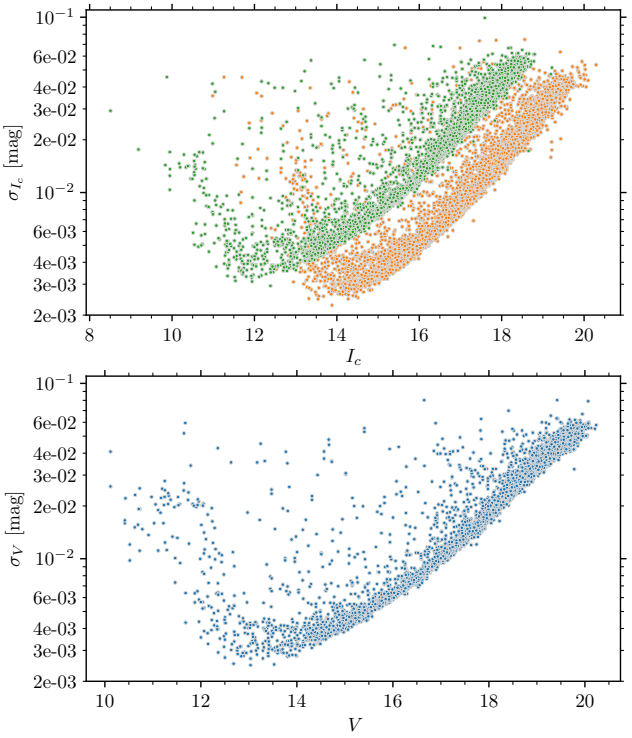

Figure 3.2: Mean photometric uncertainties of the light curves (σ) as a function of the magnitude. *Top:* In green we show values for I_c (60 s) and in orange the deep I_c (600 s). *Bottom:* Same as the upper panel but for V (120 s) data.

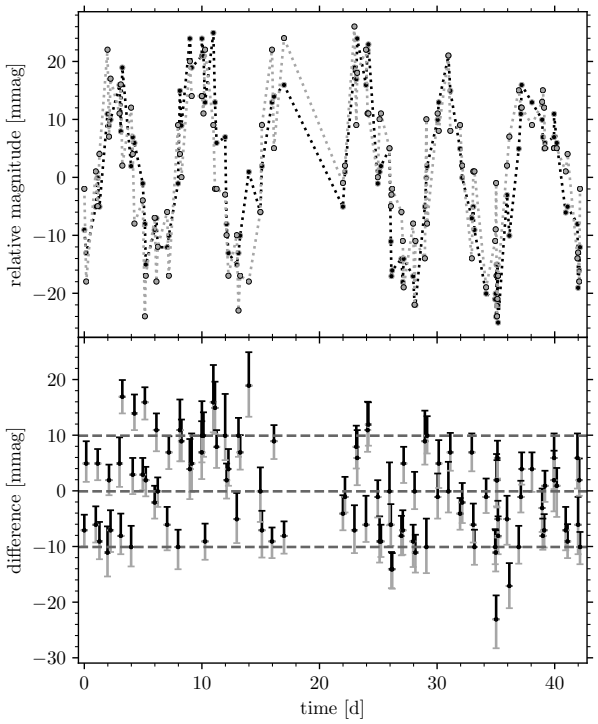

Figure 3.3: Two V band light curves of the same star Gaia DR2 5290833258325773312 from fields 1 and 2 (*upper* panel) and their differences (*lower* panel), demonstrating the extent of (dis)agreement. The uncertainties shown in the *lower* panel are those estimated by DaoPhot II for each data point. The upper part of the error bar (black) corresponds to the black light curve while the lower one corresponds to the grey light curve. The three dashed lines, from top to bottom, are the ninetieth, the fiftieth (median), and the tenth percentile of the light curve differences.

3.2.2 Photometric uncertainties

In Fig. 3.2, we show the mean uncertainties for all light curves over the magnitude range in their corresponding filters. The data are separated by kind of exposure. The deep 600 s I_c filter data exhibits the lowest noise level, as one would expect. For the 60 s I_c data a comparable uncertainty is reached for stars 2 mag brighter. This also means that those light curves deliver significantly better results for the brighter stars (which are either overexposed or saturated in the deep I_c filter frames). In combination, we achieved a precision of 4 mmag or better for the whole range from I_c = 11.0 – 16.8 mag. This corresponds to a range from solar-type to late-K stars, the core mass range for our study.

The 120 s V band observations are comparable to the short I_c ones but generally deliver a lower noise level. With the inclusion of the deep I_c frames we are able to probe stars down to I_c = 20, corresponding to $V \approx 23$ for stars on the cluster sequence.

3.2.3 Testing the uncertainties with duplicate light curves

Our observed fields on the sky were designed to overlap, significantly for the deep fields, resulting in multiple light curves from different fields for many stars. See Fig. 3.3 for an example. Our observing strategy was to cycle through the fields; consequently two photometric data points for one star in two different fields are often separated by less than one hour. Over this interval, the variability of most of the observed stars is small; hence we can assume that both photometric data points should agree to within the uncertainty given by DaoPhot II. Here we test this assumption and hence the reliability of the error estimate.

For the comparison we used all light curves of stars found in multiple fields. In total, we have 1260 pairs[6] of light curves for 658 individual stars. We calculated the differences of the light curves (DLC) from the mean-subtracted light curves rather than from zero point-adjusted photometry[7].

[6] Each filter is counted independently. A star found in two fields with photometry in both V and I_c is counted as two pairs.

[7] This might introduce some additional uncertainties, increasing the differences between the light curves. In this case the mean of the DLC is non-zero. However, the offsets observed in the DLCs are much smaller than the scatter and can be neglected.

We use the data points closest in time for the calculation of the differences and set an upper limit of six hours (i.e. half a night) after which two data points are no longer considered as a pair.

One example of our analysis is shown in Fig. 3.3. This particular star (Gaia DR2 5290833258325773312)[8] is a slow rotator, with $P_{\rm rot}$ = 7.1 d. We chose one of our rotators to illustrate the differences in the light curves because it is much easier to follow a structured light curve rather than random stellar and instrumental variability. The upper panel of Fig. 3.3 shows the two light curves from the 120 s V band exposures. In general, both light curves follow each other closely. Some outliers can be seen but the starspot induced variability is the main contribution to the flux variations.

The lower panel of Fig. 3.3 shows the differences between the two light curves at sufficiently close time stamps. The median value of the differences is very close to zero. If the uncertainties from DaoPhot II account for all the variance, we would expect all differences to agree with zero within the uncertainties. However, this is not the case, with the median value of the absolute differences being twice the median value of the uncertainties. Nevertheless, (because of what we show immediately below using all our light curves) we believe the uncertainties to be correctly estimated by DaoPhot II and ascribe the deviations to instrumental characteristics, short term atmospheric-, and maybe even stellar variations.

Beyond that particular example in Fig. 3.3, we find the median of the absolute differences between the light curves to be slightly larger than the DaoPhot II errors for most stars. This relation is shown in Fig. 3.4. As this effect is of the same order, independent of the light curve uncertainties, we feel certain that the larger differences are not caused by underestimation of the uncertainties but ought to be interpreted as short-term stellar and atmospheric variability. Therefore, we use the uncertainties as is in the analysis.

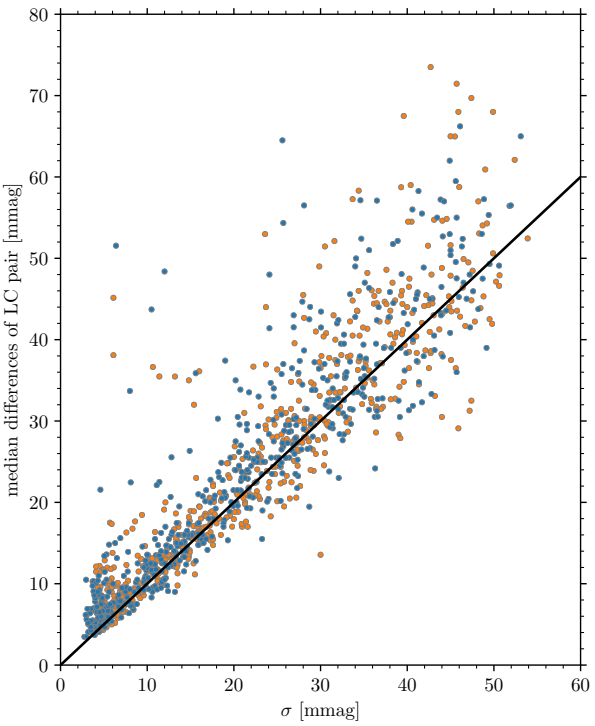

Figure 3.4: Median measurement error of a light curve as determined by DaoPhot II (σ) against the median of the absolute differences of a light curve pair. The two colours indicate the two filters (V blue, I_c orange). In black we mark the line of equality. The majority of the differences are only marginally larger than the estimated photometric uncertainties.

3.2.4 Literature photometry

For this work, we use standardized photometry available from prior work. Jeffries et al. (2001) (hereafter J01) presented a comprehensive photometric study of the NGC 2516 with essentially the same spatial coverage as our time-series photometry. Additional photometry of sub-fields of NGC 2516 was published by Sung et al. (2002) (hereafter S02) and Lyra et al. (2006). Although only J01 cover the whole area, we chose S02 as our preferred source for BVI_c photometry and supplemented that coverage with J01 because we find a certain number of erroneous magnitudes in J01 (see Sect. 3.3.4). We occasionally also supplement these with the *Gaia* DR2 photometry (Evans et al. 2018) because we have a small number of stars with light curves for which no standardized ground-based photometry is available. (Thus, we also include *Gaia* DR2 photometry for all stars in our discussion, and display our data against ($G_{\rm BP}$ – $G_{\rm RP}$) when appropriate.)

For near-infrared photometry, we use data from the Vista Hemisphere Survey (VHS, McMahon et al. 2013). This survey is deeper than 2MASS and provides precise magnitudes even for the low-mass members of the cluster. The K_s filter used in VHS is very similar to the 2MASS filter[9] and the small differences are negligible for our purposes, centred on the colour-period diagram; hence it can be used instead of 2MASS photometry without further adjustments.

3.3 Membership and colour-magnitude diagram

A well-defined membership list is the basis for every open cluster study. For NGC 2516 no such membership (incorporating several criteria) for the whole cluster was available in the literature until the day before the final submission of this

[8] The light curves are for the star with IDs *1v1471* and *4v46*.

[9] http://casu.ast.cam.ac.uk/surveys-projects/vista/technical/photometric-properties

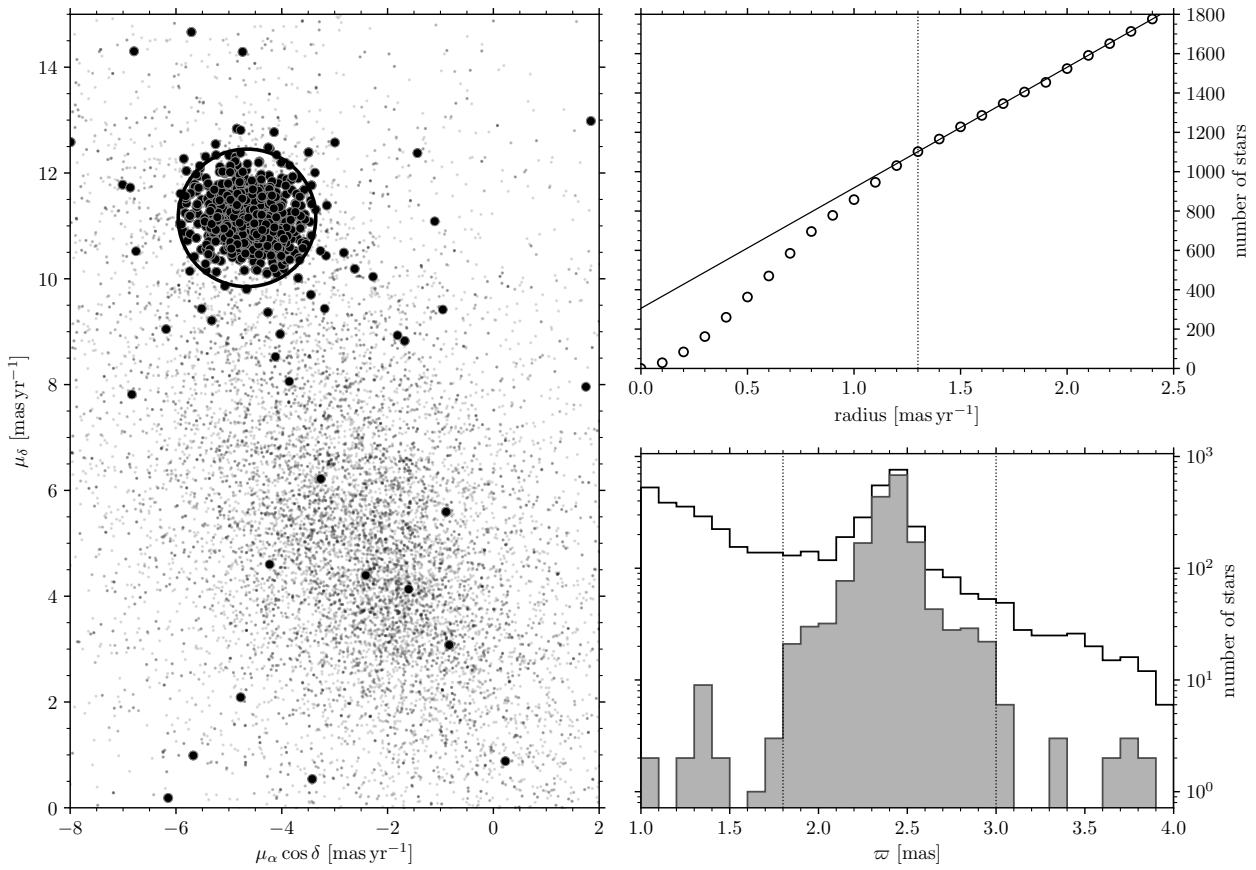

Figure 3.5: Selection of cluster members based on data from *Gaia* DR2. *Left panel:* Proper motion diagram of the field of NGC 2516. The members finally selected and satisfying at least two membership criteria are highlighted in black. All stars within the black circle (with radius of 1.3 mas yr^{-1}; see *upper right* panel) are considered proper motion members. *Top right panel:* Number of stars with proper motions against distance from the mean cluster proper motion. The vertical dotted line at 1.3 mas yr^{-1} marks the transition from non-linear to linear growth (indicated by the solid line), i.e. the transition from open cluster members to field stars, correspondingly used as the radius for the circle on the *left* plot. *Bottom right panel:* Histogram of *Gaia* DR2 parallaxes of the field (upper line) and the finally selected members (filled histogram). Stars between the vertical dotted lines are accepted as parallax-based cluster members.

manuscript[10]. However, a large number of photometric and radial velocity studies are available, each covering different fields of the cluster. Combined with the *Gaia* DR2 proper motions and parallaxes, we are able to identify the cluster members among the stars for which we have obtained light curves. We use the four criteria discussed below, first individually, and then in combination. We then construct a clean colour-magnitude diagram (CMD) for the cluster.

3.3.1 Individual membership criteria

Previously, J01 presented a photometric membership study which coincidently covers the same area as our photometry. We use this study to provide our basic photometry[11] and rely on the photometric membership presented therein (supplementing this membership as described below).

For the second element of our membership definition we use proper motions from *Gaia* DR2 (Lindegren et al. 2018). The mean proper motion of NGC 2516 is $\mu_\alpha \cos\delta = -4.6579$ mas yr^{-1}, $\mu_\delta = 11.1517$ mas yr^{-1} (Gaia Collaboration et al. 2018). We selected all stars within 1.3 mas yr^{-1} of this mean proper motion as proper motion members (Fig. 3.5 left panel). The radius was decided by plotting star counts for different radii, and marks the transition from a non-linear to a linear growth rate. See Fig. 3.5 top right panel and Fritzewski et al. (2019) for details.

[10] The results of a comparison with that work (Jackson et al. 2020) have been included in an Appendix to this paper.

[11] In addition, we use the excellent photometry from the *Gaia* DR2 as a quality check after defining the membership, but the selection of cluster members is not based on those data.

In addition to the proper motions, we include the parallax in our membership determination. Since we do not know the radial extent of the open cluster we chose to include stars within 0.6 mas of the mean cluster parallax as parallax members. With $\varpi = 2.4$ mas (Gaia Collaboration et al. 2018) this means we include stars between 330 pc and 550 pc as parallax members (Fig. 3.5, lower right panel). The aim is to remove mainly background giants and nearby low-mass stars. Among the finally selected members 96 % are parallax members[12].

Radial velocity measurements for NGC 2516 are available from multiple sources including both large surveys and dedicated work on NGC 2516. The spectroscopic surveys with radial velocity measurements for NGC 2516 are RAVE (Steinmetz et al. 2006; Kunder et al. 2017), *Gaia* ESO (Gilmore et al. 2012), GALAH[13] (De Silva et al. 2015; Buder et al. 2018), and *Gaia* DR2 (Cropper et al. 2018). Dedicated studies of NGC 2516 include the first spectroscopic studies of main sequence stars in NGC 2516 (Jeffries et al. 1998) and Terndrup et al. (2002). Jackson et al. (2016) have subsequently measured the radial velocities of low-mass stars and Bailey et al. (2018) have recently published the results of a multiplicity survey for solar-mass stars.

In order to establish a radial velocity membership list, we combined all measurements available for a given star and calculated its mean radial velocity. The zero-points of the literature data could potentially be in mild disagreement, and hence bias the mean and widen the radial velocity distribution. Placing these on the same system is beyond the scope of our work, so we have simply assigned radial velocity membership to all stars with mean radial velocities within $5\,\mathrm{km\,s^{-1}}$ of the cluster radial velocity ($v_{\mathrm{N2516}} = 23.6\,\mathrm{km\,s^{-1}}$, Jackson et al. 2016). We are aware that this procedure is likely to include a small number of non-members into our selection (as do each of the others). However, the radial velocity is only one of four input criteria for our final membership, which we expect to be much cleaner.

3.3.2 Combined membership

With the individual membership lists from the different methods at hand, we can combine them to construct a membership list that will be the basis for our further study of the open cluster. We have decided to classify a star as a member if it satisfies at least two of the membership criteria (photometry, proper motion, parallax, and radial velocity). We do not require stars to satisfy all available membership criteria because the imprecision in the photometry of the fainter stars could unjustifiably remove them from the sample. In fact, our membership criteria result in retaining many of the M dwarfs that are important for our rotational work below, and also, in contrast to many similar studies, the binary cluster members to the extent possible. An additional justification for weakening our criterion is that some stars which were classified by J01 as photometric non-members were subsequently shown to be photometric members in the *Gaia* DR2 photometry. We suspect that for those stars either the B or V magnitude has an incorrect value, placing the star off the cluster sequence in a [$B - V$, V] colour-magnitude diagram. In Sect. 3.3.4 we describe our solution to this problem.

As a consequence of the above choices, we include a small number (28) of kinematic non-members in our overall membership sample (a subset of which we will discuss individually later in the rotational analysis). By this, we mean objects that are radial velocity and proper motion non-members, but photometric and parallax members. Such kinematic non-members are likely field main sequence stars which happen to be crossing the open cluster at the observational epoch. For the time being we retain those 28 stars (= 3 %) in our membership list, but mark them for later removal from the sample, as necessary. Among these 28 stars, only 10 have multiple radial velocity measurements. Hence, the remaining 18 stars could potentially be binary cluster members (which we would of course prefer to retain).

3.3.3 Binaries

With multiple radial velocities for a number of stars, we are able to search for radial velocity variability, as arising from stellar multiplicity. For each star with multiple measurements, we calculate Δ_{RV} as the peak-to-peak difference of the set of measurements. This way we obtain well-defined values even for a sample size of only two measurements. We chose to call stars with $\Delta_{\mathrm{RV}} > 5\,\mathrm{km\,s^{-1}}$ likely binaries. This threshold was selected because certain radial velocity measurements have large uncertainties and possibly different zero-points. With this definition, we find 32 likely binaries (listed in Table 3.2) with 29 of them being members of NGC 2516. This large fraction is expected because the target selection of most radial velocity studies focused on the cluster main sequence.

Out of those 32 stars, 19 were also labelled as binaries by Bailey et al. (2018). Four of them are marked as single by Bailey et al. (2018) although the literature data show evidence for binarity[14]. Stars identified as binaries by Bailey et al. (2018) but not by our criterion usually have $\Delta_{\mathrm{RV}} < 3\,\mathrm{km\,s^{-1}}$ which is well within the uncertainty of the combined radial velocities (and reasonable in the context of a single RV study, where relative precision is better maintained.). Unfortunately, analysing the binary population further is beyond the scope of this work and we do not investigate this discrepancy here. However, for the purposes

[12] For our purposes (selecting candidate members to derive their rotation periods) this is an adequate membership selection. We note that the later derived rotation periods act as an additional membership proxy and we find 95 % of the rotators even more concentrated between 380 pc and 470 pc.

[13] The GALAH DR2 excludes most of NGC 2516 because the analysis of open clusters will be published elsewhere.

[14] This could potentially be explained by the differing baselines of the studies and also differing zero points between them.

Table 3.2: Potential radial velocity binaries in NGC 2516.

ID	*Gaia* DR2 designation	J01ID	RV ($km\,s^{-1}$)	nRV	Δ_{RV} ($km\,s^{-1}$)	B18 type	Ref.
2v1067, 2i1133	5290671630116696448	6465	74.56	2	10.15	B	4, 3
3i356, 3v336	5290672867067372672	8967	23.96	2	14.48	B	4, 2
2v430, 2i441	5290716881891963520	4125	29.34	2	10.69	...	3, 5
2v1097, 2i1164	5290719836829549056	6570	25.66	3	5.78	B	4, 3, 2
3i139, 3v140, 2i1656, 2v1524	5290720867621791488	8172	24.34	2	8.03	S	4, 5
3i84, 3v83, 2v1473, 2i1595	5290721142499618816	7962	24.38	4	5.25	S	4, 3, 5
2v1372, 2i1487	5290721864054120320	7585	27.75	3	5.07	B	4, 3, 2
2v1447, 4v62, 3v53, 4i61, 2i1568, 3i53	5290721898413863424	7864	32.54	2	10.28	SB2	4, 2
4i128, 1v1543, 1i1679, 4v127	5290722310730727040	8099	22.97	3	7.39	B	4, 3, 5
1i1319, 1v1209	5290726262100476928	6880	16.32	3	11.96	B	4, 3, 2
1v581, 2i563, 2v548, 1i619, deepW2579	5290735779747993088	4560	31.94	2	16.11	...	3, 5
1i1014, 1v939	5290738047490662016	5887	23.43	3	7.40	...	3, 2, 5
1v213	5290740040355374848	3208	18.30	4	22.20	...	3, 1, 2, 5
1v857, 1i917	5290742857853957504	5586	47.75	2	10.50	...	3, 5
3v687, 3i711	5290763095740848128	10301	27.37	3	5.32	...	3, 2, 5
3v649, 3i665	5290763160163095936	10152	-28.02	2	5.48	B	4, 3
3i1254, 3v1199	5290765397843334912	12005	15.60	2	53.60	...	3, 5
3v1116, 3i1168	5290765565341001984	11713	17.09	3	36.95	SB2	4, 3, 5
4v1274, 3v1369, 4i1360, 3i1446	5290766252535812224	12649	18.71	3	6.97	B	4, 3, 5
3i1017, 3v977	5290767115830162560	11233	7.71	3	36.06	B	4, 3, 1
3v384, 3i405	5290767562506658176	9175	27.63	3	7.13	S	4, 3, 5
3i901, 4i845, 4v789, 3v874	5290768215341699200	10863	25.84	2	9.20	B	4, 3
4v902, 4i966	5290769898968884096	11307	37.85	2	44.81	SB2	4, 3
4v321, 3v324, 4i341, 3i345	5290814875866306432	8920	25.12	2	5.67	C	3, 5
4i237, 4v225	5290816353334936576	8529	25.39	4	5.42	S	4, 3, 2, 5
4v773, 4i826	5290818964675068288	10817	25.67	3	5.01	B	4, 3, 5
4i268, deepN1774, 4v254	5290819342632176512	8634	22.27	4	9.05	B	4, 3, 1, 2
4i273, 4v259	5290820064186534144	8660	25.63	3	7.40	B	4, 3, 5
4i796, 4v746	5290821919612568064	10736	33.80	3	12.25	B	4, 3, 5
4v457, 4i490	5290822572447442176	9486	24.98	4	11.72	B	4, 3, 2, 5
1i1447, 1v1335	5290833705002367104	7328	16.56	2	6.24	...	3, 5

References. (1) Jeffries et al. (1998), (2) Terndrup et al. (2002), (3) Jackson et al. (2016) (*Gaia ESO survey*), (4) Bailey et al. (2018), (5) *Gaia* DR2

Notes. *RV* is the mean radial velocity based on the *nRV* different studies. Δ_{RV} gives the scatter around the mean radial velocity. The classification from Bailey et al. (2018) is given in the column *B18 type*. Object IDs are, in column order, our own (upto 6 detections), from Gaia DR2, and from J01.

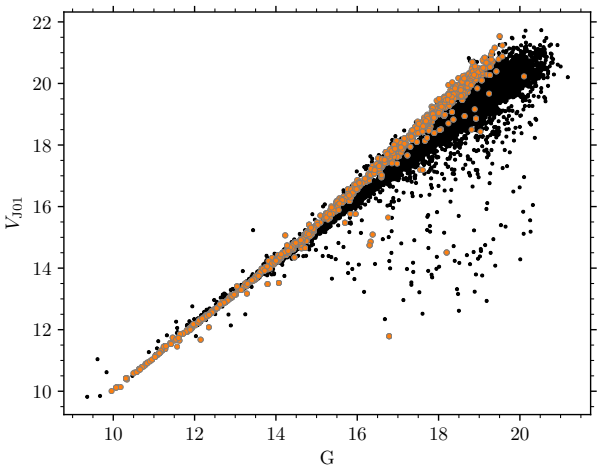

Figure 3.6: V magnitudes from J01 plotted against *Gaia* DR2 G magnitudes, with cluster members (satisfying two criteria) marked in orange. With the exception of the lower mass stars that are embedded in the background field, the member outliers below the sequences are considered for correction (as described in the text).

of this work, we include all possible photometric (from J01) and radial velocity binaries from both this study and that of Bailey et al. (2018) in the later analysis. We call out and identify the corresponding rotators when we discuss them exhaustively in Sect. 3.5.

3.3.4 Photometric anomalies

Upon inspection of our selected members in various photometric plots, we found that a small number of the measured magnitudes in J01 deviate significantly from Sung et al. (2002) and *Gaia* DR2. A comparison between Sung et al. (2002) and J01 V suggests that there is an offset of up to several magnitudes for some stars. Correspondingly, in Fig. 3.6, displaying a comparison between the *Gaia* DR2 and J01 magnitude, some stars are found well below (= brighter in V) the otherwise tight correlation between V and G. It is unusual for even highly reddened stars to be four magnitudes fainter in G than in V.

All stars with offsets are found to be brighter in the J01 photometry compared to other sources, indicating that additional flux from nearby stars likely entered the aperture in J01, who performed aperture photometry, rather than PSF fitting. Indeed, all the affected stars lie in the vicinity of brighter stars in our images, where both stars are correctly identified.

Consequently, we prefer the S02 photometry over J01 when available. Unfortunately, a number of rotators in the open cluster lie outside the FoV of S02. This motivated us to include our own photometry as a third independent data set for stars with otherwise discrepant photometry and simply to transform our instrumental values to place them on the S02 system.

Also, certain stars appear to be obvious outliers in the V vs. G diagram but we do not have a V magnitude measurement other than that from J01. For those stars, we estimated a corrected magnitude by shifting the star to the S02 system. Those magnitudes are of course relatively imprecise, but still preferable to a potentially anomalous value. All corrected magnitudes are marked as such in the membership table.

Finally, although identified as inconsistent, we retain some stellar magnitudes as published. One star (*3v580*) has neither a proper motion nor a parallax measurement from *Gaia*. This star is a binary whose second component of similar brightness was also detected by *Gaia* DR2. While both are heavily blended in our images and form a single image on the CCD, they are resolved in the *Gaia* CMD and fall onto the cluster sequence. One component appears later on the low-mass fast rotator sequence in the CPD, which fortunately, given that stars of a wide range of colour (or mass) have similar rotation periods, means that a different magnitude would not influence the shape of the rotational distribution.

We have not shifted the remaining low-mass outliers because we do not have V light curves for them. Using an estimate based on G is not useful here as even the *Gaia* cluster sequence broadens for the low mass stars and we cannot be sure about the true position in the V vs. G diagram.

3.3.5 Final membership

We have constructed a final list of cluster members from the stars which have survived our filtering as described above. It contains 844 stars (hereafter called members) and is provided as an online table with the data columns described in Table 3.3. We note that additional members, both brighter and fainter than our photometry, will undoubtedly be found in NGC 2516 in the future. As already seen from the results in Gaia Collaboration et al. (2018), NGC 2516 is one of the three richest nearby open clusters, comparable to the Pleiades (Bouy et al. 2015) and to NGC 3532 (Fritzewski et al. 2019). In summary, NGC 2516 is a very rich open cluster with 844 probable members to date within our ~1° FoV.

3.3.6 Colour-magnitude diagram

We plot the cluster colour-magnitude diagram (CMD) with the membership information in Fig. 3.7 and find that our criteria successfully retain photometric binaries. From the CMD we find that members satisfying the most criteria are usually photometrically single stars close to the cluster sequence. Stars which fulfil all four membership criteria can be found in the range from G = 11 to 18. For brighter and fainter stars, there is usually no radial velocity information available. We note that one of the cluster white dwarfs has found its way into our membership list despite our not

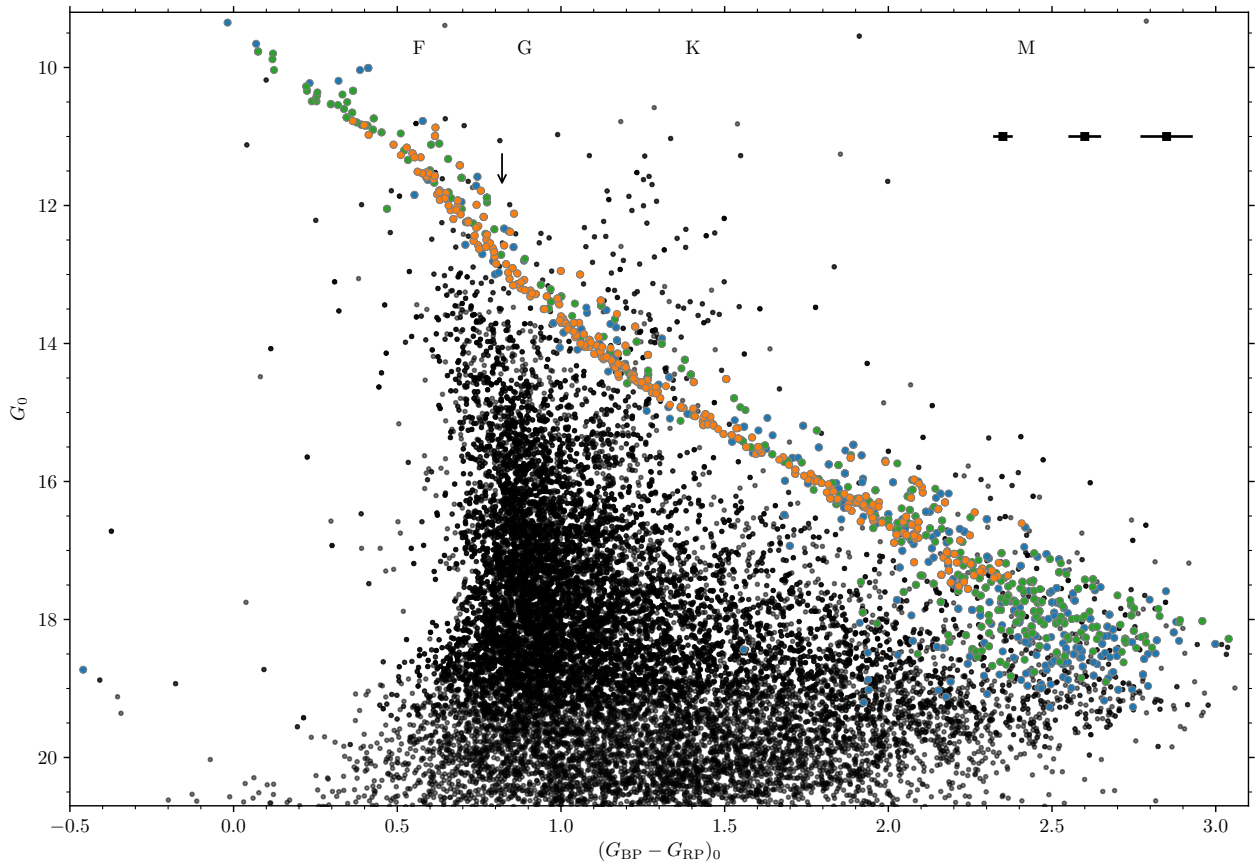

Figure 3.7: *Gaia* DR2 colour-magnitude diagram for all stars for which we constructed light curves. The best-defined members (satisfying all four criteria) are marked in orange, members according to three criteria are marked in green, and those fulfilling only two in blue. Non-members are marked in black. We note that photometric binaries are retained. The arrow indicates the colour of the Sun (Casagrande & VandenBerg 2018) for context. The spectral classifications at the top are according to Pecaut & Mamajek (2013). In the upper right we display representative uncertainties for stars on the cluster sequence. Uncertainties for $(G_{BP} - G_{RP})_0 < 2.3$ and for G are within the symbol size and are not shown here.

explicitly including white dwarfs. One could potentially include constraints from dedicated white dwarf studies (e.g. Koester & Reimers 1996) in the cluster; however our focus here is on the main sequence population of NGC 2516.

Certain stars appear to be *Gaia* photometric non-members in Fig. 3.7 but are otherwise classified as members. (Recall that *Gaia* photometry was intentionally excluded as a membership constraint.) Hence this figure provides an immediate visual impression of the false-positive rate in our membership list. However, we caution that *Gaia* DR2 photometry should not be treated as gospel truth because those data also contain misplaced stars, especially in the vicinity of brighter stars, as we will show later in Sect. 3.5.2.2 below by comparison with $(V - K_s)$ photometry for those which are found to be rotators.

3.4 Time-series analysis

Several period search algorithms are available in the literature for the determination of the rotation period (P_{rot}) from the light curve. Extensive comparisons have been published (e.g. Schwarzenberg-Czerny 1999 or Graham et al. 2013b) showing that all methods have their advantages and disadvantages depending on the type of input data or the computing time. For our study, we used an improved version of the procedure applied in our earlier work (Fritzewski et al. 2016). In the present paper we apply five different algorithms to derive the rotation period. Additionally, we filter the periods at an intermediate stage with a signal-to-noise criterion.

Our selection of algorithms includes the widely-used and robust Lomb-Scargle (LS, Lomb 1976, Scargle 1982) which is the work horse for period determination. Here we apply the generalized Lomb-Scargle (GLS, Zechmeister & Kürster 2009) which takes the photometric errors of the

Table 3.3: Description of the columns of the online Table containing the membership information for NGC 2516 constructed in this study.

Name	unit	description
ID	-	ID in this work
designation	-	*Gaia* DR2 ID
J01	-	ID from J01
RA	deg	Right ascension from *Gaia* DR2[1]
Dec	deg	Declination from *Gaia* DR2[1]
Vmag	mag	V magnitude from S02 or J01
VCorr	-	Indicates V correction (Sect. 3.3.4)
B_V	mag	$(B - V)$ from S02 or J01
bp_rp	mag	$(G_{BP} - G_{RP})$ from *Gaia* DR2
pmra	mas yr^{-1}	$\mu_\alpha \cos\delta$ from *Gaia* DR2
pmdec	mas yr^{-1}	μ_δ *Gaia* DR2
parallax	mas	Parallax from *Gaia* DR2
RV	km s^{-1}	Mean radial velocity from lit.
PMmem	-	Proper motion member (0/1)
PLXmem	-	Parallax membership (0/1)
RVmem	-	Radial Velocity membership (0/1)
PHmem	-	J01 Photometric membership (0/1)
KNM	-	Kinematic non-member (Sect. 3.3.2)

References. J01: Jeffries et al. (2001), S02: Sung et al. (2002)

Notes. [1] *Gaia* DR2 epoch is J2015.5.

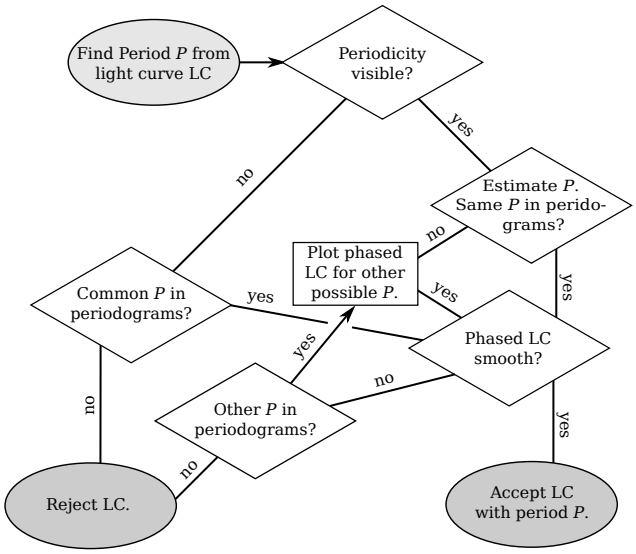

Figure 3.8: Flowchart for the determination of the preliminary period P of a given light curve (LC). All flows, with the exception of the two explicitly marked with arrows, go downwards.

light curve into account in the period determination. The (G)LS fits a combination of sine and cosine waves to the data with periods from a grid and returns the spectral power density of the light curve for each input period.

Our second method is the CLEAN periodogram (Roberts et al. 1987; Crane 2001), which is designed to suppress the window function from the periodogram and reduce the power from alias frequencies. For our ground-based observations this mainly means suppressing the one-day alias period imposed on the data by the observational frequency.

The remaining three of the five applied algorithms share the method of period search through phase-folding; nonetheless they differ from each other substantially. From this class of algorithms we chose the phase dispersion minimization (PDM, Stellingwerf 1978), string-length (SL, Dworetsky 1983), and the Gregory-Loredo Bayesian periodogram (GL Gregory & Loredo 1992, Gregory 1999). PDM uses the phase space to fold the data into a light curve with the minimal dispersion. The SL algorithm, which folds the data in the time domain and calculates the distance between consecutive points, is very similar. In addition to phase-folding, the GL periodogram uses Bayesian statistics to find the periodicity of the data. An advantageous feature of these three algorithms is that, in contrast to the sinusoidal variation used in the LS analysis, the variability of the target is not assumed to follow a specific shape.

We also experimented with the minimum entropy method (MEM, Cincotta 1999, Graham et al. 2013a) but concluded that it is not suitable for our data structure, with its median sampling of four data points per night. In most cases, even when a clear periodicity is visible in our data, the algorithm locks down on the observational frequency of 1 d and its multiples. Therefore, we have not considered this method further for our study and have limited ourselves to the five methods described above.

3.4.1 Signal-to-noise criterion

Each of the five algorithms provides a period for a light curve but does not necessarily inform us about its reliability. Although, the individual algorithms include certain measures for the spectral power of a given period which one could in principle, use to define a threshold value, we have decided not to use the power of the corresponding periodograms. Instead, we use a signal-to-noise ratio (S/N) criterion for each determined period.

For a given light curve, we obtain a set of five periods, one from each method, for which we can calculate the S/N. We then fit a sine wave for each period to the light curve. The initial phase is set to zero, and the amplitude and zero point offset are estimated from the light curve. The fitted sine is then subtracted from the light curve to estimate the noise term of the S/N. The peak-to-peak amplitude of the fitted curve is defined as our signal, and the peak-to-peak value of the residuals as the noise. The latter can be used safely because all light curves have been sigma-clipped before applying any algorithm.

The assumption of a sinusoidal shape for the light curve is appropriate because we are searching for starspot induced periodic variability. All our rotators fall into the class of sinusoidal or pseudo-sinusoidal light curves, a selection

based on this criterion is not biased towards a single class.

For each light curve, we select the period with the highest S/N as our initial period for the manual inspection and manipulation. (Further details are located in Sect. 3.4.2 below.) A comparison of the different S/N values shows that for S/N > 0.7 the values are mostly correlated, meaning that the periods of the different methods agree well. Therefore, we have chosen 0.7 as our threshold value and have manually inspected all light curves for which at least one period with S/N > 0.7 was obtained.

3.4.2 Rotation period

The initial period from the S/N criterion is preliminary, and we require a further check to ensure that it is indeed the stellar rotation period. We followed the decision-making process outlined in the flowchart displayed in Fig. 3.8. This manual procedure was only applied to our previously-determined members of NGC 2516 for two reasons: 1. it is labour-intensive, and 2. we are currently interested only in the rotation periods of the cluster members.

We inspected all available information about the light curve to evaluate whether a star exhibits convincing periodic behaviour. Apart from the light curve itself, we use all five periodograms (both in frequency and period space), and the light curve, phase-folded on the period with the highest S/N. We overplotted a sine wave with this period on the light curves in both the time domain and in phase space to guide the eye. An example for a first class rotator with light curves in multiple filters is displayed in Fig. 3.9.

Thus, our flowchart begins with visual classification of the light curve to decide whether periodic behaviour is visible at all. If so, we estimate the period by eye and examine whether this is confirmed by the periodograms. If these show evidence for the same (or similar) period as found manually, we use the phase-folded light curve. It is required to show a tight sequence of data points. In this case, we accept the period right away for further treatment (Sect. 3.4.3 below).

In certain cases, the positions of the highest peaks in the periodograms are not equal to the manually estimated period. In those cases we need to decide whether this algorithmic period is reasonable by comparing the phase-folded representation of both periods. If the phase-folded light curve is smooth we accept the algorithmic period.

In cases where no obvious periodic behaviour of the light curve is visible, we used the periodograms to seek out a common period among the different methods. If a convincing signal is present, we apply the techniques given above; otherwise the light curve is rejected as non-periodic.

Light curves with detected periods that we subsequently classify as likely aliases are treated as special cases. Those light curves are initially preferentially classified as slow rotators (i. e. the longer rotation period is preferred) with periods of a few days, together with some photometric noise. This preference is mostly supported by the periodograms themselves which confirm the longer periods. The CLEAN periodogram is especially useful in providing valuable support in these cases because it suppresses multiples of the observational frequency and the beating associated with it ($1/P_{\mathrm{beat}} = 1/P_{\mathrm{rot}} \pm 1\,\mathrm{d}^{-1}$), enabling the identification of the underlying rotation period.

Another group of stars affected by aliasing are fast rotators whose periods and corresponding aliases are both below one day. We identified several of these cases in our analysis. It is not possible to distinguish the true period from an alias without careful visual inspection. Hence, we closely inspected the light curves themselves, concentrating on the dense coverage of data points on the night of 26 March 2008, where we have up to eight images of NGC 2516 (inner fields). From this ensemble of data points, we estimated the slope of the variation, which then allows us to favour one of the possible periods. Unfortunately, the coverage is still occasionally too sparse to break the alias completely. These stars are marked as possible alias periods in our results.

Among our measured rotation periods some are of course multiples of 1 d, but for those light curves even the CLEAN periodogram confirms those periods with high significance. No signs of possible aliases can be found in those with a thorough analysis of the periodograms. And indeed, such periods are expected to occur naturally. Therefore, we have included them in our data set without further consideration.

After following the flowchart (Fig. 3.8) for all cluster members with light curves (844 stars with 1810 light curves), we identified 308 rotators (with 530 light curves). All other members are classified as showing no evidence for rotational modulation in our study. The field stars (non-members) are not considered further in this study.

3.4.3 Further treatment

The periods found above from both the light curve and the periodograms are not yet considered final. Even within a narrow range around this value each of the applied algorithms finds a slightly different period, giving us a small range of possible estimated periods.

In order to provide a mean period, we return to the periodograms and locate for each of the five the positions of the highest peak near the estimated period. For the detection, we chose a window of ±20 percent around the given period for $P_{\mathrm{rot}} > 2$ d and $\pm 0.2\,\mathrm{d}^{-1}$ for faster rotators. From the five periods derived above, we report the mean value as our period measurement and half of the range as the uncertainty.

For some light curves, the periodograms contain alias periods which are very close to the true period. Hence, they might fall into our 20 percent window and be the highest peak for one or two methods, leading to a bias of the mean period and inflation of the uncertainty. In those cases we shrank the window manually to exclude those alias peaks.

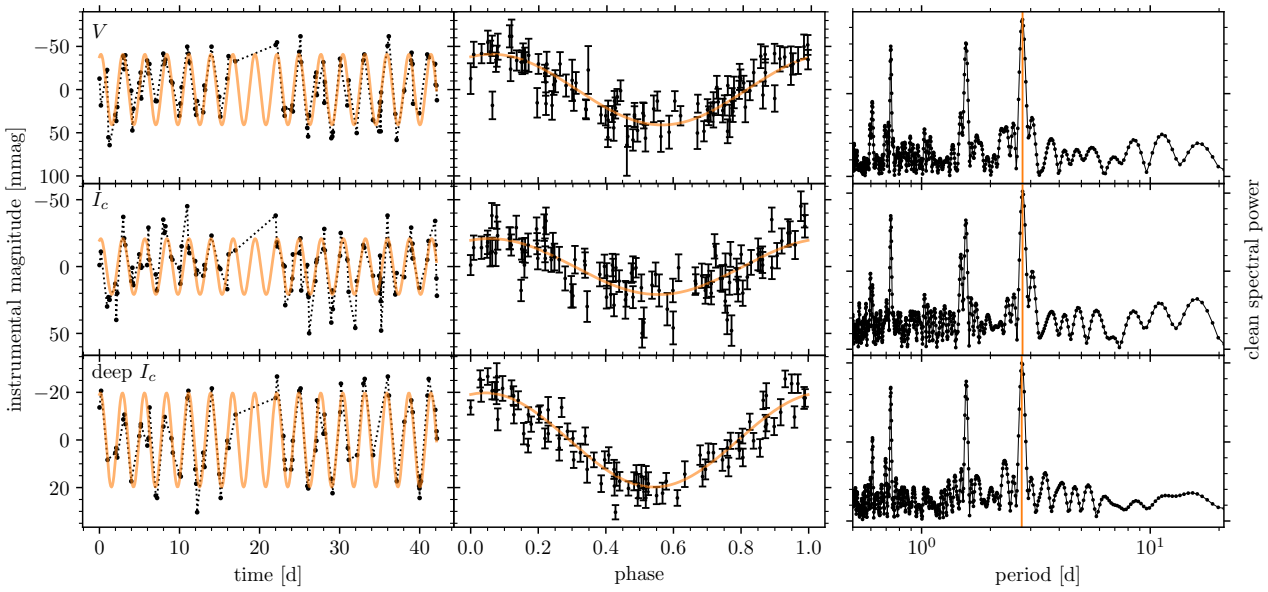

Figure 3.9: Multiple light curves for the same spectral type M1 star (Gaia DR2 5290816800011541504, V = 17.7, $(V - K_s)_0$ = 3.9) in V, I_c, and deep I_c, demonstrating both similarities and differences. From left to right, we show the light curve in the time (*left*) and phase domains (*centre*), and the CLEAN periodograms (*right*). This illustrates how a period of 2.75 d is confirmed within our data set. The rotation period is marked in the CLEAN periodogram with an orange line at the highest peak. The three highest secondary peaks in the periodogram are beat frequencies of the rotation period with the 1 d alias. This figure also shows the behaviour of measurement uncertainties in the different bands. The I_c band (*middle* row) shows especially large uncertainties relative to the light curve amplitude whereas V (*top*) and in particular the longer-exposed deep I_c (*bottom*) are more tightly correlated.

This method can lead to rather small uncertainties for those light curves with very coherent periodicity mostly fast rotators with a constant phase. Conversely, for stars with evolving spots the different methods find more diverging periods because the peaks are broader and the centre is not always at the same position.

From visual inspection we classified the light curves into three classes of confidence: (1) Stars of the first class show a clear rotational signal in both the light curve and the periodogram[15]. (2) Stars of the second class show a noisy signal in the light curve but a clear peak in the periodograms. (3) The third class consists of the possible alias periods discussed above. These classes are marked accordingly in the Figures and Tables. In Appendix Fig. 3.21, we show examples of light curves of the different classes.

3.4.4 Periods from multiple light curves

Some stars appear in multiple fields. Indeed, almost all stars in the inner fields have light curves both in V and I_c. One example with three light curves from each of the different exposure configurations is shown in Fig. 3.9. The light curves (left panels) show slightly different features that might be explained by the different observation times of the images, photometric noise and stellar activity. In general, the rotation period is visible well in all three light curves. The central column of the figure shows the phase folded light curve. It is obvious that the deep I_c light curve shows both the tightest correlation, and the smallest uncertainties. The CLEAN periodograms on the right illustrate the very good agreement of the periods for all three independent light curves. We note the presence of the clearly visible beat periods, approximately symmetric with the 1 d observing cadence.

In the most extreme case, we are in possession of eight light curves in two filters from the overlap region of all four inner fields. In such cases, even for the four light curves in the same filter, large differences in signal-to-noise are visible, showing that the detection threshold is not only a function of brightness and period, but also position on the detector. For both filters the light curve from field 1 displays the clearest variability. The poorer performance of the I_c light curves due to the lower contrast between stellar spot-group and the photosphere is also apparent.

Light curves of the same star obviously should exhibit the same period. In order to test this, we checked whether multiple periods for the same star agree within our determined uncertainties. Indeed, this is usually the case. In our whole sample of 308 stars, we found only eight stars that do not satisfy this criterion. All of them show differ-

[15] For stars in this class one could in principal determine the rotation period even without a periodogram.

Table 3.4: Description of the 555 unique-object online table containing our new 308-star stellar rotation period sample, supplemented with the 247-star sample from Irwin et al. (2007).

Name	Unit	Description
ID	-	ID in this work
designation	-	ID from *Gaia* DR2[1]
J01	-	ID from J01
RA	deg	Right ascension from *Gaia* DR2[1]
Dec	deg	Declination from *Gaia* DR2
Vmag	mag	V magnitude from S02 or J01 or corr.
B_V0	mag	$(B-V)_0$ colour from S02 or J01
V_K0	mag	$(V-K_s)_0$ colour
bp_rp0	mag	$(G_{BP}-G_{RP})_0$ colour from *Gaia* DR2
Prot	d	Rotation period
dProt	d	Uncertainty in rotation period
P90	mag	Light curve amplitude
Class	-	Classification of period
ProtI07	d	Rotation period from I07
logLxLbol	-	$\log L_X/L_{bol}$ (P06)
Ro	-	Rossby number
PMmem	-	Proper motion membership (0/1)
PLXmem	-	Parallax membership (0/1)
RVmem	-	Radial velocity membership (0/1)
PHmem	-	J01 Photometric membership (0/1)

References. J01: Jeffries et al. (2001), S02: Sung et al. (2002), I07: Irwin et al. (2007), P06: Pillitteri et al. (2006)

Notes. [1] The *Gaia* DR2 epoch is J2015.5.
The membership information provided is for both our rotators from Table 3.3, and for the additional ones from I07.

ences in their determined periods slightly larger than the estimated uncertainties. This can be seen as a test of the reliability of our uncertainty estimate. Because 2.5 percent of the stars have larger uncertainties, we conclude that the estimated uncertainties are in fact 2σ errors. This result additionally demonstrates the high reliability with which we can determine the rotation periods with our combined methods.

After having verified the agreement of all periods from different light curves, we simply average the values to determine the final period. For the uncertainty of the average period, we chose either the largest uncertainty from the various light curves, or, in the case of period differences larger than this, the amplitude of the dispersion. This procedure provides the final set of 308 rotation periods and corresponding uncertainties for NGC 2516 listed online, described in Table 3.4.

3.4.5 Variability amplitudes

An easily obtainable measure from the light curve is the variability amplitude. We define it here as the difference

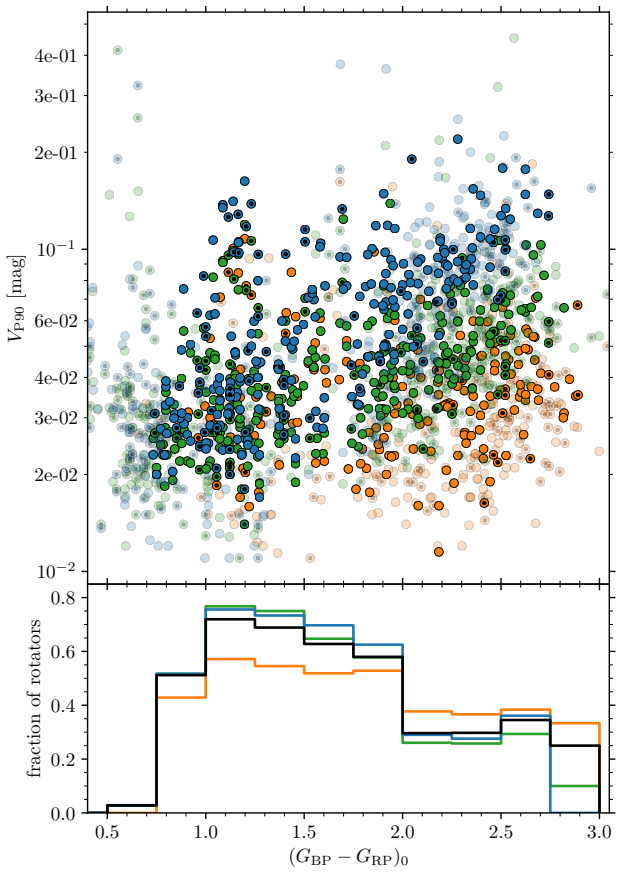

Figure 3.10: *Top:* Variability amplitude V_{P90} against the intrinsic colour $(G_{BP}-G_{RP})_0$. The colour coding is according to the exposure and filter combination (blue: V 120 s, green: I_c 60 s, orange: I_c 600 s, same as in Fig. 3.2). Stars with derived periods are highlighted and additional cluster members are shown in the background. Possible binaries (radial velocity and photometric) are indicated with additional small black dots. *Bottom:* Fraction of periodic stars as a function of colour for the different exposure and filter settings. The black line marks the overall detection rate. (It is lower for certain bins because of the additional members introduced by the deep outer fields.)

between the tenth and the ninetieth percentile of the light curve (Basri et al. 2011). This measure (V_{P90}) is robust against outliers but at the same time captures non-periodic variations. Therefore, we can calculate it for all light curves and compare the rotators to the non-rotators.

Accordingly, in the upper panel of Fig. 3.10 we display V_{P90} against $(G_{BP} - G_{RP})_0$ for all members of NGC 2516, colour-coded by the filter. It is immediately visible that both the rotators and non-rotators have very similar variability amplitudes. It follows that stars without a measured rotation period are likely have unfavourable spot configurations or evolution which do not allow the period to be measured. We have marked the possible binaries (from radial velocity and photometry) among the members and find that they too follow the same distribution.

The trend towards higher variability amplitudes with redder intrinsic colour also relates to the higher photometric uncertainty. The longest exposed light curves exhibit the lowest level of variability. Due to this trend, the detection fraction of the reddest stars is lower.

We calculate this fraction of the rotators among the cluster members and display it in the lower panel of Fig. 3.10. For the G and early K stars, we were able to derive rotation periods for up to 80 percent of the stars, mostly as a result of the ideal exposure settings. Among the M stars, the deep I_c (600 s) exposures also appear to have revealed a large number of rotators which we would have missed without these frames.

3.4.6 Comparison with prior rotation work in NGC 2516

Stellar rotation in NGC 2516 was previously studied by Irwin et al. (2007) (hereafter I07). In Fig. 3.11, we show the comparison between their periods and ours for the set of 62 common (mostly M) stars. In general the periods agree well; the data points scatter around the line of equality. However, the periods of ten stars are in disagreement, all of which are close to or exactly equal to the alias and beating periods. Hence we double-checked our periods relative to those from I07.

Among the ten stars we find five with periods in a 1:2 ratio. We have re-examined those light curves and periodograms but we cannot confirm the periods provided by I07 in our data. Hence, we conclude that our periods are preferred, especially because we are in a better position to break the aliases with our much longer baseline. Whereas I07 had two four-day windows separated by one week, we observed for 42 d with only a four day scheduling gap.

The remaining five discrepant periods are affected by beating with the observing cadence. Because both studies could suffer from this alias, it is not easy to chose between the two alternative periods. Among these five stars, two have already been classified by us as possible alias periods. For all these five stars we also detect the additional component related to the I07 period in our periodograms but for none can we unambiguously favour one or the other rotation period. Hence, we simply retain the period values we derived. All of the five affected stars are early M dwarfs where the range of observed rotation periods are large. A handful of indefinite periods will not influence the later analysis of the whole distribution as seen below.

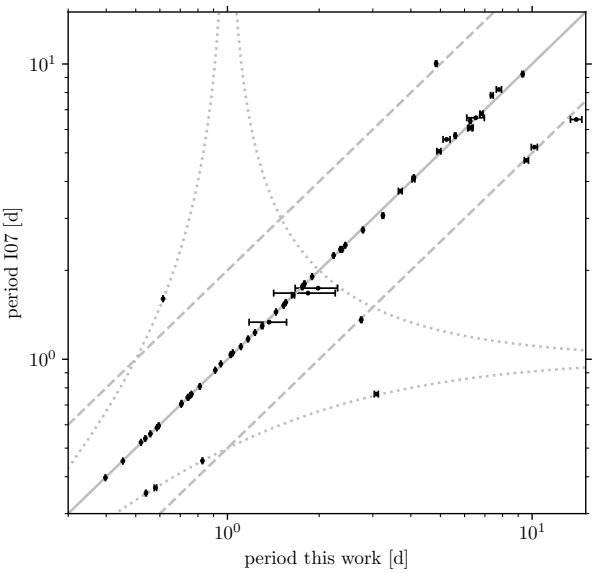

Figure 3.11: Comparison of our rotation periods with those measured by I07. The line of equality is shown as the solid grey line and the dashed lines indicate the half and double periods. The dotted lines show the beat periods of the observational period. The outliers are discussed in the text.

3.5 Colour-period diagram for NGC 2516

A standard way of displaying and discussing open cluster rotation period measurements is in a colour-period diagram (CPD), with periods plotted against any convenient colour. We therefore plot our new sample of 308 rotation periods for stars in NGC 2516 in Fig. 3.12 in a CPD using *Gaia* $(G_{BP} - G_{RP})_0$ colour, partially because of its relative precision. (Equivalent colours, $(V - K_s)_0$ and $(B - V)_0$, are also discussed below.) As expected for an open cluster of this age, we find that the distribution has a roughly triangular shape, identified by Barnes (2003b) as a key unifying feature of several ZAMS and post-ZAMS open clusters [16]. This shape has also been observed in a steadily-increasing series of open clusters since then. However, the relative absence of outliers in this member-only CPD is remarkable.

The upper boundary of the CPD is delineated by a well-defined slow rotator sequence that stretches from early G-type solar-mass stars all the way to M dwarfs. The CPD

[16] See also Kawaler (1989) in connection with the Hyades open cluster.

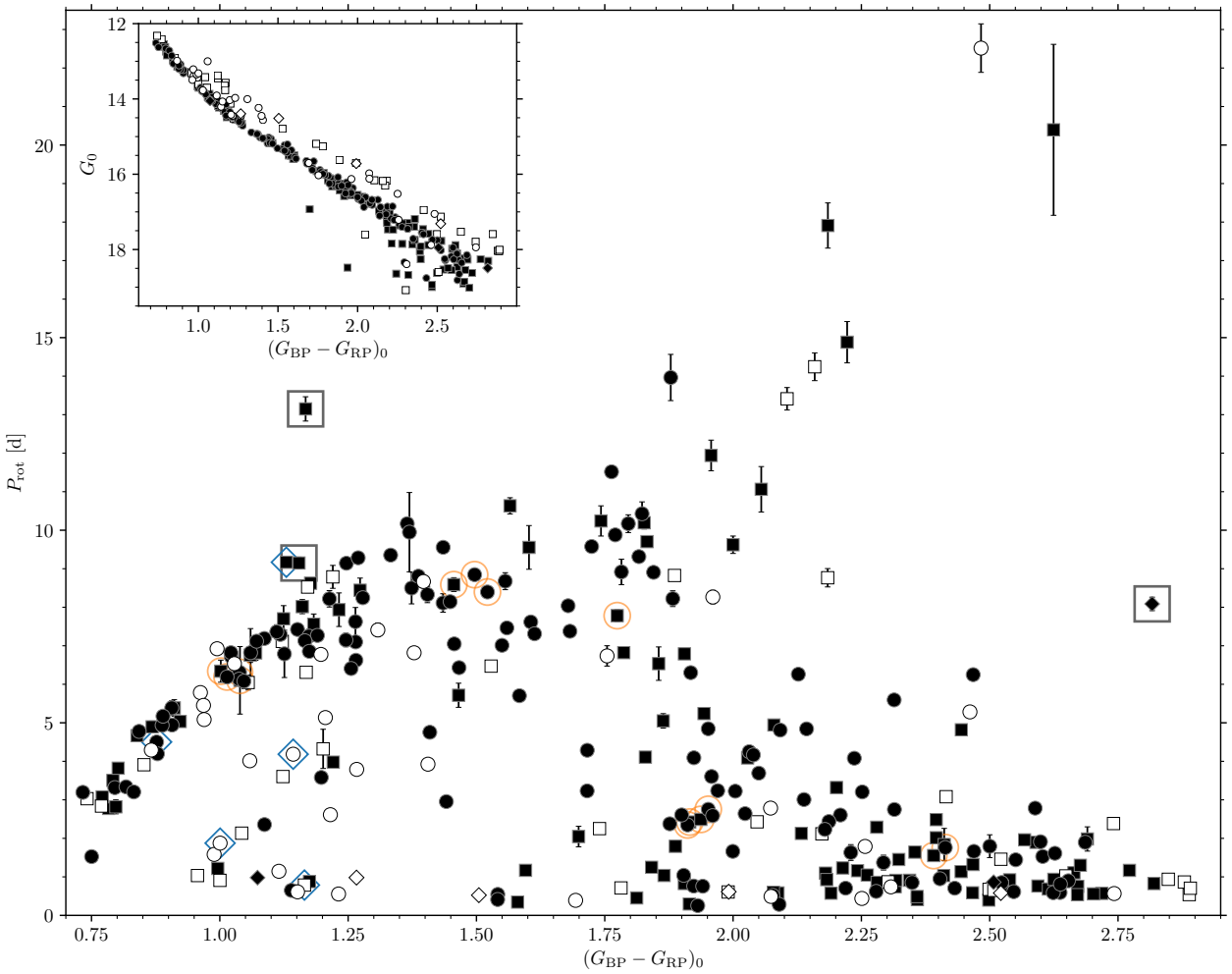

Figure 3.12: Colour-period diagram (CPD) for NGC 2516 (large figure) using $(G_{\rm BP} - G_{\rm RP})_0$ colour, with an inset displaying the corresponding colour-magnitude diagram (CMD) for the rotators. Symbols have identical meaning in both plots. A well-defined slow rotator sequence (upper boundary) is visible, as well as a fast-rotation boundary that is increasingly well-populated among cooler stars. The triangular region between these is also occupied, and the paucity of outliers is remarkable. Obvious rotation periods are marked with circles (both filled and unfilled) and less evident (algorithmic) periods with squares. (We note that the distributions are identical.) Small diamonds indicate the few possibly aliased periods. Period uncertainties are only visible when they exceed the symbol sizes. Filled symbols denote single stars (really, those without known companions to date), while open symbols indicate known or suspected binaries (of all separations), either from photometry or spectroscopy or both. Five symbols enclosed within large blue diamonds indicate those with $P_{\rm orb} < 10$ d as determined by Bailey et al. (2018), while those enclosed by large black squares are discussed individually in the text. Stars enclosed within orange circles are those whose light curves are displayed for illustrative purposes in the Appendix (Fig. 3.21).

also has a well-defined lower boundary, consisting of the fastest rotators at each colour, ranging from slightly subsolar-mass stars at $(G_{BP} - G_{RP})_0 \sim 1$ to the lowest-mass stars in the sample. Note especially that this fast rotator sample even contains Class 1 rotation periods (circular symbols, both filled and unfilled in Fig. 3.12), whose rotation periods can simply be read off the light curves without the necessity for periodogram analysis. All indicators point towards the correctness of these rotation periods, and to their being bona-fide cluster members (all plotted symbols). They should emphatically not be discarded, as in certain prior studies. As expected from prior work, the fast rotator sample is certainly less populous than the slow rotator sequence among the warmer stars, but accounts for an increasingly-large fraction of the cooler cluster member stars. The region between these boundaries, the interior of the triangular region, the so-called 'gap' region of Barnes 2003b, interpreted there as stars undergoing the uni-directional transition from fast- to slow rotation, is also occupied with both obvious (circular symbols) and algorithmic cluster member rotation periods (square symbols, both filled and unfilled). Again, the occupancy of this region represents astrophysical reality.

There are four obvious outlier rotation periods (all algorithmic), three at $(G_{BP} - G_{RP})_0 \sim 1.15$, and one possibly-aliased rotator (diamond) among the reddest stars, at $(G_{BP} - G_{RP})_0 \sim 2.8$. Careful manual inspection (Section 3.5.2 below) of the relevant data does not permit us to relocate them in any way, and we conclude that these objects are also real. We note further that these four objects are all classified as single stars to date (solid symbols of various shapes), as opposed to objects that are either photometric or radial velocity binary members (equivalent unfilled symbols).

For the CPD in Fig. 3.12, we use *Gaia* photometry because those are the only passbands where photometry is available for all stars with measured rotation periods. Later we also use $(V - K_s)_0$ as our mass proxy for two reasons. Firstly, the G_{BP} magnitude is not reliable for very low mass stars (Smart et al. 2019). Secondly, $(V - K_s)_0$ is increasingly being used in studies of open clusters, particularly as greater numbers of lower-mass stars are being measured. For instance, it is the main colour used in the recent Pleiades study (Rebull et al. 2016), our principal comparison to NGC 2516. We de-redden the photometry by rescaling appropriately from $E_{(B-V)} = 0.11$ mag (Sung et al. 2002). The optical photometry is mainly from S02 and J01, and the infrared photometry is from the Vista Hemisphere Survey (see Sect. 3.2.4). The data presented in this figure are available online, and Table 3.4 describes the columns provided.

3.5.1 Binarity

Although we do not study the binary population in NGC 2516 in detail, the literature offers significant information on multiplicity status (see Sect. 3.3.3) which we include in our analysis. We adopt the photometric binary classification from J01 and supplement this with radial velocity binaries from our analysis (Sect. 3.3.3) and from Bailey et al. (2018) without considering orbital period or separation. These stars are marked with open symbols in Fig. 3.12. We note that our current classification almost certainly includes both false-positives and false-negatives. For instance, with few exceptions, available data do not yet permit us to distinguish between those binaries that are truly interacting rotationally and those that are distant enough to be effectively single stars.

Given the above-mentioned caveats, we find that the fraction of photometric binaries among stars with $(G_{BP} - G_{RP})_0 \leq 1.8$ is 60.0 percent (12/20) for the fast rotators and a substantially-lower 18.4 percent (18/98) for the slow rotators. The gap stars have a binary fraction of 52.9 percent (9/17).

This represents a significant difference, and because it would be absurd for binaries to become single stars in the course of transitioning from fast- to slow rotation, we must conclude that this difference represents a real difference in initial conditions, that is that the rotational evolution is such that binaries preferentially emerge on the ZAMS as fast rotators, while singles preferentially appear as slow rotators.

The higher fraction of binary stars among the fast rotators and the gap stars (i.e. presumably somewhat rotationally evolved fast rotators) could point to the influence of multiplicity on the discs of young stars. For example, a (nearby) binary companion might truncate the disc, which then could dissipate faster than otherwise (Artymowicz & Lubow 1994; Mathieu 1994). In this scenario, stellar rotation would not be able to couple to the disc and the star would not have the corresponding brake on its pre-main sequence spin-up (Messina 2019). Such a mechanism would, of course, work in addition to the usual tidal interactions that are known to occur (and to influence rotation) in close binary systems. Our photometric binaries are mostly too far apart for tidal interaction to be relevant.

However, *3i1017/3v977* with $(G_{BP} - G_{RP})_0 = 1.0$, $P_{rot} = 1.89$ d, marked with a blue diamond in Fig. 3.12 is one particularly interesting case. For this fast rotator[17] Bailey et al. (2018) have obtained a radial velocity time series, allowing them to estimate the orbital period. They find a periodicity in the radial velocity data of 1.9 d. The near-exact match between the orbital and rotational periods indicates a tidally-locked system, or at least the presence of a large spot in phase with the orbital period[18]. The shape of the light curve shows a very clean rotational signal, with no sign of an eclipse.

We identified four additional stars with orbital periods below 10 d in the intersection of our data and that of Bailey et al. (2018) (marked in Fig. 3.12). However, these orbital periods are larger than two days, all unequal to the rotation

[17] UCAC4 ID 146-012601 in Bailey et al. (2018)

[18] The radial velocity amplitude is too large to originate from stellar activity.

periods (which have a large range), and show no sign of tidal-locking at the age of NGC 2516. Among these four stars, two are classified as single by Bailey et al. (2018), but with a small radial velocity amplitude, likely indicating the presence of a sub-stellar companion.

Any remaining binaries, with orbital periods $\gtrsim$10 d can, in any case, be considered effectively single stars for rotational studies of young open clusters (Meibom & Mathieu 2005; Fleming et al. 2019).

3.5.2 Outliers

Certain stars in both the CPD (Fig. 3.12) and CMD (Fig. 3.7) can be considered outliers with respect to the observed sequences. We have emboxed certain obvious rotational outliers in the CPD in Fig. 3.12. The photometric outliers were defined in Sect. 3.3.5, and are discussed now. We note that small numbers of outliers are a standard feature of open cluster CPDs, even when the rotation periods derived are completely secure. For instance, equivalents are also visible in the Pleiades and M 35 clusters. Nor do any of these particular stars display overt signs of being binaries. However, we show below that the most egregious outlier is a non-member.

3.5.2.1 Outliers in the colour-period diagram

Star *dS1490* with $P_{\rm rot}$ = 13.15 d at $(G_{\rm BP} - G_{\rm RP})_0$ = 1.15 is an obvious outlier well above the slow rotator sequence. From our membership, we can easily see that this star is a kinematic non-member because both the radial velocity and the proper motion are not consistent with cluster membership. However, it has the same distance as the cluster and is located on the main sequence, leading to classification as a photometric member because our threshold requirement that two criteria be matched for membership leads to its being included as a member (see Sect. 3.3.2). This star is apparently an older field star that is passing through the cluster. From its rotation period, we estimate its age to be 870 Myr[19], which is older than even the Hyades cluster. Therefore, we have removed this star, and the three other kinematic non-members in our sample of rotation periods, from further analysis, and from the figures[20].

The two stars *3v516* and *3v924* ($(G_{\rm BP} - G_{\rm RP})_0$ = 1.15, $P_{\rm rot}$ = 9 d) are cluster members fulfilling all four membership criteria. However, they appear to be slightly above the slow rotator sequence. When comparing the NGC 2516 CPD to that of the Pleiades in Sect. 3.7.1.4 (below), we find additional stars in this region of the CPD ($(V - K_s)_0 \approx 2.2$) which also seem to be outliers. A discussion of possible reasons and consequences is postponed to Sect. 3.7.1.4 below.

The star *dE2352* can only be found on the CPD with *Gaia* photometry at $(G_{\rm BP} - G_{\rm RP})_0$ = 2.8, $P_{\rm rot}$ = 8.09 d but not in the other figures because we do not possess either visual and infrared photometry for this star, despite its being well-exposed in our images. We find no other star in this area of the CPD, but note that our (determined) period of 8.28 d has a beat period with the 1 d observing period at 1.14 d. That would put it in the same location in the CPD as other fast rotators in NGC 2516. The CLEAN periodogram has a peak at that period but it is not as high as the main peak. We were unable to confirm the shorter period although it would fit the overall picture in the CPD. As the highest peak is found for 8.28 d in the periodograms, we do provide this period in the data table, but flag it as a possible alias.

3.5.2.2 Photometric non-members

In Sect. 3.3.5, we found a few photometric non-members in our membership list shown in Fig. 3.7. Among the rotators, the photometric outliers are found mostly at the faint end of the cluster sequence. In the CMD inset in Fig. 3.12, three somewhat bluer stars appear below the main sequence (with $(G_{\rm BP} - G_{\rm RP})_0 \lesssim 2.1$). A detailed analysis of the available photometry from the various publications reveals that the bluer the filter the more off-set the stars are from the cluster sequence. Visual identification on images shows much brighter stars located in the vicinity of the affected cluster members. Hence, we infer that scattered light influences the determination of the flux in the bluest pass bands[21] and redder colour indices such as $(V - K_s)$ are barely influenced. As a result we do not flag or remove any of those stars but use $(V - K_s)$ colour instead.

3.5.3 Inclusion of rotation periods from Irwin et al. (2007)

The prior study of I07 used a larger telescope in search of exoplanets among the fainter stars of NGC 2516. Although their baseline coverage (of two 4-night runs, with a one week gap) was optimized for planet discovery, they also derived a large number of rotation periods for the low-mass M dwarfs in NGC 2516. In contrast, our sensitivity (long and baseline) is optimized for the solar-mass, K, and early-M stars, making the two studies complementary.

In order to obtain the richest possible distribution of rotation periods for NGC 2516, we append the periods for the low-mass stars determined by I07 to those from our sample. However, with both the improved astrometry from the *Gaia* mission and the radial velocity study by Jackson & Jeffries (2010) we are now in a position to remove non-member contaminants. To clean the I07 sample, we therefore applied the same membership criteria as we applied to our own data.

[19] We have used the Barnes (2010) formula for age here and assumed that the star is not otherwise pathological.

[20] The other identified kinematic non-members among our rotational sample have only one radial velocity measurement each. Additionally, all of them fall onto the sequences in the CPD. Hence, they could potentially be binary cluster members, and thus have not been removed.

[21] This shows that even the relatively precise *Gaia* photometry can occasionally be erroneous.

We found 41 of the 350 rotators in I07 to be non-members. Notably, these are often the outliers described by I07 in their Section 5.1.2, explaining their abnormal behaviour. Additionally, the two bluest slow rotators and the overall slowest rotating star in their sample are also non-members, despite their agreement with the general distribution of stars in the CPD. The remaining non-members are among the fast-rotating stars, hidden within the distribution of members.

In Fig. 3.13, we display both datasets in a CPD[22]. After removing the overlap between the two samples, we finally compiled a list of 555 unique individual rotators, which we subsequently use for comparison with the Pleiades distribution[23].

The additional low-mass stars contribute in particular to the connecting region in the CPD between the slow rotator sequence and the M dwarf fast rotator sequence, and to the fast rotating tail of very late-type M dwarfs. Thus, the union of the two data sets provides what we consider to be a relatively comprehensive picture of the rotation period distribution of FGKM stars in NGC 2516.

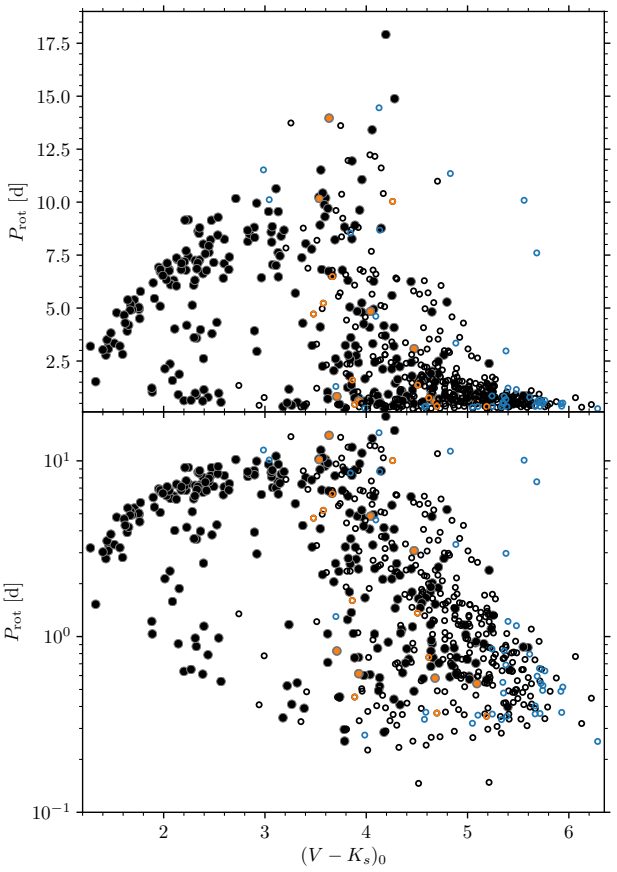

Figure 3.13: Colour-period diagram for NGC 2516 with our data (solid) and the data from I07 (open) on both linear and logarithmic scales. Periods in disagreement between the two data sets are marked in orange (with solid circles for this work, open circles for I07). Blue symbols indicate non-members from I07 (subsequently suppressed), identified as such by us using the improved astrometry and new radial velocity measurements.

3.6 Comparison with models of stellar rotation

A comparison of rotation period measurements with theoretical models can help to constrain them and provide insight into stellar activity physics. Here, we display a comparison of the NGC 2516 data with five such models from the literature in order to provide an overview of the current state[24]. We present the selected models chronologically and include comments on their differences and distinctive features.

3.6.1 Model of Barnes & Kim (2010) and Barnes (2010)

The oldest of the models considered is the Barnes & Kim (2010), Barnes (2010) model, developed as an improvement upon the original gyrochronology formulation presented in Barnes (2003b). This model consists of an analytic overlay on regular stellar structure models for the main sequence[25], from which it extracts and uses in particular the convective turnover timescale. Thereafter, the model evolves an assumed initial (ZAMS) distribution of rotation periods forward in time, as required by the age of the cluster being discussed. Guided by observations then available in the youngest ZAMS clusters, this initial distribution was specified by Barnes (2010) to range from 0.12 d to 3.4 d, although this can in principle be modified as necessary. As in prior work by our group, we here retain all features exactly as in that decade-old model to maintain consistency.

The model contains only two parameters, namely the two dimensionless constants $k_c = 0.646\,\mathrm{d\,Myr^{-1}}$ and $k_I = 452\,\mathrm{Myr\,d^{-1}}$, which together with the extracted convective turnover timescale, τ_c, of the stellar model, govern the rotational evolution timescales in the fast- and slow-rotator regimes respectively. These particular parameter choices were specified by comparison with all relevant observations available at that time, and of course, with respect to the convective turnover timescales tabulated in Barnes

[22] 2MASS data are used here for the stars of I07 because the VHS did not cover the whole area observed by I07.

[23] Ten of these 555 rotators have recently been classified as non-members by Jackson et al. (2020) using somewhat stricter membership criteria. We list the IDs of these stars in Appendix 3.C.

[24] To a greater or lesser extent, the models presented here include insights from prior theoretical models, including MacGregor & Brenner (1991), Pinsonneault et al. (1989), Kawaler (1988), extending to Endal & Sofia (1979).

[25] There is little change in these quantities on the main sequence, but the model can of course be extended to make the underlying quantities dynamic.

& Kim (2010). These timescales are included mathematically symmetrically in the model for the rotation period evolution and the formulation is such that the transition from fast- to slow rotation occurs automatically at the fixed Rossby Number, $Ro = P/\tau_c = \sqrt{(k_I k_c)} = 0.06$, where the numerical value in the final equality is specified with respect to the convective turnover timescales in Barnes & Kim (2010)[26]. A slow rotator sequence develops naturally in this model, with an asymptotic shape specified by the convective turnover timescale on the main sequence. In this model that asymptotic shape is $P \propto \sqrt{\tau_c}$.

Figure 3.14 displays this model (with two green curves) for the fast and slow rotator boundaries of the allowed distribution calculated for the isochrone age of 150 Myr, against the NGC 2516 rotation period measurements. (We note that a G2 star has $(V - K_s)_0 = 1.56$ (Pecaut & Mamajek 2013), which means that the warm end of our rotation period distribution is at F9 (Pecaut & Mamajek 2013); the Pleiades rotation periods (see Sect. 3.7) appear to extend the distribution to approximately the convective-radiative boundary.) Inspection of the lower boundary of the rotation period distribution shows that its fast edge is described adequately by this model. In fact, the uplift of the curve for the warmer stars with $(V - K_s)_0 \sim 1.3$ reasonably describes the shorter spin-down timescale for these stars and the corresponding early development of the slow rotator sequence for stars warmer than this, at which point spin-down is heavily curtailed as the star transitions into the slow rotator regime.

On the other hand, the location of the slow rotators in NGC 2516 is problematical in this model (upper green curve). For stars warmer than solar, the initial rotation period of 3.4 d is clearly too long because that is already significantly above the NGC 2516 data. The cluster being at the ZAMS, it is clear that not enough time has elapsed for the initial rotation period distribution to have been forgotten. This is again an issue for the coolest M-type stars (with $(V - K_s)_0 \gtrsim 4$) in that the initial rotation period of 3.4 d is clearly an overestimate[27], and in any case, probably meaningless in a context where the stars are still on the pre-main sequence. As regards the K-M type stars with $2 < (V - K_s)_0 < 4$, because the NGC 2516 data are significantly above the model, it is correspondingly also clear that either the assumed 3.4 d initial period is too short, or this model is not sufficiently aggressive in spinning down the slow rotators. However, this model does have the very desirable feature of retaining fast rotation for the lower-mass stars, as seen in the fact that the isochrone dips towards faster rotation for $(V - K_s)_0 \gtrsim 3.5$.

Finally, we check whether the Barnes & Kim (2010) and Barnes (2010) model is able to separate the fast- and slow rotators adequately. The separation between these groups (which will become more obvious in Sect. 3.7) was called the 'rotational gap' and proposed in Barnes (2010) to be a line of constant Rossby Number (Ro), located at $Ro = P/\tau_c = 1/\sqrt{k_I k_C}$, i. e. $P = 0.06\,\tau_c$, using the numerical constants k_C and k_I in that model. Accordingly, we plot the line $P = 0.06\,\tau_c$ in Fig. 14, using the values of τ_c in Barnes & Kim (2010)[28]. We observe that this line is able to separate these two groups of stars relatively effectively in the F, G, K spectral range. One could argue that this line is located at overly-long rotation periods for M-type stars. For the present, we are uncertain whether to implicate the model itself, the turnover timescales, the intermediate colour transformation required, or even the behaviour of the stars themselves, given that they are still in the pre-main sequence phase of evolution.

3.6.2 Model of Matt et al. (2015)

The model presented in Matt et al. (2015) is similar to the Barnes (2010) model in that it also expresses the torque on an (assumed) solid-body stellar model as a function of the convective turnover timescale, albeit a higher (second) power. The remaining dependencies apart from the rotation rate in the (separable) torque formulation are absorbed into a function $T_0 = T_0\,(T_\odot, M_\star, R_\star, Q, m)$ which itself includes adjustable powers, m, of the mass ($M_\star$) and radius ($R_\star$) of the star, a tunable parameter Q, and a constant, $T_\odot$, that is scaled to reproduce the torque on the current Sun. It also parametrizes the stellar magnetic field and mass loss rate jointly as a separate power, p, of the Rossby Number Ro. Consequently, it has a few more degrees of freedom than the Barnes (2010) model. The resulting spin-down timescales for both the fast and slow rotator regimes have similar mass dependencies to those in Barnes (2010), as can be seen explicitly in Fig. 1 in Matt et al. (2015), where a number of other older models are also displayed for comparison.

In Fig. 3.14, we show the asymptotic spin rates (in blue) from the Matt et al. (2015) models for ages of 150 Myr (as with other models) and 100 Myr, together with our NGC 2516 rotation periods. The reason for displaying a younger 100 Myr age in addition to the 150 Myr isochronal age of NGC 2516 is that the younger model is significantly closer to the NGC 2516 data than the older one. In this connection, we note that a difference between the model age and another age estimate, such as an isochronal age, is not necessarily a problem unless the rotation periods are used in deriving ages via gyrochronology, as opposed to generally understanding angular momentum evolution. As already pointed out by Matt et al. (2015), the asymptotic

[26] Other published timescales may also be used because timescales from differing publications tend to differ only by a scaling constant, but then the dimensionless constants k_c and k_I should be adjusted accordingly.

[27] The stated reason for this in Barnes (2010) was the desire to retain a simple flat initial rotation period distribution at the ZAMS, and then to show that the shape of the slow rotator sequence would develop automatically.

[28] The constants k_I and k_C are particular to the Barnes & Kim (2010) convective turnover timescales and will require slight recalibration if other timescales are used.

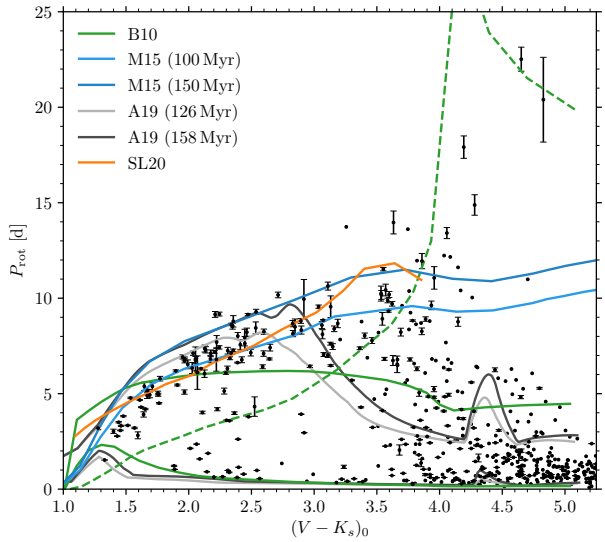

Figure 3.14: Colour-period diagram for NGC 2516 comparing multiple rotational isochrones (chronological by date of publication top to bottom in the legend). Green curves show the upper and lower boundaries of models from Barnes (2010) (B10) with corresponding initial periods of 3.4 d and 0.12 d respectively. The dashed line indicates the transition ($Ro = 0.06$) between fast- and slow rotation in the B10 model. The blue curves show the asymptotic spin rate from Matt et al. (2015) (M15) for 150 Myr (upper blue) and 100 Myr (lower blue). The grey curves show the models of Amard et al. (2019) (A19) for 158 Myr and 126 Myr, each for both the slow and fast rotators. The orange curve shows the two-zone model of Spada & Lanzafame (2020) (SL20) for 150 Myr. (See the text for a detailed comparison of each model with the data.)

model plotted is not descriptive of the behaviour of the fast rotating M dwarfs at the low-mass end of the distribution. We conclude from the comparison that the spin-down in this model is somewhat more aggressive than warranted by the NGC 2516 data.

3.6.3 Model of Garraffo et al. (2018)

Garraffo et al. (2018) have proposed a model using scaling laws from Garraffo et al. (2016) for angular momentum loss rates as a function of magnetic morphology. In this model, the magnetic morphology of cool stars is proposed to be a smoothly-changing function of the Rossby number, *Ro*. This functional dependence is analogous to the period derivative dependence in Barnes (2010) in that here the dependence is also on the Rossby number and its inverse, and includes two related dimensionless constants a and b (see their Eq. 5). This form for n permits drastic changes in the angular momentum loss rates, as noted in Kawaler (1988), Barnes & Sofia (1996), and reaching back to Mestel (1968). Ignoring any possibly additional parameters in the derivation of the scaling laws, one finds that $\dot{P} = \dot{P}(c, a, b, I, B, P, \tau)$, where I is the star's moment of inertia, assumed to be constant. This is therefore a seven parameter model in general, although the term with the magnetic field strength, B, is apparently allowed to be suppressed under certain conditions, as in their paper.

Garraffo et al. (2018) were able to produce a desirable bifurcation in P because of the features described above. However, their models have very significant departures from the shape of the open cluster rotation period distributions at various ages (including Pleiades and NGC 2516 age), as one can see in the comparisons shown in Fig. 4 of their paper, and as can be seen by calculating asymptotic solutions. Unfortunately, their models are not available in a form that we can readily reproduce in Fig. 3.14 to compare directly with our data.

3.6.4 Model of Amard et al. (2019)

Amard et al. (2019) have largely implemented the Matt et al. (2015) prescription of angular momentum loss into the Geneva/Montpellier stellar models[29], together with additional parameters and initial conditions tuned to reproduce various open cluster rotation observations. (For instance, a disk-locking timescale is included on the pre-main sequence.) The computed mass dependence of rotation for the slower and warmer stars is almost identical to that of Matt et al. (2015), as one might expect from the adoption of that prescription here and as can be seen from the grey curves corresponding to this model in Fig. 3.14. However, Amard et al. (2019) have modified the (*Ro*-based) threshold for saturation significantly to retain fast rotation for longer timescales among lower mass stars, making it similar to the one from Barnes (2010). Consequently, this model has even more degrees of freedom than that of Matt et al. (2015).

We display the Amard et al. (2019) models for two different ages, 126 Myr, the age they assign to the Pleiades, and 158 Myr, the model they provide that is closest in age to the isochrone age of NGC 2516. The linear rotation period scale in our plot, together with the improved dataset, allows a more detailed view of the comparison than the logarithmic plot in Amard et al. (2019).

The slow rotator curves for both ages, especially the older one, in the Amard et al. (2019) models can be observed to be located at significantly longer periods than allowed by the NGC 2516 data for $(V - K_s)_0 \lesssim 2 - 3$. The spindown is clearly over-aggressive. However, the modification of the threshold for saturation noted above allows the isochrones (displayed in Fig. 3.14) to deviate away from the slow rotator sequence at $(V - K_s)_0 > 2.7$ and approach the fast-rotating region for M dwarfs. The turndown of the cooler slow rotator models towards shorter rotation periods is clearly a

[29] These also permit radial differential rotation in radiative regions.

positive feature of the model, even if it is not quite happening at the correct stellar mass. We hesitate to speculate about the clearly-visible kinks in the Amard et al. (2019) models at $(V - K_s)_0 \sim 2.5$ and $(V - K_s)_0 \sim 4.5$, presuming them to be isochrone-related artefacts.

Amard et al. (2019) also include a model for the fast rotators in their paper, enabling us to display the corresponding comparison in Fig. 3.14. These models are quite similar to the model from Barnes (2010) across the entire mass range, particularly with respect to being able also to produce a noticeable spindown among the warmer stars $(V - K_s)_0 \sim 1.3$. (This was first successfully modelled by Barnes (2010) (green curve), invoking a Rossby Number-based transition from fast- to slow-rotation.) However, the NGC 2516 observations, because they are significantly above the fast rotator model curves, appear to inform us here that the Amard et al. (2019) models should be spun down somewhat more aggressively here than they currently are.

3.6.5 Model of Spada & Lanzafame (2020)

Our final model comparison is to one devoted exclusively to the slow rotator sequence that is presented in Spada & Lanzafame (2020), further developing the two-zone model presented in Lanzafame & Spada (2015), where the radiative core is permitted to decouple from the convective envelope. This model is overlaid on the Yale stellar models and the basic angular momentum loss formulation is taken from Barnes & Kim (2010) and Barnes (2010). Consequently, it has an additional degree of freedom above that of Barnes (2010) in that it implements one additional (strongly mass dependent) coupling timescale between the two zones, applicable to the slow rotator sequence itself. This timescale is presumably independent of the (also strongly mass-dependent) fast- to slow-rotator transition that is observed in young open clusters. The fast rotators are not addressed in this model.

In Fig. 3.14, we show the 150 Myr model from Spada & Lanzafame (2020) in orange. This curve generally follows the slow rotator sequence of NGC 2516 reasonably well for stars of lower mass than the Sun ($(V - K_s)_0 \gtrsim 1.5$). This is perhaps unsurprising, given that the Pleiades (assumed to be 120 Myr) were used as a reference cluster (although not an exclusive one) for the model. There appears, however, to be some deviation towards slower-than-observed periods for the solar- and higher-mass stars, as one can see especially well when we include the Pleiades rotation periods (in the next section). The spindown is also perhaps somewhat too aggressive for the slow rotators cooler than $(V - K_s)_0 \sim 3$. Finally, since this model is formulated exclusively for the slow rotators, it does not model the lowest mass fast rotators.

3.6.6 Suggestions for the applications of angular momentum models

In summary, each of these models has certain advantages, and is able to reproduce particular aspects of the CPD, all at the expense of having increased the number of degrees of freedom over Barnes (2010), with Spada & Lanzafame (2020), Garraffo et al. (2018), Matt et al. (2015), and Amard et al. (2019) in order of increasing number of parameters. Our recommendation, therefore, is instead to consider the data presented here as specifying both the initial (near-ZAMS) distribution for rotational evolution models aimed at older main sequence populations and as the target distribution for pre-main sequence models.

3.7 Comparison with other similar open clusters, especially the Pleiades

We noted in Sect. 3.1 that the Pleiades is the best open cluster for comparison with NGC 2516. In addition to the similar age and richness, the Pleiades is one of the best-studied open clusters and is often seen as the archetype ZAMS open cluster. One might therefore ask whether there is such a thing as an archetypical open cluster for rotation, or whether cluster-to-cluster variations actually exist. After a detailed comparison with the Pleiades, we briefly investigate other similarly-aged open clusters with respect to those questions.

3.7.1 Comparison between the Pleiades & NGC 2516

We use the very rich and most complete K2 dataset presented in Rebull et al. (2016) for our detailed comparison with the Pleiades rotational distribution. We also consider questions raised by Stauffer et al. (2016) about specific features in the rotational distribution of the Pleiades. For NGC 2516 we used the above-presented rotation periods together with the cleaned period sample from I07 (Sect. 3.5.3).

We note that biases exist in the data, and can influence the comparison; therefore, awareness of limitations is important. For instance, the variability amplitude imposes a significant detection limit on our ground-based data for NGC 2516, whereas this is largely irrelevant for the space-based (Kepler/K2) Pleiades data. Therefore, any possibly-identified voids in our rotational distribution should be treated with caution, and detectability ought to be considered[30]. However, the overall completeness of the membership information is excellent for both open clusters, and should not be a limiting factor.

3.7.1.1 Pleiades & NGC 2516: Full distribution of rotation periods

We display the Pleiades rotation periods from Rebull et al. (2016) in the left panel of Fig. 3.15 (orange) together with

[30] Readers might wish to refer back to Sec 3.4.5 and Fig. 3.10 at this point.

our rotation periods for NGC 2516 (black) in a $(V-K_s)_0$ CPD. The two clusters present the same morphology across the entire colour-period diagram, making the visual appearance of the two clusters almost indistinguishable. In particular, the tight slow rotator sequences follow each other closely at the warm end of the distribution, as do the fast rotators at the cool end. Despite the larger (and apparently intrinsic) rotational scatter among the intermediate-mass (K - M) stars ($(V-K_s)_0 \sim 3-4$), the two distributions are also essentially visually indistinguishable. Finally, both clusters contain sequences of early-M stars with very long (up to ~23 d) rotation periods. In fact, we find that almost every group of stars in one CPD, with the exception of the brightest ones in NGC 2516 (which are saturated in our images), has a corresponding group in the other CPD.

Nevertheless, certain minor differences between the two distributions are present, which we wish to highlight quantitatively. For each star in the NGC 2516 CPD, we measure the distance to the nearest star in the Pleiades CPD. As our difference metric, we simply chose the Euclidean distance (hereafter simply distance) in the normalized CPD. We normalized both the $(V-K_s)_0$ and $P_{\rm rot}$ axes to the interval $[0,1]$ with the end points chosen such that the values from NGC 2516 fill the whole range. In order to avoid being distracted by the visually-obvious larger separations among the long-period rotators, we limited the comparison region to periods $P_{\rm rot} < 10.5$ d[31]. Correspondingly, the right panel of Fig. 3.15 shows the CPD of NGC 2516 with each star colour-coded by its distance from the closest Pleiades star. (The Pleiades stars are also displayed unobtrusively with grey dots in the background.) The distance is normalized to the standard deviation of the distribution.

The smallest distances are found for the stars on the two clear fast- and slow rotational sequences. (These stars are yellow in the colour map chosen.) Stars towards the edges of those sequences are somewhat sparser in the CPD, and consequently are more distant from the corresponding stars in the Pleiades, as can be visually appreciated through their darker colours in Fig. 3.15. A number of stars are several standard deviations away from their nearest counterparts in the Pleiades. Those groups of stars are labelled with encircled numerals in the right panel of Fig. 3.15 to enable us to discuss them individually below.

3.7.1.2 NGC 2516 vs. Pleiades: Fast rotators

The fastest rotators (marked with an encircled numeral *1* in Fig. 3.15) in both clusters are very similar. In particular, their appearance as distinct sequences with $P_{\rm rot} \lesssim 1$ d and a mostly empty region above it in the CPD is notable. This sequence extends from the warmest stars in the CPD, where it meets the slow rotator sequence, to the coolest M dwarfs.

We observe a slight lift of the fast rotator sequence in both clusters (*2*) for $(V-K_s)_0 \sim 1-2$. In particular, when combining the two samples the rise of the fast rotator sequence is visible best in Fig. 3.15. All stars in this colour range seem to have spun down by a factor of two or so, from their initial ZAMS rotation period, hence this feature could indicate the evolution of both clusters beyond the rotational ZAMS, suggesting a very similar age. However, the exact counterparts for the higher-mass stars in NGC 2516 are missing. Such stars have very low variability amplitudes (c.f. Fig. 3.10), which means that we likely do not detect them with our ground-based photometry, despite their likely existence in NGC 2516.

3.7.1.3 NGC 2516 vs. Pleiades: Rotational gap

As stars spin down from the fast to the slow rotator sequence, they eventually have to cross the gap region (*3*) between the two sequences. Indeed, we find a group of intermediate ~4 d rotators in NGC 2516 that are relatively isolated in the gap region. These stars have no equivalent in the Pleiades and are among the stars with the largest distance to any Pleiades star. Curiously, their measured periods are approximately half that of the slow rotator sequence at this colour. We have therefore re-checked their light curves carefully to exclude a half or double period alias and to identify systematic trends like peaks of alternating height, none of which we see at the level of precision of our light curves. We therefore consider these period measurements to be genuine and list them as such. This view is supported by their X-ray activity (see Sect. 3.8 below), which is also noticeably lower than for the fast rotators but higher than for slow rotators of the same colour. Hence, we conclude that this group constitutes an intrinsic feature of the NGC 2516 CPD.

Such a group of gap stars has also been found in the nearby stellar stream Meingast 1 (Meingast et al. 2019; Ratzenböck et al. 2020) by Curtis et al. (2019). A comparison of the rotation periods between this stream and the Pleiades revealed that the two objects have similar ages. With the knowledge that the gap stars found in this stream are also present in the slightly older NGC 2516, we conclude that they are not a sign of youth relative to the Pleiades, as proposed by Curtis et al. (2019).

In conclusion, the existence of gap stars in NGC 2516 and Meingast 1 suggests that they are an intrinsic feature. The fact that only a fraction of the fast rotators have evolved into the gap stars provides evidence that the transition from fast to slow rotators is not occurring at the same age even for all stars of the same mass (or colour) but with a degree of randomness, or perhaps 'metastability' in the language of Brown (2014).

3.7.1.4 NGC 2516 vs. Pleiades: Slow rotators

The slow rotator sequences of both clusters are very similar and correspondingly we find the shortest distances ($\lesssim$1 S.D.; yellow) here. Although this result appears to be trivial it is

[31] This approach was chosen because CPDs are usually displayed with near-equal aspect ratios, despite the fact that the rotation periods span over one order of magnitude. The normalization ensures a result that simply quantifies the qualitative results obtained through visual inspection.

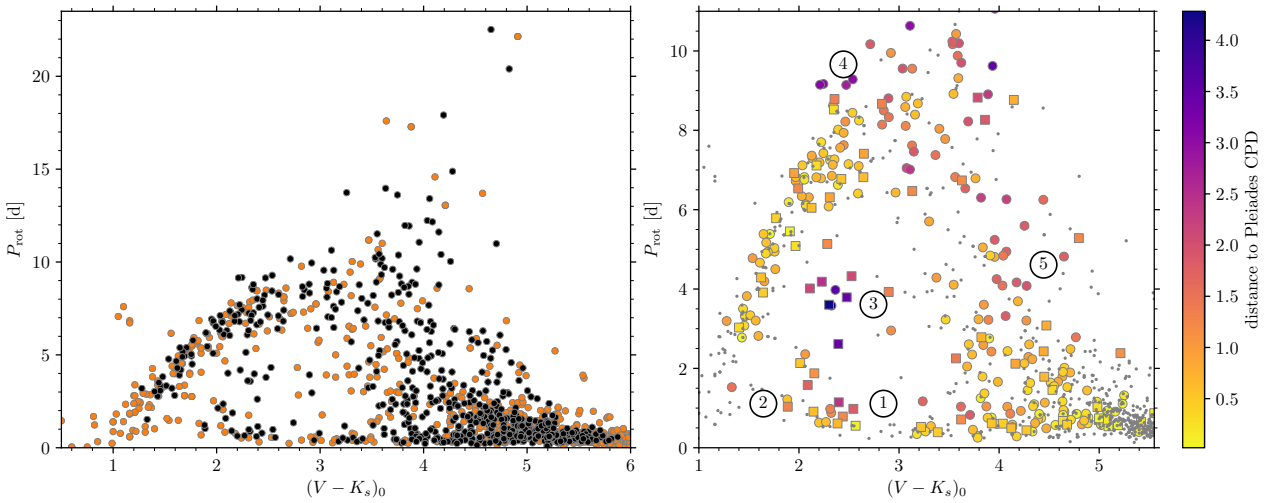

Figure 3.15: *Left:* Colour-period diagram for both NGC 2516 (black, union of data from this work and I07) and the Pleiades (orange). The similarity of the two distributions across all sampled regions of the colour-period diagram is noticeable. *Right:* Distance of a given NGC 2516 star (coloured symbols) in the CPD to the corresponding Pleiades star. Distance is measured in standard deviations (see text), and colours range from yellow (very near) to deep purple (most distant; see scale). The fast- and slow sequences, representing the edges of the rotation distributions, are mostly very close (yellow), while the intermediate and sparsely populated regions of the CPD are quite distant (deep purple.) The Pleiades data are displayed with grey dots in the background. Circular symbols indicate single stars, while square symbols indicate possible binaries. The encircled numerals from 1 to 5 indicate specific regions discussed in detail in the text. (This panel has a restricted period axis range compared to the left panel.)

very important for the validity of gyrochronology, which can only be used effectively if otherwise similar (nearly-)coeval open clusters show (near-)identical slow rotator sequences. However, it has to be noted that we find a number of stars in NGC 2516 that rotate slightly slower than the corresponding Pleiades stars towards the red end of the slow rotator sequence (*4*, $(V - K_s)_0 \approx 2.2 - 3$). These stars also appear to be above the rest of the slow rotator sequence of NGC 2516. Among them are not only the stars *3v516* and *3v924*, pointed out in Sect. 3.5.2, but additional stars with large distance to the Pleiades as seen in Fig. 3.15.

All of these stars are cluster members according to all four membership criteria. This makes it very unlikely that they are non-members. All of the light curves show some scatter around the maxima, possibly indicating two spot groups on the stellar surface. The proximity of the two spots could bias the period determination towards a longer period. However, the noise level of these light curves does not permit a definitive statement of whether two spots are present. Hence, those apparently slower rotating stars might not form a genuine feature of NGC 2516.

We note that *3v516* (marked with a blue diamond in Fig. 3.12 at $(G_{\rm BP} - G_{\rm RP})_0 = 1.15$, $P_{\rm rot} = 9$ d at, and here located at $(V - K_s)_0 = 2.1$) potentially hosts a sub-stellar companion (Bailey et al. 2018 and discussion in Sect. 3.5.1) but we do not believe it to have had an impact on the rotation period. In particular the large number of stars above the sequence are unlikely to all host low-mass companions. Finally, with respect to the slow rotators, a paucity at $(V - K_s)_0 \sim 2.6$ was noted among the Pleiades stars on the slow rotator sequence, and was called the 'kink' by Stauffer et al. (2016). This is separately discussed in Sect. 3.7.1.7 below.

3.7.1.5 *NGC 2516 vs. Pleiades: M stars - fast and intermediate rotation*

So far we have only considered the FGK stars. Those stars have arrived on the main sequence. In contrast most M stars at the age of NGC 2516 are still in the pre-main sequence phase. The fast rotators are in very similar positions in both clusters, as indicated by the small distances (yellow), especially for the reddest objects in our study. At intermediate rotation periods ($P_{\rm rot} \sim 5$ d), we observe somewhat larger distances between the two clusters.

In Fig. 3.15 the M stars with intermediate rotation periods (*5*) seem to be of slightly redder colour than in the Pleiades. We are not certain whether this is an expression of an age difference (in the sense of NGC 2516 being marginally older) or simply occurring by chance because of the low numbers (~10) of stars.

3.7.1.6 NGC 2516 vs. Pleiades: M stars - extended slow rotator sequence

In the uppermost region of the CPD (left panel of Fig. 3.15) at $P_{\rm rot} \gtrsim 10$ d, a group of slowly rotating M stars is present[32]. These are well above the usual locations of the majority of the M-type stars discussed in the previous section. Furthermore, they appear to be an extension of the slow rotator sequence. Stauffer et al. (2016) labelled the very slow rotating M dwarfs in the Pleiades 'abnormal' and questioned their membership. We, however, find such stars in NGC 2516 in similar locations in the CPD. Consequently, we propose that those stars are not abnormal but instead are the continuation of the slow rotator sequence in the low-mass regime. We call this the 'extended slow rotator sequence'.

In the case of NGC 2516 we are quite certain about the membership of these stars. Five of the eight slowest rotators are members satisfying all four membership criteria (Sect. 3.3). One additional star lacks radial velocity measurements and therefore satisfies only three criteria. Among the remaining two stars, one star is technically a photometric non-member, located slightly below the main sequence, but is a kinematic member at the cluster distance. The final one has no proper motion or parallax measurements from *Gaia* DR2 because it is a (photometric) binary. Consequently, none of these can be considered as non-members, and we conclude that all eight stars are indeed cluster members.

The stars on the extended slow rotator sequence are all obviously pre-main sequence (PMS) stars at the age of NGC 2516 and they are still contracting, hence would spin up in the absence of angular momentum loss. However, their long rotation periods suggest either very efficient loss mechanisms (meaning early spindown), or else a greatly delayed spinup.

We note that very slowly rotating M dwarfs have been discovered among field stars (Newton et al. 2016, 2018), and that it is possible that we are observing the young equivalent of those stars. Newton et al. (2016, 2018) proposed that these stars spin down strongly only after their PMS phase to reach the long periods. It is difficult to say how our observations of extremely slow rotators in NGC 2516 relate to this assertion.

An extended slow rotator sequence has likely not yet been observed in older open clusters because either the time baseline of the observations is too short (typical for ground-based monitoring) or this small group of stars was simply overlooked in prior studies as such stars appear to be similar to noise from non-members in the CPD[33].

[32] We include their light curves in Fig. 3.22 so that readers can appreciate the confidence with which these periods are determined.

[33] Indeed, slowly rotating M dwarfs well above the continuation of the slow rotator sequence are observed in Praesepe (Douglas et al. 2017).

With the evidence that those slow rotators are indeed members of young open clusters, more questions arise. In particular it is unclear where those stars come from. Why do those M dwarfs show such low rotation rates in the first place? NGC 2516 is only the second young cluster (after the Pleiades) where M dwarfs of such slow rotation are observed; hence their evolution might not yet be described adequately with the current wind-braking models. This leaves their true rotational evolution as an open question.

3.7.1.7 NGC 2516 vs. Pleiades: The kink (or not) in the Pleiades slow rotator sequence

As a final detail, we inquire whether the kink observed in the Pleiades period distribution is also present in NGC 2516. Stauffer et al. (2016) noted a paucity in the slow rotator sequence at $(V-K_s)_0 \sim 2.6$. At this colour the slowest rotators are faster than expected from the overall shape of the slow rotator sequence. In NGC 2516 this kink is simply absent (Fig. 3.15). Indeed, we find five stars which perfectly fill the gap observed in the Pleiades. The slow rotator sequence in NGC 2516 is flattening around this colour and hence is not following the slope of the bluer slow rotator sequence. No obvious kink in the data is observed.

Gallet et al. (2018) suggest that the kink is caused by tidal interaction with planets of those stars in the Pleiades. If this were the case, then the absence of such a feature in NGC 2516 would mean that the corresponding stars there do not have tidally-interacting planets. Now, recall that in both the Pleiades and NGC 2516 five slow rotators are observed in the range $2.6 < (V-K_s)_0 < 3.0$. If one followed the logic of their suggestion to its obvious conclusion, one would have to find some way of designing planetary architectures in such a way that stars in that narrow mass range in the Pleiades would host tidally-interacting planets, but not the corresponding stars in NGC 2516. We find this arbitrary and therefore unconvincing.

3.7.2 Comparison with other clusters: M 35, M 50, and Blanco 1

Beyond the very well-studied Pleiades cluster, there are three others that have measured rotation period distributions and ages close enough to make them suitable for comparison, which we do in turn below. The open clusters M 35 and M 50 are 150 Myr (Meibom et al. 2009) and 130 Myr old (Irwin et al. 2009), respectively (each with an uncertainty of ~20 Myr). Given the age uncertainties we consider both to be coeval with NGC 2516, and now compare their rotation periods with those in NGC 2516 (see Fig. 3.16). Blanco 1 is believed to be 115±10 Myr old (Juarez et al. 2014), marginally younger than the others, but close enough to the FGK star ZAMS. M 35 and M 50 are both roughly 1 kpc distant, while Blanco 1 is much closer, at 240 pc (Gaia Collaboration et al. 2018) distance.

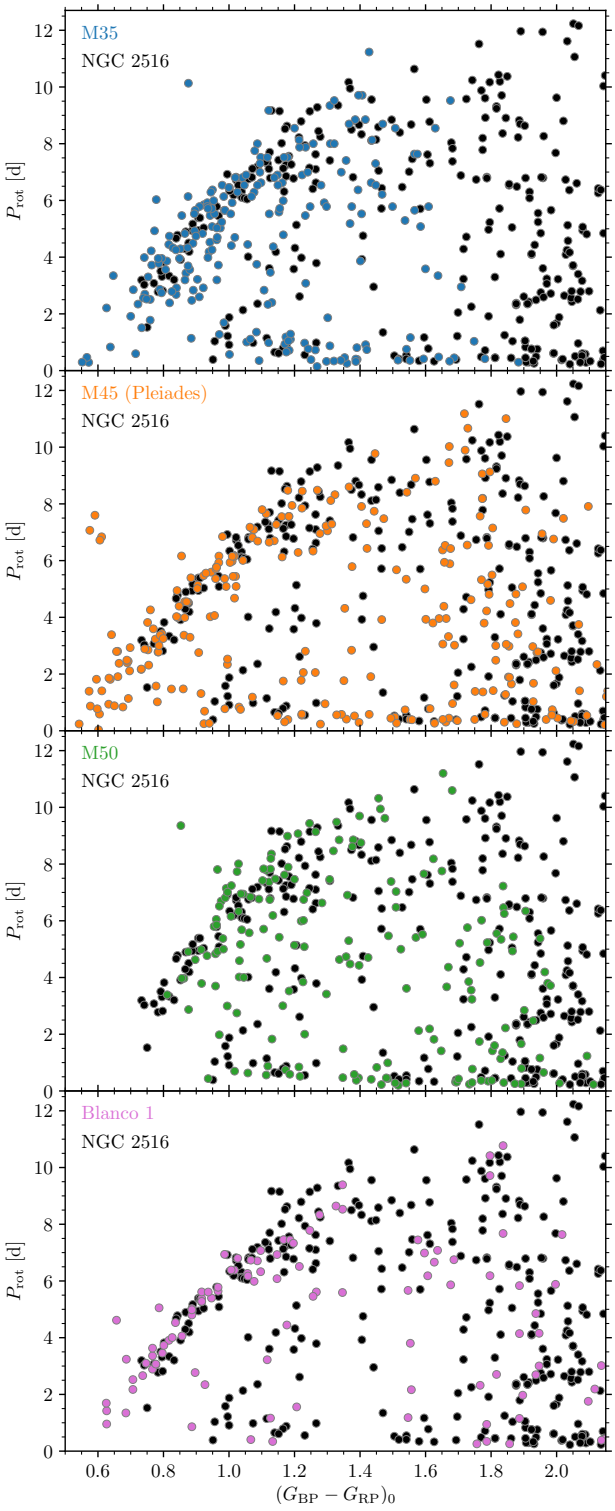

Figure 3.16: Colour-period diagrams for the four similarly-aged open clusters (varying colours) available to date, compared with the measured one for NGC 2516 (black in each panel). The clusters are (from top to bottom) M 35, M 45 (Pleiades), M 50, and Blanco 1, with $E_{(B-V)}$ values taken from the respective publications, and scaled for *Gaia* colour. Note that their rotational distributions are visually essentially indistinguishable from that for NGC 2516 to within the sensitivities of the individual studies. (See Fig. 3.23 in the Appendix for the equivalent figure in $B - V$ colour, and the text for further details.)

3.7.2.1 M 35

For M 35, Meibom et al. (2009) include not only long-baseline rotation period measurements (especially important in discovering long rotation periods), but also detailed membership and binarity information from extensive time-series radial velocity data presented soon thereafter in Geller et al. (2010). We have updated their membership list with the current *Gaia* DR2 astrometric measurements in a manner similar to our work on NGC 2516.

Comparing the M 35 rotational distribution (first panel in Fig. 3.16) with that of NGC 2516 reveals them to be visually indistinguishable in all the regions of the CPD where both have derived periods. In particular, both the fast- and slow rotator sequences lie one over the other, except that the M 35 study is sensitive to somewhat warmer stars, and consequently samples the late-F fast-rotator region of the slow rotator sequence. M 35 also has visibly more scatter on its slow rotator sequence than NGC 2516, one likely caused by the relatively large (and also differential) reddening towards this cluster. In Fig. 3.16, following prior work, we have dereddened the photometry with a single value for all stars. The fast rotator sequence (where colour differences are largely irrelevant) is essentially indistinguishable from that for NGC 2516. The stars between the sequences in M 35, the so-called 'gap' stars, are equally sparse in both clusters, so essentially similar. The only truly visible difference between the distributions is that the low-mass (M star) rotation periods are missing in M 35, perfectly understandable given its much-larger distance. We therefore conclude that M 35 and NGC 2516 have essentially identical rotation period distributions.

3.7.2.2 M 50

The visual impression in the comparison for M 50 (third panel in Fig. 3.16) is again that its rotational distribution (Irwin et al. 2009) is equally indistinguishable from that for NGC 2516. The slow- and fast rotator sequences are both positioned in identical locations, although it must be admitted that the slow rotator sequence in M 50 has somewhat greater scatter. A caveat needs to be mentioned here - no radial velocity membership is available for this cluster, so we have had to use the *Gaia* data exclusively for membership information. The cluster's distance of 1 kpc results in the retrieval of relatively few members from among the M 50 M dwarfs listed in Irwin et al. (2009). This is because they are typically fainter than $G = 18$, which renders the *Gaia* astrometry too imprecise for effective use.

There is also another issue. We find a larger proportion of stars in the rotational gap between the fast- and slow rotators. We suspect that this effect might originate in the sampling pattern of the observations, one optimized for finding exoplanets, and not rotation periods. Consequently, a certain number of the stars in the gap region could actually be half-periods, in analogy with the observations of I07 of NGC 2516 which were obtained in the same observing programme. We are obviously not in a position to resolve this issue without additional observations. However, given the excellent agreement in the locations of the primary rotational sequences, we consider M 50 and NGC 2516 to have equivalent rotational distributions.

3.7.2.3 Blanco 1

While we were finalizing this work, Gillen et al. (2020) published new rotation periods for the 115 Myr-old open cluster Blanco 1. They found the rotation period distribution to be identical to that for the Pleiades. To improve our comparison with NGC 2516, we have supplemented those data with rotation periods from Cargile et al. (2014) for the most complete picture of rotation in Blanco 1, displayed in the final panel of Fig. 3.16. We observe that the distributions of both clusters follow each other closely, along both the fast- and slow rotator sequences. The only little difference we notice is that NGC 2516 hosts several stars with slower rotation at $(G_{BP} - G_{RP})_0 \approx 1.2$. We presume that this can be attributed to Blanco 1 being of somewhat younger age, as already noted by Cargile et al. (2014). The other areas of the CPD are too sparsely populated to show any obvious difference.

3.7.2.4 No evidence for cluster-to-cluster variations

In summary, we are able to find no compelling evidence for cluster-to-cluster variations. All the (minor) differences between the Pleiades and NGC 2516 rotational distributions can be explained plausibly, without questioning the universal validity of stellar physics and angular momentum evolution. Additional comparisons with the M 35, M 50, and Blanco 1 distributions also reveal no palpable differences.

In a prior comparison of the NGC 2516 and Pleiades $v \sin i$ distributions, Terndrup et al. (2002) also found no significant differences. (This is unsurprising because of the relative insensitivity of $v \sin i$ data.) Such issues also led to Jeffries et al. (1998) finding no fast rotators ($v \sin i > 20\,\mathrm{km\,s^{-1}}$) and consequently claiming that there are stars with faster rotation in the Pleiades than in NGC 2516. Our stance is that photometric rotation period comparisons are a far more unambiguous tool for answering those questions.

It should be noted that earlier studies of NGC 2516 assumed a much lower photometric metallicity than is obtained from modern (high-resolution) spectroscopy. The low photometric metallicity from Cameron (1985) [Fe/H]= −0.4 is in strong contrast to the nearly solar values obtained by Bailey et al. (2018) ([Fe/H]= -0.08 ± 0.01) and Terndrup et al. (2002) ([Fe/H]= 0.05 ± 0.06). This is potentially important because metallicity could be a driver of cluster-to-cluster variations in the rotational evolution. A non-solar metallicity would imply different convection zone properties, and therefore somewhat different spindown on the main sequence (Jeffries et al. 1997). However, the measured near-solar metallicity of NGC 2516 makes that argument moot.

Some evidence of cluster-to-cluster variations in the rotation periods for certain clusters have been proposed before by Coker et al. (2016). Their conclusion was that the

cluster environment could influence the rotational evolution. However, Coker et al. (2016) compared h Per (13 Myr) to the older Pleiades (125 Myr) and therefore had to make large (and in our view, unacceptable) assumptions about the rotational evolution to arrive at their conclusion.

3.7.3 A representative ZAMS rotational distribution

We find the rotational distribution of the five zero-age main sequence open clusters to be nearly indistinguishable, at least to the extent allowed by characteristics of the relevant studies. The comparison of NGC 2516 with the Pleiades, M 35, M 50, and Blanco 1 is in fact the strongest evidence to date against the existence of cluster-to-cluster variations.

To highlight this cluster-to-cluster similarity and emphasize the existence of this representative ZAMS rotation period distribution we display the full range of the measured rotation period distributions in both *Gaia* $(G_{BP} - G_{RP})_0$ and $(B - V)_0$ colours[34] in Fig. 3.17. The separate component distributions in $(B - V)_0$ are shown in the Appendix 3.B. The very close correspondence between all the component distributions is obvious[35]. Incidentally, the slow and fast rotation limits of this representative distribution can be reproduced simply in any desired colour by the use of the approximating functions $P = \tau_c/8$ and $P = 45/\tau_c$, as we show in the Fig 3.24. We also display the critical Rossby Number line $P = \tau_c/\sqrt{k_I k_C} = 0.06\,\tau_c$, which serves as an approximate dividing line for fast- and slow rotators, especially in the F, G, K spectral range.

3.8 X-ray activity of the rotators

We now turn to the X-ray activity of NGC 2516, where our rotation periods permit the first X-ray activity vs. Rossby Number diagram for the cluster to be constructed. We discuss this with particular reference to the corresponding diagrams for the Pleiades and Blanco 1.

Fortunately, a substantial amount of X-ray data is available for NGC 2516 because this open cluster was among the plate-scale calibration targets for both the XMM-Newton (Gondoin et al. 2000) and *Chandra* missions (Wolk et al. 2004). It is also being used in the recently-launched eROSITA mission (Predehl et al. 2010; Freyberg & Dennerl 2012).

The first X-ray studies with *ROSAT* data had already found a large number of X-ray active members (Dachs & Hummel 1996; Jeffries et al. 1997; Micela et al. 2000). The calibration data from *Chandra* (Harnden et al. 2001) and XMM-Newton (Sciortino et al. 2001) identified many additional members.

For this study, we use the two deep surveys from Damiani et al. (2003) (*Chandra*) and Pillitteri et al. (2006) (XMM-Newton). Because of the deeper detection threshold, we prefer the XMM-Newton data over the *Chandra* data for stars with multiple measurements[36]. In general these measurements are in good agreement. Damiani et al. (2003) have also published a list of upper limits for photometric cluster members which we add for completeness. Among the members with detected rotation periods, we identify 191 objects with a measured X-ray luminosity or an upper limit.

3.8.1 Rotation-activity diagram for NGC 2516

Together with the newly-measured rotation periods for NGC 2516, the X-ray data mentioned above allow us to construct the first rotation-activity diagram[37] for FGKM stars in NGC 2516 shown in Fig. 3.18. The general shape of our rotation-activity diagram is familiar, and resembles those from other open clusters, with a saturated branch for $Ro \lesssim 0.06$ and an unsaturated branch for higher Rossby numbers, the latter delineating stars that are believed to obey the rotation-activity relationship. The so-called gap stars denoting those in the colour-period diagram that are in transition from fast to slow rotation are located near the knee of the rotation-activity diagram ($Ro \sim 0.06$), emphasising their transitional nature (Barnes 2003a).

The Rossby number is defined as usual as $Ro = P_{rot}/\tau_c$ with τ_c as the convective turn-over timescale. To estimate it, we use the theoretical values tabulated in Barnes & Kim (2010) and calculate τ_c via the effective temperature T_{eff}, which itself was estimated for most stars in NGC 2516 from the *Gaia* data and is included in the second data release (Andrae et al. 2018)[38]. Values of $\log L_X/L_{bol}$ were taken directly from Pillitteri et al. (2006) and Damiani et al. (2003).

There also appear to be a certain number of outliers with lower $\log L_X/L_{bol}$ value than the majority of the stars in the diagram. We find a secondary peak at longer rotation period in the periodogram for two of them. (Star *2i1383*, with $P_{rot} = 1.17$ d ($Ro = 0.010$), has a secondary peak in the power spectrum at $P_{rot} \approx 8.5$ d, and Star *1v1504/4v79*, with $P_{rot} = 1.52$ d ($Ro = 0.037$), has a secondary peak at $P_{rot} \approx 3.2$ d). The secondary periods would lie in perfectly reasonable regions of the CPD. Hence, their Rossby numbers could potentially be greater, putting both back onto the sequence in the X-rays vs. *Ro* plot in Fig. 3.18 in line

[34] The $(B - V)_0$ values are calculated from $(G_{BP} - G_{RP})_0$ using a relationship derived in Gruner & Barnes (in prep.).

[35] Note that the individual studies contributing to this distribution have their own selection effects, in brightness, rotation period sensitivity, etc., so that while the locations of stars in the CPD are likely robust, the relative numbers of stars in different locations of these CPDs should be treated with caution.

[36] The spatial resolution, however, is significantly better with *Chandra*.

[37] We note, in fairness, that Jackson & Jeffries (2010) have also provided a similar diagram, although restricted to M-type stars, because they were only able to use the low-mass rotation periods derived in I07.

[38] The *Gaia* T_{eff} values are adequate for our purposes, considering that possible systematic errors and uncertainties in the calculated convective turnover timescales are likely to be of greater significance.

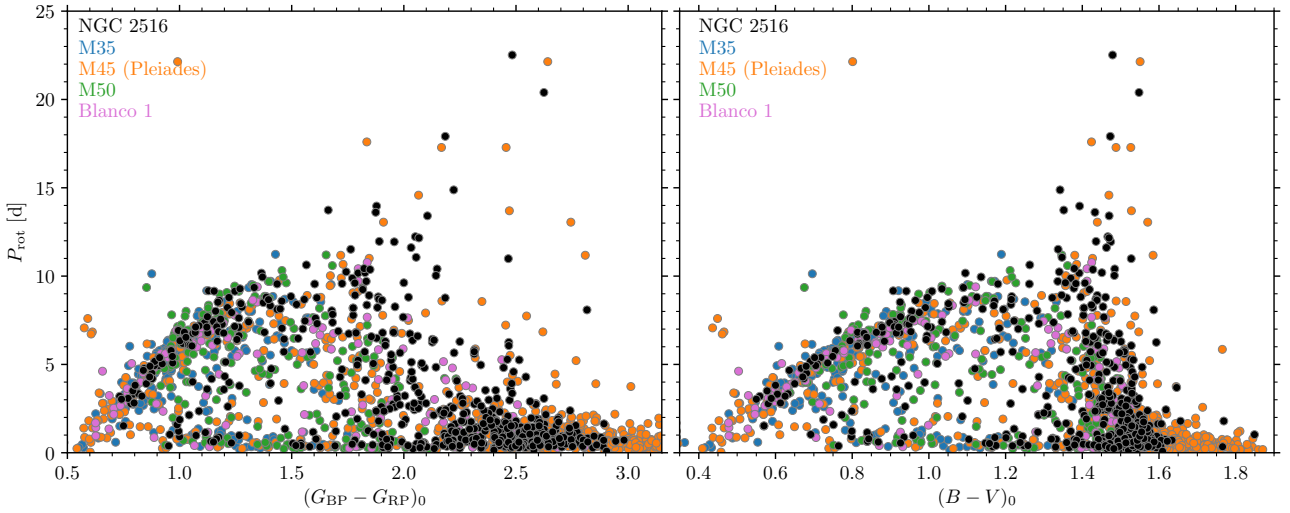

Figure 3.17: Representative ZAMS rotation period distribution shown in combined colour-period diagrams of all considered open clusters in both *Gaia* $(G_{\rm BP} - G_{\rm RP})_0$ (*left*) and $(B - V)_0$ colours (*right*). The fast and slow sequences, including the extended slow rotator sequence are evident, as is the less-densely occupied region between the sequences. The display colours of the individual open clusters are the same as in Fig. 3.16, and Fig. 3.23 provides separate comparison panels for the individual clusters in $B - V$ colour. See Fig. 3.24 for an approximate way to represent this distribution in a colour-independent way using elementary functions of the convective turnover timescale.

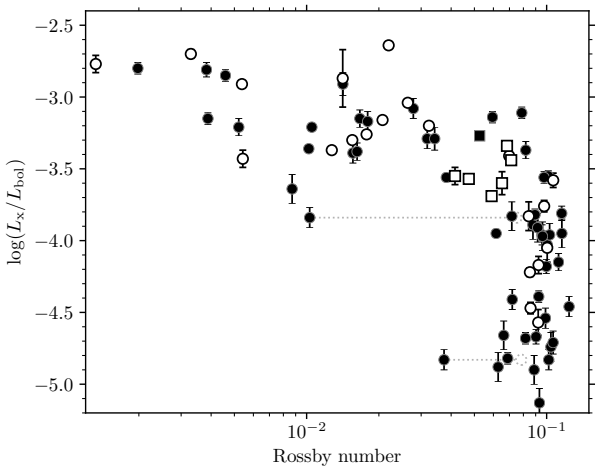

Figure 3.18: X-ray activity against Rossby number $Ro = P/\tau_c$ for NGC 2516. Single stars are shown with filled symbols, while known binaries (of all separations) are displayed with open symbols. Square symbols indicate the gap stars ($Ro \approx 0.06$) that are in transition from fast- to slow rotation. The dotted line indicates the alternative position of the two possible alias periods in our sample.

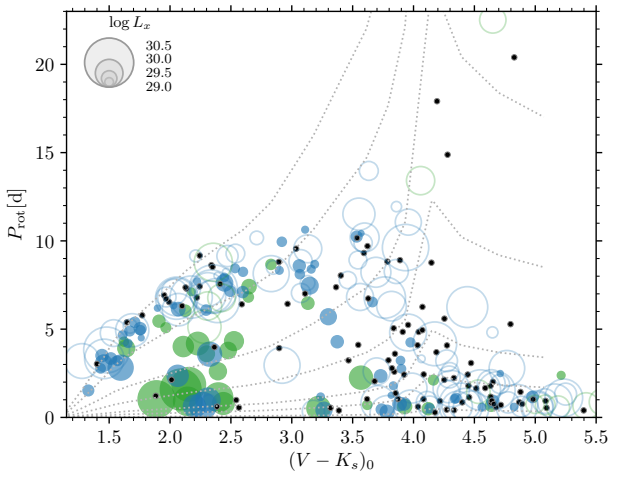

Figure 3.19: Colour-period diagram for NGC 2516 encoded with the X-ray luminosities of the rotators in NGC 2516 (data from both *Chandra* and XMM-Newton). Green symbols indicate radial velocity and photometric binaries, while all other stars are in blue. Filled circles are detected members, while open circles denote upper limits from the *Chandra* observations. Black points show the locations of all stars without measured X-ray luminosities. The dotted lines trace (from top to bottom) $Ro = \{0.15, 0.1, 0.05, 0.025, 0.01, 0.005, 0.001\}$.

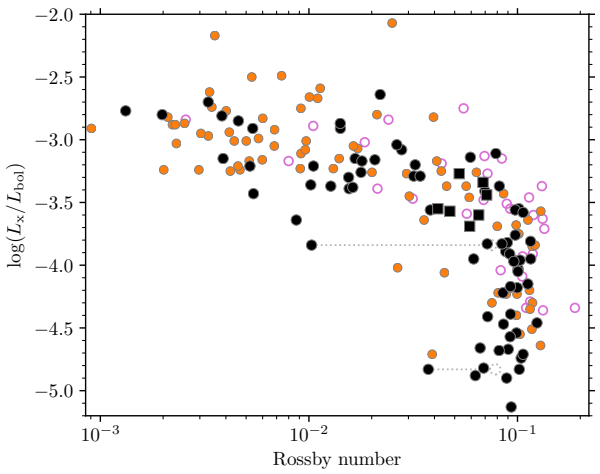

Figure 3.20: X-ray luminosity against Rossby number *Ro* for NGC 2516 (black), the Pleiades (orange), and Blanco 1 (unfilled purple). The gap stars in transition from fast to slow rotation in NGC 2516 are marked using squares and the alternative position of possible alias periods with the dotted lines. The distributions are almost indistinguishable.

with the other data points here. However, we consider it inadvisable to alter our rotation period measurements for such cosmetic purposes, and instead quote the rotation periods as derived, and interpret the ratio 2/89 = 2% as indicating our rotation period alias rate. (There could be four additional such stars in our 308-star sample.)

The usage of the Rossby number as a proxy for stellar rotation entails the loss of the direct connection to the colour-period diagram. In order to reconnect the two we display the X-ray data in a CPD in Fig. 3.19. The sizes of the data points are proportional to the measured X-ray luminosities themselves ($\log L_X$), rather than normalized to the bolometric luminosities. Additionally, we indicate the lines of equal Rossby number for easier comparison with Fig. 3.18. The largest luminosities correspond to the warmest fast rotators. However, most of these stars are in binary systems, which are believed to be somewhat X-ray bright. Corresponding, all but one of our likely binaries has an X-ray activity measurement. On the other hand, as clearly visible in Fig. 3.18, the single- and binary stars clearly populate the same regions of the diagram at the current level of precision.

3.8.2 Comparison with the Pleiades and Blanco 1

Prior studies comparing the X-ray activity of the Pleiades and NGC 2516 have found the latter to be less X-ray luminous for G and K stars (e.g. Micela et al. 2000, Harnden et al. 2001). A possible explanation was sought in the differing rotation rates (Micela et al. 2000; Pillitteri et al. 2006), ascribed to the age difference believed to exist at that time between the clusters (Terndrup et al. 2002), or to non-member contamination (Harnden et al. 2001). The latter has of course been mostly removed in our study. We now investigate this claim in light of the clean and large samples of rotation periods available now for both open clusters.

We display the prior Pleiades X-ray activity from Micela et al. (1999) in Fig. 3.20 together with the new data for NGC 2516. We have restricted the Pleiades data to the same mass range as our NGC 2516 data and recalculated the Rossby numbers in the same manner as for NGC 2516, to enable a fair comparison. We observe the overall X-ray vs. *Ro* distributions of both clusters to be essentially identical. Notably, we see no sign for any under-luminosity of NGC 2516 with respect to the Pleiades in our rotationally selected sample. The few stars in the Pleiades above the saturated level in Fig. 3.20 have large uncertainties in their ROSAT-based count rates, as tabulated in Micela et al. (1999). Consequently, we ascribe any corresponding scatter above the NGC 2516 saturated stars to measurement uncertainties or non-member contamination.

We noted in Sect. 3.7 that the one small difference visible in the colour-period diagrams of the two clusters was a small excess of stars in the rotational gap between the fast- and slow rotator regimes. No corresponding stars are found in the Pleiades CPD. The different X-ray luminosities might originate from this. Indeed, the gap stars in NGC 2516, as marked in Fig. 3.18, are arguably visually slightly less X-ray luminous than the overall population of stars with the same Rossby number in the Pleiades.

It is not feasible to construct the X-ray luminosity function with and without the gap stars with the standard tool of X-ray astronomy, the Kaplan-Meier estimator. When removing a certain group of stars from the sample, we no longer have randomly censored data and the survival analysis with the Kaplan-Meier estimator would be biased (Feigelson & Nelson 1985).

In addition to the gap stars, we note that the unsaturated sequence extends to lower L_X/L_{bol} by about 0.4 dex. This is an observational effect because the XMM-Newton observations for NGC 2516 are much deeper than the *ROSAT* data. The proximity of the Pleiades cannot compensate fully for this effect.

The new rotation periods provided in Gillen et al. (2020) (joined with Cargile et al. (2014)) enable us to also include Blanco 1 in the rotation-activity diagram in Fig. 3.20. Previously, Cargile et al. (2009) compared the X-ray luminosities of stars in Blanco 1 and the Pleiades and found the Pleiades to be more luminous. In the rotationally selected sample we find the Blanco 1 distribution also to be in agreement with that of NGC 2516. The similarities of the rotation-activity diagrams of all three open clusters is additional evidence against cluster-to-cluster variations.

3.9 Conclusions

Our study of the southern open cluster NGC 2516 confirms and extends prior findings that it is very similar to the well-

studied Pleiades cluster in the north in age, richness, and other properties. As such it contributes to the establishment of a Southern Pleiades-like benchmark cluster.

Our work is particularly aimed at elucidating the rotation periods and activity of the cool stars in the cluster. This is leveraged off a 42 d-long time-series photometric campaign at CTIO in the V and I_c filters of ~1 sq. degree centred on NGC 2516.

We used all available information to construct a membership list for NGC 2516 over our survey area. This list identifies 844 single and binary members of NGC 2516 among the ~14 000 distinct sources for which we obtained light curves. This identification uses the photometric membership from various sources, radial velocities from the literature and several large surveys, and also proper motions and parallaxes from *Gaia* DR2. *Gaia* DR2 is subsequently used as a check, and to hunt down outliers.

Using a combination of several period-search methods applied to our time-series photometry, supplemented by *manual verification of all light curves and periodicity*, we find 308 rotation periods among the members of NGC 2516. Evaluation of the membership status of stars observed by I07 yields 247 additional rotation periods, mostly for M dwarfs, and enlarges the sample to 555 stars. This rich dataset allows us to construct rich, high-fidelity colour-period diagrams (CPDs) for NGC 2516, enabling detailed comparisons with equivalent work in the Pleiades and other similarly young open clusters.

NGC 2516 and the Pleiades appear to have near-identical rotation period distributions across the entire rotation period and colour range, confirming the similar ages ascribed to both clusters in the literature. We also identify about a dozen unusually slowly-rotating ($P_{\rm rot}$~10 – 23 d) late-K and M dwarfs among our NGC 2516 members, thereby also confirming their counterparts in the Pleiades. These stars appear to prolong the slow rotator sequence in the CPD to lower masses and far longer periods than previously thought possible for ZAMS open clusters. We call this branch the 'extended slow rotator sequence'.

We compare the NGC 2516 rotation period distribution with those of the three other similarly-aged open clusters M 35, M 50, and Blanco 1. For various reasons, these comparisons are not as authoritative as the one with the Pleiades. Nevertheless, we can discern no substantive differences between them, leading us to conclude that they are all intrinsically similar and likely a natural outcome of pre-main sequence evolution, and perhaps even the star formation process preceding it. We provide a simple colour-independent way to mark the boundaries of this representative ZAMS rotational distribution approximately.

We also compare the NGC 2516 rotation data with a number of models constructed over the past decade. The models are summarized in relation to one another and their strengths and weaknesses described. In each case, we find significant detailed issues in describing the measured NGC 2516 rotation period distribution. Consequently, we tend to favour empirical inter-comparisons of the relevant cluster rotational distributions.

Our new rotation periods also enable us to construct the first rotation–X-ray activity diagram for the FGKM stars in NGC 2516 and to compare it with those for the Pleiades and Blanco 1. As expected from prior work in the Pleiades and elsewhere, we see saturated behaviour in X-rays for $Ro < 0.06$, and a sharp drop beyond for the unsaturated stars. The X-ray-saturated stars in NGC 2516 are on the same level as stars in the Pleiades and Blanco 1, suggesting that the similarity in their rotational distributions extends to that in their activity distributions.

In summary, we find that the very rich rotation period distributions for NGC 2516 and the Pleiades are mostly indistinguishable, as are their stellar X-ray activity distributions. Thus, we conclude that the Pleiades and NGC 2516 are not only comparable in age, richness, and metallicity, but also in their rotation-activity properties, so that they may be considered as northern and southern benchmark counterparts. The similarity in rotation and X-ray distributions also extends to the other available young open clusters M 35, M 50, and Blanco 1. More generally, this work provides the strongest evidence to date against the existence of cluster-to-cluster variations in rotation and suggests that the star formation process in different cluster environments is sufficiently similar to result in statistically identical outcomes for the rotational distributions of their cool stars.

Acknowledgements. We are grateful to the anonymous referee for a helpful and detailed report, and to Dr. Richard Jackson for prompt pre-publication access to related data in Jackson et al. (2020). SAB and DJJ thank the staff of Cerro Tololo Inter-American Observatory (CTIO) for their valuable support during the observations. A. Schwope is thanked for useful comments on the manuscript. SAB acknowledges support from the Deutsche Forschungs Gemeinschaft (DFG) through project number STR645/7-1. D.J.J. acknowledges support from the National Science Foundation (AST-1440254) and from a John Templeton Foundation award to Harvard University's Black Hole Initiative. This work is based in part on observations at Cerro Tololo Inter-American Observatory, National Optical Astronomy Observatory (2008A-0476; S. Barnes) and the SMARTS consortium through Vanderbilt University (D. James), operated by the Association of Universities for Research in Astronomy (AURA) under a cooperative agreement with the National Science Foundation. This research has made use of NASA's Astrophysics Data System Bibliographic Services. This research has made use of the SIMBAD database and the VizieR catalogue access tool, operated at CDS, Strasbourg, France. This paper includes data that has been provided by AAO Data Central (datacentral.aao.gov.au). This publication makes use of the RAVE survey. Funding for RAVE has been provided by: the Australian Astronomical Observatory; the Leibniz-Institut für Astrophysik Potsdam (AIP); the Australian National University; the Australian Research Council; the French National Research Agency; the German Research Foundation (SPP 1177 and SFB 881); the European Research Council (ERC-StG 240271 Galactica); the Istituto Nazionale di Astrofisica at Padova; The Johns Hopkins University; the National Science Foundation of the USA (AST-0908326); the W. M. Keck foundation; the Macquarie University; the Netherlands Research School for Astronomy; the Natural Sciences and Engineering Research Council of Canada; the Slovenian Research Agency; the Swiss National Science Foundation; the Science & Technology Facilities Council of the UK; Opticon; Strasbourg Observatory; and the Universities of Groningen, Heidelberg and Sydney. The RAVE web site is at https://www.rave-

survey.org. Based on observations made with ESO Telescopes at the Paranal Observatories under programme ID 188.B-3002 (*Gaia*-ESO survey) and programme ID 179.A-2010 (VHS). This work has made use of data from the European Space Agency (ESA) mission *Gaia* (`https://www.cosmos.esa.int/gaia`), processed by the *Gaia* Data Processing and Analysis Consortium (DPAC, `https://www.cosmos.esa.int/web/gaia/dpac/consortium`). Funding for the DPAC has been provided by national institutions, in particular the institutions participating in the *Gaia* Multilateral Agreement. The GALAH survey is based on observations made at the Australian Astronomical Observatory, under programmes A/2013B/13, A/2014A/25, A/2015A/19, A/2017A/18. We acknowledge the traditional owners of the land on which the AAT stands, the Gamilaraay people, and pay our respects to elders past and present. This publication makes use of data products from the Two Micron All Sky Survey, which is a joint project of the University of Massachusetts and the Infrared Processing and Analysis Center/California Institute of Technology, funded by the National Aeronautics and Space Administration and the National Science Foundation. The Digitized Sky Survey was produced at the Space Telescope Science Institute under U.S. Government grant NAG W-2166. The images of the Digitized Sky Survey are based on photographic data obtained using the Oschin Schmidt Telescope on Palomar Mountain and the UK Schmidt Telescope.

Software: DaoPhot II was kindly provided by Peter. B. Stetson. This research made use of Astropy, a community-developed core Python package for Astronomy (Astropy Collaboration et al. 2013). This work made use of Topcat (Taylor 2005) and Astrometry.net (Lang et al. 2010). This research made use of the following Python packages: Pandas (McKinney 2010); NumPy (Walt et al. 2011); MatPlotLib (Hunter 2007); IPython (Pérez & Granger 2007); SciPy (Jones et al. 2001); Scikit-learn (Pedregosa et al. 2011)

References

Amard, L. et al. 2019, A&A 631, A77
Andrae, R. et al. 2018, A&A 616, A8
Artymowicz, P., & Lubow, S. H. 1994, ApJ 421, 651
Astropy Collaboration et al. 2013, A&A 558, A33
Bailey, J. I., Mateo, M., White, R. J., Shectman, S. A., & Crane, J. D. 2018, MNRAS 475, 1609
Barnes, S. A., Spada, F., & Weingrill, J. 2016a, Astronomische Nachrichten 337, 810
Barnes, S., & Sofia, S. 1996, ApJ 462, 746
Barnes, S. A. 2003a, ApJ 586, L145
— 2003b, ApJ 586, 464
— 2007, ApJ 669, 1167
— 2010, ApJ 722, 222
Barnes, S. A., & Kim, Y.-C. 2010, ApJ 721, 675
Barnes, S. A., Weingrill, J., Fritzewski, D., Strassmeier, K. G., & Platais, I. 2016b, ApJ 823, 16
Barnes, S. A. 1997, PhD thesis (Yale University)
Basri, G. et al. 2011, AJ 141, 20
Bouvier, J. et al. 2014, in: Protostars and Planets VI, ed. by H. Beuther, R. S. Klessen, C. P. Dullemond, & T. Henning, 433
Bouy, H. et al. 2015, A&A 577, A148
Brown, T. M. 2014, ApJ 789, 101
Buder, S. et al. 2018, MNRAS 478, 4513
Cameron, L. M. 1985, A&A 147, 39
Cantat-Gaudin, T. et al. 2018, A&A 618, A93
Cargile, P. A., James, D. J., & Platais, I. 2009, AJ 137, 3230
Cargile, P. A. et al. 2014, ApJ 782, 29
Casagrande, L., & VandenBerg, D. A. 2018, MNRAS 479, L102
Cincotta, P. M. 1999, MNRAS 307, 941
Coker, C. T., Pinsonneault, M., & Terndrup, D. M. 2016, ApJ 833, 122
Crane, P. C. 2001, Sol. Phys. 203, 381
Cropper, M. et al. 2018, A&A 616, A5
Curtis, J. L., Agüeros, M. A., Mamajek, E. E., Wright, J. T., & Cummings, J. D. 2019, AJ 158, 77
Dachs, J., & Hummel, W. 1996, A&A 312, 818
Damiani, F. et al. 2003, ApJ 588, 1009
De Silva, G. M. et al. 2015, MNRAS 449, 2604
Delorme, P. et al. 2011, MNRAS 413, 2218
Douglas, S. T., Agüeros, M. A., Covey, K. R., & Kraus, A. 2017, ApJ 842, 83
Douglas, S. T. et al. 2019, ApJ 879, 100
Dworetsky, M. M. 1983, MNRAS 203, 917
Endal, A. S., & Sofia, S. 1979, ApJ 232, 531
Evans, D. W. et al. 2018, A&A 616, A4
Feigelson, E. D., & Nelson, P. I. 1985, ApJ 293, 192
Fleming, D. P., Barnes, R., Davenport, J. R. A., & Luger, R. 2019, ApJ 881, 88
Freyberg, M. J., & Dennerl, K. 2012, in: Observatory Operations: Strategies, Processes, and Systems IV, vol. 8448, Society of Photo-Optical Instrumentation Engineers (SPIE) Conference Series, 84480Y
Fritzewski, D. J. et al. 2016, MNRAS 462, 2396
Fritzewski, D. J. et al. 2019, A&A 622, A110
Gaia Collaboration et al. 2018, A&A 616, A10
Gallet, F., Bolmont, E., Bouvier, J., Mathis, S., & Charbonnel, C. 2018, A&A 619, A80
Garraffo, C. et al. 2018, ApJ 862, 90
Garraffo, C., Drake, J. J., & Cohen, O. 2016, A&A 595, A110
Geller, A. M. et al. 2010, AJ 139, 1383
Gillen, E. et al. 2020, MNRAS 492, 1008
Gilmore, G. et al. 2012, The Messenger 147, 25
Gondoin, P. et al. 2000, in: X-Ray and Gamma-Ray Instrumentation for Astronomy XI, ed. by K. A. Flanagan, & O. H. Siegmund, vol. 4140, Society of Photo-Optical Instrumentation Engineers (SPIE) Conference Series, 1
Gossage, S. et al. 2018, ApJ 863, 67
Graham, M. J., Drake, A. J., Djorgovski, S. G., Mahabal, A. A., & Donalek, C. 2013a, MNRAS 434, 2629
Graham, M. J. et al. 2013b, MNRAS 434, 3423
Gregory, P. C. 1999, ApJ 520, 361
Gregory, P. C., & Loredo, T. J. 1992, ApJ 398, 146
Harnden F. R., J. et al. 2001, ApJ 547, L141
Hartman, J. D., Bakos, G. Á., Kovács, G., & Noyes, R. W. 2010, MNRAS 408, 475
Hunter, J. D. 2007, Computing in Science & Engineering 9, 90
Irwin, J. et al. 2007, MNRAS 377, 741
Irwin, J. et al. 2009, MNRAS 392, 1456
Jackson, R. J., & Jeffries, R. D. 2010, MNRAS 407, 465

Jackson, R. J. et al. 2016, A&A 586, A52
Jackson, R. J. et al. 2020, arXiv e-prints, arXiv:2006.09423
Jeffries, R. D., James, D. J., & Thurston, M. R. 1998, MNRAS 300, 550
Jeffries, R. D., Thurston, M. R., & Hambly, N. C. 2001, A&A 375, 863
Jeffries, R. D., Thurston, M. R., & Pye, J. P. 1997, MNRAS 287, 350
Jones, E., Oliphant, T., Peterson, P., et al. 2001
Juarez, A. J., Cargile, P. A., James, D. J., & Stassun, K. G. 2014, ApJ 795, 143
Kawaler, S. D. 1988, ApJ 333, 236
— 1989, ApJ 343, L65
Koester, D., & Reimers, D. 1996, A&A 313, 810
Kron, G. E. 1947, PASP 59, 261
Kunder, A. et al. 2017, AJ 153, 75
Lang, D., Hogg, D. W., Mierle, K., Blanton, M., & Roweis, S. 2010, AJ 137, 1782
Lanzafame, A. C., & Spada, F. 2015, A&A 584, A30
Lindegren, L. et al. 2018, A&A 616, A2
Lomb, N. R. 1976, Ap&SS 39, 447
Lyra, W., Moitinho, A., van der Bliek, N. S., & Alves, J. 2006, A&A 453, 101
MacGregor, K. B., & Brenner, M. 1991, ApJ 376, 204
Mathieu, R. D. 1994, ARA&A 32, 465
Matt, S. P., Brun, A. S., Baraffe, I., Bouvier, J., & Chabrier, G. 2015, ApJ 799, L23
McKinney, W. 2010, in: Proceedings of the 9th Python in Science Conference, ed. by S. van der Walt, & J. Millman, 51
McMahon, R. G. et al. 2013, The Messenger 154, 35
Meibom, S., & Mathieu, R. D. 2005, ApJ 620, 970
Meibom, S., Mathieu, R. D., & Stassun, K. G. 2009, ApJ 695, 679
Meibom, S. et al. 2015, Nature 517, 589
Meingast, S., Alves, J., & Fürnkranz, V. 2019, A&A 622, L13
Messina, S. 2019, A&A 627, A97
Mestel, L. 1968, MNRAS 138, 359
Meynet, G., Mermilliod, J. .-., & Maeder, A. 1993, Astronomy and Astrophysics Supplement Series 98, 477
Micela, G., Sciortino, S., Jeffries, R. D., Thurston, M. R., & Favata, F. 2000, A&A 357, 909
Micela, G. et al. 1999, A&A 341, 751
Newton, E. R., Mondrik, N., Irwin, J., Winters, J. G., & Charbonneau, D. 2018, AJ 156, 217
Newton, E. R. et al. 2016, ApJ 821, 93
Parker, E. N. 1958, ApJ 128, 664
Pecaut, M. J., & Mamajek, E. E. 2013, ApJS 208, 9
Pedregosa, F. et al. 2011, Journal of Machine Learning Research 12, 2825
Pérez, F., & Granger, B. E. 2007, Computing in Science & Engineering 9, 21
Pillitteri, I., Micela, G., Damiani, F., & Sciortino, S. 2006, A&A 450, 993
Pinsonneault, M. H., Kawaler, S. D., Sofia, S., & Demarque, P. 1989, ApJ 338, 424
Predehl, P. et al. 2010, in: Space Telescopes and Instrumentation 2010: Ultraviolet to Gamma Ray, vol. 7732, Society of Photo-Optical Instrumentation Engineers (SPIE) Conference Series, 77320U
Ratzenböck, S., Meingast, S., Alves, J., Möller, T., & Bomze, I. 2020, arXiv e-prints, arXiv:2002.05728
Rebull, L. M. et al. 2016, AJ 152, 113
Roberts, D. H., Lehar, J., & Dreher, J. W. 1987, AJ 93, 968
Scargle, J. D. 1982, ApJ 263, 835
Schwarzenberg-Czerny, A. 1999, ApJ 516, 315
Sciortino, S. et al. 2001, A&A 365, L259
Skumanich, A. 1972, ApJ 171, 565
Smart, R. L. et al. 2019, MNRAS 485, 4423
Soderblom, D. R., Laskar, T., Valenti, J. A., Stauffer, J. R., & Rebull, L. M. 2009, AJ 138, 1292
Spada, F., & Lanzafame, A. C. 2020, A&A 636, A76
Stauffer, J. et al. 2016, AJ 152, 115
Stauffer, J. R., Schild, R. A., Baliunas, S. L., & Africano, J. L. 1987, PASP 99, 471
Stauffer, J. R., Schultz, G., & Kirkpatrick, J. D. 1998, ApJ 499, L199
Steinmetz, M. et al. 2006, AJ 132, 1645
Stellingwerf, R. F. 1978, ApJ 224, 953
Stetson, P. B. 1987, PASP 99, 191
— 1994, PASP 106, 250
Stetson, P. B., Bruntt, H., & Grundahl, F. 2003, PASP 115, 413
Strassmeier, K. G. 2009, A&A Rev. 17, 251
Sung, H., Bessell, M. S., Lee, B.-W., & Lee, S.-G. 2002, AJ 123, 290
Taylor, M. B. 2005, in: Astronomical Data Analysis Software and Systems XIV, ed. by P. Shopbell, M. Britton, & R. Ebert, vol. 347, Astronomical Society of the Pacific Conference Series, 29
Terndrup, D. M. et al. 2002, ApJ 576, 950
van Leeuwen, F., & Alphenaar, P. 1982, The Messenger 28, 15
van Leeuwen, F., Alphenaar, P., & Meys, J. J. M. 1987, A&AS 67, 483
Walt, S. van der, Colbert, S. C., & Varoquaux, G. 2011, Computing in Science & Engineering 13, 22
Weber, E. J., & Davis Jr., L. 1967, ApJ 148, 217
Wolk, S. J. et al. 2004, ApJ 606, 466
Zechmeister, M., & Kürster, M. 2009, A&A 496, 577

3.A Light curves

3.B Additional colour-period diagrams

3.C Potential non-members

After our analysis was completed, we learned about a new membership study of stars in open clusters (including NGC 2516) by Jackson et al. (2020). Their membership mostly confirms our own independent analysis, but 10 of these 555 rotators are classified as non-members in their

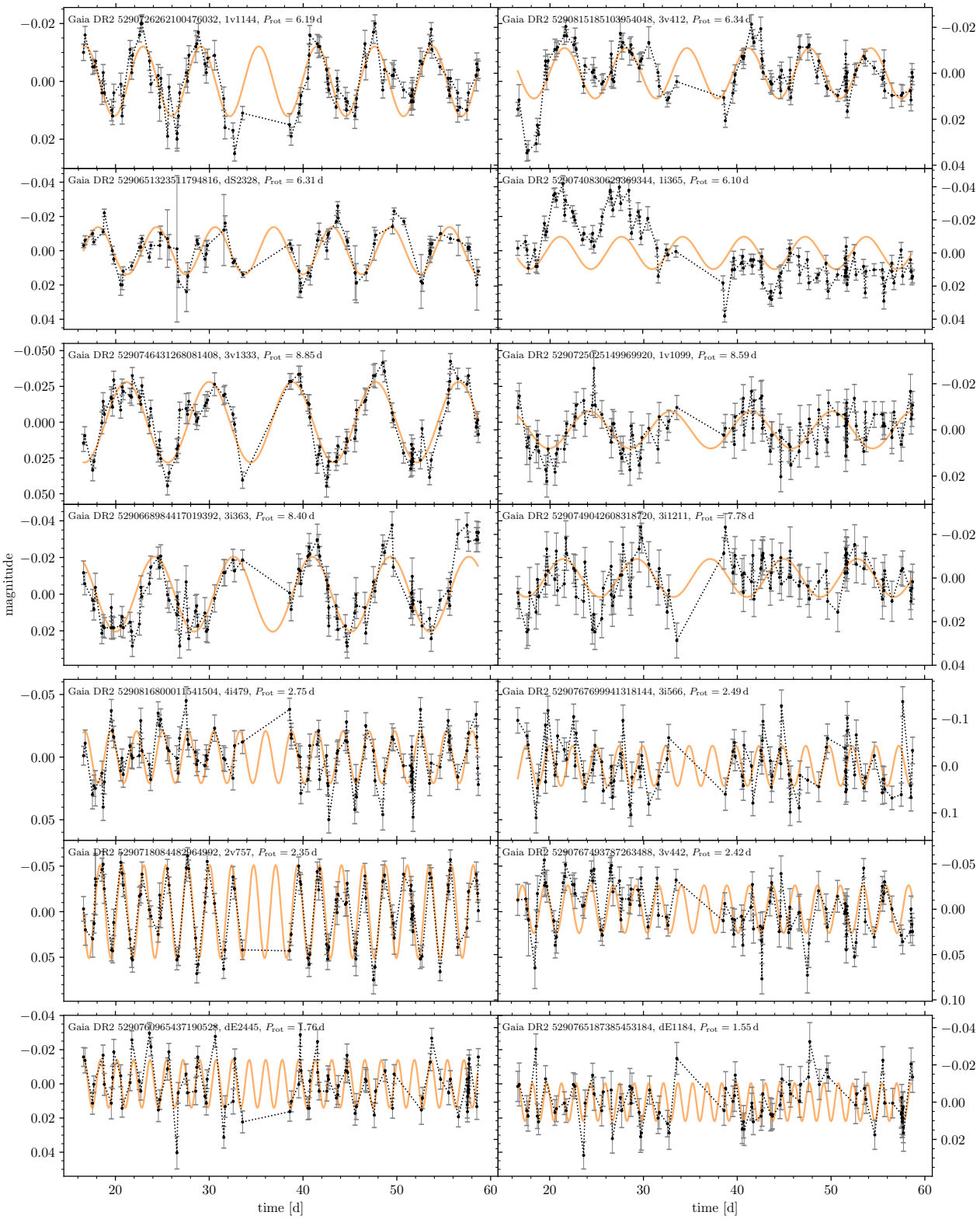

Figure 3.21: Light curves for selected stars (marked in Fig. 12) displaying their differing characteristics. In the *left* column, we show light curves of stars with first class (obvious) rotation periods, and in the *right* column those of second class (algorithmic). Each figure block contains light curves of stars of similar colour and period, arranged from early (top) to later-type stars (bottom), as marked in Fig. 3.12.

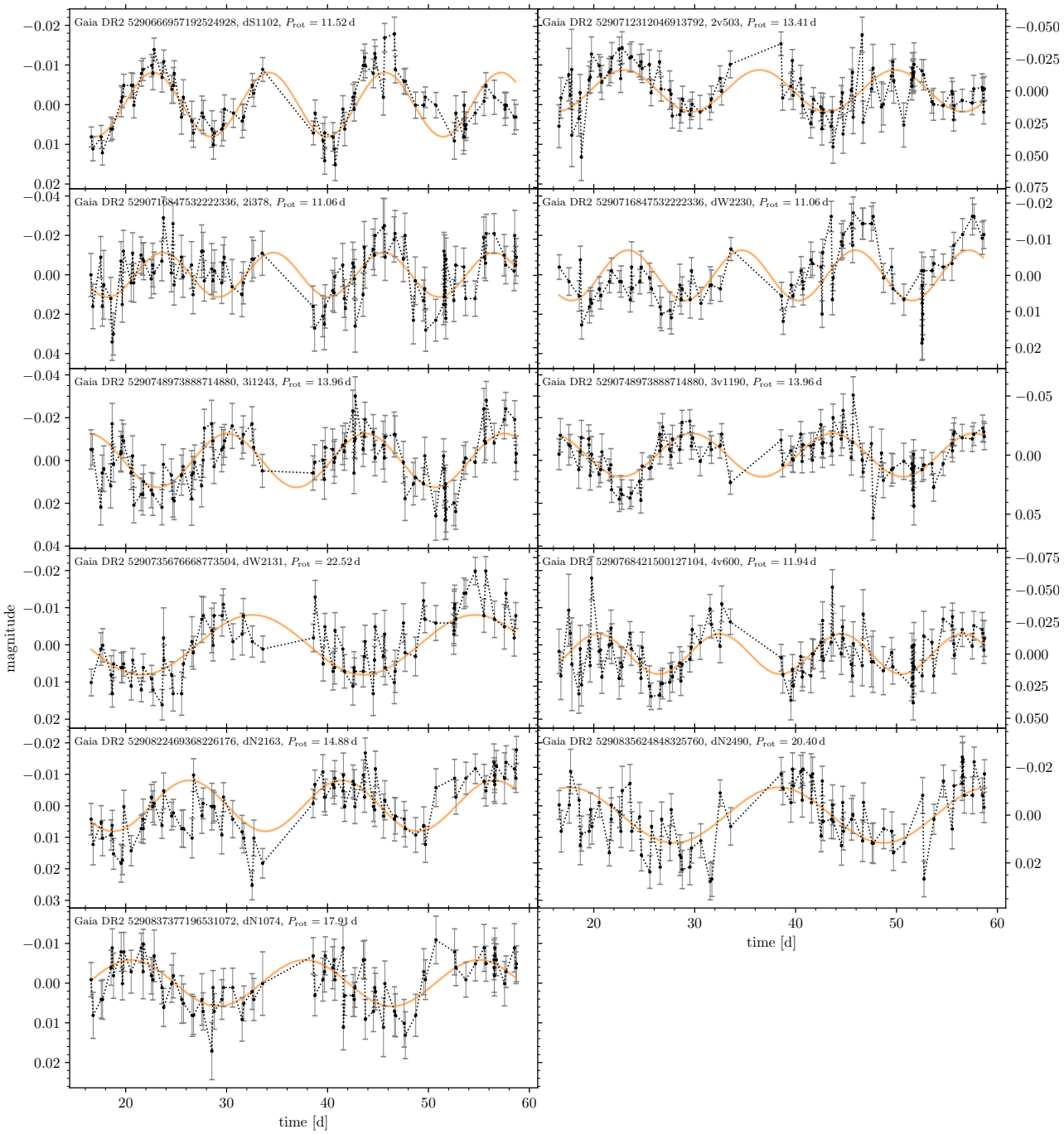

Figure 3.22: Light curves for the slowly rotating early M dwarfs. We show the data in black, along with the photometric uncertainties. The dashed line simply connects the data points and the orange line is a sinusoidal fit to the data with our determined period. In the second and third row both columns show light curves of the same star in two different bands.

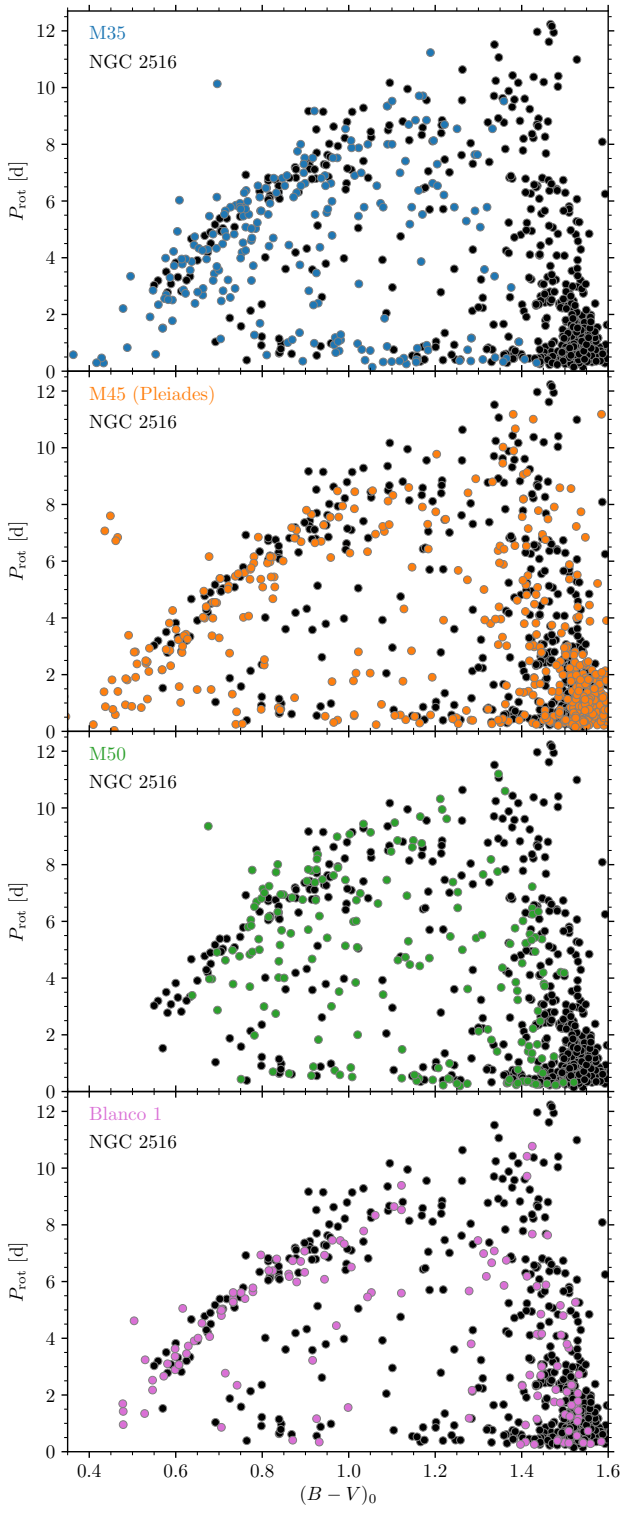

Figure 3.23: Colour-period diagrams in $(B - V)_0$ colour, equivalent to those with *Gaia* colour in Fig. 3.16, comparing NGC 2516 (black in all panels) with the four open clusters M 35, Pleiades, M 50, and Blanco 1. The $(B-V)_0$ colours were obtained by transformation from *Gaia* $(G_{\rm BP} - G_{\rm RP})_0$ photometry (Gruner & Barnes, in prep.) except for NGC 2516, where the observed $B - V$ values were used when available.

Table 3.5: List of stars in our sample of rotators that have recently been classified as non-members in Jackson et al. (2020).

ID	*Gaia* DR2 designation	J01ID	I07ID
…	5290003638143523968	…	2-5-2476
…	5290646719306810880	…	1-2-1929
1i1014, 1v939	5290738047490662016	5887	…
1i1524, 1v1402	5290820648301994112	7596	…
2v421	5290713136680635136	4089	…
deepS2147	5290649811683301888	9790	1-7-105
1i1128, 1v1045	5290725849783612288	6268	…
4v950	5290769933328623616	11485	…
deepW1367	5290734027401142400	2277	…
3v260	5290672660908938752	8645	…

work. However, all of these appear to be radial velocity members of the cluster, and none of these is an outlier in our rotational distribution. Apart from three of them lying in the 'gap' region between the fast- and slow sequences (thereby lowering the fraction of gap-type stars), they are otherwise normally located, and none of them is on the 'extended slow rotator sequence'. Their presence or absence does not alter any of our conclusions, but we favour retaining them in our rotational distribution. However, for the convenience of readers, we include the IDs of the potential non-members in Jackson et al. (2020) in Table 3.5.

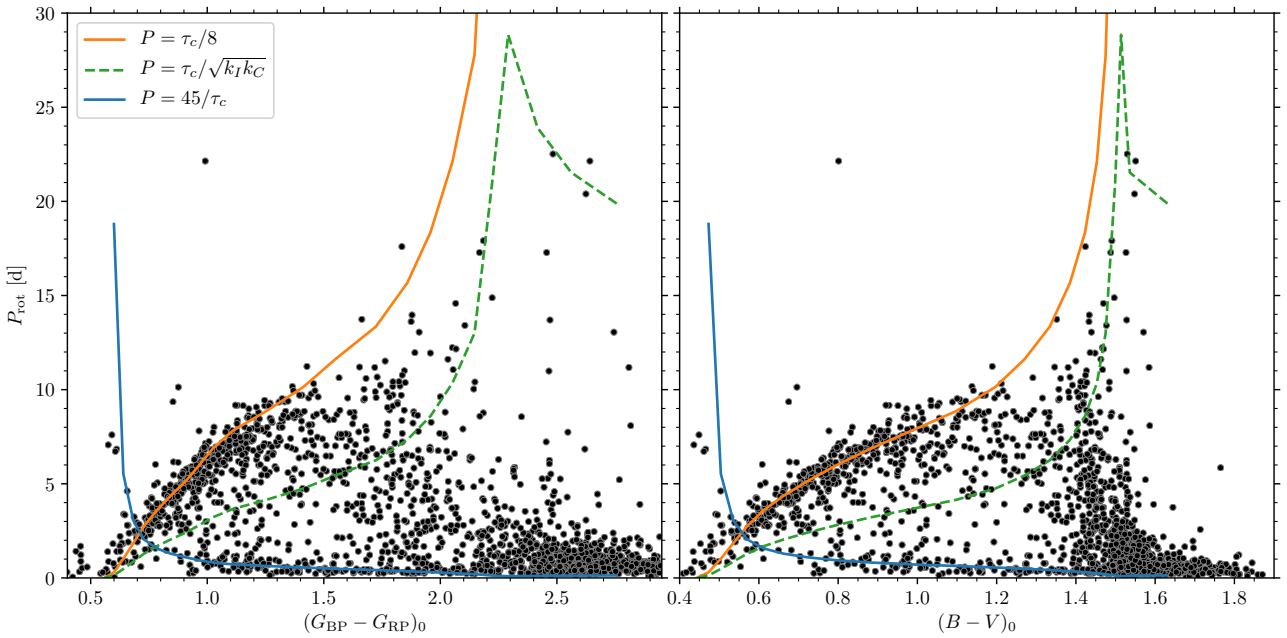

Figure 3.24: Simple colour-independent way to reproduce the ZAMS rotational distribution. Colour-period diagrams in *Gaia* $G_{BP} - G_{RP}$ and $B - V$ colours for the combined representative ZAMS distribution (data as in Fig. 3.17), showing how the elementary functions $P = 45/\tau_c$ and $P = \tau_c/8$, of the convective turnover timescale τ_c may be used to specify its fast and slow rotation limits. The dashed line $P = \tau_c/\sqrt{k_I k_C}$ separates the fast and slow rotator regions in the Barnes & Kim (2010) model and approximately describes the less-densely occupied region between the fast- and slow rotator regions. This model is not relevant for the M dwarfs that are still on the pre-main sequence. See text in Sect. 3.7.3.

4

Rotation periods for cool stars in the open cluster NGC 3532

The transition from fast to slow rotation

D. J. Fritzewski, S. A. Barnes, D. J. James, K. G. Strassmeier

Abstract

Context: A very rich cluster intermediate in age between the Pleiades (150 Myr) and the Hyades (600 Myr) is needed to probe the rotational evolution, especially the transition between fast and slow rotation that occurs between the two ages.
Aims: We study the rich 300 Myr-old open cluster NGC 3532 to probe this important transition, and to provide constraints on angular momentum loss. Measuring the rotation periods builds on our prior work of providing spectroscopic membership information for the cluster, and supports the chromospheric activity measurements of cluster stars that we provide in a companion paper.
Methods: Using 42 d-long photometric time series observations obtained with the Yale 1 m telescope at CTIO, we measured rotation periods for members of NGC 3532 and compared them with the predictions of angular momentum evolution models.
Results: We directly measured 176 photometric rotation periods for the cluster members. An additional 103 photometric rotation periods were identified using activity information, described fully in the companion paper, resulting in a total sample containing 279 rotation periods for FGKM stars in NGC 3532. The colour-period diagram constructed from this rich data set shows a well-populated and structured slow rotator sequence, and a fast rotator sequence evolved beyond ZAMS age whose stars are in transition from fast to slow rotation. The slow rotator sequence itself is split into slightly-slower and faster rotators, a feature we trace to photometric binary status. We also identify an extended slow rotator sequence extending to $P \sim 32$ d, apparently the analogue of the one we identified in NGC 2516 earlier. We compare our period distribution to rotational isochrones in colour-period space and find that all considered models have certain shortcomings. Using more detailed spin-down models, we evolve the rotation periods of the younger NGC 2516 forward in time, and find that the spindown of the models is too aggressive with respect to the slow rotators. In contrast, stars on the evolved fast rotator sequence are not spun down strongly enough by these models. Our observations suggest a shorter crossing time for the rotational gap, one we estimate to be ~ 80 Myr for early-K dwarfs.

This chapter was published in *Astronomy & Astrophysics* 652, A60, 2021, reproduced with permission

4.1 Introduction

The vast majority of solar-type stars in young open clusters rotate either fast ($P_{\rm rot} \lesssim 2$ d) or slowly ($P_{\rm rot} \gtrsim 3$ d), forming two distinct, mass-dependent groups. These groups often appear as sequences when cluster rotation periods are plotted against stellar colour or an equivalent variable. Over their early main-sequence lifetime (meaning between Pleiades and Hyades age) all FGK stars apparently converge onto the latter group, a narrow sequence of slow rotators, erasing the evidence of the prior rotational evolution (Barnes 2003). While the existence and evolution of the slow rotators themselves has been explored extensively both observationally (e.g. Radick et al. 1987, Meibom et al. 2015, Barnes et al. 2016, Gruner & Barnes 2020) and theoretically (e.g. Barnes 2010, Matt et al. 2015, Spada & Lanzafame 2020), measuring the transformation of stars from fast- to slow rotators and understanding the characteristics of that transition demands special effort.

Such work requires the study of the richest-available open clusters, excellent membership information, supporting spectroscopic studies, and of course similar sensitivity to rotation periods, allowing both rotational branches and more generally the entire relevant rotational distributions to be populated. We previously published a detailed study of the rich 150 Myr-old zero-age main sequence (ZAMS) open cluster NGC 2516 (Fritzewski et al. 2020), based on a 42 d observing baseline. Here, we present an equivalent study of the rich 300 Myr-old open cluster NGC 3532 which provides the best opportunity for sampling the ZAMS-to-Hyades age transition. NGC 3532 was observed in the same observing run, in parallel with NGC 2516, essentially assuring comparable rotation period sensitivity.

The first fast rotators ($P_{\rm rot} \sim 0.5$ d) were discovered in the Pleiades (van Leeuwen & Alphenaar 1982; van Leeuwen et al. 1987). Shortly thereafter, Stauffer & Hartmann (1987) showed that they cannot spin down with the same rate as the slow rotators, whose angular momentum loss rate ($\mathrm{d}J/\mathrm{d}t$) scales with the cube of the angular velocity (Ω): $\mathrm{d}J/\mathrm{d}t \propto -\Omega^3$ (Kawaler 1988). Such a strong dependence on the angular velocity would brake the fast rotators in the Pleiades on timescales shorter than their main sequence age and one would not observe them at all. In fact, fast rotators can also be observed in older open clusters. To resolve this issue, the idea emerged of a spin-down that depends linearly (rather than cubically) on the angular velocity (MacGregor & Brenner 1991; Soderblom et al. 1993; Chaboyer et al. 1995). In this framework, the large-scale magnetic field is thought to saturate and the spin-down becomes less efficient. See et al. (2019b) observe this saturation for the fastest rotators but even with this evidence it is not understood how the transition from fast to slow rotation occurs and whether it is stochastic (Brown 2014) or driven by a different magnetic field configuration (Barnes 2003; Garraffo et al. 2018; See et al. 2019a).

Rotation periods are the primary observable of the stellar angular momentum content. We measure rotation periods from starspot-modulated photometric light curves (Kron 1947; van Leeuwen et al. 1987; Strassmeier 2009). Such photometric rotation periods are routinely obtained with high precision for low-mass pre- and main sequence stars of all ages (e.g. Herbst & Mundt 2005, Barnes et al. 2016). Stars in open clusters are of particular interest because such populations can be arranged in an age-ranked sequence, providing valuable information in understanding the stellar spin-down.

At the zero-age main sequence five open clusters [NGC 2516 (Irwin et al. 2007; Fritzewski et al. 2020), M 35 (Meibom et al. 2009), M 50 (Irwin et al. 2009), Pleiades (Hartman et al. 2010; Rebull et al. 2016), and Blanco 1 (Cargile et al. 2014; Gillen et al. 2020)] with measured rotation periods provide a cornerstone for the angular momentum evolution of cool main sequence stars. In Fritzewski et al. (2020) (hereafter F20), we have shown that these clusters host a universal rotation period distribution which confirms their isochrone-based ages, and facilitates the reliable age ranking of other open clusters. M 34 at 220 Myr (Irwin et al. 2006; James et al. 2010; Meibom et al. 2011) provides the first evolutionary step beyond the zero-age main sequence. However, M 34 is not a particularly rich open cluster, and its age of 220 Myr is not advanced enough to observe significant rotational evolution unambiguously.

Significant further rotational evolution can be observed in the 300 Myr-old NGC 3532 (Fritzewski et al. 2019). Not only is it unique in age among the nearby open clusters, but it provides a very large stellar population. Fritzewski et al. (2019) showed that it is one of the richest open clusters within the 500 pc horizon, enabling the identification and study of details of stellar rotation not visible elsewhere, and in particular the evolution of the fast rotators at this key age. As part of our efforts on this rich Southern open cluster, potentially a benchmark object, we have already provided membership information (Fritzewski et al. 2019, hereafter F19) based on radial velocity observations, multi-colour photometry by Clem et al. (2011), and *Gaia* astrometry. This membership work provides a strong foundation for a careful study of the rotation rates (really, periods) of its cool star members in the present paper. Furthermore, we analyse the chromospheric activity and its connection to stellar rotation in a companion study (Fritzewski et al. 2021, hereafter F21act).

In consequence, this uniquely-aged, rich open cluster provides a snapshot of the on-going evolution from fast to slow rotation and, together with the period distributions in the group of younger open clusters, provides empirical constraints on the time-scale of the transition from fast to slow rotation.

NGC 3532 is located in a crowded Galactic field in Carina at a distance of ~484 pc and has slightly sub-solar metallicity ([Fe/H] = −0.07 ± 0.1, F19, $[\mathrm{Fe/H}]_{\rm NLTE}$ = −0.10 ± 0.02, Kovalev et al. 2019). The interested reader can find further

details and a historical overview in the introduction of F19.

The nearest older open cluster with measured rotation periods is M 48 at 450 Myr (Barnes et al. 2015), followed by M 37 (550 Myr) (Hartman et al. 2008). The former is relatively sparse, and the latter is distant. Very few FGK-type fast rotators are observed at such ages. By the age of the benchmark open cluster Hyades (Radick et al. 1987; Delorme et al. 2011; Douglas et al. 2016, 2019) and the similarly aged Praesepe (Delorme et al. 2011; Rebull et al. 2017) (both ~600 Myr), all solar-like stars have settled onto the slow rotator sequence.

Based on observational studies such as the ones summarized above, (semi-)empirical relations between the spin-down of the slow rotators and stellar age have been derived. Skumanich (1972) was the first to show that $v_{\rm eq} \propto t^{-0.5}$ for solar-type stars (where $v_{\rm eq}$ is the equatorial rotation velocity and t the stellar age). This laid the foundation for quantitative relations between the rotation period and the stellar age, subsequently including an additional mass dependence. This gyrochronology, introduced by Barnes (2003) and recalibrated later (Barnes 2007, Mamajek & Hillenbrand 2008, Meibom et al. 2009, Barnes 2010), is a successful method to determine ages of slowly rotating stars (Barnes et al. 2016; Lorenzo-Oliveira et al. 2020). The ages of stars being otherwise difficult to obtain, the spin-down must be studied carefully if gyrochronology is to yield useful ages.

Fast rotators either might not be useful in determining stellar ages due to ambiguities, or else they may provide an additional sensitive probe to distinguish small age differences between otherwise similar open clusters. Understanding their transition to slow rotation could also provide insights into the effect of planetary companions on angular momentum loss (Cohen et al. 2010) and into the atmospheric evolution of those companions (Johnstone et al. 2015). Finally, the fast rotators are known to have activity behaviours that differ significantly from those of the slow rotators which tend to follow what is generally known as the rotation-activity relationship. The measurement of their periods is essential to understanding their activity properties, as detailed in the companion paper (F21act).

This paper is structured as follows. In Sect. 4.2, we describe our observations, data reduction and photometry in relation to the previously obtained membership. The time-series analysis is carried out in Sect. 4.3, yielding a large set of rotation periods. In the companion paper on stellar activity in NGC 3532, we derive further activity-informed rotation periods from the same photometric time series. We present and analyse the complete dataset in Sect. 4.4. In Sect. 4.5, we compare the rotation period distribution in colour-period space to available rotational isochrones. Because of the inadequacies of the models in describing our NGC 3532 data, we compare the rotational distribution in Sect. 4.6 directly to open clusters of bracketing ages, and also spin down our prior NGC 2516 rotational distribution to attempt to recreate the NGC 3532 rotational distribution. We also examine the transition from fast to slow rotation and estimate the transition timescale as well as the spin-down rate. Finally, in Sect. 4.7, we provide our conclusions.

Table 4.1: Number of visits for all observed fields.

Field name	Filter	Exposure time (s)	Number of visits
F1	I_c	60	120
	V	120	119
F2	I_c	60	120
	V	120	121
F3	I_c	60	121
	V	120	120
F4	I_c	60	120
	V	120	117
F5 (Deep North)	I_c	600	97
F6 (Deep East)	I_c	600	90
F7 (Deep South)	I_c	600	95
F8 (Deep West)	I_c	600	94

4.2 Time series photometry

4.2.1 Observations

We observed the Galactic open cluster NGC 3532 from the Cerro Tololo Inter-American Observatory (CTIO) with the Yale 1 m telescope operated by the SMARTS consortium between 19 February 2008 and 1 April 2008. Over the course of these 42 d, we obtained time-series photometry without any loss due to weather. However, the observations contain a scheduling gap of four nights (from 8 March 2008 to 11 March 2008), slightly offset from the middle of our observing campaign. The image scale of the *Y4KCam* camera mounted at the CTIO Yale 1 m telescope is $0\farcs289\ \mathrm{px}^{-1}$ which gives a $19.3' \times 19.3'$ field of view with the 4064 px × 4064 px STA CCD detector. The average detector read noise was $4.8\ e^-\ \mathrm{px}^{-1}$.

We observed four inner fields of NGC 3532 in both V and I_c filters, with exposure times of 120 s and 60 s respectively. We also observed four deeper outer fields for 600 s in the I_c filter. The positions on sky of the eight fields are shown in Fig. 4.1 (centred at α = 11:05:39, δ = -58:45:07 (J2000.0)). For the inner fields, we obtained ~120 frames per field and for the deeper outer, fields ~95 frames per field (see Table 4.1). We note that the cluster extends significantly beyond even this relatively wide observing area.

The data presented in this work were obtained in the course of the same observing campaign as the observations of NGC 2516 which are presented in F20. Consequently, the time baselines of the two photometric time series observations are identical, and the observing cadence is very similar, ensuring similar period sensitivity and comparability. Further information about the observations and the data analysis is available in that publication.

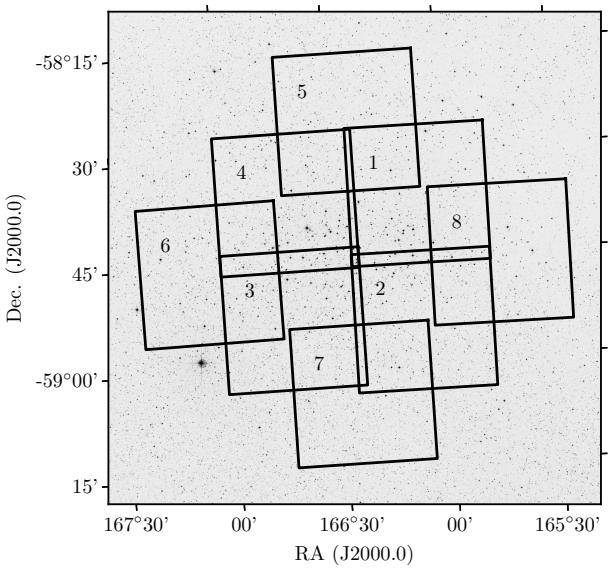

Figure 4.1: Field of NGC 3532, as seen in the Digitized Sky Survey 2 (red filter), with the individual observed fields indicated. The brightest cluster stars are located in the inner four fields (1 to 4). Their shorter exposure times were optimized for the solar-like stars. The outer fields (5 to 8) were exposed longer, with the fainter stars optimized. (Field numbers are positioned in the North-East corners.)

4.2.2 Data reduction and photometry

We obtained zero-second bias images and per-filter sky-flat fields each night to enable routine calibration. A median bias frame was subtracted from all calibration and science images using IRAF[1]. Additionally, we corrected the science data in each filter for pixel-to-pixel sensitivity differences using a per-filter balance frame. Dark current correction was not applied to the images because the dark current of *Y4Kcam* is sufficiently low (21 e^- px^{-1} h^{-1}).

Because the cluster is located at low Galactic latitude (b = 1.36°), the field of NGC 3532 contains many background stars from the Galactic disc. In order to extract the best possible light curves from this crowded field, we performed PSF photometry with DaoPhot II (Stetson 1987, 1994; Stetson et al. 2003). We decided to use a shared approach with both data sets (NGC 2516 and NGC 3532) to obtain comparable results. Hence, we followed the same workflow for the PSF photometry as summarized here, described in detail in F20, and to which we direct interested readers.

After initial source identification on the reference frame for each field, we selected the PSF stars. We matched all frames to this reference frame in the main photometric run to use the same set of PSF stars in each frame. We created a PSF model from this set for each image and used it to extract the stellar flux in DaoPhot II. Thereafter, we used the DaoMaster software to cross-match the frames down to 0.3 px and to create the individual light curves.

In total, we extracted ~200 000 light curves for ~110 000 individual stars. Stars with multiple light curves have either been observed in both filters, or in different fields, or in a combination of both. These are retained and analysed separately to provide redundancy, as in F20.

The distribution of the mean photometric measurement uncertainties for the individual stars are shown in Fig. 4.2 as a function of stellar magnitude for each of the filter/exposure time combinations[2]. The deep I_c images (600 s) have the smallest photometric uncertainties among all three configurations for stars fainter than I_c = 14. In the range between V = 12.5 and V = 14, we achieved a V band photometric accuracy better than 3 mmag for a small fraction of the stars. For fainter stars, the photon noise-limited uncertainties are only slightly larger than for the deep I_c photometry. Although both the deep I_c and the V observations have similar uncertainty distributions in their respective filters, the deep I_c observations provide more precise photometry for a given star in the photon noise-limited case. For example, a cluster member at I_c = 17 has an intrinsic colour of $(V - I_c)_0$ = 2.5. Hence, the deep I_c observations are comparable to a V = 19.5 star and we reach an accuracy $\sigma_{I_c} \leq 0.01$ at this magnitude. The short (60 s) I_c photometry has larger uncertainties at the same I_c magnitude, but is very valuable for the brighter stars. In F20, we analysed the photometric uncertainties in detail, providing confidence that the estimated values reflect the true measurement errors.

4.2.3 Membership

Well-defined open cluster members are crucial in constructing the clean, coeval, and chemically homogenous stellar samples needed to explore angular momentum evolution reliably. As part of our analysis of NGC 3532, we have already provided such a membership determination in Fritzewski et al. (2019). There, we obtained radial velocity observations of >1 000 photometric members of NGC 3532 and found 660 exclusive member stars (with the inclusion of literature radial velocity data and *Gaia* DR2 astrometry). Fig. 4.3 shows the cluster sequence in a colour-magnitude diagram (CMD) with Gaia DR2 photometry (Evans et al. 2018). (CMDs in other filters, including $BV(RI)_c$, are presented in F19.) Although we were unable to survey the entire open cluster on account of its extent on sky, this set of bona-fide cluster members is much larger than for most other nearby open clusters. Hence, it is particularly well suited to the study

[1] IRAF is distributed by the National Optical Astronomy Observatories, which are operated by the Association of Universities for Research in Astronomy, Inc., under cooperative agreement with the National Science Foundation.

[2] These values do not contain any contribution from stellar variability and should not be confused with the variability amplitude, whose analysis we defer to the companion paper (see Sect. 4.3.3 for a brief summary.)

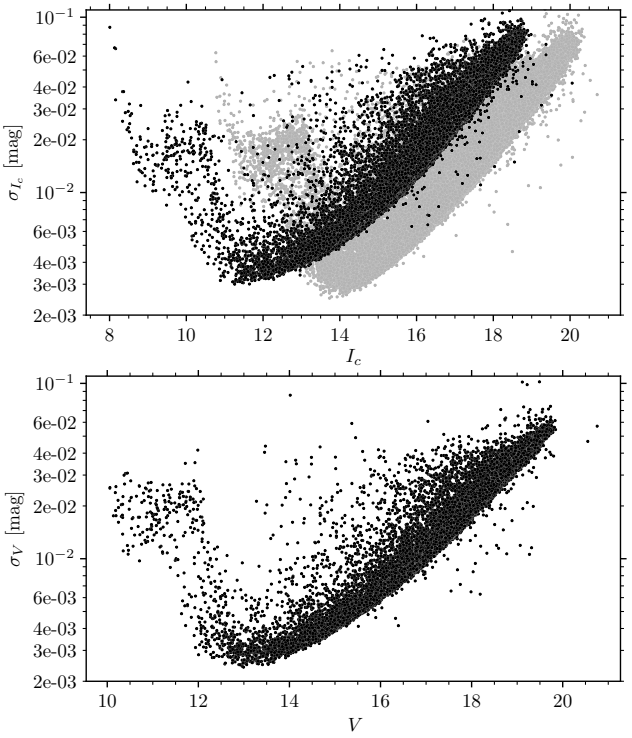

Figure 4.2: Photometric uncertainties (σ) in our time series observations for the relevant filter and exposure time combinations. *Top:* Uncertainties for the two different I_c exposure settings, 60 s (black) and 600 s (grey). *Bottom:* Uncertainties for the 120 s V exposures. In combination, we are able to ensure a measurement precision better than 10 mmag for a large fraction of the observed stars with time series.

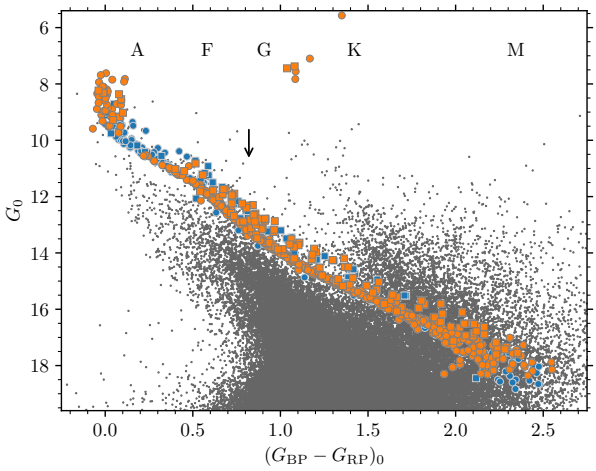

Figure 4.3: Colour-magnitude diagram in *Gaia* DR2 colour for NGC 3532 with cluster members highlighted. Radial velocity members from Fritzewski et al. (2019) are marked in orange and additional proper motion members in blue. The enormous field star population is shown in grey in the background. All data are dereddened with the average reddening value towards NGC 3532 ($E_{G_{BP}-G_{BP}}$ = 0.046). Likely binaries are marked with squares. At the top, we indicate the different spectral types from Pecaut & Mamajek (2013) for orientation. The arrow indicates the Solar colour (Casagrande & VandenBerg 2018). For colour-magnitude diagrams in other colours see Fig. 4.5 below and Fig. 14 of F19.

of stellar rotation periods in NGC 3532. In this work, we exclusively use these members, and conduct no additional membership analysis.

4.2.4 Multiplicity

We also identify likely binaries among the cluster stars. Unfortunately, the radial velocity binaries from F19, identified as part of our membership work, concern either stars brighter than the cool ones of interest here, or non-members. However, we have identified likely binaries in NGC 3532 using two methods.

Firstly, we classify all cluster members 0.25 mag brighter than the stellar main sequence locus as potential binaries. In F19, we have provided this MS locus in various colours. The difference between the locus and the observed G_0 magnitude is the offset above the main sequence. We limit our search for stars in the range $0.5 < G_{BP} - G_{BP} < 2.3$ because (a) bluer stars are not of interest in our study of cool star rotation, and (b) for redder stars the photometric uncertainties become too large for meaningful results. Secondly, as in prior studies (e. g. Belokurov et al. 2020), we use the *Gaia* EDR3 (Lindegren et al. 2021) renormalized unit weight error (RUWE) as a binarity criterion. We classify all stars with RUWE > 1.2 as astrometric binaries.

In total we identify 151 likely binaries among the radial velocity and proper motion members, corresponding to a binary fraction of 22 %. This is in reasonable agreement with the modelled binary fraction of 26.7 % of Li et al. (2020) for NGC 3532, although that too is probably an underestimate. More binaries will undoubtedly be identified with looser criteria, and of course additional data. The combined set of binaries identified according to the above criteria is marked in the CMD in Fig. 4.3 and in other relevant diagrams below.

4.3 Rotation periods

Because this paper is restricted to a discussion of the rotation periods only of members of NGC 3532 and because of the presence of a large number of field stars in our photometry[3], we confine our time series analysis only to cluster members of NGC 3532. We applied the same algorithm and the same pipeline for these data as we did for NGC 2516 (F20) to construct the light curves from the time-series photometry, to analyse the time series, and to obtain rotation

[3] The field around NGC 3532 contains $\gtrsim$100 000 sources of which ~1% are possible cluster members.

periods. Because the data were obtained in parallel, the light curves for both clusters are so similar in data structure that we were able to apply many tools developed for the one cluster without adjustments to the other cluster. The workflow presented below is described in greater detail in F20. (See especially the decision tree in Fig. 8 in that paper.)

4.3.1 Initial periods

As in F20, we applied five algorithms to determine the stellar rotation periods ($P_{\rm rot}$): Lomb-Scargle (Lomb 1976; Scargle 1982), in the form of the generalized Lomb-Scargle periodogram (Zechmeister & Kürster 2009), the CLEAN algorithm (Roberts et al. 1987; Crane 2001), phase dispersion minimization (PDM, Stellingwerf 1978), string length (Dworetsky 1983), and the Gregory-Loredo periodogram (Gregory & Loredo 1992; Gregory 1999)

After applying each algorithm to all light curves (examples of which are displayed in the Appendix in Fig. 4.14), we selected a common period following the scheme presented in F20 (summarized in Fig. 8 there). We examined each set of light curves and periodograms manually to assure ourselves that periodic variability is indeed present in the data, and to determine the common period from the (usually) multiple estimates.

In cases where possible alias periods are present, we carefully double-checked the light curves and periodograms before assigning a preliminary period. An example of such a case is displayed in Fig. 4.4. The periodograms picked up both the preferred rotation period ($P_{\rm rot}$ = 0.839 d) and the alias period[4] ($P_{\rm alias}$ = 5.18 d), with equal power. Indeed, during our initial manual classification, we also interpreted this light curve as having a ~5.2 d period with a noisy light curve, based on the majority of our periodograms. However, the CLEAN periodogram (designed precisely for such cases) damps down the beat frequency caused by the observing cadence, and enabled us to identify the alias to assign the star what we believe is the true period of 0.839d. In fact, manual inspection shows that successive data points on a given night follow the short-period sinusoid without exception, in marked contrast to the habitual excursions of the data from the longer-period sinusoid.

While some of the final published periods are multiples of 1 d, even the CLEAN periodogram confirms them with high significance. We cannot detect any signs of possible aliases despite thorough analyses of the periodograms. Consequently, we believe these periods to be real (and indeed expected), and include them in the final data set. Finally, it should be noted that the analysis in the companion stellar activity paper has additionally confirmed all rotation periods in the set considered therein, consisting of those stars for which we were able to obtain spectroscopy, and therefore chromospheric activity measurements.

[4] $P_{\rm alias} = 1/(1/P_{\rm rot} - 1)$

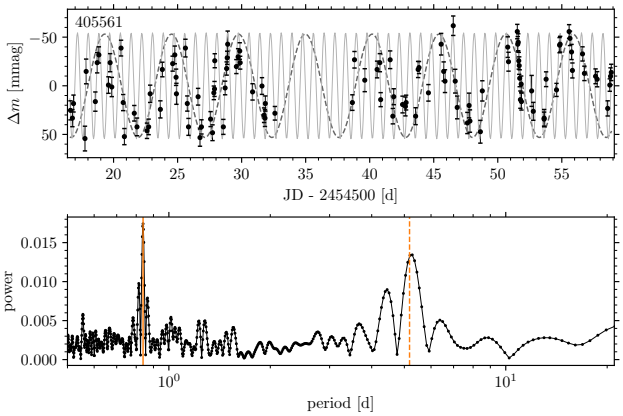

Figure 4.4: *Top:* Example of a light curve with a strong alias. To guide the eye, sine waves for both the preferred period ($P_{\rm rot}$ = 0.8385 d, solid line) and the alias period ($P_{\rm alias}$ = 5.18 d, dashed line) are added to the data (black dots). The shorter period fits the data more closely as is shown by the fact that the simple sine connects nearly all data points. *Bottom:* Corresponding CLEAN periodogram with both periods marked with vertical lines. The alias period is not located exactly at the peak in the periodogram due to the coarser resolution at longer periods.

4.3.2 Further steps to final periods

The above-determined period for each light curve is considered preliminary and imprecise because each of the applied algorithms provides a slightly different estimate for the underlying final period. We therefore combine the results of all methods by seeking the most likely period near the agreed period in each periodogram, and take the mean value from the five different methods as our final period. Our uncertainty is taken to be the maximum difference of any of the initial periods from the mean period. As seen in F20, periods for the same star from different light curves agree to within this uncertainty estimate at a 2σ-level.

As a result of our visual inspection, we classified the light curves into three classes. Stars of the primary class ("1" in the corresponding table) show a clear rotational signal, in both the light curve and the periodogram, which could in principle be found visually without any periodogram analysis. Stars of the secondary class (2) have a noisier light curve, a wide peak in the periodogram, or the periodogram contains secondary peaks with significant power. We additionally marked all stars which could potentially be affected by an alias with a "0" in the table.

Among the radial velocity cluster members with light curves (549 stars with 1158 light curves), we find 165 rotators. Additionally, we searched for periodicity among the *Gaia* DR2 proper motion members from F19 for which we have not obtained radial velocity data, and find 11 additional rotators among them.

There is an additional set of photometric periods beyond those that are obvious from their light curve vari-

Table 4.2: Description of the columns of the online Table with the measured rotation periods.

Name	Unit	Description
ID	-	ID in this work and F19
designation	-	ID from *Gaia* DR2
CLWH	-	ID from Clem et al. (2011)
RA	deg	Right ascension from Clem et al. (2011)
Dec	deg	Declination from Clem et al. (2011)
Vmag	mag	V magnitude from Clem et al. (2011)
BV0	mag	$(B-V)_0$ colour from Clem et al. (2011)[1]
VK0	mag	$(V-K_s)_0$ colour with K_s from 2MASS
Prot	d	Rotation period
dProt	d	Uncertainty on rotation period
Amp	mag	Light curve amplitude
Class	-	Classification of period [0, 1, 2, 3][2]
Binary	-	Binary status (True/False)

Notes. [1] Dereddened with $E_{(B-V)} = 0.034$, $E_{(V-K_s)} = 0.095$ (F19).
[2] Classes are 0: possible alias, 1: first class, 2: algorithmic periods, 3: activity-informed periods.

ability alone. These are stars for which we have obtained chromospheric activity measurements, and for which the well-defined relationship between stellar activity and rotation period (really Ro, the Rossby Number) has allowed us to predict a rotation period for the star from the corresponding activity measurement. Subsequently, we were able to identify the actual photometric rotation period in our data, typically within an interval of ±1 d of the predicted period. This procedure is fully explained in our companion publication (F21act), and enables us to uncover 103 additional (photometric) rotation periods from our light curves. This third class of rotation periods, identified with the help of their chromospheric activity measurements, are marked with the numeral "3" in the accompanying table.

Hereafter, we use the full set of 279 rotation periods regardless of their origin. However, we mark them with distinguishing symbols in the main colour-period diagram in Sect. 4.4 so that the reader can appreciate that their distributions are essentially indistinguishable. All stellar rotation periods, accompanied by the corresponding period uncertainties, the classification and other relevant information, are provided in an accompanying online Table. (See Table 4.2 for a specification of the data available.)

4.3.3 Light curve amplitudes

A simple and direct measure of photospheric activity that can be obtained from the light curves is the amplitude of variability. This provides an indication of starspot size, convolved of course, with the star's rotational inclination angle, and the degree of asymmetry of starspot distribution with longitude. For completeness, we also provide the variability amplitudes of the rotators in Table 4.2. However, the discussion of the variability amplitudes themselves, and their relationship with other activity indicators is carried out in the companion paper (Sect. 4 and Fig. 2 therein). In brief, as with other stellar activity indicators, the variability amplitudes follow a distinct correlation with the Rossby number (defined as the ratio between the rotation period and the convective turn-over time). Additionally, from the comparison with NGC 2516, we show that variability amplitudes of the slow rotators decrease with age due in concert with the stellar spin-down and the accompanying decrease in magnetic field strength.

4.3.4 Rotators in the colour-magnitude digram

To sum up our rotation period derivations for NGC 3532, we mark all identified stars with derived rotation periods in the colour-magnitude diagram (Fig. 4.5). The rotators (including both those obtained only from the photometry, and those obtained from the photometry, but with the help of the activity information) can be seen to be distributed across the whole cool star region of the cluster sequence ranging from spectral type late-F to mid-M. The histogram in the right panel of Fig. 4.5 shows a clear peak for stars around $V \approx 14.5$, corresponding to early K dwarfs in NGC 3532 ($(V-K_s) \approx 2$). Here, we detect rotation periods for 87 % of the NGC 3532 members. Across the whole magnitude range $V = 13-17$, we are able to find rotation periods for more than half of the member stars. For fainter and redder stars the detection fraction decreases strongly as a result of decreasing sensitivity, so that stars with $V \geq 17$ are only occasionally identified as rotators.

4.4 Colour-period diagram for NGC 3532

Because the rotation periods of open cluster stars are now well-known to have a strong dependence on stellar mass, it is particularly useful to discuss the measured periods for the NGC 3532 stars in concert with their photometric colours, a precisely measured proxy for their masses (or spectral types). This section therefore discusses the NGC 3532 colour-period diagram (CPD) that our rotation periods allow us to construct.

This CPD for NGC 3532, using the final set of 279 rotation periods, is displayed in Fig. 4.6 using the $(V-K_s)_0$ intrinsic colour[5] as the independent variable. (CPDs in other useful colours will also be provided below when relevant.) Rotation period uncertainties are only visible when they exceed the sizes of the corresponding symbols, each explained in the figure caption. The absence of outliers, especially in the upper left region of the CPD is notable[6].

[5] With V from Clem et al. (2011) and K_s from 2MASS (Skrutskie et al. 2006).

[6] We ascribe this both to better sampling of the light curves, resulting in better rotation period derivation, and also the availability of better membership information, as compared with prior work, including earlier work on the same cluster in the otherwise unpublished PhD thesis work of Barnes (1997).

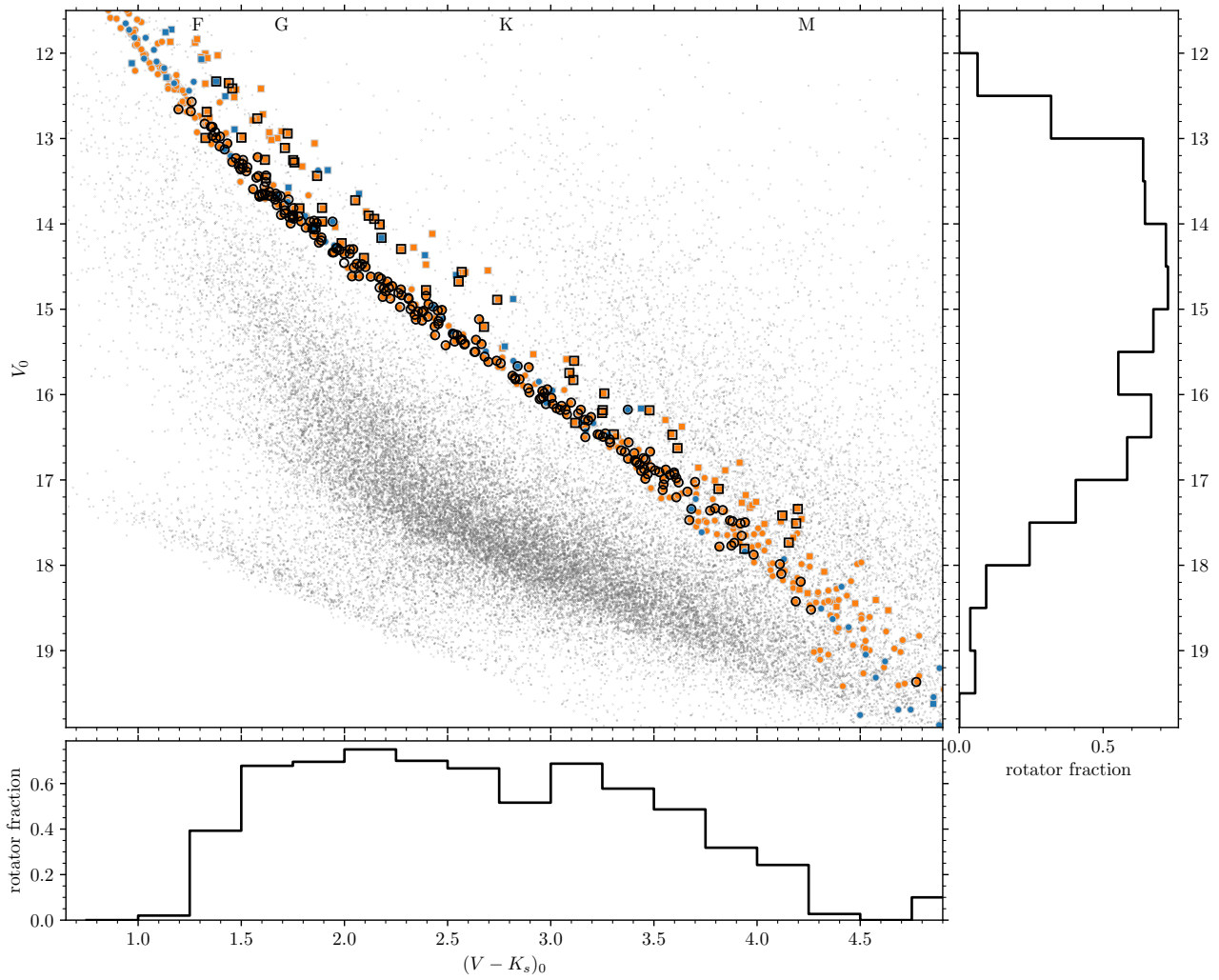

Figure 4.5: *Left:* Colour-magnitude diagram of NGC 3532 highlighting the identified rotators (black outline). Rotation periods have been measured for the majority (detection fraction > 50 %) in the G2 to K8 spectral type range. The colour scheme is the same as in Fig. 4.3, with radial velocity members of NGC 3532 in orange and additional proper motion members in blue. Likely cluster binaries are marked with squares. *Right* and *bottom:* Histograms showing the fraction of periodic rotators identified among the members. The decline for $(V - K_s)_0 > 3.2$ and $V_0 > 16.5$ arises from the decreasing sensitivity for fainter stars.

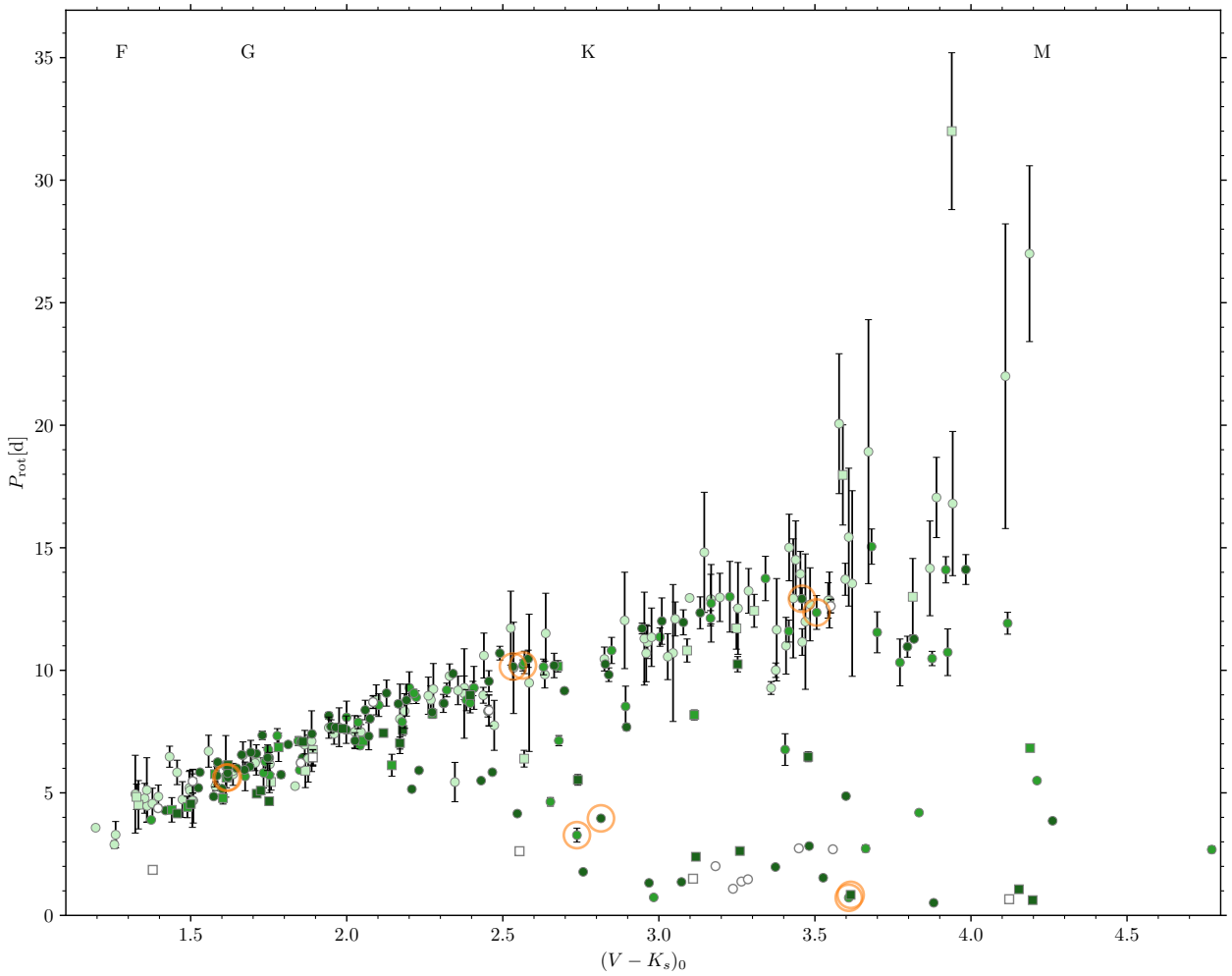

Figure 4.6: Colour-period diagram for members of NGC 3532 with rotation periods. A well-populated slow rotator sequence is visible, as well an evolved fast rotator sequence. The continuation of the slow rotators into the M dwarf regime, the "extended slow rotator sequence" is also apparent. The paucity of warmer fast rotators relative to younger open clusters is remarkable, and emphasises the mass dependence of the transition from fast to slow rotation. The best photometric rotation periods are marked in dark green and less evident (algorithmic) periods in lighter green. The lightest green symbols indicate the activity-informed photometric rotation periods from the companion paper (Fritzewski et al. 2021). The few periods with strong aliases are marked with unfilled symbols. Circles indicate likely single members and squares binaries. We show example light curves in Fig. 4.14 for the stars encircled in orange. The bluest datum consists of two stars with nearly identical positions in the CPD, so that only one circle is visible. The period uncertainties are only visible when they exceed the symbol size.

4.4.1 Specific regions of the CPD

The CPD of NGC 3532 features a very prominent slow rotator sequence that stretches diagonally from ~3 d for late F-type stars to beyond 15 d for early M dwarfs. The highest-mass rotator in this range of spectral types has M~1.3 $M_\odot$ and the least massive M~0.5 $M_\odot$[7]. The sequence is remarkably well-populated and linear in this colour, as compared with open clusters of ZAMS age (discussed further below). The blue end of the slow rotator sequence begins at $P_{\rm rot}$~3 d. From space-based photometry of younger (e. g. NGC 2516; Healy & McCullough 2020) and older clusters (e. g. NGC 6811; Meibom et al. 2015, Curtis et al. 2019) we know that stars blueward of our detections are likely to have even shorter rotation periods as they approach the break in the Kraft (1967) curve of rotational velocity against colour. Our data are not sensitive enough to locate this break point in photometric colour, well-known to be where the onset of surface convection zones among cooler stars trigger stellar spin-down via magnetized winds. At the red end of the slow rotator sequence, we find an "extended slow rotator sequence", with early M-dwarfs rotating as slowly as 32 d. This feature appears to be the older counterpart of the extended slow rotator sequence (ESR sequence) that we identified in our prior work (F20) on the open cluster NGC 2516.

We also find a sizeable number of fast rotators that clearly form a different population as compared with the slow rotators. These are present among the cooler stars of our sample, and are essentially absent for stars bluer than $(V - K_s)_0 < 2.1$. The fastest rotators ($P_{\rm rot} \lesssim 3$ d) of this group appear to delineate a flat sequence of roughly constant rotation period for $(V - K_s)_0 > 3$. Their earlier counterparts with ($(V-K_s)_0 \approx 2-3$) have evolved noticeably upwards from their initially shorter rotation periods (as in the ZAMS clusters NGC 2516 and Pleiades), and appear to have formed an elevated sequence of rotating stars in transition from fast to slow rotation. For even warmer stars neither the fast rotators nor their evolved counterparts are observed. In fact, as we show in the companion paper on the activity of NGC 3532 stars, such stars do not exist in NGC 3532, having all evolved into slow rotators.

The slow rotator sequence of NGC 3532 appears to be largely straight, with rotation period increasing linearly with $(V - K_s)_0$ colour. Those of significantly younger or older open clusters feature more strongly-curved sequences. This linear appearance appears to be an intrinsic feature of open clusters near the age of NGC 3532, as we shall see below in Sect. 4.6.1, where NGC 3532 is compared with two open clusters (M 34 and M 48) that are immediately adjacent in age. We will also show below, in Sect. 4.6.2, that the curved slow rotator sequence of the younger NGC 2516 open cluster in fact straightens out when it is evolved forward to the age of NGC 3532 using evolutionary angular momentum models. Consequently, the change of shape of the slow rotator sequence appears to be a natural result of the mass-dependent angular momentum evolution, one which spins down the later-type stars on the slow rotator sequence much stronger than the warmer stars in the considered time frame.

Among the lower-mass late-K and early-M dwarfs ($(V - K_s)_0 > 3.5$), the membership information available is limited, and as a result, this region of the CPD is more sparsely populated. This particularly impacts the expected, but only barely sampled, wide distribution of rotation periods among early-M dwarfs (with 0.5 d $\lesssim P_{\rm rot} \lesssim$ 10 d) and the fast rotating tail which extends to the lowest-mass stars. Two additional factors are at work: Firstly, the signal-to-noise ratio of the light curves is low for these faint stars, hindering unambiguous determination of the short rotation periods. Secondly, because the stellar activity of these stars is saturated, we are unable to derive activity-informed rotation periods for such stars in the companion paper. Yet from the colour-activity diagram, we know that such stars are present in NGC 3532.

The CPD has a sparsely populated gap in the vicinity of $(V - K_s)_0 = 2.75$. This is a consequence of the usage of $(V - K_s)_0$ colour, with a large extent in colour space representing only a small mass range, and hence fewer stars fall into that region in the CPD. (The CMD in Fig. 4.5 also shows a similar feature.). We find one obvious outlier below the slow rotator sequence among the bluest stars. We would not normally expect any stars in this region because such stars tend to evolve onto the slow rotator sequence. However, this rotation period is a possibly-aliased period of comparatively low quality. The membership of this star is also based only on *Gaia* data, without radial velocity confirmation. The star could also potentially be in a tidally locked binary system, as is the case for one of the equivalent rotators in NGC 2516. In conclusion, we cannot find a reason to disregard this rotator, and retain it as is for this work.

4.4.2 Bifurcation of the slow rotator sequence

We now discuss a curious feature of the slow rotator sequence that has not, to our knowledge, been seen in any prior open cluster. The slow rotator sequence itself (in the range $(V - K_s)_0 = 1.6 - 2.3$) shows a clear separation into an upper (slower = S) and a lower (faster = F) sequence, particularly when the activity-assisted rotation periods (with larger errors) are ignored. The effect remains observable when the noisier activity-assisted periods are added, even though the larger period uncertainties of those stars introduce an additional scatter (Fig. 4.6).

Such a spread in the slow rotator sequence cannot be attributed to differential reddening displacing a subset of stars in colour from the true sequence. Given the low reddening ($E_{(B-V)} = 0.034$ mag, F19) towards NGC 3532, such an effect is impossible. Colour effects could potentially also be introduced through inaccurate photometry. However, when

[7] Even lower mass stars are present, and will be discussed separately below.

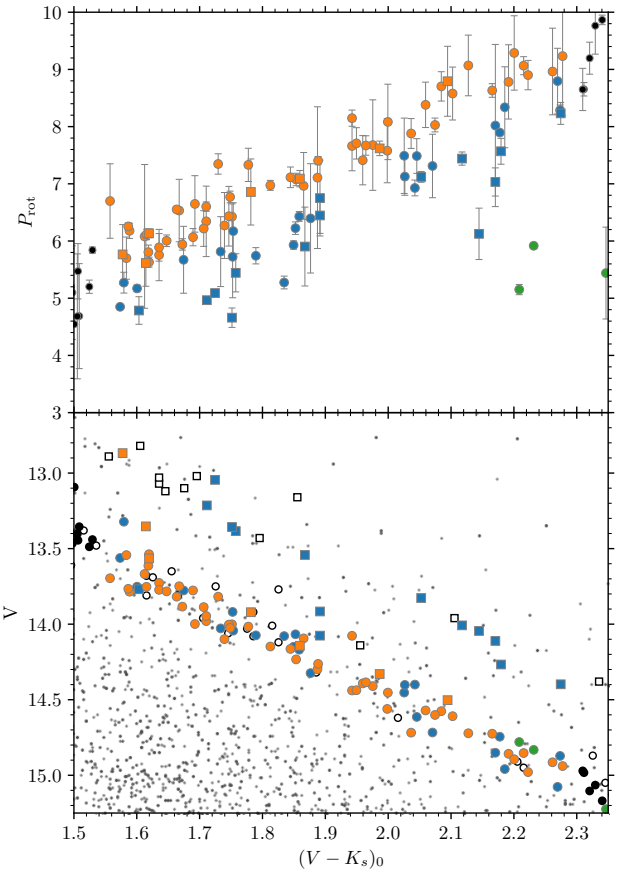

Figure 4.7: *Top*: Zoom-in on the region of the colour-period diagram in which the bifurcation of the slow rotator sequence is observed. The longer-period sequence (S-slow rotators) is shown in orange and the shorter-period sequence (F-slow rotators) in blue. Additional slow rotators outside the region of interest are marked in black, and fast rotators in green. Squares indicate binaries. *Bottom*: Corresponding colour-magnitude diagram (same symbols as above) with additional cluster members without determined rotation periods marked with open symbols. The equal-mass binary sequence is almost exclusively populated by the F-slow rotators, indicating a connection between faster rotation and binarity.

we plotted our CPD with different colour combinations – including ($G_{\rm BP}$ – $G_{\rm RP}$) from *Gaia* DR2 – the gap running through the middle of the slow rotator sequence remains, and appears to be independent of the chosen colour combination. We also verified the correctness of our periods. Having re-examined the light curves and periodograms to exclude any possibly falsely-assigned periods, we conclude that all periods displayed are genuine.

We also checked whether the two sequences could belong to two different stellar populations. The results are negative, with both groups apparently spread out evenly in proper motion, radial velocity, parallax, and sky position, disallowing recourse to a merger scenario for the NGC 3532 cluster, for instance.

To display this effectively, we colour-code the slower- and faster rotational branches of the slow rotator sequence (hereafter S-slow rotators and F-slow rotators, respectively) as indicated in the CPD (Fig. 4.7, upper panel) and also plot them separately in the colour-magnitude diagram (Fig. 4.7, lower panel). We see that the equal-mass binary sequence in the CMD is essentially composed of only the F-slow rotators. These stars have the same colours as their individual components in the CMD. Consequently, no colour shift is possible in the CPD either. The few photometric binaries between the single star main sequence and the equal-mass binary sequence[8] also tend to belong to the F-slow rotators, while the astrometric binaries (orange squares) on the cluster sequence belong to the S-slow rotators. We note that not all F-slow stars are demonstrably binaries. Among the F-slow rotators, the binary fraction is 37.8 ± 10.1 %, somewhat elevated with respect to the overall binary fraction in this colour range, which is 27.2 ± 4.7 %. Despite the higher binary fraction, we also find apparently single stars (based on decade-baseline radial velocity time-series, F19, and astrometry, Sect. 4.2.4) among the F-slow rotators, a fact that suggests that the bifurcation cannot be attributed to tidal effects alone.

We note that a statistically significant rotational offset between the overall rotation period distributions of single and primary stars in close binaries beyond the reach of tides has also been noted by Meibom et al. (2007). Furthermore, we note that the binary fraction among the fast rotators of NGC 3532 is also significantly elevated. For the fast- and evolved fast rotators, we find 32.4 ± 9.4 % to be binaries. We can compare this number to the model of Li et al. (2020), who estimate the binary fraction in different mass-regimes in NGC 3532. They find a binary fraction[9] of 19.4 ± 2.2 % for lower-mass stars with $G < 15.06$. This magnitude cut coincides with the bluest stars on the evolved fast rotator sequence. Since this number is smaller than the observed fraction, we conclude that the fast rotator sequence of NGC 3532 is enhanced in binaries as compared

[8] These are expected to be displaced slightly redward.

[9] They include all binaries, in particular non-equal-mass binaries on the photometric single stars sequence.

with the overall population, although it also includes many stars with no trace of binarity whatsoever.

The connection between fast rotation and binarity is not necessarily a tidal interaction, but could be a natural result of star formation. The binarity could influence the stellar rotation indirectly through the dissipation of the proto-planetary disc (Artymowicz & Lubow 1994; Mathieu 1994). Cieza et al. (2009) have found short disc lifetimes in binary systems and Messina (2019) has observed that young binary stars generally rotate faster. All together, one finds that the majority of binary stars rotate faster than average at young ages.

Continuing this chain of reasoning, we conclude that the F-slow rotators were initially fast rotators because: (1) they rotate faster than the S-slow rotators; (2) they have a larger binarity fraction, and (3) the initial fast rotators have evolved to slow rotators while preserving their binarity fraction during the transition. The stars of this group rotate faster because they have not yet settled onto the asymptotic slow rotator sequence. Such an effect could be the result of stellar spin-down being strongest during the crossing of the rotational gap (Barnes 2010), and weakening near the slow rotator sequence. When arriving on the slow rotator sequence, the braking is only marginally stronger than for the initial slow rotators which spin down Skumanich-like. Hence, the former fast rotators require some time to finally settle onto the sequence.

Our observations suggest that the influence on rotation beyond tidal interactions is apparently restricted to binaries of intermediate separations which are both unresolved and have a near-equal mass ratio, i. e. photometric binaries. Pure astrometric binaries are less likely to be found on the F-slow branch. Such stars could either be very wide binaries, with both components photometrically resolved, or have a low mass ratio, placing them on the single star main sequence. Disentangling this effect will clearly require more detailed work.

In conclusion, we can observe the transition from fast to slow rotation not only when the stars are spinning down through the rotational gap but also post that extremely rapid phase. Unfortunately, NGC 3532 is unique in its age, richness, and proximity. Hence it is currently not possible to observationally test[10] whether the bifurcation exists in other open clusters of similar age, or to specify how long it might persist.

4.5 Comparison with rotational isochrones

A number of models of stellar rotation have provided "rotational isochrones," enabling a direct comparison between the predictions of the model and the measured rotation periods across a wide range of cool star masses. These isochrones in the (colour/mass)-period space can be placed directly onto the data to enable, among other things, an estimation of the rotational age of the open cluster with respect to the model in question. Here, we examine four recent models, all of which were compared in detail in connection with our prior work (F20) in NGC 2516. Below, we only provide the briefest description of each model. In order to intercompare the models on the same basis, we use the same age (300 Myr) as the relevant comparison age for all models. These are displayed in comparison with one another and with the measured rotation period data for NGC 3532 in Fig. 4.8.

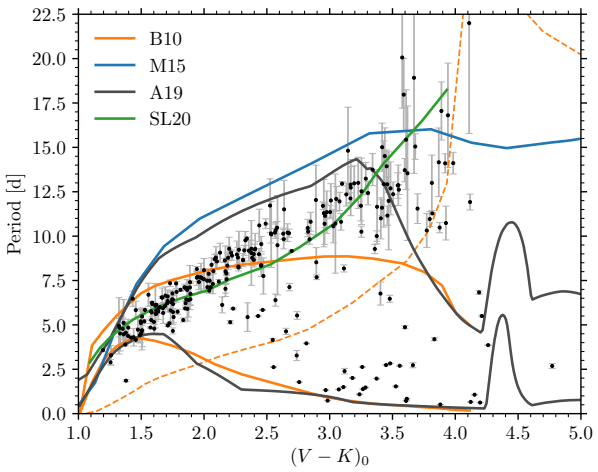

Figure 4.8: Comparison between the NGC 3532 rotation periods and 300 Myr stellar rotation models. In orange, we show both the slow and fast rotator model from Barnes (2010). The dashed line indicates the position of the rotational gap from B10. The asymptotic spin rate from Matt et al. (2015) for 300 Myr is shown in blue and the isochrones from Amard et al. (2019) for both the fast and slow rotators are given in grey, while the slow rotator isochrone from Spada & Lanzafame (2020) is shown in green.

4.5.1 Barnes (2010)

The oldest model in our comparison (Barnes 2010, hereafter B10) has a mathematically simple symmetric form in the period derivative, $\mathrm{d}P/\mathrm{d}t$, and provides isochrones which depend only on the convective turn-over timescale τ_c which serves as the underlying independent variable for the stellar mass, and for which we use the values provided in Barnes & Kim (2010). (The table therein itself provides the $(V-K)$ colours required for the comparison.)

This model is plotted using orange lines in Fig. 4.8, the lower one corresponding to an initial period $P_0 = 0.1$ d, and the upper one to $P_0 = 3.4$ d, uniform for stars of all masses. The dashed orange line indicates the boundary between fast and slow rotators in the B10 model. We see that the location of this boundary line is plausible, in the sense

[10] As seen in Sect. 4.6.2, theoretical angular momentum models are not yet advanced enough to test such small effects through simulations.

that, as predicted by the model, the density of rotation period measurements is actually somewhat lower in its vicinity. However, the line clips the measured slow rotator sequence among the M dwarfs, suggesting an issue with either the rotation period prediction or with the predicted stellar colours. The prediction for the fast rotators is also good for stars of solar mass and warmer, as well as for the late-K and early M stars. However, stars of late-G and early-K spectral type ($1.8 < (V - K_0) < 2.6$) clearly spin down faster than the model. The prediction of the B10 model for the slow rotators is clearly above the NGC 3532 data blueward of $(V - K)_0 = 2.2$, and below for redder colours. A large part of this mismatch can be traced to the uniform (and therefore unrealistic) initial period $P_0 = 3.4$ d that was chosen to generate this isochrone. In Sect. 4.6.2 below, we show that using the measured NGC 2516 periods at 150 Myr as a starting condition goes much of the way towards fixing this problem.

4.5.2 Matt et al. (2015)

The Matt et al. (2015) model (hereafter M15) also uses the convective turnover timescale, τ_c, in cool stars via the Rossby Number, $Ro = P/\tau_c$. The problem is formulated in terms of a spin-down torque that is expressed as a function of the mass, radius, and magnetic field of the star, with the magnetic field itself parametrized as a function of the Rossby number, mass, and radius. The result produces a mass dependence of the spin-down timescales in both the fast and slow rotator regimes that is similar to that in the B10 model (see Fig. 1 in Matt et al. (2015)), albeit with additional parameters. This spin-down formulation is then applied to stellar evolution models from Baraffe et al. (1998) to obtain the rotational evolution results. The asymptotic spin rate for this model for 300 Myr is shown in Fig. 4.8 with the blue curve.

As can be seen in Fig. 4.8, the 300 Myr model appears at face value to have over-estimated the rotation periods over nearly the whole mass-range. It is only among the F-type stars that it approaches the slow rotator sequence, but it does so with too steep a slope as compared to the NGC 3532 observations. However, the isochrone from this model promisingly runs roughly parallel to the data redward of $(V - K_s)_0 \approx 1.6$, suggesting that parameter changes (such as age) could potentially permit closer reproduction of the data. The fast rotators in NGC 3532 cannot be addressed by the asymptotic spin rate formalism. (We will show a more detailed comparison below that includes the fast rotators, and also relaxes the age constraint of 300 Myr.)

4.5.3 Amard et al. (2019)

Amard et al. (2019) (A19) have integrated the M15 angular momentum model into the Geneva/Montpellier stellar models, while also updating some parameters and tuning the initial conditions to reproduce rotation period distributions of various open clusters. Consequently, the prediction of their model is similar to that of M15 in the slow rotator regime, where it also over-predicts the rotation periods with the 300 Myr model. In contrast, the fast rotator isochrone that is included in A19 predicts faster rotation than is observed in NGC 3532 over the G-K mass range. As a result, the predicted dispersion in rotation period is far greater than that actually observed in this mass range. We discuss implications of this mismatch in Sect. 4.6.2.2 below.

4.5.4 Spada & Lanzafame (2020)

The final isochrone considered is that from Spada & Lanzafame (2020) (SL20), one formulated only for the slow rotators in open clusters. The key feature of this model is the (re-)introduction of the two-zone model in which the radiative core rotates initially independently of the outer convective envelope[11]. The associated coupling is superimposed on the spin-down formulation from the B10 model, requiring one additional parameter that describes the power-law dependence of the coupling timescale on stellar mass. It allows the angular momentum reservoir hidden within the star to be tapped on that mass-dependent timescale, correspondingly allowing cool stars to avoid spinning down at key ages, as observed in older open clusters. For instance, it is the model that most accurately describes the rotation period distribution in the 2.5 Gyr-old Ru 147 (Gruner & Barnes 2020).

From the rotational coupling time-scale determined by Spada & Lanzafame (2020) (their Fig. 6) one finds that for a 300 Myr-old open cluster the coupling is dominant for stars with $M_\star \gtrsim 0.9\,M_\odot$ (equivalent to $(V - K_s)_0 \lesssim 1.9$). The two-zone model should describe the rotation period distribution better than a model based on pure wind braking in this regime.

Indeed, Fig. 4.8 shows that in this colour range Spada & Lanzafame (2020) describe the slow rotator data adequately. However, for lower mass stars the rotation periods appear to be slightly underestimated in a mass-dependent way. This means that the braking is not efficient enough for these stars. Yet for the lowest-mass stars in the model, it is in good agreement with the observations of the beginning at the extended slow rotator sequence. The fast rotators are not modelled by Spada & Lanzafame (2020).

4.5.5 Conclusions about rotational isochrones

In summary, with respect to the slow rotator sequence, we find the two-zone model of Spada & Lanzafame (2020) to provide the closest match to the NGC 3532 rotation period measurements. The M15 and A19 models significantly overestimate the rotation periods for the slow rotators in the G-K star regime, at least to the extent that 300 Myr models are used. The B10 model, the earliest of the set, is inadequate for the slow rotators, probably because of the unrealistic

[11] This concept was initially modelled by MacGregor & Brenner (1991).

uniform initial rotation period of 3.4 d chosen. As regards the fast rotators, only B10 and A19 make readily testable predictions. These are nearly identical, transitioning stars warmer than solar onto the slow sequence as observed, reproducing the lower envelope for warmer than G2 spectral type and cooler than mid-K. However, neither of them appears to spin stars down aggressively enough in the region between. We conclude that while the currently available theoretical work is plausibly in the region of the rotation period data, detailed reproduction of the data will require further work, even for the NGC 3532 cluster itself. In the following, we directly employ spin-down relations in order to understand these discrepancies.

4.6 Detailed comparison with other open clusters and evolutionary models

The comparison between the NGC 3532 rotation period data and the available rotational isochrones being less than satisfactory, we now perform a direct comparison with rotation periods from two open clusters that most closely bracket NGC 3532 in age. We then take the rotation period distribution of the ZAMS open cluster NGC 2516 that was studied by F20 (one with essentially the same rotation period sensitivity), and evolve it forward in time to examine the extent to which two rotational evolution models are able reproduce the NGC 3532 data on a star-by-star basis, while relaxing certain assumptions and choices inherent in constructing rotational isochrones. This procedure is a deeper (and more fair) comparison than the prior one, and permits an appreciation of how the rotational age of a cluster currently depends on the underlying spin-down model.

4.6.1 Comparison with clusters bracketing NGC 3532 in age

The unique age of NGC 3532 prevents us from directly comparing it to another coeval open cluster (as we were able to do in F20 for the case of NGC 2516).

In Fig. 4.9, we compare the rotation period distributions of NGC 3532 (300 Myr, centre panel) to the nearest younger cluster with measured rotation periods, M 34 (220 Myr, Meibom et al. 2011, left panel), and to the nearest older cluster, M 48 (450 Myr, Barnes et al. 2015, right panel). These are all post-ZAMS clusters, each stepping forward ~ 100 Myr in age. We wish to know (among other things) whether the rotational distributions are sufficiently different to be visually recognizable. To enable a visual comparison, we distil the NGC 3532 rotation period distribution into dashed lines that empirically represent the fast and slow rotator sequences in a similar manner to that in Barnes (2003), and place that distilled empirical NGC 3532 distribution onto the comparison cluster data in each panel of Fig. 4.9.

Using the lines of the distilled NGC 3532 distribution, it is immediately apparent that stars on the slow rotator sequence of M 34 are mostly below the lines, and thus rotate faster for a given mass (or colour) than stars in NGC 3532. In contrast, the slow rotators in M 48 are almost all located above the NGC 3532 lines, and can be seen to rotate significantly slower than their counterparts in NGC 3532. This age-ranked succession allows us to conclude immediately that the rotational age of NGC 3532 is between those of M 34 and M 48, and must be in the vicinity of ~ 300 Myr. This is in qualitative agreement with the isochronal age of the cluster, assuming that those of the comparison clusters are substantially correct.

The evolution and dissipation of the fast rotator sequence, in contrast, is much greater than the small (if significant) evolution of the slow rotator sequences from M 34 age to M 48 age. In M 34, early K dwarfs ($(B-V)_0 \approx 0.8$) are still on this fast sequence. By the age of NGC 3532, they have evolved from $P_{\rm rot} \approx 1$ d to slow rotators with $P_{\rm rot} \approx 6$ d. In NGC 3532, stars rotating that fast can now only be found among the mid- to late-K and M stars. In M 48, no such stars are observed, although this could potentially be an effect of the sampling of the light curves, and the relative insensitivity to late K and early M dwarfs in the study of Barnes et al. (2015). Nevertheless, the dramatic evolution of the fast rotators is potentially a sensitive age indicator which could be used to distinguish between open clusters of very similar isochronal ages.

We conclude that a ~100 Myr age difference between young (below Hyades-aged) open clusters is large enough that the differences between their rotational distributions can be appreciated by simple inspection, without the necessity for sophisticated analysis.

4.6.2 Comparison with spin-down models

We now evolve the rotation period distribution of the ZAMS open cluster NGC 2516 from F20 forward to mimic the measured NGC 3532 distribution. We have shown in F20 that the rotational distribution on the zero-age main sequence is universal in the sense that the distribution of one cluster is indistinguishable from those of other comparable ZAMS open clusters. Furthermore, both NGC 2516 and NGC 3532 were observed quasi-simultaneously during the same observing run, with the same instrumentation, observing baseline, near-similar cadence, and analysis techniques, ensuring that the rotation period sensitivities for both clusters are almost identical. These features make the two datasets the best-comparable ones.

The rotational distributions of both datasets are correspondingly shown in the CPD in Fig. 4.10 using $(G_{\rm BP}-G_{\rm RP})_0$ colour (Gaia Collaboration et al. 2018; Evans et al. 2018). Both distributions can be observed to have the now-familiar cuneiform shape that characterizes the CPDs of young open clusters, with well-defined slow rotator sequences, and no outliers in the upper left of the figure. We see that in the interval between the ages of NGC 2516 and NGC 3532, the slow rotators have clearly moved upwards across every

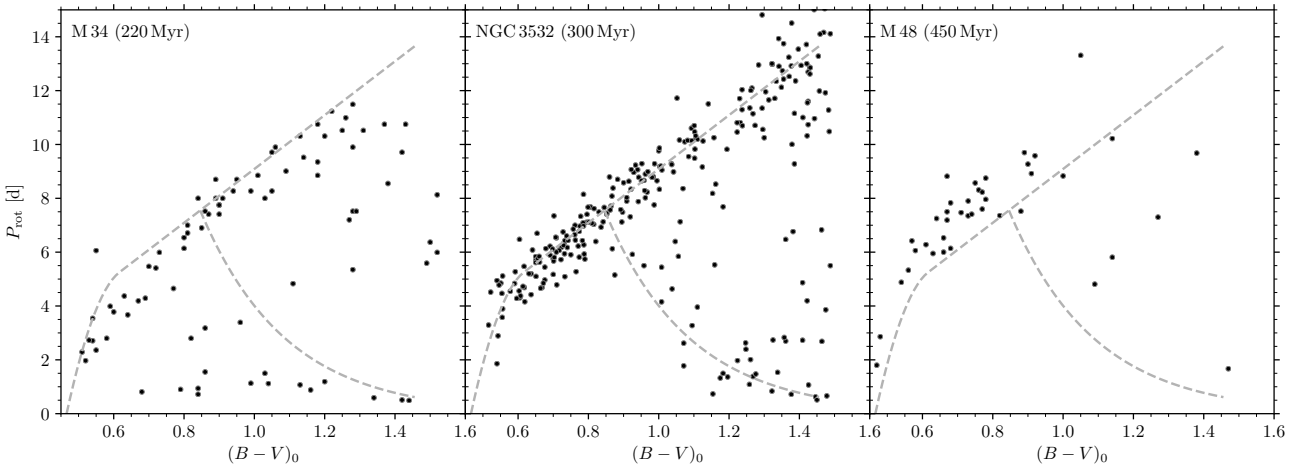

Figure 4.9: Colour-period diagrams for M 34 (Meibom et al. 2011), NGC 3532 (this work), and M 48 (Barnes et al. 2015) (from left to right) showing the period evolution in this 220 – 450 Myr age range. Fiducial lines for NGC 3532 (dashed) are reproduced in the panels for M 34 and M 48. We see that the M 34 rotation period distribution is mostly below the NGC 3532 fiducials while the M 48 distribution is above them. This informs us that M 34 is younger than NGC 3532 while M 48 is older.

mass bin sampled. We also see that the fast rotators with $(G_{\rm BP}-G_{\rm RP})_0 \leq 1.5$ have experienced very strong spin-down, while those that are redder display little, if any, spin-down.

The extended slow rotator sequence also appears to have spun down significantly, although the relatively small number of periods derived is a potential issue. We concentrate below on the traditional slow and fast rotators, and explore whether spin-down models can reproduce their evolution.

For this evolution, we apply the two spin-down prescriptions provided in Barnes (2010) (B10) and Matt et al. (2015) (M15), both of which can be implemented easily. Despite the similarity in their predictions, both models are calculated in significantly different ways. While the B10 model is formulated solely in terms of the convective turn-over timescale (which then accounts for the mass dependence of the spin-down in that model), the M15 model requires the stellar parameters from evolutionary models. Although the latter is tuned to be used with Baraffe et al. (1998), a different stellar evolution model can in principle be used, and we correspondingly apply the updated models from Baraffe et al. (2015)[12]. For both models, we use the same convective turn-over time (τ_c) as in the original works. Hence, the B10 model is calculated with Barnes & Kim (2010) and the M15 one with Cranmer & Saar (2011). (The two differ essentially by only a scaling constant.)

For simplicity, we assume in all calculations that an assigned mass or convective turn-over time is constant over time. Because most stars have already reached the main sequence by the age of our clusters, this assumption is justified. To evolve the periods, we applied to each individual

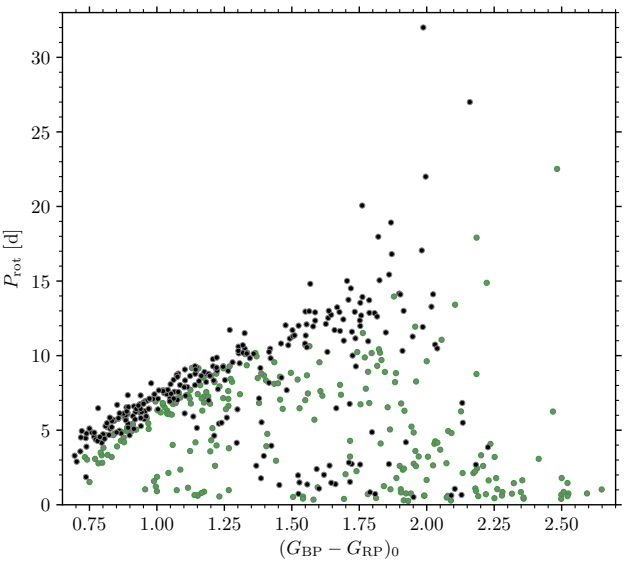

Figure 4.10: Colour-period diagram comparing NGC 2516 (green, 150 Myr, F20) with NGC 3532 (black, 300 Myr) based on *Gaia* DR2 $(G_{\rm BP}-G_{\rm RP})_0$ colour. The upward displacement of the slow rotator sequence of NGC 3532 relative to NGC 2516, as well as the dramatic evolution of its fast rotators onto the slow rotator sequence are visible well.

[12] We also tested other stellar models, finding the final results to be the same within the uncertainties.

measured period in NGC 2516 Eq. 10 from B10:

$$\frac{\mathrm{d}P_{\mathrm{rot}}}{\mathrm{d}t} = \left(\frac{k_I P_{\mathrm{rot}}}{\tau_c} + \frac{\tau_c}{k_C P_{\mathrm{rot}}} \right)^{-1} \tag{4.1}$$

(with $k_I = 452\,\mathrm{Myr\,d^{-1}}$ and $k_C = 0.646\,\mathrm{d\,Myr^{-1}}$), exactly as in B10.

For M15, we apply Eq. 14 from M15:

$$\frac{\mathrm{d}\Omega_\star}{\mathrm{d}t} = \frac{T}{I_\star} - \frac{\Omega_\star}{I_\star}\frac{\mathrm{d}I_\star}{\mathrm{d}t}, \tag{4.2}$$

where $I_\star$ is the stellar moment of inertia from a stellar model, $\Omega_\star$ is the angular rotation rate, and T is the wind torque (Eqs. 6 and 7 from M15):

$$T = \begin{cases} -T_0 \left(\frac{\tau_c}{\tau_{c,\odot}}\right)^2 \left(\frac{\Omega_\star}{\Omega_\odot}\right)^3 & \text{(unsaturated)} \\ -T_0 \chi^2 \left(\frac{\Omega_\star}{\Omega_\odot}\right) & \text{(saturated)} \end{cases} \tag{4.3}$$

with the Solar values of $\tau_{c,\odot} = 12.9\,\mathrm{d}$ and $\Omega_\odot = 2.6 \cdot 10^{-6}\,\mathrm{Hz}$. χ is the inverse solar-scaled Rossby number, with the de-saturation-limit $\chi = 10$ and

$$T_0 = 6.3 \cdot 10^{30}\,\mathrm{erg} \left(\frac{R_\star}{R_\odot}\right)^{3.1} \left(\frac{M_\star}{M_\odot}\right)^{0.5}, \tag{4.4}$$

as in Matt et al. (2019). We use a simple forward Euler method, and chose an increment of 1 Myr.

We focus first on the evolution of the slow rotators to estimate gyro-ages (= rotational ages). Later, we consider the evolution of the fast rotators, and in particular the stars in transition from fast to slow rotation.

4.6.2.1 *Slow rotators, and the gyro-age of NGC 3532*

A visual comparison of the NGC 2516 distribution evolved to an age of 300 Myr with the observed NGC 3532 distribution confirms our expectations that both rotational evolution models are over-aggressive. We therefore ask whether these models can reproduce the observed NGC 3532 distribution when the age constraint is relaxed, and if so, what the relevant age would be for each of the models. As noted before, an age-offset between the isochronal and the rotational age is not a problem per se, and could potentially be used to adjust the rate of spin-down if the evolved rotation period distribution agrees with the observations. This would tell us that the mass dependence of the spin-down formulation is still substantially correct. Hence, we seek the best-fitting age to determine this difference.

For each age step, we calculate the distance between the slow rotator sequences of the evolved distribution and the NGC 3532 observations. As defined and initially described in F20, this distance is measured for each period in the evolved data set to the closest star in the NGC 3532 observations in a normalized CPD[13].

[13] The $(V - K_s)_0$ colour index is normalized and restricted to the range of the slow rotator sequence of NGC 2516 ($1.3 < (V - K_s)_0 < 2.0$). In contrast, the rotation periods are normalized to the range of NGC 3532 within this colour range because this cluster exhibits the longer periods.

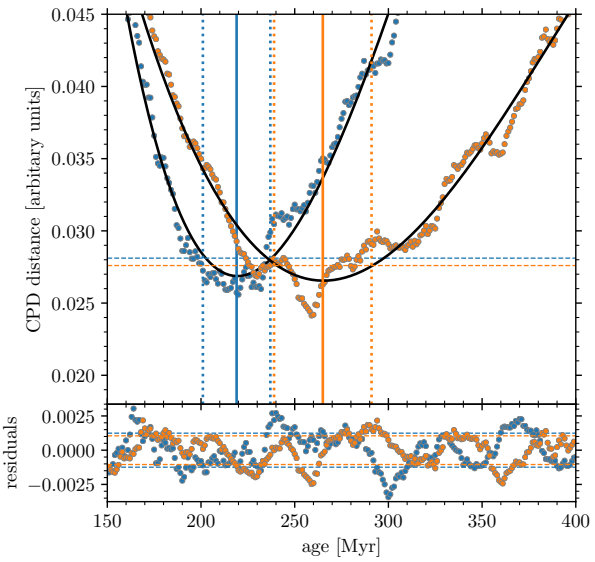

Figure 4.11: Rotational age for NGC 3532 with respect to the M15 (blue) and B10 (orange) models using the NGC 2516 rotation period observations as the starting point at 150 Myr. *Top*: Median distance between the slow rotator sequence of NGC 3532 and the evolved sequence of NGC 2516 against age. Coloured points show the measured distance and the solid black lines are the fitted polynomials. Their minima (219 Myr and 265 Myr) are marked by the solid vertical lines. The age uncertainties (18 Myr and 26 Myr) are indicated by the vertical dotted lines. The dashed horizontal line for each model marks the sum of minimum of the polynomial and the standard deviation of the residuals to illustrate the calculation of the age uncertainty. *Bottom:* Residuals of the fits with their standard deviations are marked using dashed lines.

The median value of all the individual distances is then calculated for each age step. The distribution of these median distances against the age is shown in Fig. 4.11 for both models. The distributions have very wide minima which are not clearly defined due to the scatter around the general trend. Consequently, the best age might not be found at the absolute minimum of the distribution. Therefore, we fit the data with a polynomial of fourth degree and take its minimum as our gyro-age[14].

To estimate the age uncertainties, we calculate the standard deviations of the residuals (Fig. 4.11, lower panel) and add them to the respective minimum values of the polynomial fits. The ages at which the polynomial takes these values (dotted lines in Fig. 4.11) are the lower and upper age bounds. The differences with respect to the best-fitting ages are the corresponding uncertainties.

For the B10 model, we find NGC 3532 to be 265 ± 26 Myr

[14] The apparent oscillation around the polynomial in Fig. 4.11 might be caused by the split sequence (Sect. 4.4.2).

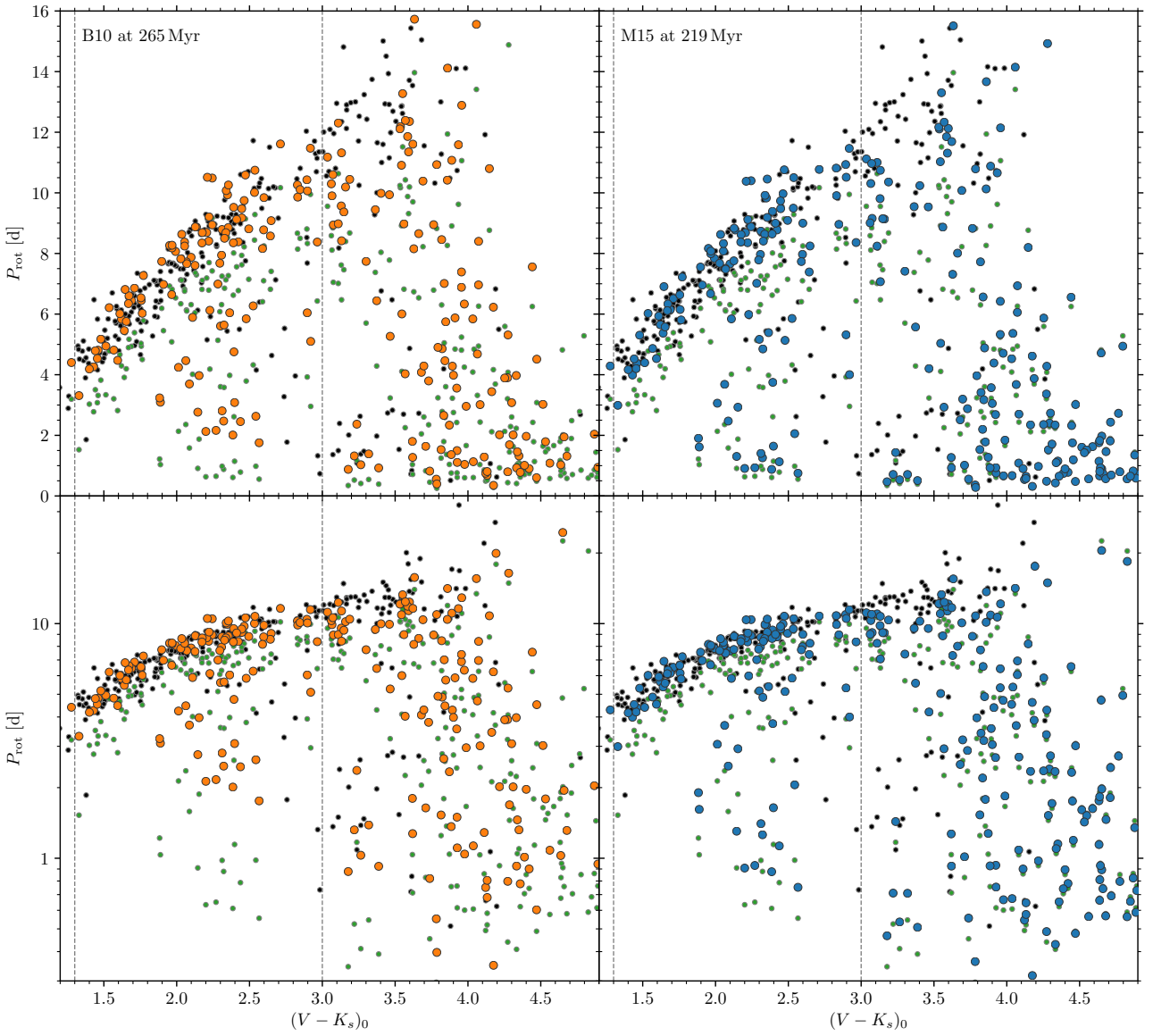

Figure 4.12: Comparison between the evolved rotation periods (orange and blue) with the observed NGC 3532 distribution (black). The starting distribution is that of NGC 2516 (green) and the models aim to match the observed NGC 3532 rotation periods. *Left:* Evolution to 265 Myr with the B10 model. We see that, although the fast rotators in the NGC 2516 distribution spin down significantly, the spin-down in the B10 model is still not aggressive enough to transform them to the fast rotator sequence of NGC 3532 or sufficiently close to it. *Right:* Evolution to 219 Myr with the M15 model. The transition from fast to slow rotation seems to be even more strongly underestimated, with the fast rotators of the NGC 2516 distribution not having evolved significantly upwards at all. We note that the lowest-mass stars of the NGC 2516 sample, which are still on the pre-main sequence, have spun up due to contraction. The vertical dashed lines in all panels indicate the colour range used to calculate the best-fitting slow rotator model. In this range both models represent the slow rotators of the target distribution equally well. The *lower* panels (logarithmic in period) feature the full period range, while the *upper* panels are restricted $P_{\rm rot} < 16$ d.

old, somewhat shy of the canonical isochrone age for the cluster, assuming 150 Myr for the age of NGC 2516. Hence, NGC 3532 is 115 Myr older than NGC 2516. For the M15 model, we find a younger rotational age of 219 ± 18 Myr. This is significantly short of the canonical isochrone age for NGC 3532, and only about the isochronal age of M 34, which we showed in Sect. 4.6.1 to be rotationally significantly younger. Hence, we can directly conclude that the spin-down for the slow rotators in both models, especially M15, is too strong, and the corresponding estimated rotational ages too young. We show the CPDs with both models in Fig. 4.12 for the corresponding best-fitting ages of 265 Myr (B10) and 219 Myr (M15).

Ignoring the absolute age differences and concentrating on the mass dependence of the spin-down, both models show good agreement between the evolved periods and the NGC 3532 slow rotator sequence. The linear shape of the slow rotator sequence also seems to be adequately reproduced. However, neither the reddest stars on the slow rotator sequence in NGC 3532 ($(V - K_s)_0 = 3 - 4$) nor the extended slow rotator sequence are reproduced by the models.

In summary, we find that the B10 and M15 models both overestimate the braking of warmer stars (the latter much more so), while simultaneously underestimating the braking of the cooler stars.

4.6.2.2 (Evolved) fast rotators: properties and problems

The strongest mismatch between the evolved periods and NGC 3532 is found among the stars in transition from fast to slow rotation. The spin-down models underestimate the braking drastically (Fig. 4.12), in contrast to the slow rotators, where the spin-down is overestimated. In order to match the observed transitional rotator periods, we would have to evolve NGC 2516 up to a model age of ~400 Myr with B10, and even more with M15.

This increase of age is of course not allowable for the other rotators of the cluster. Two consequences would follow. Firstly, stars on the slow rotator sequence would spin down to longer rotation periods than observed. Secondly, lower-mass stars, which are still on the fast rotator sequence in NGC 3532, would start to evolve off this sequence.

In particular, the latter effect highlights the mismatch between the models and observations. It is rooted in the fact that only stars from a small colour (or mass) range are observed in transition. From the CPD in Fig. 4.6, we find stars of $2.1 < (V - K_s)_0 < 3.0$ (corresponding to $0.8 \gtrsim M_\star/M_\odot \gtrsim 0.7$, Pecaut & Mamajek 2013) with $1\,\mathrm{d} < P_{\mathrm{rot}} < 7\,\mathrm{d}$ in a well correlated mass-ranked sequence, showing the sudden and rapid, yet collective transition. However, the current angular momentum models propose a more gradual evolution, as seen from the much wider colour, and yet a narrower period range of evolved fast rotators in the forward model (Fig. 4.12).

To evaluate the validity of the angular momentum models for the remaining fast rotators, we concentrate on the lower panels of Fig. 4.12, where the logarithmic scale emphasises the fast rotators. Stars still on the fast rotator sequence ($(V - K_s)_0 > 3.0$) have been spun down with the B10 model to very similar periods as observed in NGC 3532. Hence, their evolution is accurately described, and we expect the warmer fast rotators to be described correspondingly well at younger ages. In contrast, M15 barely spins down the fast rotators and the stars in transition. This effect can also be seen in Fig. 4.8 where the B10 fast rotator isochrone lies above the Amard et al. (2019) isochrone (which is an updated version of M15).

In conclusion, we have identified two main problems: 1) The transition from fast to slow rotation is occurring on timescales shorter than currently anticipated; stronger braking is needed than in the models, and 2) The mass-dependence of the transition is much steeper than in the models. However, given the stronger spin-down through the rotational gap, this issue might resolve itself because the warm end of the transition sequence reaches the slow rotator sequence earlier, and only a small fraction of stars (in a narrow mass range) is in transition at a given time.

4.6.3 Empirical insights into the transition

4.6.3.1 Evolved fast rotators: empirical constraints on the transition timescale

A short transition timescale is supported not only by the comparison with models but also by the observations from the age-ranked succession of open clusters. In Fig. 4.9, we compare NGC 3532 to the ~80 Myr younger M 34. In this open cluster, stars with $(B - V)_0 \approx 0.8$ (~$0.9 M_\odot$) are among the bluest fast rotators, while in NGC 3532 they have just arrived on the slow rotator sequence. Hence, the comparison between the two open clusters gives directly a transition time from fast to slow rotation of $\tau_{\mathrm{transition}} \approx 80$ Myr (for a $0.9 M_\odot$, K2 star).

From investigations of stars in M 34 Meibom et al. (2011) found a transition timescale of 100 Myr for early K dwarfs. This value is in good agreement with our observations. A similar transition timescale (of 80 Myr) was found by Brown (2014) from fits of his model to open cluster data, in particularly M 34.

Using this transition timescale, one finds a mean spin-down rate during the evolution from fast to slow rotation of $\Delta P/\Delta t \approx 5\,\mathrm{d}/80\,\mathrm{Myr} = 0.063\,\mathrm{d\,Myr^{-1}}$. Hence, the maximum braking rate is certainly larger. In comparison, the B10 model gives for Ro = 0.06 – the position of the rotational gap and the maximum spin-down – $\Delta P/\Delta t = 0.019\,\mathrm{d\,Myr^{-1}}$. (For M15 the spin-down rate is about the same as for B10.) In conclusion, the spin-down is apparently underestimated by a factor of at least three[15].

[15] Indeed, Meibom et al. (2011) calculated the same values for the spin-down. Yet, no theoretical work since has addressed this issue.

4.6.3.2 *Evolved fast rotators: Properties of the transition*

The transition from fast to slow rotation is determined not only by the transition time but also the astrophysical properties that initiate it. Currently, two main ideas have been proposed. In the deterministic approach, the fast rotators spin down magnetically (with a low braking efficiency) until they attain a certain Rossby number (e.g. Barnes 2003, Barnes 2010, Matt et al. 2015). At this critical point, the rotation and stellar activity desaturate, meaning either the magnetic field configuration (Barnes 2003; Garraffo et al. 2018) or properties which determine the torque (Shoda et al. 2020) become (strongly) dependent on the rotation rate. The probabilistic idea (Brown 2014) replaces the gradual approach into the desaturated regime with a probabilistic transition towards stronger spin-down.

Our well-defined transition sequence can help to discriminate between the two possibilities. A gradual and common approach of all stars towards the threshold rotation rate would result in a well-defined lower limit of the transition sequence. In contrast, a probabilistic regime change would cause a wide spread in periods at a constant colour. The period spread of the transition sequence (at a fixed colour) is certainly larger than observed on the slow rotator sequence. However, it represents the initial period spread of the fast rotator sequence which is, in relative numbers, much larger than in the slow rotator sequence. Additionally, the sequence is sheared in period direction because of the different braking efficiencies over the whole period range. The lower boundary is relatively smooth, favouring a deterministic transition. In conclusion, the tight colour correlation among the stars in transition indicates a deterministic, rather than a probabilistic, regime change. Still, our observations do not answer the question of why the transition is deterministic.

4.6.3.3 *Extended slow rotator sequence: Same spin-down rate as warmer stars*

The final feature we investigate is the extended slow rotator sequence which is the continuation of the slow rotator sequence into the M dwarf regime, with rotation periods up to 32 d in NGC 3532. In Fig. 4.13, we show the portion of the CPD with this sequence. It includes all three clusters with known extended slow rotator sequences: NGC 2516 (F20), the Pleiades (Rebull et al. 2016), and NGC 3532. Our identification of the extended slow rotator sequence in NGC 3532 allows us to make the first assessment of the evolution of such stars between ~150 Myr and 300 Myr. From the CPD in Fig.4.13, it becomes clear that these stars actually spin down in that time interval. This evidently occurs despite the fact that many of them are on the pre-main sequence at the age of NGC 2516, and hence still contracting. Additionally, the extended slow rotator sequence may actually consist of multiple populations.

In order to investigate the spin-down, we show lines of equal Rossby number in Fig. 4.13. The Rossby number, being a mass-normalized rotation period, provides insight onto the rotational state of the stars. Hence, stars connected by these lines can be considered equivalent in the rotational sense. Indeed, they tell us that the extended slow rotator sequence consists of true slow rotators with Ro $\approx$ 0.12 (similar to their higher mass counterparts) and a group of stars in the rotational gap (Ro = 0.06) in transition to the slow rotator sequence.

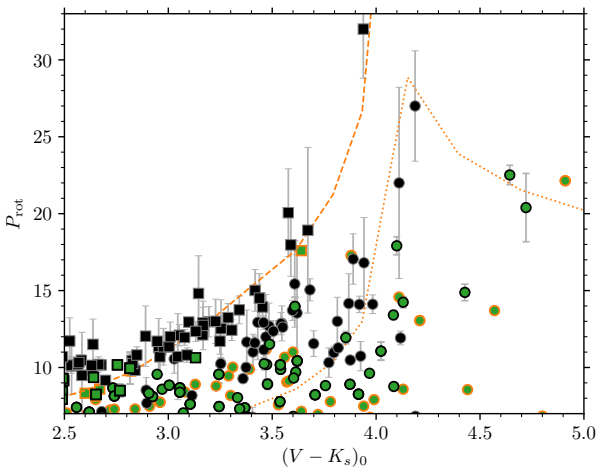

Figure 4.13: Positions of the extended slow rotator sequences of NGC 3532 (black) and the coeval Pleiades and NGC 2516 (green). Both sequences consist of true slow rotators (squares) and gap stars (circles) meaning that each sequence consists of two populations: true slow rotators, and stars still in transition. The orange lines are lines of equal Rossby number and describe the position and rotational state of the two populations in the CPD. The dotted line shows Ro = 0.06 and describes the position of the rotational gap in Barnes (2010). The orange dashed line is at Ro = 0.12, approximately the Rossby number representing the slow rotator sequence in NGC 3532.

To estimate the spin down from between the age of the Pleiades and NGC 3532, we have to assume that we observe the same groups in both open clusters. For $(V-K_s)_0 \approx 4.15$, we find a large group of stars in the younger open clusters with $P_{\rm rot} \approx 15\,d$. In NGC 3532 two stars with $P_{\rm rot} \approx 25\,d$ are observed. If these two groups of stars correspond to each other at the different ages, than it follows that $\Delta P/\Delta t$ = 10 d/150 Myr = 0.067 d Myr^{-1}. Unfortunately, the higher mass stars cannot unambiguously be separated. Yet, the approximate spin down for the early M dwarfs is the same value as we find for the early K dwarfs (Sect. 4.6.3.1). Hence, we conclude that the spin down rate through the rotational gap is mass independent and only a function of the Rossby number as was proposed in B10.

4.7 Conclusions

Despite the ubiquity of fast rotators among cool stars in young open clusters, their evolution and transition to slow rotation has previously not been investigated in detail. We do this using the very rich open cluster NGC 3532, whose membership we determined carefully in our prior study, F19. In contrast to the plentiful occurrence of ZAMS clusters, NGC 3532 is uniquely aged for a local cluster, effectively probing the large changes in the rotational evolution of stars between the ZAMS, where rotation has a large spread, and 600 Myr, where rotation has mostly converged onto a single sequence of period against colour.

In this work, we have described extensive ground-based observations of the 300 Myr-old open cluster NGC 3532 with time series photometry to probe this transition. We determine 279 rotation periods for members of NGC 3532 from our photometric time series, spanning stars from late-F to early-M spectral types. These rotation periods range from 0.5 d to 32 d. While all of these are photometrically determined periods, some of these periods were identified with the help of activity measurements (described in detail in the companion paper, F21act).

The periods delineate a well-populated slow rotator sequence for FGK stars in the colour-period diagram, and a fast rotator sequence for the K dwarfs that is significantly evolved beyond that seen in ZAMS-age clusters. Among the late K and M dwarfs, we discern both a fast rotator sequence, and an extended slow rotator sequence, the counterpart of the one we (F20) identified in the ZAMS open cluster NGC 2516.

We observe a split in the slow rotator sequence itself among the warmer stars, one we trace to the single-star vs. binary star sequences in the CMD, allowing us to interpret the observed rotational split as the residual imprint of the spun-down fast rotators. In this framework, although the fast rotators spin down rapidly through the rotational gap, they appear not to have fully reached the slow rotator sequence at this age.

A comparison with the rotation period distributions of open clusters that are nearest in age, M 34 (220 Myr) and M 48 (450 Myr), shows that, as expected, the slow rotator sequence of NGC 3532 is clearly above that of the former, and below that of the latter, demonstrating that ~100 Myr age differences between young clusters are visually recognizable in colour-period diagrams. The empirical intercomparison also highlights the dramatic and mass-dependent spin-down of the fast rotators through the rotational gap.

A comparison with rotational isochrones calculated from four prominent models shows detailed issues with reproducing the observed rotational distribution of NGC 3532. The mass-dependent dispersion in rotation periods is clearly difficult to achieve, there are issues with the shape of the slow rotator sequence, and the spin-down of the slow rotators is overestimated, while that of the fast rotators is somewhat underestimated.

In an effort to understand the shortcomings of the angular momentum evolution models, we directly evolved the rotation periods of the zero-age main sequence open cluster NGC 2516 forward in time using two spin-down models, avoiding the possible influence of assumptions regarding initial conditions. These give gyro-ages for NGC 3532 of 219 ± 18 Myr (M15), and 265 ± 26 Myr (B10), short of the canonical 300 Myr age for the cluster. This confirms our prior conclusion that spin-down of slow rotators is overaggressive in rotational models.

The detailed comparison also shows that current models underestimate the spin-down of fast rotators. The observed spin-down is steeper as a function of stellar mass. Based on the comparison with the younger cluster M 34, we estimate a spin-down timescale as short as 80 Myr and a braking rate $\Delta P/\Delta t \approx 0.06\,\mathrm{d\,Myr^{-1}}$ for early K dwarf fast rotators. The shape of the sequence suggests that the transition is occurring in a deterministic, rather than a probabilistic, manner.

The sensitivity of our study to long periods enables us to identify in NGC 3532 the counterpart to the extended slow rotator sequence previously identified by F20 in NGC 2516. A similar braking rate is estimated for the slowly rotating M dwarfs, taking the age difference between the NGC 2516 and Pleiades and NGC 3532 as the baseline. The rate of spin-down through the rotational gap is apparently not a function of mass, but rather a simple function of the Rossby number, as initially proposed in Barnes (2010).

In summary, we have performed a comprehensive rotational study of the most populous available open cluster between Pleiades and Hyades age, namely NGC 3532, permitting a deeper empirical understanding of the rotational transition between fast rotation at ZAMS age and slow rotation at 600 Myr. This allows us to place strong mass-dependent constraints on the corresponding requirements for models of stellar rotational evolution.

Acknowledgements. We are obliged to the referee for a careful and helpful report. SAB acknowledges support from the Deutsche Forschungs Gemeinschaft (DFG) through project number STR645/7-1. Based in part on observations at Cerro Tololo Inter-American Observatory, National Optical Astronomy Observatory (2008A-0476; S. Barnes, SMARTS consortium through Vanderbilt University), which is operated by the Association of Universities for Research in Astronomy (AURA) under a cooperative agreement with the National Science Foundation. This research has made use of NASA's Astrophysics Data System Bibliographic Services. This research has made use of the SIMBAD database and the VizieR catalogue access tool, operated at CDS, Strasbourg, France. This research has made use of NASA's Astrophysics Data System Bibliographic Services. The Digitized Sky Survey was produced at the Space Telescope Science Institute under U.S. Government grant NAG W-2166. The images of the Digitized Sky Survey are based on photographic data obtained using the Oschin Schmidt Telescope on Palomar Mountain and the UK Schmidt Telescope. This publication makes use of data products from the Two Micron All Sky Survey, which is a joint project of the University of Massachusetts and the Infrared Processing and Analysis Center/California Institute of Technology, funded by the National Aeronautics and Space Administration and the National Science Foundation. This work has made use of data from the European Space Agency (ESA) mission *Gaia* (`https://www.cosmos.esa.int/gaia`), processed by the *Gaia* Data Processing and Analysis Consortium

(DPAC, https://www.cosmos.esa.int/web/gaia/dpac/consortium). Funding for the DPAC has been provided by national institutions, in particular the institutions participating in the *Gaia* Multilateral Agreement.
Software: DaoPhot II was kindly provided by Peter. B. Stetson. This research made use of Astropy, a community-developed core Python package for Astronomy (Astropy Collaboration et al. 2013). This work made use of Topcat (Taylor 2005) and Astrometry.net (Lang et al. 2010). This research made use of the following Python packages: Pandas (McKinney 2010); NumPy (Walt et al. 2011); MatPlotLib (Hunter 2007); IPython (Pérez & Granger 2007); SciPy (Jones et al. 2001); Scikit-learn (Pedregosa et al. 2011)

References

Amard, L. et al. 2019, A&A 631, A77
Artymowicz, P., & Lubow, S. H. 1994, ApJ 421, 651
Astropy Collaboration et al. 2013, A&A 558, A33
Baraffe, I., Chabrier, G., Allard, F., & Hauschildt, P. H. 1998, A&A 337, 403
Baraffe, I., Homeier, D., Allard, F., & Chabrier, G. 2015, A&A 577, A42
Barnes, S. A., Weingrill, J., Granzer, T., Spada, F., & Strassmeier, K. G. 2015, A&A 583, A73
Barnes, S. A. 2003, ApJ 586, 464
— 2007, ApJ 669, 1167
— 2010, ApJ 722, 222
Barnes, S. A., & Kim, Y.-C. 2010, ApJ 721, 675
Barnes, S. A., Weingrill, J., Fritzewski, D., Strassmeier, K. G., & Platais, I. 2016, ApJ 823, 16
Barnes, S. A. 1997, PhD thesis (Yale University)
Belokurov, V. et al. 2020, MNRAS 496, 1922
Brown, T. M. 2014, ApJ 789, 101
Cargile, P. A. et al. 2014, ApJ 782, 29
Casagrande, L., & VandenBerg, D. A. 2018, MNRAS 479, L102
Chaboyer, B., Demarque, P., & Pinsonneault, M. H. 1995, ApJ 441, 865
Cieza, L. A. et al. 2009, ApJ 696, L84
Clem, J. L., Landolt, A. U., Hoard, D. W., & Wachter, S. 2011, AJ 141, 115
Cohen, O., Drake, J. J., Kashyap, V. L., Sokolov, I. V., & Gombosi, T. I. 2010, ApJ 723, L64
Crane, P. C. 2001, Sol. Phys. 203, 381
Cranmer, S. R., & Saar, S. H. 2011, ApJ 741, 54
Curtis, J. L., Agüeros, M. A., Douglas, S. T., & Meibom, S. 2019, ApJ 879, 49
Delorme, P. et al. 2011, MNRAS 413, 2218
Douglas, S. T. et al. 2016, ApJ 822, 47
Douglas, S. T. et al. 2019, ApJ 879, 100
Dworetsky, M. M. 1983, MNRAS 203, 917
Evans, D. W. et al. 2018, A&A 616, A4
Fritzewski, D. J., Barnes, S. A., James, D. J., Järvinen, S. P., & Strassmeier, K. G. 2021, A&A 656, A103
Fritzewski, D. J., Barnes, S. A., James, D. J., & Strassmeier, K. G. 2020, A&A 641, A51
Fritzewski, D. J. et al. 2019, A&A 622, A110
Gaia Collaboration et al. 2018, A&A 616, A1
Garraffo, C. et al. 2018, ApJ 862, 90
Gillen, E. et al. 2020, MNRAS 492, 1008
Gregory, P. C. 1999, ApJ 520, 361
Gregory, P. C., & Loredo, T. J. 1992, ApJ 398, 146
Gruner, D., & Barnes, S. A. 2020, A&A 644, A16
Hartman, J. D., Bakos, G. Á., Kovács, G., & Noyes, R. W. 2010, MNRAS 408, 475
Hartman, J. D. et al. 2008, ApJ 675, 1254
Healy, B. F., & McCullough, P. R. 2020, ApJ 903, 99
Herbst, W., & Mundt, R. 2005, ApJ 633, 967
Hunter, J. D. 2007, Computing in Science & Engineering 9, 90
Irwin, J. et al. 2006, MNRAS 370, 954
Irwin, J. et al. 2007, MNRAS 377, 741
Irwin, J. et al. 2009, MNRAS 392, 1456
James, D. J. et al. 2010, A&A 515, A100
Johnstone, C. P. et al. 2015, ApJ 815, L12
Jones, E., Oliphant, T., Peterson, P., et al. 2001
Kawaler, S. D. 1988, ApJ 333, 236
Kovalev, M., Bergemann, M., Ting, Y.-S., & Rix, H.-W. 2019, A&A 628, A54
Kraft, R. P. 1967, ApJ 150, 551
Kron, G. E. 1947, PASP 59, 261
Lang, D., Hogg, D. W., Mierle, K., Blanton, M., & Roweis, S. 2010, AJ 137, 1782
Li, L. et al. 2020, ApJ 901, 49
Lindegren, L. et al. 2021, A&A 649, A2
Lomb, N. R. 1976, Ap&SS 39, 447
Lorenzo-Oliveira, D., Meléndez, J., Ponte, G., & Galarza, J. Y. 2020, MNRAS 495, L61
MacGregor, K. B., & Brenner, M. 1991, ApJ 376, 204
Mamajek, E. E., & Hillenbrand, L. A. 2008, ApJ 687, 1264
Mathieu, R. D. 1994, ARA&A 32, 465
Matt, S. P., Brun, A. S., Baraffe, I., Bouvier, J., & Chabrier, G. 2015, ApJ 799, L23
— 2019, ApJ 870, L27
McKinney, W. 2010, in: Proceedings of the 9th Python in Science Conference, ed. by S. van der Walt, & J. Millman, 51
Meibom, S., Mathieu, R. D., Stassun, K. G., Liebesny, P., & Saar, S. H. 2011, ApJ 733, 115
Meibom, S., Mathieu, R. D., & Stassun, K. G. 2007, ApJ 665, L155
— 2009, ApJ 695, 679
Meibom, S. et al. 2015, Nature 517, 589
Messina, S. 2019, A&A 627, A97
Pecaut, M. J., & Mamajek, E. E. 2013, ApJS 208, 9
Pedregosa, F. et al. 2011, Journal of Machine Learning Research 12, 2825
Pérez, F., & Granger, B. E. 2007, Computing in Science & Engineering 9, 21
Radick, R. R., Thompson, D. T., Lockwood, G. W., Duncan, D. K., & Baggett, W. E. 1987, ApJ 321, 459
Rebull, L. M. et al. 2016, AJ 152, 113
Rebull, L. M. et al. 2017, ApJ 839, 92

Roberts, D. H., Lehar, J., & Dreher, J. W. 1987, AJ 93, 968
Scargle, J. D. 1982, ApJ 263, 835
See, V. et al. 2019a, ApJ 886, 120
See, V. et al. 2019b, ApJ 876, 118
Shoda, M. et al. 2020, ApJ 896, 123
Skrutskie, M. F. et al. 2006, AJ 131, 1163
Skumanich, A. 1972, ApJ 171, 565
Soderblom, D. R., Stauffer, J. R., MacGregor, K. B., & Jones, B. F. 1993, ApJ 409, 624
Spada, F., & Lanzafame, A. C. 2020, A&A 636, A76
Stauffer, J. R., & Hartmann, L. W. 1987, ApJ 318, 337
Stellingwerf, R. F. 1978, ApJ 224, 953
Stetson, P. B. 1987, PASP 99, 191
— 1994, PASP 106, 250
Stetson, P. B., Bruntt, H., & Grundahl, F. 2003, PASP 115, 413
Strassmeier, K. G. 2009, A&A Rev. 17, 251
Taylor, M. B. 2005, in: Astronomical Data Analysis Software and Systems XIV, ed. by P. Shopbell, M. Britton, & R. Ebert, vol. 347, Astronomical Society of the Pacific Conference Series, 29
van Leeuwen, F., & Alphenaar, P. 1982, The Messenger 28, 15
van Leeuwen, F., Alphenaar, P., & Meys, J. J. M. 1987, A&AS 67, 483
Walt, S. van der, Colbert, S. C., & Varoquaux, G. 2011, Computing in Science & Engineering 13, 22
Zechmeister, M., & Kürster, M. 2009, A&A 496, 577

4.A Light curves

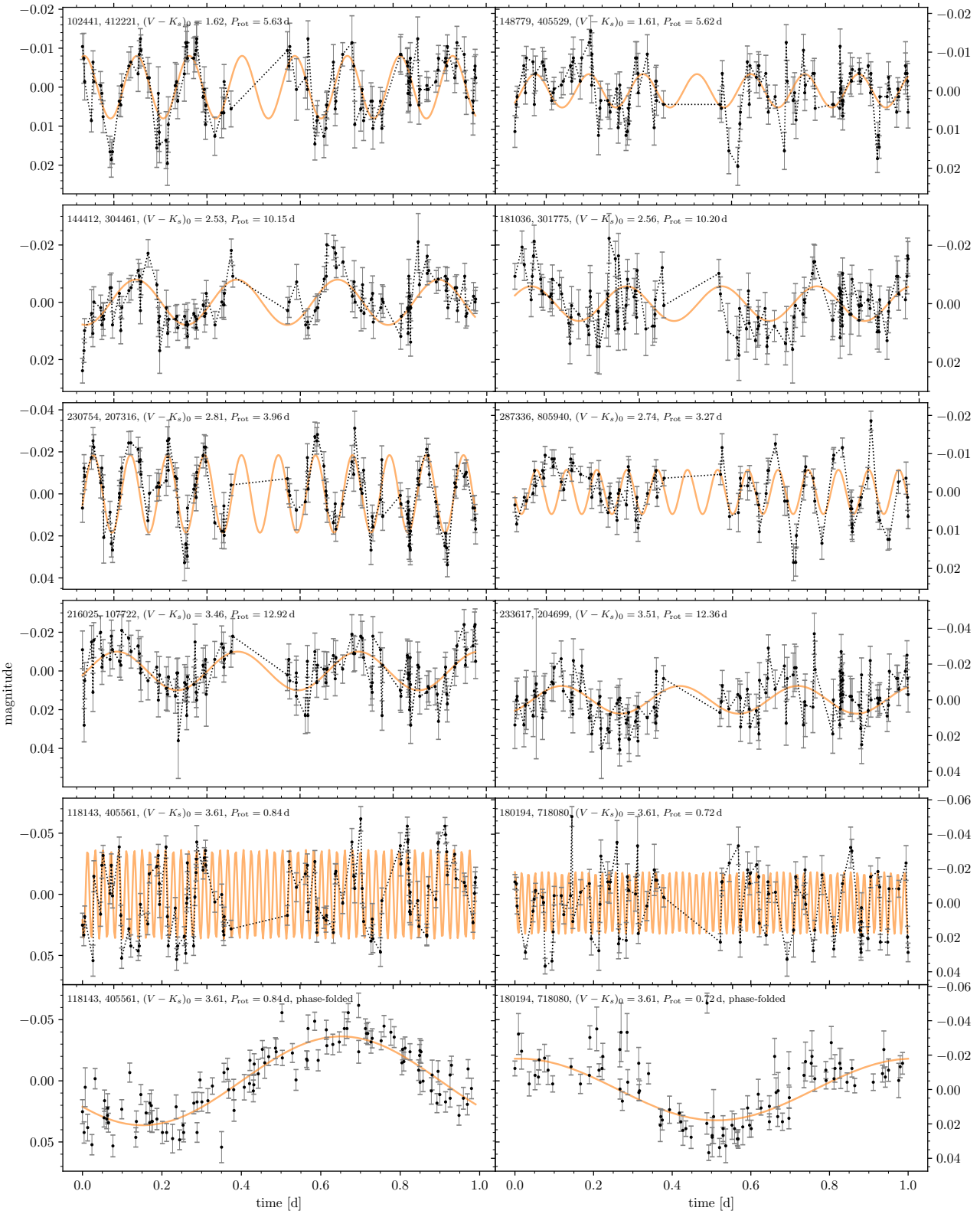

Figure 4.14: Examples of light curves with measured rotation periods. The stars are also marked in the CPD of Fig. 4.6. The *left* column shows light curves classified as first class and the *right* column the noisier algorithmic ones. The bottom row features the phase-folded light curves of the fast rotators in the row immediately above. Each light curve is over-plotted with a sine of the same periodicity as our final rotation period. The ID numbers in each panel are from Clem et al. (2011) and F19.

5

A detailed understanding of the rotation-activity relationship using the 300 Myr old open cluster NGC 3532

D. J. Fritzewski, S. A. Barnes, D. J. James, S. P. Järvinen, K. G. Strassmeier

Abstract

Context: The coeval stars of young open clusters provide insights into the formation of the rotation-activity relationship that elude studies of multi-age field populations.
Aims: We measure the chromospheric activity of cool stars in the 300 Myr old open cluster NGC 3532 in concert with their rotation periods to study the mass-dependent morphology of activity for this transitional coeval population.
Methods: Using multi-object spectra of the Ca II infrared triplet region obtained with the AAOmega spectrograph at the 4 m Anglo-Australian Telescope, we measure the chromospheric emission ratios R'_{IRT} for 454 FGKM cluster members of NGC 3532.
Results: The morphology of activity against colour appears to be a near-mirror image of the cluster's rotational behaviour. In particular, we identify a group of 'desaturated transitional rotators' that branches off from the main group of unsaturated FGK slow rotators, and from which it is separated by an 'activity gap'. The few desaturated gap stars are identical to the ones in the rotational gap. Nevertheless, the rotation-activity diagram is completely normal. In fact, the relationship is so tight that it allows us to predict rotation periods for many additional stars. We then precisely determine these periods from our photometric light curves, allowing us to construct an enhanced colour-period diagram that represents 66 % of the members in our sample. Our activity measurements show that all fast rotators of near-solar mass (F-G type) have evolved to become slow rotators, demonstrating that the absence of fast rotators in a colour-period diagram is not a detection issue but an astrophysical fact. We also identify a new population of low-activity stars among the early M dwarfs, enabling us to populate the extended slow rotator sequence in the colour-period diagram.
Conclusion: The joint analysis of chromospheric activity and photometric time series data thus enables comprehensive insights into the evolution of the rotation and activity of stars during the transitional phase between the Pleiades and Hyades ages.

This chapter was published in *Astronomy & Astrophysics* 656, A103, 2021, reproduced with permission

5.1 Introduction

The magnetic dynamo of cool stars is believed to be driven jointly by stellar rotation and convection. Although the magnetic field plays a vital role in the creation of various stellar activity phenomena, it is observationally less accessible than these phenomena. Because of this difficulty, magnetic activity is typically accessed, especially in larger samples, through certain indicators, such as 'excessive' chromospheric emission. Such emission was first observed by Eberhard & Schwarzschild (1913) in the reversal of the Ca II H and K lines in objective-prism spectra of bright stars and was immediately connected to sunspot-like features on other stars.

For the majority of stars, one observes decreasing activity with decreasing rotation rate. This correlation between the chromospheric emission and stellar rotation rate can be traced back to Kraft (1967) and Skumanich (1972) and similar studies of the time evolution of different activity tracers. Noyes et al. (1984) made an important advance, showing that the chromospheric activity of a sample of field stars is particularly well correlated with a mass-normalised version of the rotation period called the Rossby number, $\mathrm{Ro} = P_{\mathrm{rot}}/\tau_c$ (with P_{rot} representing the stellar rotation period and τ_c the convective turnover timescale). The corresponding reduction in the dimensionality of the problem[1] allows all cool stars to be considered as part of the same continuum despite differences in their evolutionary timescales. Indeed, this rotation-activity correlation has repeatedly been shown to be fundamental in understanding stellar activity. It is observed not only in chromospheric activity, but also in the coronal X-ray activity of solar-like (Pizzolato et al. 2003) and fully convective stars (Wright & Drake 2016; Newton et al. 2017).

However, the dimensional reduction at the heart of the relationship also conceals some of the underlying activity behaviours of cool stars. Certain stars could potentially be over- or under-active as compared with otherwise similar stars. Likewise, a small change in a single underlying parameter, such as mass or rotation period, could result in a substantial change in activity. Such dependences are best addressed in open clusters, where the coevality and homogeneity of the underlying population tame the parameter dependences, permitting more detailed examination than with field star samples.

A number of tracers are available for probing stellar activity in different layers of outer stellar atmospheres. In the photosphere, one observes starspots (e.g. Strassmeier 2009, Basri & Nguyen 2018) and flares (e.g. Pettersen 1989). In the chromosphere, emission in certain spectral lines (e.g. Hα, Ca II H and K, and the even bluer Mg II h and k) are tracers of heating beyond radiative equilibrium (Hall 2008). Finally, in the corona, the outer layer of the stellar atmosphere, emission in soft X-rays is the most prominent activity tracer (Schmitt 1997; Güdel 2004).

The early work of Eberhard & Schwarzschild (1913) on the Ca II H and K lines was followed up, most famously, by extensive monitoring of the chromospheric activity variability of the same lines by the Mt. Wilson survey (Wilson 1978; Baliunas et al. 1995). However, the well-known Fraunhofer H and K lines are not the only spectral lines of Ca II that are affected by chromospheric activity. In this work, we analyse the Ca II infrared triplet (IRT) lines at 8498 Å, 8542 Å, and 8662 Å.

These lines were first used by Linsky et al. (1979) to probe stellar activity because they are formed by the same upper energy level as the H and K lines (Linsky et al. 1979; Foing et al. 1989) and hence can be used in a similar manner. Their position in the near infrared (photometric I band) enables observations of cool main sequence stars, which have their peak emission in the near infrared, out to larger distances. In fact, the IRT lines have not only been used to study field stars (e.g. Linsky et al. 1979, Žerjal et al. 2013) but also stellar activity in open clusters[2].

Yamashita et al. (2020) have studied the youngest stars in open clusters and star forming regions, and have found that most of the T-Tauri stars in their sample show magnetically-induced activity similar to that seen in older stars. Marsden et al. (2009) have observed the open clusters IC 2391 and IC 2602 which host F and G type zero-age main sequence stars and pre-main sequence stars of lower mass. Soderblom et al. (1993) studied the solar-like stars in the zero-age main sequence Pleiades cluster, and Jackson & Jeffries (2010) have observed M dwarfs in NGC 2516. The oldest open cluster to date with stellar activity measured from the IRT lines is the 220 Myr-old NGC 6475 (M 7, James & Jeffries 1997). Finally, Soderblom & Mayor (1993) have measured stellar activity with the IRT lines for stars in the sparsely populated Ursa Major Moving Group. However, its age is not well-constrained (Jones et al. 2015 and references therein). In this work, we extend the age sequence with the 300 Myr-old open cluster NGC 3532, and analyse the rotation-activity connection in detail using its rich coeval population.

Yamashita et al. (2020) studied the youngest stars in open clusters and star forming regions and found that most of the T-Tauri stars in their sample show magnetically induced activity similar to that seen in older stars. Marsden et al. (2009) observed the open clusters IC 2391 and IC 2602, which host F- and G-type zero-age main sequence (ZAMS) stars and pre-main sequence stars of lower mass. Soderblom et al. (1993) studied the solar-like stars in the ZAMS Pleiades cluster, and Jackson & Jeffries (2010) observed M dwarfs in NGC 2516. The oldest open cluster to date with stellar activity measured from the IRT lines is the 220 Myr old NGC 6475 (M 7; James & Jeffries 1997). Finally, Soderblom & Mayor (1993) measured stellar activity with

[1] We mean plotting activity vs. Ro, rather than activity vs. both P_{rot} and mass or a suitable mass proxy.

[2] With the future *Gaia* DR3, many more spectra of the IRT region will become available, enabling activity studies on the Galactic scale, including on numerous open clusters.

the IRT lines for stars in the sparsely populated Ursa Major Moving Group. However, its age is not well constrained (Jones et al. 2015 and references therein). In this work we extend the age sequence with the 300 Myr old open cluster NGC 3532 and analyse the rotation-activity connection in detail using its rich coeval population.

NGC 3532 is a very populous open cluster that is potentially capable of becoming a benchmark object. It is located in Carina, at a distance of 484 pc, and is somewhat embedded in the Galactic disc. For a recent detailed overview of NGC 3532 and related work, we refer the reader to the introduction of (Fritzewski et al. 2019, hereafter F19). Our prior efforts on NGC 3532 include a spectroscopic membership study (F19) and, in a companion paper, measurements of the stellar rotation periods of its cool star members (Fritzewski et al. 2021, hereafter F21rot). Here, we present measurements of the chromospheric activity in this cluster, examine their patterns, especially with respect to the rotation periods, and use this knowledge to determine a set of activity-guided photometric rotation periods.

This paper is structured as follows. In Sect. 5.2 we present our observations, followed by the measurement of the chromospheric emission in Sect. 5.3. In Sect. 5.4 we compare the chromospheric activity to the photospheric one. Afterwards, we combine the chromospheric activity with photometric rotation periods of stars in NGC 3532 in Sect. 5.5 to study the colour-rotation-activity connection in detail. Here, we construct a colour-activity diagram (CAD) and gain insight into the rotational state of stars without photometric rotation periods. In Sect. 5.6 we construct and analyse the first rotation-activity diagram for NGC 3532. Furthermore, we derive activity-informed photometric rotation periods for members of NGC 3532. The rotational implications of these new periods are analysed in detail in the companion paper (F21rot).

5.2 Observations, data reduction, and cluster membership

5.2.1 Spectroscopy

We observed NGC 3532 with the AAOmega multi-object spectrograph on the 3.9 m Anglo-Australian Telescope (ATT) on 10 and 11 March 2017 primarily from the viewpoint of the membership study presented in F19. The spectrograph is fed by the 392-fibre 2dF fibre positioner (Lewis et al. 2002), for which we used three different fibre configurations to observe 1060 stars with the 1700D grating (R = 10 000). Two of the fibre setups targeted the brighter stars (I_c = 12 – 15) with a total exposure time of 30 min each, each split into three sub-exposures per spectrum. The final fibre configuration targeted the fainter stars (I_c = 15 – 17) and was exposed for 120 min.

The data were reduced with the 2dFr pipeline (AAO Software Team 2015, version 6.28), as described in F19; we use the final data products from that work for the present analysis. Before measuring the equivalent widths (EWs), we normalised each spectrum with a fifth-order Chebyshev polynomial. In addition to the spectra, we use the measured radial velocity shifts (in pixel) from F19.

5.2.2 Photometry

The time series photometry used in this work was obtained between 19 February 2008 and 1 April 2008 from the Cerro Tololo Inter-American Observatory (CTIO) with the Yale 1 m telescope operated by the SMARTS consortium. We observed eight different fields in NGC 3532 with three different exposure settings in both the V (120 s) and I_c (60 s and 600 s) filters. After standard data reduction, we performed point-spread function photometry with DaoPhot II. The observations, data reduction, photometry, time series analysis, and rotation period determinations are described in the companion paper (F21rot) where these observations are the centrepiece.

For the standardised photometry, we used the optical $BV(RI)_c$ cluster survey of Clem et al. (2011) (C11) and combined it with 2MASS (Skrutskie et al. 2006) K_s for the primary colour $(V - K_s)_0$ of our analysis. The photometry was de-reddened with the mean reddening towards NGC 3532 of $E_{(B-V)}$ = 0.034 mag.

5.2.3 Membership and multiplicity

The spectroscopic observations presented here were originally obtained to establish a radial velocity membership list for NGC 3532. In F19, we presented a set of 660 exclusive members of NGC 3532 based on our own observations as well as survey and literature radial velocities. Here, we analyse the stellar activity of the exclusive members within our spectroscopic dataset. In Fig. 5.1, we show the spectroscopically observed members of NGC 3532 and highlight different subsets of stars with measured rotation periods ('rotators' hereafter).

Unidentified close binaries could potentially skew our results because binarity can influence a star's magnetic and rotational history (e.g. Meibom & Mathieu 2005, Meibom et al. 2007). To assist the analysis of stellar activity and rotation, we searched for potential binaries among the cluster members in the companion paper F21rot. There, we classified cluster members as binaries if their distance to the main sequence locus is $\Delta G > 0.25$ mag (photometric criterion) or their re-normalised unit weight error (RUWE) from Gaia early data release 3 (Lindegren et al. 2021) satisfies RUWE > 1.2 (astrometric criterion, Belokurov et al. 2020). In combination, we find 151 potential binaries (22 %). These are marked in all relevant figures with squares.

5.3 Chromospheric emission measurement

Previous studies of stellar chromospheric emission in open clusters in the IRT lines (e.g. Marsden et al. 2009) used spectra of inactive stars and subtracted them from their target

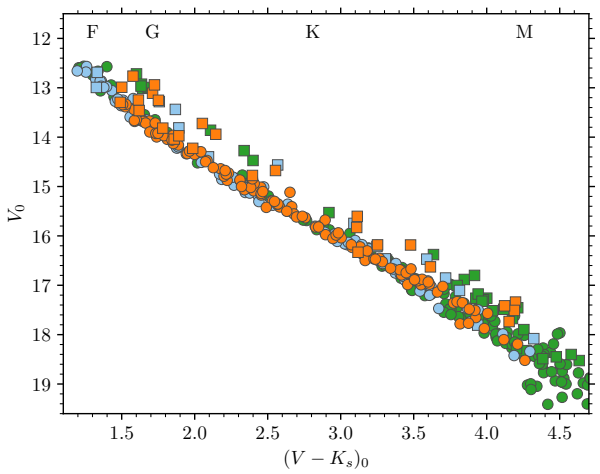

Figure 5.1: Colour-magnitude diagram of the spectroscopically observed members of NGC 3532. In orange we show the rotators from Fritzewski et al. (2021) and in light blue from this work. We were unable to determine rotation periods for stars marked in green. Single stars are indicated with circles and candidate binaries from photometry and astrometry with squares.

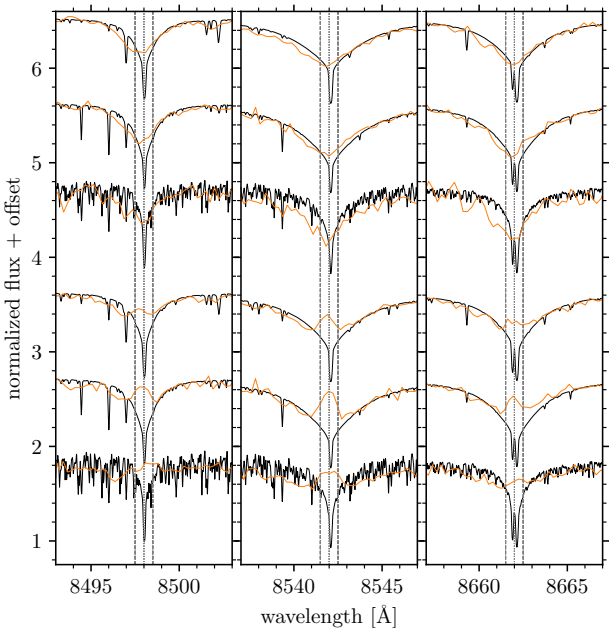

Figure 5.2: Spectral cutouts for example stars of different chromospheric activity (orange) and their corresponding Phoenix spectra. Each panel is centred on one IRT line and shifted to the rest frame. The line centre is marked with a dotted line and the limits of the 1 Å wide integration window with dashed lines. The spectra are grouped into low-activity (*top*) and high-activity stars (*bottom*). The latter feature prominent fill-ins of the line cores. Earlier spectral types are higher. The topmost spectrum is from a G2 star, and the lowest is from an M3 star. All six stars are marked with squares in the colour-activity diagram in Fig. 5.5a.

spectra to obtain the chromospheric emission. However, this approach is not possible with our dataset because the observations were initially planned as a pure membership survey without the (intentional) inclusion of inactive field stars. The number of true main sequence non-members (in radial velocity, proper motion, and parallax) is too small to build a grid of reference spectra. Stars that pass one or more of the membership criteria could still potentially be members, meaning young and active, and can certainly not be considered inactive. The empirical estimates of the basal flux of inactive stars (Busà et al. 2007; Martin et al. 2017) were also excluded because of their incompleteness with respect to our sample.

Given the lack of suitable reference spectra, we followed a different approach and measured the EW in a 1 Å-wide window in each of the three line cores without prior subtraction of a reference spectrum. We note that a similar approach is often chosen for the Ca II H and K lines (e.g. Baliunas et al. 1995) because the tight 1 Å (triangular) spectral window includes only the line core that contains the signature of the stellar activity – the chromospheric emission.

The resolution of the AAOmega spectra is too low to simply integrate over a 1 Å bandpass. Therefore, we linearly interpolated between the pixels in a 2 Å-wide window and oversampled by a factor of ten. Thereafter, we placed the 1 Å bandpass according to the stellar radial velocity shift (Fig. 5.2) and integrated over it to obtain the EW in terms of λ and the measured and continuum fluxes

$$EW = \Delta\lambda \sum_{i=0}^{n} \frac{F_i}{F_{\mathrm{cont.},i}}. \tag{5.1}$$

We defined the continuum flux $F_{\mathrm{cont.}}$ with an error-weighted least-squares linear fit to the continuum outside of the IRT lines. The fit was evaluated at the position of the integration window, creating a local pseudo-continuum. We followed the approach presented by Cenarro et al. (2001) and used their spectral windows. Cenarro et al. (2001) explain that such a fit improves the continuum determination, in particular in the near infrared with many sky lines and varying signal-to-noise ratio[3].

In contrast to the Ca II H and K lines, the Ca II IRT lines have a significant photospheric component. We are unable to remove this flux using inactive stars observed with the same instrument, as explained earlier. Hence, we measured the EW of the IRT lines in the same manner in down-sampled model spectra[4] from the Phoenix spectral library

[3] Due to the prior normalisation with polynomials, the continuum level is only marginally different from 1 in our case.

[4] The model spectra in Fig. 5.2 are displayed in full resolution to

(Husser et al. 2013). These spectra do not contain a chromospheric component. The PHOENIX EWs were linearly interpolated over the effective temperature and act as a substitute for our inactive 'reference stars'.

To connect this EW scale to our observation, we estimated the effective temperature for each spectrum of the NGC 3532 members from the relations by Mann et al. (2015) through the $(V-I_c)_0$ colour index and subtracted the photospheric flux (in EW) of the corresponding PHOENIX model from the measured EWs. The sum of the EW differences of all three lines is defined as the chromospheric emission in the IRT. It was converted to an excess flux ($F'_{\rm IRT}$) through the empirical flux scale of Hall (1996)[5]. In addition to the surface flux in the IRT, we calculated the bolometric flux $F_{\rm bol}$, assuming a black body, with the Stefan-Boltzmann law. The flux ratio in the IRT follows as (cf. Marsden et al. 2009):

$$\log R'_{\rm IRT} = \log\left(F'_{\rm IRT}/F_{\rm bol}\right) = \log F'_{\rm IRT} - (\log\sigma + 4\log T_{\rm eff})\,. \tag{5.2}$$

For each data point, we propagated the resulting uncertainty from the observations. In addition, we also include the uncertainty in the estimated effective temperature (80 K, Mann et al. 2015). When subtracting the photospheric flux, we also calculated the chromospheric emission of an 80 K warmer reference and include the difference in the uncertainty. The temperature uncertainty was also considered in the calculation of the bolometric luminosity.

In our estimate, we ignored the uncertainty associated with the Hall (1996) flux scale for two reasons. Firstly, when considering equally massive stars in the colour-activity diagram, the conversion factor from equivalent width to chromospheric flux is constant. Hence, no matter how large the uncertainty is, the scatter among the sequence is determined by the measurement of the EW and the intrinsic spread. Secondly, we do not find evidence in either the colour-activity diagram or the rotation-activity diagram that the observed spread is an effect of the flux conversion. Hence, we conclude that the uncertainty estimated by Hall (1996) is too large[6] and can even be ignored in the case of a coeval group, such as an open cluster[7]. The IRT excess-EW, the corresponding flux $F'_{\rm IRT}$, and the chromospheric emission ratio $\log R'_{\rm IRT}$, including their respective uncertainties, are provided in Table 5.1.

Among the spectroscopically observed stars in the AAO campaign, we find 454 radial velocity members. For each spectrum, we are able to measure the chromospheric emission, providing one of the largest sets of chromospheric activity measurements in any open cluster to date[8]. Out of these 454 stars, 387 stars fall within the field of our photometry, meaning that we have light curves for them. We were able to obtain photometric rotation periods for 142 of them, as described exhaustively in the companion paper F21rot.

These periods enable us to probe the rotation-activity relation in this 300 Myr old population and to understand the connection between rotation and activity in a mass-dependent manner. Furthermore, we are able to increase the number of photometric rotation periods through an activity-informed search in the time series data among the 245 (= 387 − 142) remaining stars with light curves but without directly measured prior periods. Prior to these analyses (Sect. 5.5 & 5.6), we use the light curves of all stars in the spectroscopic sample to probe the connection between photospheric and chromospheric activity.

5.4 Chromospheric against photospheric activity

5.4.1 Photospheric activity

Stellar activity manifests itself in various forms and can be observed in all layers of the stellar atmosphere. In the photospheric layer, starspots are a widely observed magnetic feature of solar-type stars (e.g. Strassmeier 2009), and are often probed using photometric time series observations. The simplest measure of such photospheric activity is the variability amplitude of the light curve, which we can obtain from our own photometric time series. We use the difference between the fifth and the ninety-fifth percentile of the sigma-clipped light curve (Basri et al. 2011). We note that a similar measure is called $R_{\rm rng}$ in Basri et al. (2011) and measured as a flux difference. In our work we measure it as a magnitude difference and hence call it $V_{\rm P95}$ to indicate the difference[9].

Because the variability amplitude is a proxy for the photospheric stellar activity, it appears to have similar dependences on stellar rotation and magnetic field as chromospheric and coronal activity measures. The left panel in Fig. 5.3 shows the variability amplitude against the intrinsic colour for NGC 3532. (We note that the $(V-K_s)_0$ colour of a Sun-like G2 star is approximately 1.5.) We removed the bluest stars of our sample because they are overexposed. In data optimised for such stars, the activity is observed to be low, in keeping with the thinning of convection zones as the Kraft break is approached. In contrast, the higher variability among the lowest-mass stars is intrinsic, and an expression of their faster rotation.

give the reader a sense of the spectral features; for all calculations, the spectra have been resampled to the resolution of the observed spectra.

[5] The more accurate empirical flux scale by Lorenzo-Oliveira et al. (2016) is optimised for solar-mass stars and is unfortunately not established for M dwarfs.

[6] This is also seen in the good agreement between Hall (1996) and Lorenzo-Oliveira et al. (2016).

[7] This is unlikely to be the case when studying field stars because two stars of the same mass can have widely different rotational and activity properties.

[8] The largest set we found in the literature contains 516 members of Praesepe for which Douglas et al. (2014) measured the chromospheric activity in Hα.

[9] In practice, both versions are nearly identical and can be used in a direct comparison.

Table 5.1: Chromospheric activity measurements, including uncertainties and auxiliary data, for members of NGC 3532. The full table is available online.

RAJ2000 (deg)	DEJ2000 (deg)	C11	$(V-K_s)_0$ (mag)	$T_{\rm eff}$ (K)	excess EW (Å)	ΔEW (Å)	$F'_{\rm IRT}$ (10^6 erg s^{-1} cm^{-2})	$\Delta F'_{\rm IRT}$ (10^6 erg s^{-1} cm^{-2})	$\log R'_{\rm IRT}$	$\Delta \log R'_{\rm IRT}$	$P_{\rm rot}$ (d)	$\Delta P_{\rm rot}$ (d)	Ro	ΔRo
167.39084	-58.49086	5654	4.711	3454	0.4	0.14	5.8382	0.00031	-4.068	0.071	…	…	…	…
167.37893	-58.34141	6980	4.039	3748	1.2	0.04	6.4094	0.00002	-3.639	0.027	…	…	…	…
167.39199	-59.16781	8911	4.000	3750	1.1	0.05	6.3632	0.00001	-3.687	0.029	…	…	…	…
167.37271	-58.69355	9857	3.462	4061	0.5	0.06	6.0964	0.00002	-4.092	0.037	…	…	…	…
167.35756	-58.58843	11976	2.326	5028	1.2	0.01	6.7122	0.00002	-3.847	0.011	…	…	…	…
167.35757	-58.89454	13437	4.171	3688	0.3	0.16	5.7948	0.00012	-4.226	0.079	…	…	…	…
167.35080	-58.72758	13824	1.876	5379	0.5	0.02	6.4335	0.00001	-4.243	0.014	6.40	0.96	0.1421	0.0228
167.33891	-58.81675	16353	3.374	4094	0.7	0.04	6.2720	0.00001	-3.930	0.025	10.00	0.29	0.0943	0.0066
167.32970	-58.63617	17130	3.982	3712	0.7	0.07	6.1779	0.00004	-3.854	0.040	…	…	…	…
…														

Notes. *C11*: ID from Clem et al. (2011); $(V-K_s)_0$ with V from Clem et al. (2011) and K_s from 2MASS, de-reddened with $E_{(B-V)} = 0.034$ mag; $T_{\rm eff}$ estimated from $(V-I_c)_0$ with Mann et al. (2015); $P_{\rm rot}$ from the companion paper and this work; $Ro = P_{\rm rot}/\tau$ with τ from Barnes & Kim (2010).

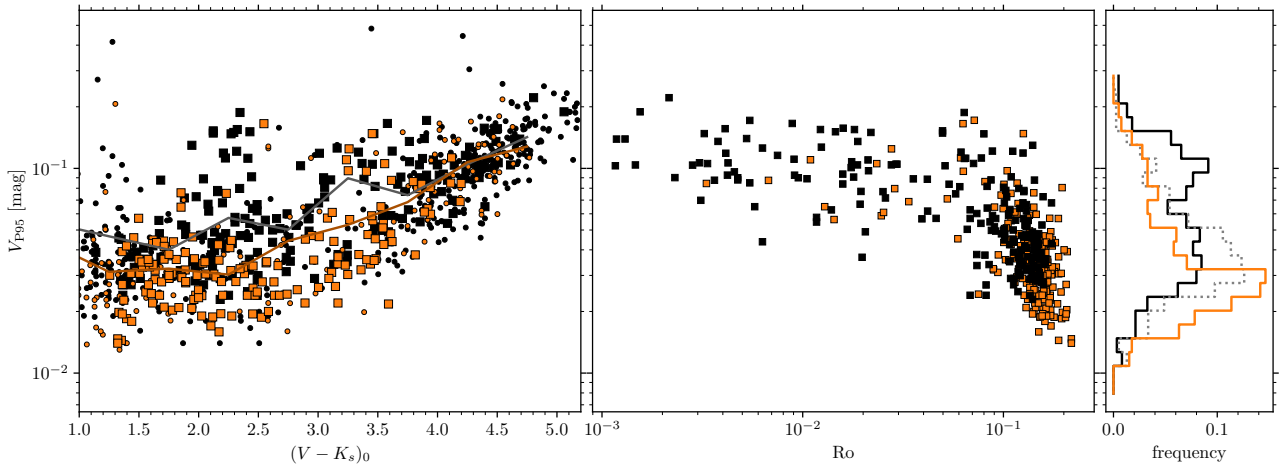

Figure 5.3: *Left:* V band variability amplitude ($V_{\rm P95}$) for stars in NGC 3532 (orange), compared with those of the zero-age main sequence open cluster NGC 2516 (black) for both stars with periods (squares) and those without (circles). Stars in NGC 3532 generally have lower variability, as seen by the mean amplitudes expressed by the solid lines. *Centre:* $V_{\rm P90}$ against Rossby number Ro for the rotators in NGC 3532 and NGC 2516. The distribution can be seen to resemble the activity-rotation relation previously known from chromospheric and coronal activity, and it shows that the photospheric activity amplitude has a similar structure. *Right:* Histogram of the variability amplitudes for the members of the two open clusters, showing that the high-amplitude stars of NGC 3532 are far less numerous in comparison with those of NGC 2516. The dotted grey histogram is restricted to NGC 2516 stars with $(V-K_s)_0 < 4$ and confirms that the high-amplitude peak in NGC 2516 is mostly attributed to the fast-rotating M dwarf members, a population absent from our NGC 3532 data.

For comparison, we added the variability amplitudes of members in the 150 Myr-old (ZAMS) open cluster NGC 2516 (F20) and show the mean amplitude in 0.5 mag-wide colour bins. We find that the NGC 2516 stars generally have higher photospheric activity levels as compared with stars in NGC 3532 except for the very variable M dwarfs, where no difference is perceptible. This shift towards lower variability and activity with increasing age is expected from the stellar spin-down over time and the corresponding decrease of the magnetic field strength.

Indeed, the lower activity of stars in NGC 3532 is exclusively driven by the slow rotators, as can be clearly seen in the central panel of Fig. 5.3. Here, we show the variability against the Rossby number for the periodic rotators in both open clusters. This diagram resembles the well-known rotation-activity correlation from Ca II H and K chromospheric- and coronal activity (e.g. Noyes et al. 1984, Pizzolato et al. 2003). The stars with the highest variability amplitudes are found in a flat region among the fastest rotators in a mass-independent way – the saturated regime. In this regime, no difference between stars in NGC 2516 and NGC 3532 is observed, with stars from both clusters occupying the same elevated region across a wide swath in Rossby number. The situation is different in the regime of larger Rossby numbers (Ro $\gtrsim$ 0.06), where the variability amplitudes are well correlated with the Rossby number, a behaviour seen in other activity indicators such as coronal X-rays. This diagram clearly shows that the lower photometric variability of stars in NGC 3532 is a function of the Rossby number and therefore a sign of the slower rotation compared to NGC 2516.

The lower overall variability can also be seen in the histogram in the rightmost panel of Fig. 5.3. The distribution for NGC 3532 has the majority of stars between 14 mmag and 40 mmag (median amplitude 32 mmag), with a single-peaked distribution. For the younger NGC 2516, in contrast, we find a double-peaked distribution between 20 mag and 120 mmag (median 67 mmag). The double-peaked structure can be traced to the prevalence of many fast-rotating M dwarfs in NGC 2516. If we restrict the colour range to $(V - K_s)_0 < 4$ (thereby removing the M dwarfs), the peak at the higher amplitudes disappears. However, even in this restricted sample the median amplitude for NGC 2516 is higher than that for NGC 3532.

5.4.2 Connection between photospheric and chromospheric activity

Because the photospheric activity shows the same structure as is observed in chromospheric activity, we expect the two to be correlated. In Fig. 5.4, we therefore show the photometric variability amplitude in the V band $V_{\mathrm{P90,V}}$ against the chromospheric emission ratio $\log R'_{\mathrm{IRT}}$. A clear trend (correlation coefficient $r = 0.665$) is visible in this comparison, with higher photometric variability visible at higher chromospheric flux. The large scatter in the trend

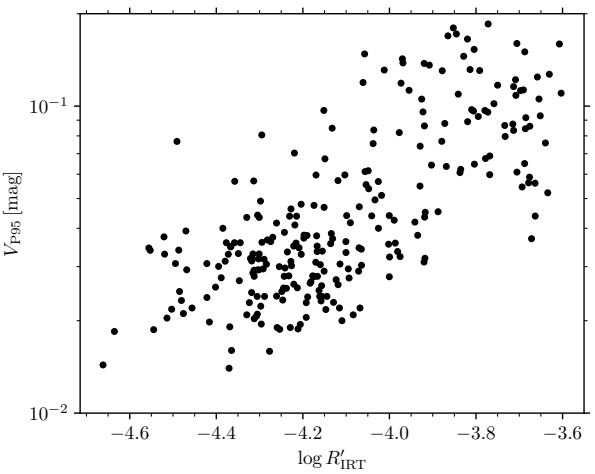

Figure 5.4: Photometric variability amplitude in the V band V_{P95} against chromospheric emission ratio $\log R'_{\mathrm{IRT}}$. The two activity indicators are correlated and represent two facets of the underlying magnetic activity.

can potentially be traced to short-term activity observed in the light curves[10]. Additionally, the inclination angle is expected to influence the variability amplitude. We note that the spectroscopic and photometric data are not even nearly contemporaneous, but were obtained nine years apart. Despite this significant time difference, the chromospheric and photospheric activity are well correlated, not unexpected because of the underlying common origin – the stellar magnetic field and the stellar rotation, both of which evolve on much longer timescales.

In related work, Zhang et al. (2020) have compared variability amplitudes of stars in the *Kepler* field to their Ca H and K chromospheric emission. They found similar results but were able to compare stars of different spectral types because their sample includes stars of various activity levels caused by the inhomogeneous stellar ages in the *Kepler* field. This kind of comparison is not possible in our coeval dataset because all F and G dwarfs have very similar chromospheric activity. Radick et al. (2018) found a similar correlation between chromospheric activity and photometric activity for young and active stars. Other work on the temporal correlation between photospheric and chromospheric activity found anti-correlations (Morris et al. 2018) and a comparison between two chromospheric activity indicators found a correlation only for very active stars (Rauscher & Marcy 2006).

5.5 Chromospheric activity and stellar rotation in the colour-activity diagram

Because chromospheric activity is closely linked to the stellar rotation rate, we study both properties jointly in Fig. 5.5

[10] A longer baseline timescale could reduce this scatter.

to emphasise this connection. Our large number of measurements and our provision of rotation periods (instead of $v \sin i$ measurements) will be seen to allow more detailed connections between IRT activity and the relevant quantities than was possible in the most notable prior cluster studies to date, those of the Pleiades (Soderblom et al. 1993) and NGC 6475 (James & Jeffries 1997).

In panel a, we display the measured activity $\log R'_{\rm IRT}$ against the intrinsic $(V - K_s)_0$ colour to investigate its mass dependence[11]. The second diagram in panel b features the colour-period diagram (CPD) from the companion rotational study. The final panel c shows the rotation-activity diagram for NGC 3532[12]. Stars with common features in panel b have been grouped together and colour-coded so that their locations in all three panels can be recognised. This enables the detailed analysis of the rotation-activity connection even in the colour-activity diagram (CAD), which otherwise does not contain the rotational information.

The CAD in Fig. 5.5a is analogous to a colour-magnitude diagram (CMD) or a CPD, and it shows the chromospheric emission ratio against the intrinsic colour. Our CAD also contains a large number of NGC 3532 cluster members for which we were unable to derive rotation periods (unfilled symbols). As in a CMD or CPD the (main sequence) open cluster members form narrow bands in the CAD, but notably, what was previously believed to constitute a 'dispersion' in activity values here appears to resolve into distinct sequences and gaps that mirror the behaviour in the CPD. The most prominent of these sequences runs diagonally in the CAD from low stellar activity levels in the warmest (F) stars to high levels among the M dwarfs. From this main feature a branch of higher-activity stars splits off at $(V - K_s)_0 \approx 2.1$. At the red end of the CAD, among the lowest-mass stars, we observe a large spread in the activity levels. A similar spread is observed in the stellar rotation periods. We discuss each group of stars separately below.

5.5.1 Unsaturated slow rotators

With the help of the colour-coding, the main feature in the CAD can easily be associated with the slow rotator sequence in the CPD (Fig. 5.5b). There is a very well-defined sequence of FGK dwarfs with $\log R'_{\rm IRT} \lesssim -4.1$ in the CAD that mirrors the clean slow rotator sequence of such stars in the CPD (dark grey). We therefore call these stars the 'unsaturated slow rotators' (USRs). It is strengthened considerably by additional stars for which we have been unable to derive rotation periods (open symbols). In agreement with prior work on the rotation-activity connection, the slow rotators clearly correspond to the lowest-activity stars in each mass bin in the open cluster. In keeping with this idea, we identify the M dwarfs with $\log R'_{\rm IRT} \lesssim -4.2$ as the continuation of the sequence of unsaturated stars. These will be found later to lie on the extended slow rotator sequence in the CPD. At this stage, the classification of the M dwarfs marked in purple is ambiguous. We discuss them separately below, and argue below that they should not be considered as USRs because of their increased activity (although short of saturation level) and shorter rotation periods. We refer to them here as 'desaturated slow M dwarfs' (DSMs). The significantly lower activity of the warmest (F and G) stars relative to the K dwarfs, is also unsurprising because they have far shallower surface convection zones.

Three stars (C11: 70134, 72069, 121200, marked with black diamonds in Fig. 5.5a.) fall below the well-defined unsaturated sequence. Given the correlation between rotation and activity, those stars might be expected to rotate much slower than other equally massive stars in the cluster, implying that they are likely field stars of an older age. However, all three stars are bona fide cluster members in radial velocity, proper motion, parallax, and photometry. Unfortunately, their light curves and periodograms are too noisy to determine their photometric rotation periods.

We find only one star with an elevated activity level ($\log R'_{\rm IRT} = -4.1$ at $(V - K_s)_0 = 1.7$) that places it above this well-defined sequence for the F and G dwarfs in the CAD. Our measured rotation period, however, places it in agreement with the other slow rotator stars in the CPD (rather than much faster, for instance). This star is a photometric binary, and it is possible that binary-induced activity is responsible for its elevated position in the CAD. Alternatively, we could have captured it by pure chance during a phase of increased stellar activity.

5.5.2 Desaturated transitional rotators and activity gap

We have identified an unexpectedly tight sequence of G-K stars with activity above the USR level, but below the saturated level. As can be seen from Fig. 5.5a, near $(V - K_s)_0 \gtrsim 2.0$, $\log R'_{\rm IRT} \gtrsim -4.1$ a branch of higher-activity stars emerges from the unsaturated sequence. Cross-comparison of this higher-activity branch with the CPD reveals these stars to be associated with the stars in transition from fast to slow rotation (marked in orange). In fact, the association is one-to-one for stars with measured rotation periods. This branch of higher-activity stars reaches the saturation level[13] at $(V - K_s)_0 \approx 3.0$, at which point all of its stars are classified as fast rotators (light grey) in the CPD. We propose the name 'desaturated transitional rotators' (DTRs) to capture their transitional rotation-activity behaviour. There are four binaries (squares) in this group, but the majority (seven) of these stars show no evidence of binarity (circles).

In the gap between the two sequences in the CAD discussed above, we find a small number of stars (marked

[11] Readers might consider comparing this with the CAD in Fig. 5 of James & Jeffries 1997, which shows a similar, but noisier, correlation.

[12] A suitable prior comparison for this panel is Fig. 19 of Soderblom et al. (1993).

[13] The saturation observed in the chromospheric emission is the same as observed in the coronal X-ray emission.

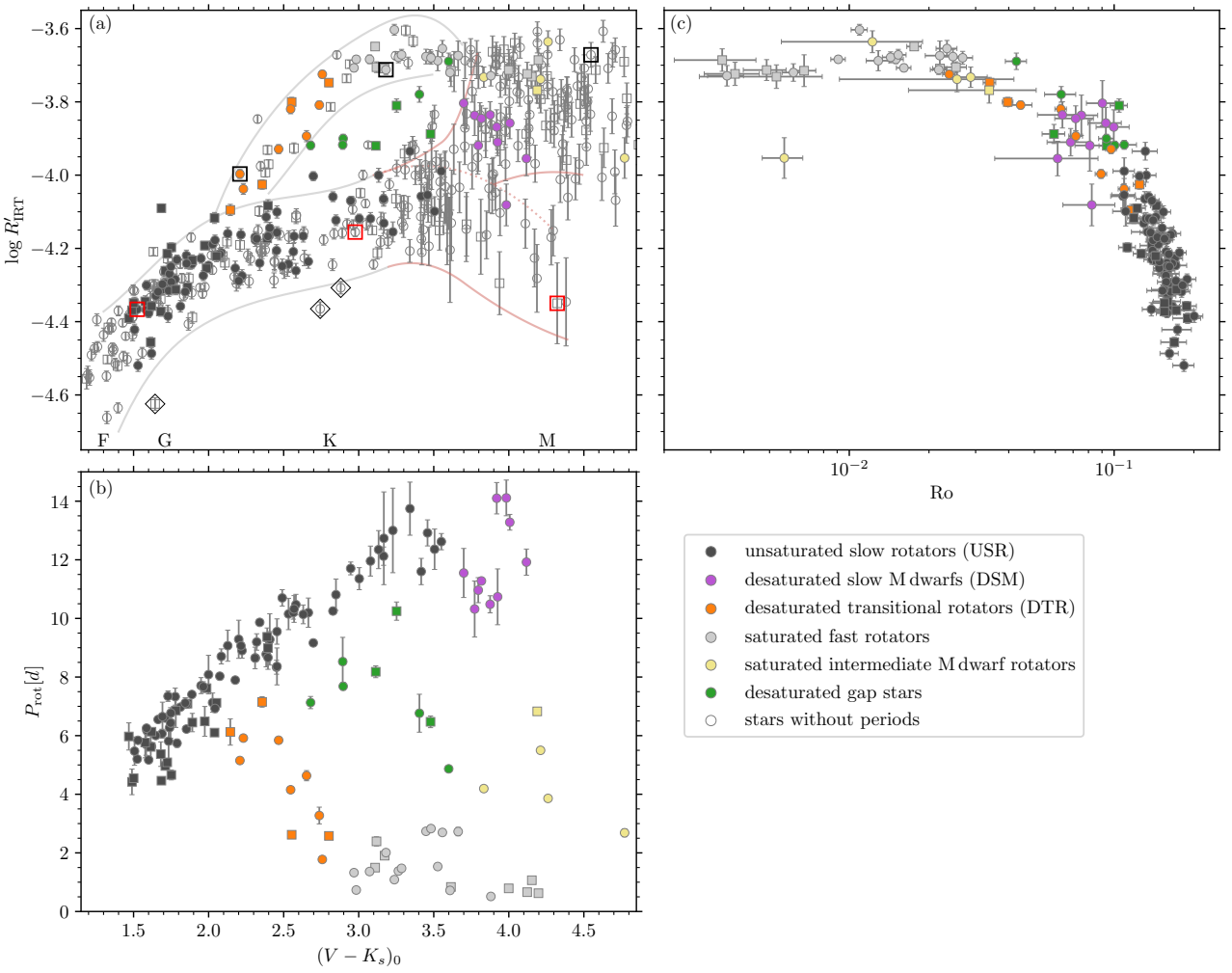

Figure 5.5: Interconnection between chromospheric activity, rotation, and mass. The colour-activity diagram (*a*) connects the colour-period diagram (*b*) with the rotation-activity diagram (*c*). *(a)*: Chromospheric emission ratio log $R'_{\rm IRT}$ against intrinsic $(V - K_s)_0$ colour for members of NGC 3532. Member stars with measured rotation periods are shown with filled symbols and those without photometric rotation periods with open symbols. Likely binaries are indicated with squares, whereas single stars are marked with circles. The majority of the data points delineate very clear sequences, indicating the cohesion of chromospheric activity evolution within the coeval stars of an open cluster. The colour coding of the different groups is indicated in the legend on the lower right and is the same in all three panels. The thin lines indicate the sequences described in the text. The stars emboxed in red and black squares are the low-activity and high-activity stars, respectively, shown in Fig. 5.2 (top to bottom in Fig. 5.2 corresponds to left to right in this figure). The bluest of these stars has roughly the Solar colour. Stars marked by diamonds are outliers (discussed in the text). *(b)*: Colour-period diagram of NGC 3532, with groups of stars distinguished by colour. This diagram is nearly a mirror image of the colour-activity diagram, with higher-activity stars being clearly mapped one-to-one onto the faster rotators. *(c)*: Corresponding rotation-activity diagram, showing the chromospheric emission ratio against the Rossby number *Ro*. The rotation-activity diagram is remarkably clean despite the diversity in chromospheric activity.

in green) that correspond exactly to the stars in the rotational gap of NGC 3532. With this knowledge, we can clearly define the rotational gap in the CPD separating the sequences. In fact, the correspondence with the CPD, where these stars are in transition from fast to slow rotation, tells us that these stars in the CAD are in transition from the high-activity branch to the low-activity one. In keeping with prior terminology for the rotational gap, and also to reflect the intermediate activity level of these stars, we refer to them as 'desaturated gap stars'.

We note that the DTRs have a higher binarity fraction compared to USRs of the same colour. Yet, as the rotational analysis in the companion paper shows, these stars do not spin faster due to binary tidal interactions (as for example in Praesepe; Douglas et al. 2019) but are the remainder of the initial fast rotators that emerge from the star formation process. In the companion paper (F21rot), we interpret the higher binarity fraction among the fast rotators with the shorter disc lifetime in binary systems. Even so, only a minority of the DTRs show any sign of binarity, and the higher activity with faster rotation appears not to be directly caused by binarity.

The absence of additional (elevated) stars bluewards of the transitional DTR sequence in the CAD (orange) is also notable, and very important in understanding angular momentum evolution because it clearly shows that even stars without determined photometric rotation periods fall onto the low activity and slow rotator branch in this colour range. Conversely, this correspondence assures us that all fast rotators down to a certain mass limit have already transitioned to the slow rotation phase. The lack of fast-rotating stars in the CPD for solar-mass stars is therefore astrophysical, and not an observational bias caused by small variability amplitudes.

Given the accurate correspondence between the CAD and the CPD, the branching-off point of the DTRs could potentially be used to age-rank young open clusters with high relative sensitivity. As shown in the companion rotational study, the transition from fast- to slow rotation happens on short timescales (tens of megayears), and hence is very age-sensitive. Using a CAD would correspondingly allow potentially accurate age-ranking to be obtained from a single multi-object spectroscopic observation[14], rather than a time series, as needed for photometric rotation periods.

5.5.3 Diversity in activity of low-mass stars

As one approaches the lower-mass stars towards late K and early M dwarfs ($(V - K_s)_0 \gtrsim 3.2$), the activity of the stars is more diverse, and the structure of the CAD becomes correspondingly more complicated. The diversity is not related to multiplicity as seen from Fig. 5.5(a) where the fraction of likely binaries in this regime is seen to be comparable to the USRs. We discuss this mass regime (indicated by the red outlines in Fig. 5.5a) sequentially from high to low activity.

At the top of the CAD, in the saturated regime ($\log R'_{\rm IRT} > -3.8$), we find two corresponding groups in the CPD: the fast rotators (light grey) and a group of stars rotating slightly more slowly (yellow). Despite the latter stars rotating more slowly than the former, their chromospheric activity is still saturated. The large number of M dwarfs with saturated activity and as yet undetected periods must therefore all belong to one of these two groups. We infer that we likely did not have the photon sensitivity to directly detect periods for them.

In a band with $-3.8 > \log R'_{\rm IRT} > -4.0$, we find a group of lower-activity stars that are also significantly slower rotators than the saturated activity ones. These are grouped tightly together in both the CAD and the CPD, where they are marked in purple. We call these the 'desaturated slow M dwarfs' (DSMs) to reflect both their reduced activity levels as compared to their saturated counterparts, and their location in the CPD, near the slow rotator sequence, if not quite on it. Because of these joint intermediate behaviours, we suggest that these stars are distinct from the low-activity M dwarfs (discussed immediately below), and that they should not be considered as a continuation of the USR sequence in the CAD. That continuation instead is provided by the sizeable group of low-activity M dwarfs below them in the CAD.

Finally, we find a group of M dwarfs with $\log R'_{\rm IRT} < -4.0$. They form a sequence of declining activity with declining mass (below the red dotted line). This sequence connects smoothly to the USRs (dark grey), and we identify these stars as the continuation of the USR sequence into the M dwarf regime. At this stage of the discussion, we have no rotation periods for any of them, and thus no counterparts for them in the CPD. We have likely ignored their rotation periods with our demand for a clearly recognisable rotation period. (We reappraise this in the following section and derive their photometric rotation periods, thereby justifying the classification here.)

A sparsely populated gap appears between the two sequences traced among the M dwarfs. Our data are not numerous enough to provide sufficient insight into the reality of such a gap between the low-activity M dwarfs and the more active stars. However, we note that a gap is present between the fast rotators and the slow rotators among the M dwarfs in the ZAMS open clusters Pleiades and NGC 2516 (Rebull et al. 2016; Fritzewski et al. 2020), a hint of which is found in the CAD. Ca II H and K and Hα observations of the Pleiades show a similar feature (Fang et al. 2018). It should also be noted that Fang et al. (2018) have questioned the Pleiades membership of the least active stars despite the very slowly rotating stars already known in the Pleiades (Rebull et al. 2016).

A gap between slow and fast rotators also exists in field M dwarfs. The chromospheric emission measurements ($L_{\rm H\alpha}/L_{\rm bol}$) presented by Newton et al. (2017) show two dis-

[14] Unlike $v \sin i$, which can also be obtained from a single observation, our method is also very sensitive to slow rotators.

tinct groups of high and low activity. They correspond to rapidly and slowly rotating stars that are separated by a gap (Newton et al. 2016). With the gap also present in the field star population, it should be well defined and very sparsely populated in open clusters. However, more observations of mid-M stars are needed to constrain its extent.

5.6 Rotation-activity relationship and additional rotation periods

Having discussed the mass dependence of the observed stellar activity in the CAD, we move on to investigating the dependence of the IRT activity on rotation. The wide difference in activity between stars with the same rotation periods (for instance the USRs and the DTRs with similar rotation periods of 4 – 6 d) shows that this dependence is not direct, and that a star's mass (or suitable proxy) has to be considered as well. Such comparisons are therefore typically performed using a mass-normalised version of the rotation period called the Rossby number, to compensate for the variation in activity with stellar mass. The first such diagram was devised and presented by Noyes et al. (1984), and has since been constructed not only for the chromospheric emission of solar-type stars, but also for their coronal emissions (e.g. Pizzolato et al. 2003) and also for the activity of fully convective stars (e.g. Wright et al. 2011).

However, a drawback of the Rossby number is that it depends on the convective turnover timescale, which is not directly accessible from observations, and one has to rely on stellar models or empirically calibrated relations. For this work, we use the relation between $T_{\rm eff}$ and the convective turnover timescale from Barnes & Kim (2010) to derive it for our stars. The effective temperature has already been estimated in Sect. 5.3 through the relationship given by Mann et al. (2015). The uncertainty in Ro was estimated from the period uncertainty and the corresponding calculation for τ_c using offsets of $\Delta T_{\rm eff} = 80$ K. As with the uncertainties for $\log R'_{\rm IRT}$, this approach only includes the measurement and not model-dependent uncertainties. The latter typically differ by only a scaling constant, implying that the underlying power-law dependences are unchanged.

5.6.1 The rotation-activity relationship

Upon transformation to Ro, we find that all stars with measured rotation periods follow a remarkably tight rotation-activity relationship (Fig. 5.5c). The separate groups and even sequences of stars in the CPD and CAD collapse onto a single relationship, obscuring their diverse behaviours in those diagrams. Ours echoes similar relationships seen in chromospheric (Noyes et al. 1984) and coronal activity (Pizzolato et al. 2003). Two regimes known from prior work are instantly recognisable. In the saturated regime of low Rossby numbers, the chromospheric emission is independent of the rotation period and has a value of $\log R'_{\rm IRT} \sim -3.7$. After a curved transition region (in this log-log representation) in the vicinity of $Ro \approx 0.1$, the chromospheric emission declines steeply with Ro to define the unsaturated regime, where activity depends strongly on rotation.

Our prior division of stars in the CPD into distinct groups provides further insight into the different activity regimes. While it is unsurprising that the warmest of the slow rotators are the most evolved from an activity standpoint, and that the fastest M dwarfs are all saturated and thus least evolved, we see from the colour-coded divisions made earlier that there is indeed an order in which the activity evolves. The first stars to evolve after the unsaturated slow rotators (dark grey) are the desaturated slow M dwarfs (purple) and the activity gap stars (green), finally followed by the saturated intermediate rotators (yellow), and then the saturated fast rotators (light grey). Perhaps unsurprisingly, the desaturated transitional rotators (orange) which span a large range of Rossby number, stretch in the rotation-activity diagram all the way from the unsaturated to the saturated stars.

The correlated, unsaturated, part of the rotation activity relation is sometimes described as a power-law (e.g. Pizzolato et al. 2003, Wright et al. 2011), and at other times with a log-linear function (Mamajek & Hillenbrand 2008). We find the log-linear function to follow our data better than a power-law. This suits our goal of effectively locating the stars without measured rotation periods in the activity-rotation space. We fit the correlation in the unsaturated regime with a linear function of the form $\log R'_{\rm IRT} = a + b\,Ro$ using Orthogonal Distance Regression[15] (ODR; Boggs & Rogers 1990) from the SciPy package. We perform the fits over two ranges, once for the slow rotators alone (defined as having $Ro > 0.11$) and once for all unsaturated stars (those for which $Ro > 0.06$). We show both results in the rotation-activity diagram in Fig. 5.6.

For the slow rotators alone, we find

$$\log R'_{\rm IRT} = (-2.970 \pm 0.134) + (-8.293 \pm 0.906)\,Ro, \quad (5.3)$$

and including all unsaturated stars the relation is

$$\log R'_{\rm IRT} = (-3.429 \pm 0.029) + (-5.276 \pm 0.222)\,Ro. \quad (5.4)$$

The root of the differing slopes for both fits might be found among the least active stars. Due to small numbers, we find the scatter among these stars to be smaller compared to other regions of the rotation-activity diagram. Yet the fit to the slow rotators ($Ro > 0.11$) matches these data points because it has fewer constraints among the more active stars.

5.6.2 Lower activity among M dwarfs?

All stars, with only one exception, are seen to follow the activity-rotation relation. That star (ID 707560, C11: 210716)

[15] Unlike ordinary least-squares, ODR includes the uncertainties in both variables.

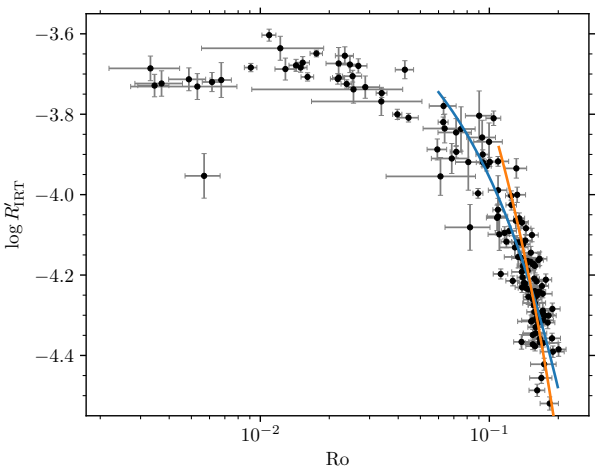

Figure 5.6: Rotation-activity diagram with two possible log-linear fits to two regions of interest: all unsaturated stars (blue, Ro > 0.06) and only the slow rotators (orange, Ro > 0.11).

falls 0.3 dex (well below) the saturated branch. It has a short rotation period ($P_{\rm rot}$ = 2.76 d) that is associated with a clear peak in the periodograms, and shows no alias periods with significant power. The light curve and the periodograms can be found in Fig. 5.8. Given such properties, we would normally expect it to fall into the saturated regime.

However, the star is peculiar in more than its activity; it is also the lowest-mass rotator in our sample. Unfortunately, we were not able to derive rotation periods for other stars of similar mass and activity. Indeed, a large spread in activity can be found among the least-massive stars in the CAD. Given the connection between rotation and activity, we would also expect a correspondingly large spread in periods. However, 707560 is already among the least active stars in the fully convective regime ($(V-K_s)_0 \gtrsim 4.6$), with a rotation period significantly faster than for other early M dwarfs of similar activity.

In conclusion, we cannot specify whether this star has an unusually low activity or whether such low-mass stars simply do not follow the rotation activity relation of the higher-mass stars. Jackson & Jeffries (2010) have found a decline of the activity, measured in the IRT, with colour for mid-M dwarfs in NGC 2516. In their work mid-M dwarfs populate an unstructured rotation-activity diagram. Such behaviour was not observed by Douglas et al. (2014) who use Hα as their tracer of chromospheric activity. Similarly, again using Hα, Newton et al. (2017) find the rotation-activity relation to be valid for mid- and later-M dwarfs. These stars, however, are field stars and likely not young. Unfortunately, our rotation periods do not extend to lower masses and thus do not allow us to study the activity-rotation relation for mid-M dwarfs or to probe whether the unstructured rotation-activity diagram from Jackson & Jeffries (2010) is intrinsic to the chromospheric emission in the IRT.

5.6.3 Activity-informed period search

As already pointed out by Noyes et al. (1984), the relation between chromospheric activity indicators and Rossby number in principle allows one to estimate the stellar rotation period (e.g. Wright et al. 2004). We are in the advantageous position of possessing light curves of most of the stars in our activity sample. This allows us not only to estimate the rotation period from the activity, but also subsequently to determine the actual photometric rotation period from the photometry.

The estimated rotation period serves as a prior to our period search, and we calculated it for every star that falls either onto the slow rotator branch of the CAD ($\log R'_{\rm IRT} < -4.0$) or in the transition and gap region ($\log R'_{\rm IRT} < -3.8$ and $(V-K_s)_0 < 3.6$). We excluded the saturated stars (mostly M dwarfs) for which the activity level obviously cannot provide a useful prediction for the rotation period. We calculated the estimated rotation period $P_{\rm est}$ = Ro τ_c from Eqs. 5.3 and 5.4, respectively, for the two samples. The spread in Rossby number among the stars on the slow rotator sequence is ~10 %. The same relative uncertainty is assigned to $P_{\rm est}$ as $\Delta P_{\rm est}$.

As described exhaustively in the companion paper, we calculated periodograms for each light curve with five different methods. However, for this particular phase of the work we use only four, discarding the string length method on account of its periodogram becoming noisy for low S/N light curves. Additionally, this method often does not agree with the other four methods, unnecessarily inflating our uncertainties. In the periodograms, we search for the highest peak within $2.5\Delta P_{\rm est}$ of $P_{\rm est}$. A manual selection process verifies the existence of a periodic signal in the light curve with this period. A visualisation of this process is given with the example light curves in Fig. 5.9. We show the estimated period and the search range in the different periodograms. In keeping with the period determination algorithm in the companion paper, we calculate the final period as the mean of all four possible values, and its uncertainty as the spread among the four initial values. During this process, we restricted the search range for ~15 light curves to assign the activity-guided period, and not a (chance) higher secondary or alias peak in the periodogram. We confirm all of our previously determined rotation periods, showing that we have included no alias periods among the slow rotators. Additionally, we find 116 new rotation periods among stars previously classified as non-rotators. By definition all of these rotation periods follow the rotation-activity relation. We provide the newly found periods in Table 5.1 along with the chromospheric activity data.

The success of this method can be attributed to multiple reasons. Firstly, the stellar activity measurement narrows the possible period range and enables us to choose the

correct peak in noisy periodograms. It gives us confidence in assigning a period to a noisy light curve and enables us to find the true period in light curves with evolving spots. A second major reason is the breaking of aliases. Since we know that all of our stars are slow rotators (or in the rotational gap), the rotation period cannot be near 1 d for instance, and hence we break the alias with the observational cadence. Finally, we are also able to break the half and double period alias because a factor of two is a very large offset in the rotation-activity diagram. Jointly, these reasons increase the yield of rotation periods for our ground-based observations from 37 % to 66 % (255/387 stars[16] with AAO spectra) in the correlated regime.

However, we are unable to assign a rotation period to every light curve in this set of slow rotators. Among the 184 considered stars, we were not able to assign a rotation period to nine. In some cases the light curve is just too noisy, resulting in periodograms without distinctive peaks. Occasionally, although peaks are found, the different methods provide inconsistent results. In both cases, we do not assign a rotation period.

5.6.4 Unsaturated M dwarfs on the extended slow rotator sequence

We now turn to an unexpected feature in the CAD – the unsaturated early M dwarfs. Among the stars in that region only one rotator was found in the original analysis of the light curves. We define this area as $(V - K_s)_0 > 3.7$ and $\log R'_{\mathrm{IRT}} < -4.05$. Using the period estimation method described above, we find nine stars with periodic light curve variations. We examine these stars particularly closely because some of these rotation periods are longer than what we would normally have assigned with a 42 d long time series. (Generally, we have required that two complete phases be visible over the observational baseline.) However, the stellar activity provides additional information that can justify these long periods. In Table 5.2, we list all such stars with activity informed rotation periods that can be found in the CAD on the declining branch among the M dwarfs.

Despite the good agreement of the new slowly rotating stars in the general activity and the rotational properties of stars in NGC 3532, we reinvestigated their membership status for additional assurance. We applied stronger quality cuts than in our previous membership work (F19) in order to include only high-probability cluster members.

After reconsidering all membership criteria (Table 5.2), we reclassified three stars as likely non-members because their distances locate them farther from the cluster centre than the others. (We still list them in Table 5.2 so that they can be reinstated if or when more definitive membership information becomes available.) The remaining six stars are cluster members with very high probability. We note, for completeness, that all considered stars are photometric cluster members. However, the non-member 612827 is on the photometric binary sequence and the member 304320 is a potential astrometric binary (RUWE = 1.64).

We show the light curves for the six likely members, together with the generalized Lomb-Scargle (Zechmeister & Kürster 2009), as well as the CLEAN (Roberts et al. 1987; Crane 2001) periodograms in Fig. 5.10. The chosen periods do not always coincide with the highest peak in the periodograms for two reasons. Firstly, for the long rotation periods the peaks chosen are near or beyond the typical limit we set for our periods in the companion paper, where we require two cycles in our time series. Secondly, the rotation periods are assigned in concert with the chromospheric activity, which restricts the possible periods. In particular the two peaks that are seen in most periodograms in Fig. 5.10 are typically aliases of each other. The chromospheric activity helps to break the half and double period alias effectively.

5.6.5 New periods in colour-activity-rotation space

With the large number (103) of new rotation periods, we are able to update the central figure of this work (Fig. 5.5), and show the complete picture, including the slowly rotating M dwarfs, in Fig. 5.7. We note that the *Gaia* parallaxes for 13 stars place them far from the cluster centre, despite all other membership criteria being fulfilled. We have conservatively excluded these stars from the rotational analysis despite their being potential cluster members, so as to avoid any contamination of our sample.

The newly found periods can be observed to strengthen all key regions of the CAD with the exception of the saturated stars. Most notably, we are now able to assign periods to the least active, highest-mass stars of our sample, thus finding many additional periods along the whole slow rotator sequence, to fill it out substantially. In the corresponding rotation-activity diagram (Fig. 5.7c) all new stars can be seen to follow the same relation as the previously identified rotators. Since the fit to this diagram was the constraint on the new periods, this result is not unexpected, and serves mainly as a check on the results.

The CPD is where we find the most noticeable changes. Not only is the slow rotator sequence much more densely populated than before, but F-type stars are also now present, and the relationship now also extends into the M dwarf regime out to periods of ~30 d. Slowly rotating M dwarfs in this period regime were also discovered in the Pleiades (Rebull et al. 2016) and NGC 2516 (F20). The stars in NGC 3532 have certainly spun down, and we analyse their rotational evolution in the companion paper (F21rot). The fact that these stars are both located on the rotation-activity relation and extend the slow rotator sequence seamlessly likely indicates that they share a dynamo-regime with the earlier-type stars despite being still on the pre-main sequence. A similar conclusion for main sequence stars was also drawn by Wright & Drake (2016), working with a sample of older,

[16] Excluding three potential non-members among the M dwarfs (see Sect. 5.6.4).

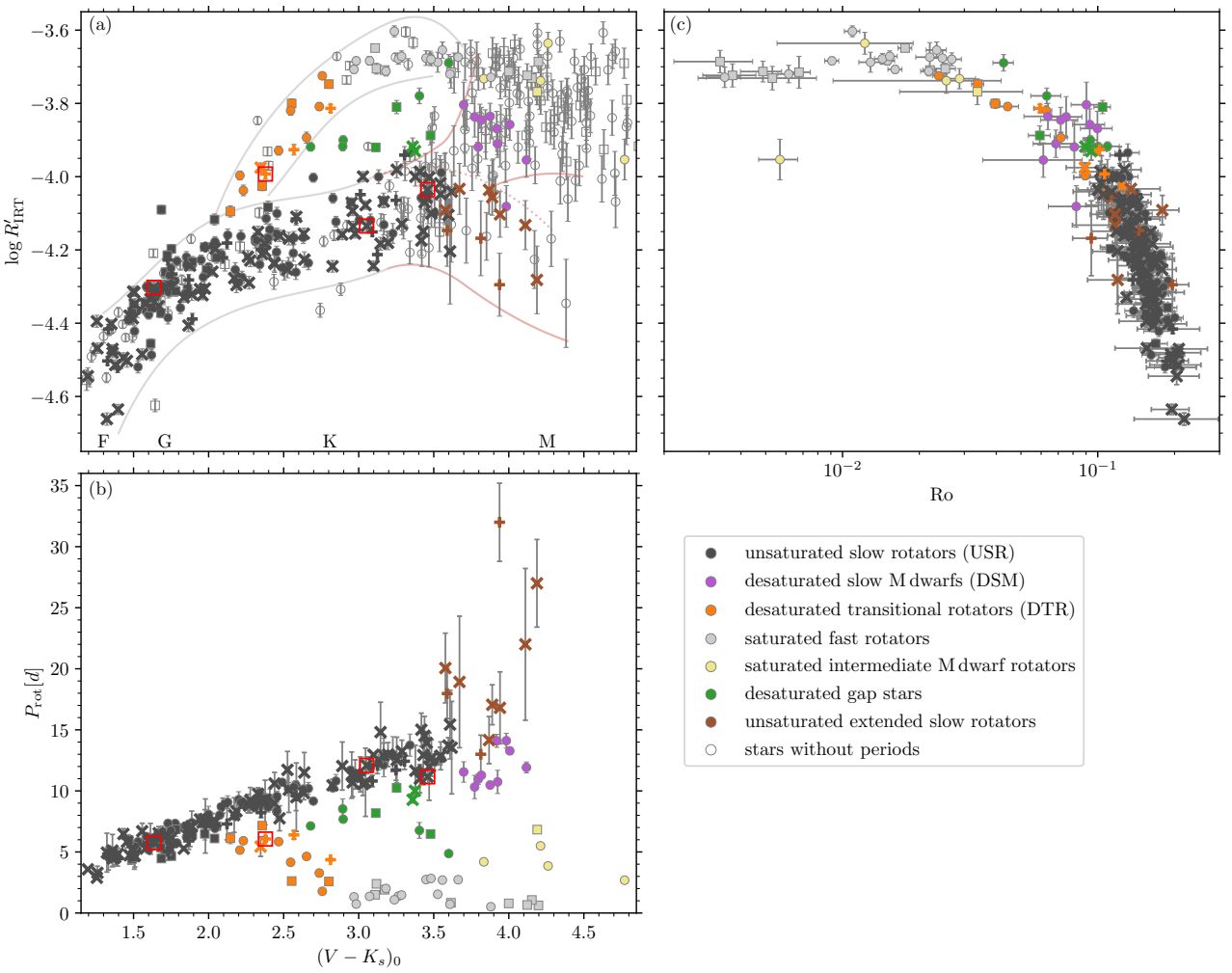

Figure 5.7: Same as Fig. 5.5 but now including the newly identified (activity-informed) rotation periods; single stars are marked with crosses and possible binaries with plus symbols. Each new period is also colour-coded to match the previously determined rotational groups, enabling cross-identification as in Fig. 5.5. This diagram includes the unsaturated extended slow rotator sequence (brown), absent in Fig. 5.5. The light curves and periodograms of the four stars marked with red squares (both in the CAD and CPD) are displayed in Fig. 5.9 of the appendix to demonstrate the viability of deriving these activity-informed periods.

Table 5.2: Rotation periods for unsaturated M dwarfs and cluster membership criteria.

ID	C11	$(V-K_s)_0$ (mag)	$P_{\rm rot}$ (d)	$\Delta P_{\rm rot}$ (d)	$p_{\rm RV}$	d (pc)	$d_{\rm pm}$ (mas yr^{-1})	Comment
102025	248532	3.868	14.2	1.9	0.94	509	0.58	
304320	145504	3.938	32.0	3.5	0.86	497	0.23	likely astrometric binary
400454	179867	4.110	22.0	6.2	0.94	468	0.60	
400856	172827	3.718	20.6	1.8	0.66	390	0.97	likely non-member
522220	143090	4.295	30.0	3.5	0.94	521	1.02	likely non-member
604445	87263	3.889	17.1	1.6	0.93	469	0.30	
612827	48244	4.322	48.0	6.0	0.92	561	0.38	photometric binary, likely non-member
716466	184783	3.941	16.8	2.9	0.94	481	0.74	
801059	305389	4.187	27.0	3.6	0.93	471	0.17	

Notes. *C11*: ID from Clem et al. (2011); $p_{\rm RV}$: Membership probability from radial velocity (F19); d Distance from Bailer-Jones et al. (2018), mean cluster distance d = 484 pc; $d_{\rm pm}$: distance from cluster centre in proper motion space μ_α = −10.37, μ_δ = 5.18, based on *Gaia DR2* (Gaia Collaboration et al. 2018).

slowly rotating field M dwarfs. An in-depth analysis of the whole CPD is provided in the companion rotational study.

5.7 Conclusions

We have measured the chromospheric activity of cool stars in the 300 Myr old, rich open cluster NGC 3532 using the Ca II infrared triplet lines and have used these to explore and better define the corresponding colour-activity-rotation relationships. The cluster occupies an important transitional location between the well-studied ZAMS clusters (e.g. Pleiades, NGC 2516) and the 600 Myr old Hyades cluster, and its richness makes it especially valuable. This study follows on the heels of our prior spectroscopic membership study (F19) and a detailed study of the rotation period distribution in the companion paper (F21rot).

We showed how the chromospheric activity is well correlated with the photospheric activity, the latter measured from the starspot-induced variability amplitude of light curves. The correlation holds despite the fact that the two datasets are not contemporaneous, an encouraging sign from the observational perspective, and is ultimately rooted in their shared stellar rotation and its mass and age dependences.

We constructed one of the richest colour-activity diagrams (CAD) available to date for any open cluster. The diagram is remarkably rich in information, with a prominent (main) sequence of lower-activity stars and a side branch of higher-activity stars, the two separated by an 'activity gap'. The CAD appears to be a near-mirror image of the colour-period diagram (CPD) of the cluster. Colour-coding specific groups of rotators to show the correspondence emphasises that such a correspondence occurs on a star-by-star, rather than statistical, basis. This correspondence suggests that the two quantities (rotation and activity) are potentially predictable from each other to a greater extent than previously thought possible.

In particular, the close correspondence between the activity and the rotation period shows that the absence of higher-mass fast rotators in our photometric work is an astrophysical fact and not a detection issue. We conclude that all stars down to a certain mass seem to have transitioned to the slow rotator sequence, showing the universality and strong mass dependence of this transition. The CAD hosts an unexpected group of low-activity M dwarfs, for which the stellar activity declines with declining mass. In contrast to the majority of young M dwarfs, these stars are clearly in the unsaturated regime.

We also constructed the first rotation-activity diagram for stars in NGC 3532 and, as expected, find the two well-known regimes (saturated and unsaturated) connected by a very wide transition region that can be traced back to the rotational gap in the CPD. The relationship is remarkably tight in relation to prior work, and there is only one outlier.

From this rotation-activity correlation, we predicted rotation periods for stars in the unsaturated regime, searched for and identified the photometric rotation periods using the photometric light curves obtained for the companion rotational study. We recovered all previously found periods and were able to find 103 additional membership-justified rotation periods with the help of this activity-informed period search. Using the activity as a guideline allows us to break aliases and to assign photometric rotation periods to noisier light curves. The new periods include stars on the extended slow rotator sequence.

In conclusion, the analysis of chromospheric activity in combination with photometric time series analysis enabled us to perform a detailed study of the activity-rotation period correspondence over a wide range of stellar masses among cool stars in NGC 3532, showing that the relationship is tight enough to be predictive over a wide parameter range. In particular, it allows us to substantially increase the number of photometric rotation periods derived. In combination with prior work, this study has contributed to-

wards the establishment of NGC 3532 as a benchmark open cluster and has wider implications for the era of massive multi-object spectroscopic surveys.

Acknowledgements. We thank Marcel Agüeros for the detailed review. SAB acknowledges support from the Deutsche Forschungs Gemeinschaft (DFG) through project number STR645/7-1. SPJ is supported by the German Leibniz-Gemeinschaft, project number P67-2018. Based on data acquired at the Anglo-Australian Telescope under program S/2017A/02. We acknowledge the traditional owners of the land on which the AAT stands, the Gamilaraay people, and pay our respects to elders past and present. Based in part on observations at Cerro Tololo Inter-American Observatory, National Optical Astronomy Observatory (2008A-0476; S. A. Barnes, SMARTS consortium through Vanderbilt University), which is operated by the Association of Universities for Research in Astronomy (AURA) under a cooperative agreement with the National Science Foundation. This work has made use of data from the European Space Agency (ESA) mission *Gaia* (`https://www.cosmos.esa.int/gaia`), processed by the *Gaia* Data Processing and Analysis Consortium (DPAC, `https://www.cosmos.esa.int/web/gaia/dpac/consortium`). Funding for the DPAC has been provided by national institutions, in particular the institutions participating in the *Gaia* Multilateral Agreement. This research has made use of NASA's Astrophysics Data System Bibliographic Services. This research has made use of the SIMBAD database and the VizieR catalogue access tool, operated at CDS, Strasbourg, France. **Software:** This research made use of Astropy, a community-developed core Python package for Astronomy (Astropy Collaboration et al. 2013). This research made use of the following Python packages: Pandas (McKinney 2010); NumPy (Walt et al. 2011); MatPlotLib (Hunter 2007); IPython: (Pérez & Granger 2007);

References

AAO Software Team 2015, Astrophysics Source Code Library
Astropy Collaboration et al. 2013, A&A 558, A33
Bailer-Jones, C. A. L., Rybizki, J., Fouesneau, M., Mantelet, G., & Andrae, R. 2018, AJ 156, 58
Baliunas, S. L. et al. 1995, ApJ 438, 269
Barnes, S. A., & Kim, Y.-C. 2010, ApJ 721, 675
Basri, G., & Nguyen, H. T. 2018, ApJ 863, 190
Basri, G. et al. 2011, AJ 141, 20
Belokurov, V. et al. 2020, MNRAS 496, 1922
Boggs, P. T., & Rogers, J. E. 1990, Contemporary Mathematics 112, 186
Busà, I., Aznar Cuadrado, R., Terranegra, L., Andretta, V., & Gomez, M. T. 2007, A&A 466, 1089
Cenarro, A. J. et al. 2001, MNRAS 326, 959
Clem, J. L., Landolt, A. U., Hoard, D. W., & Wachter, S. 2011, AJ 141, 115
Crane, P. C. 2001, Sol. Phys. 203, 381
Douglas, S. T. et al. 2014, ApJ 795, 161
Douglas, S. T. et al. 2019, ApJ 879, 100
Eberhard, G., & Schwarzschild, K. 1913, ApJ 38, 292
Fang, X.-S., Zhao, G., Zhao, J.-K., & Bharat Kumar, Y. 2018, MNRAS 476, 908
Foing, B. H., Crivellari, L., Vladilo, G., Rebolo, R., & Beckman, J. E. 1989, A&AS 80, 189
Fritzewski, D. J., Barnes, S. A., James, D. J., & Strassmeier, K. G. 2020, A&A 641, A51
— 2021, A&A 652, A60
Fritzewski, D. J. et al. 2019, A&A 622, A110
Gaia Collaboration et al. 2018, A&A 616, A1
Güdel, M. 2004, A&A Rev. 12, 71
Hall, J. C. 1996, PASP 108, 313
— 2008, Living Reviews in Solar Physics 5, 2
Hunter, J. D. 2007, Computing in Science & Engineering 9, 90
Husser, T. .-. et al. 2013, A&A 553, A6
Jackson, R. J., & Jeffries, R. D. 2010, MNRAS 407, 465
James, D. J., & Jeffries, R. D. 1997, MNRAS 292, 252
Jones, J. et al. 2015, ApJ 813, 58
Kraft, R. P. 1967, ApJ 150, 551
Lewis, I. J. et al. 2002, MNRAS 333, 279
Lindegren, L. et al. 2021, A&A 649, A2
Linsky, J. L., Hunten, D. M., Sowell, R., Glackin, D. L., & Kelch, W. L. 1979, ApJS 41, 481
Lorenzo-Oliveira, D., Porto de Mello, G. F., Dutra-Ferreira, L., & Ribas, I. 2016, A&A 595, A11
Mamajek, E. E., & Hillenbrand, L. A. 2008, ApJ 687, 1264
Mann, A. W., Feiden, G. A., Gaidos, E., Boyajian, T., & von Braun, K. 2015, The Astrophysical Journal 804, 64
Marsden, S. C., Carter, B. D., & Donati, J. .-. 2009, MNRAS 399, 888
Martin, J. et al. 2017, A&A 605, A113
McKinney, W. 2010, in: Proceedings of the 9th Python in Science Conference, ed. by S. van der Walt, & J. Millman, 51
Meibom, S., & Mathieu, R. D. 2005, ApJ 620, 970
Meibom, S., Mathieu, R. D., & Stassun, K. G. 2007, ApJ 665, L155
Morris, B. M. et al. 2018, AJ 156, 203
Newton, E. R. et al. 2016, ApJ 821, 93
Newton, E. R. et al. 2017, ApJ 834, 85
Noyes, R. W., Hartmann, L. W., Baliunas, S. L., Duncan, D. K., & Vaughan, A. H. 1984, ApJ 279, 763
Pérez, F., & Granger, B. E. 2007, Computing in Science & Engineering 9, 21
Pettersen, B. R. 1989, Sol. Phys. 121, 299
Pizzolato, N., Maggio, A., Micela, G., Sciortino, S., & Ventura, P. 2003, A&A 397, 147
Radick, R. R., Lockwood, G. W., Henry, G. W., Hall, J. C., & Pevtsov, A. A. 2018, ApJ 855, 75
Rauscher, E., & Marcy, G. W. 2006, PASP 118, 617
Rebull, L. M. et al. 2016, AJ 152, 113
Roberts, D. H., Lehar, J., & Dreher, J. W. 1987, AJ 93, 968
Schmitt, J. H. M. M. 1997, A&A 318, 215
Skrutskie, M. F. et al. 2006, AJ 131, 1163
Skumanich, A. 1972, ApJ 171, 565
Soderblom, D. R., & Mayor, M. 1993, AJ 105, 226
Soderblom, D. R., Stauffer, J. R., Hudon, J. D., & Jones, B. F. 1993, ApJS 85, 315
Strassmeier, K. G. 2009, A&A Rev. 17, 251

Walt, S. van der, Colbert, S. C., & Varoquaux, G. 2011, Computing in Science & Engineering 13, 22
Wilson, O. C. 1978, ApJ 226, 379
Wright, J. T., Marcy, G. W., Butler, R. P., & Vogt, S. S. 2004, ApJS 152, 261
Wright, N. J., & Drake, J. J. 2016, Nature 535, 526
Wright, N. J., Drake, J. J., Mamajek, E. E., & Henry, G. W. 2011, ApJ 743, 48
Yamashita, M., Itoh, Y., & Takagi, Y. 2020, PASJ 72, 80
Zechmeister, M., & Kürster, M. 2009, A&A 496, 577
Žerjal, M. et al. 2013, ApJ 776, 127
Zhang, J. et al. 2020, ApJS 247, 9

5.A Light curves of selected stars

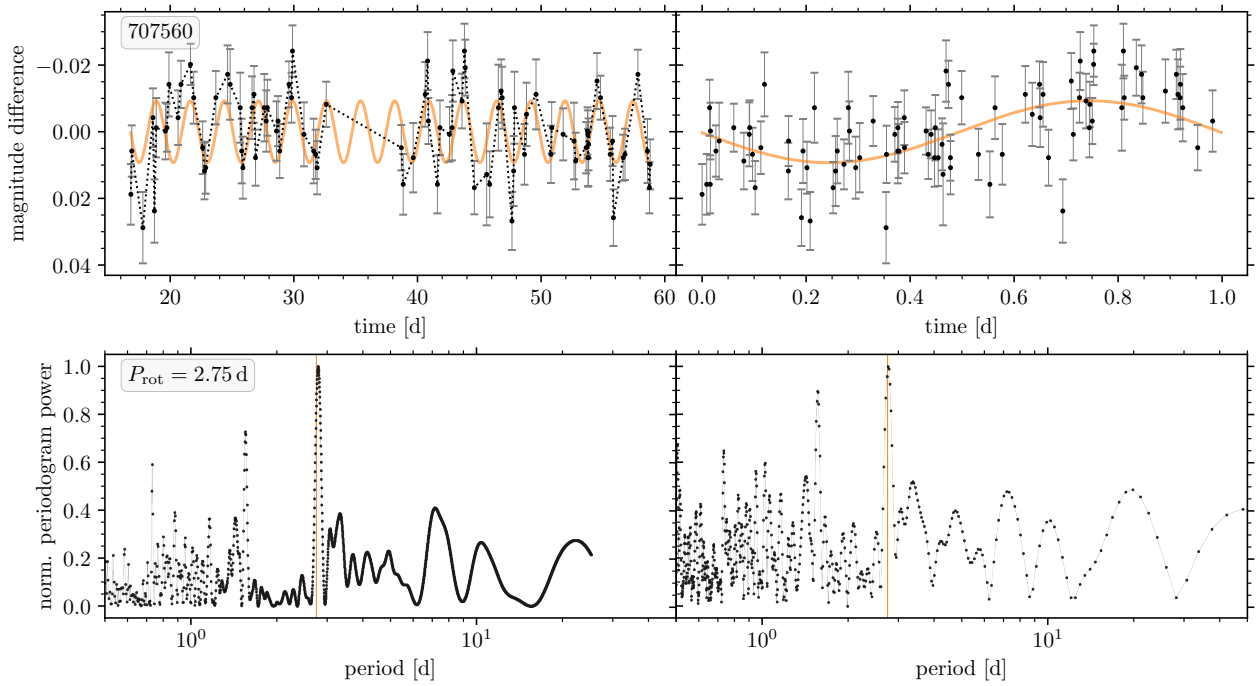

Figure 5.8: Light curve in time (*top left*) and phase space (*top right*) as well as the Lomb-Scargle periodogram (*bottom left*), and CLEAN periodogram (*bottom right*) for the outlier (707560) in the rotation-activity diagram.

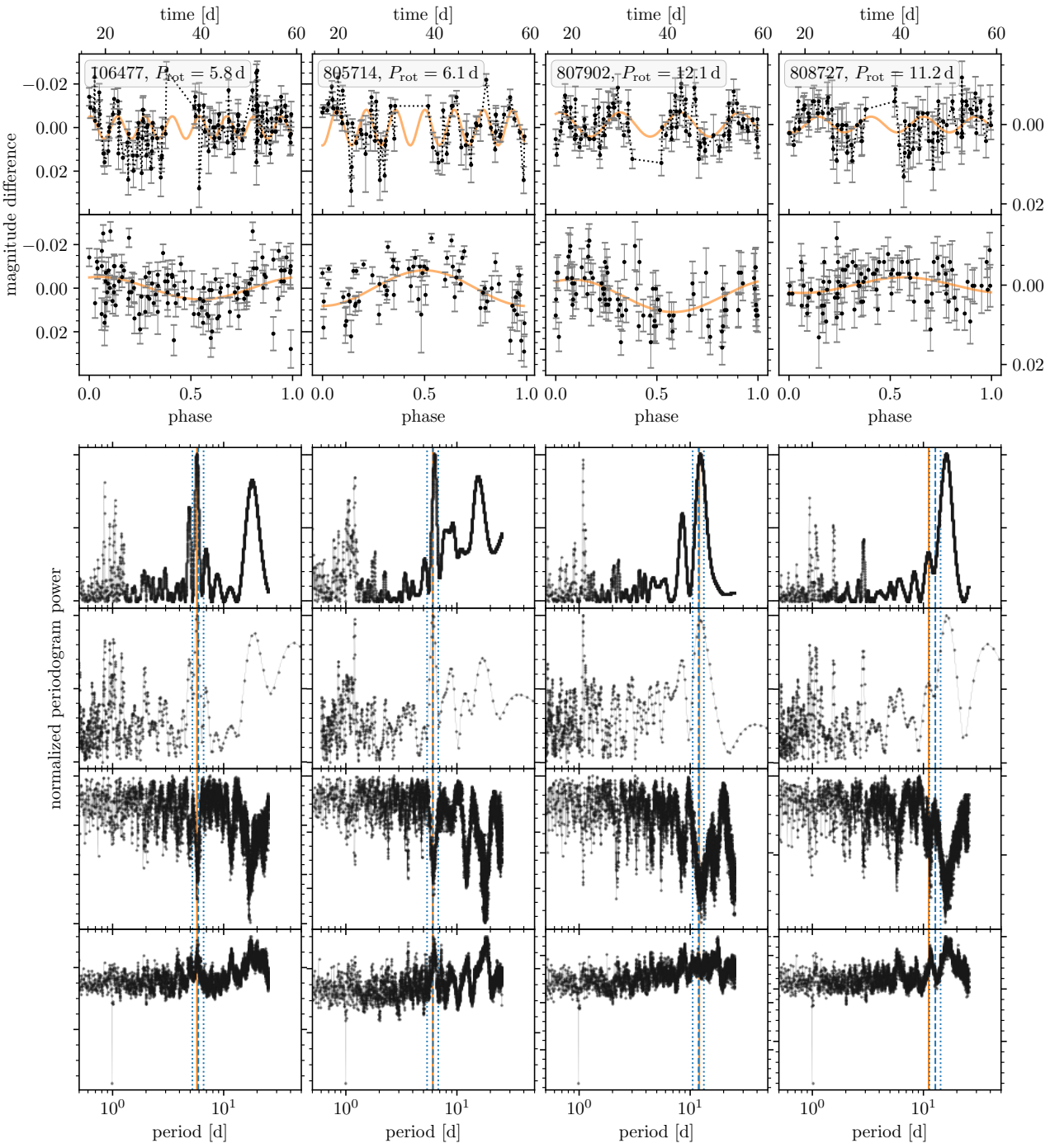

Figure 5.9: Four examples of light curves and their associated periodograms for (non-M) stars with newly identified, activity-informed rotation periods. Each column shows the data for one star. The two *upper* panels show the light curves in both the time and phase domains. We fit a sine with the rotation period and display it along with the data. The left scale is valid for the two leftmost plots, while the right scale is for the two light curves on the right. The *lower* panels show, from top to bottom, the Lomb-Scargle, CLEAN, phase-dispersion minimization, and Gregory-Loredo periodograms. In each periodogram, we mark both the rotation period (orange line) and the period estimated from the activity and its uncertainty (blue lines). Unlike the other periodograms, in the phase-dispersion minimization the best periods are represented by dips.

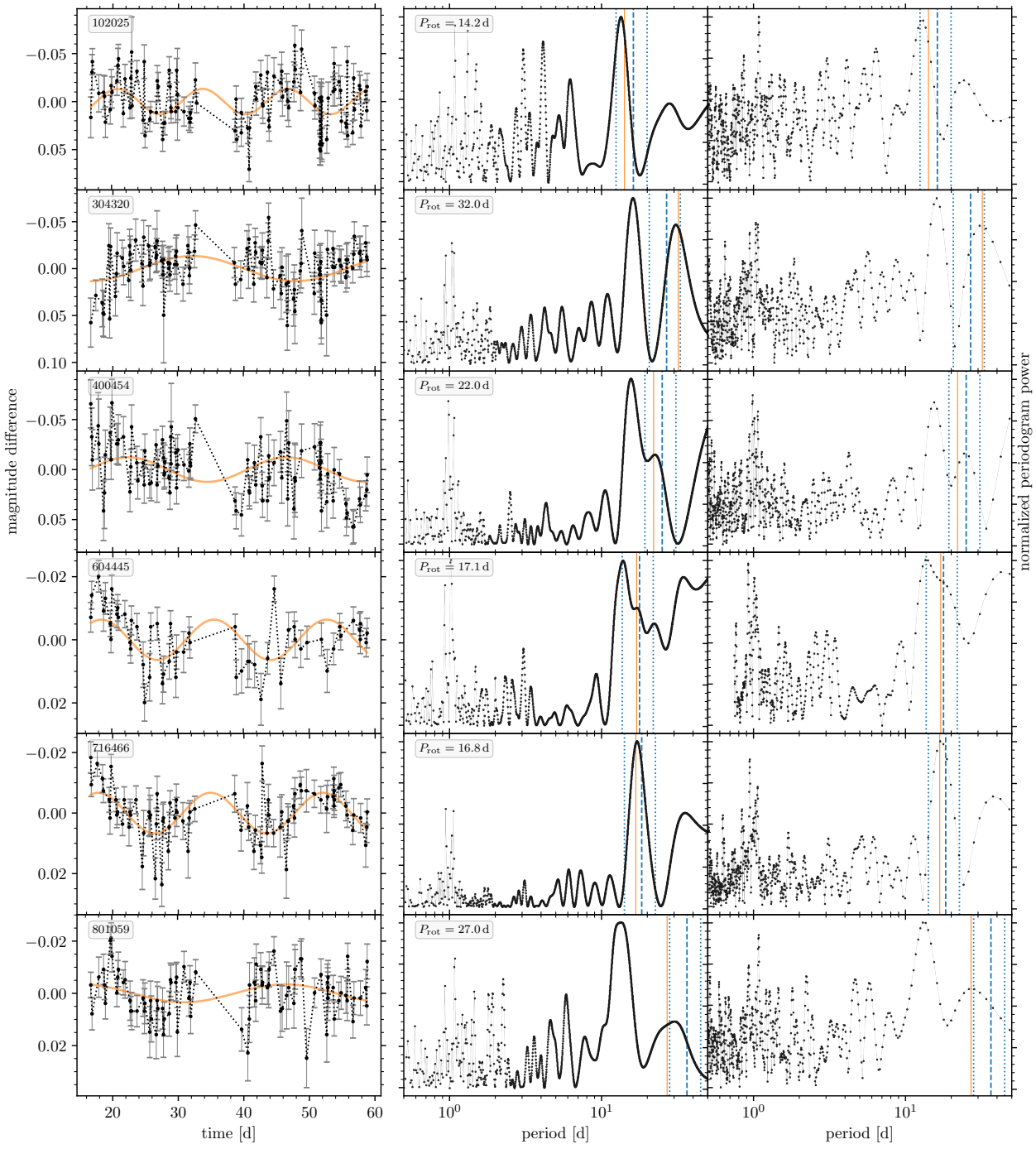

Figure 5.10: *Left column*: Light curves for the early M dwarfs of low stellar activity in NGC 3532 that have newly identified rotation periods. The orange line is a sine fit to the data with the newly identified likely rotation period. The first two light curves (from the top) are from V 120 s exposures, while all others are from I_c 600 s images. *Centre column*: Corresponding normalised generalized Lomb-Scargle diagram, with the selected rotation period marked by the orange vertical line. The dashed blue line indicates the rotation period estimated from the chromospheric activity measurement, and the dotted lines delineate the search range, which is derived from the period uncertainty. *Right column*: Same as the centre column but with the CLEAN periodogram. The offset between the peaks and the position of the best period for 102025 in the first row is due to the different peak positions in the phase-dispersion minimization and Gregory-Loredo periodograms (not displayed).

6 Discussion

The aim of this thesis is to provide observational insights into the transition from fast to slow rotation in young cool main-sequence stars. Despite the well-known fact that these stars spin down during their early main-sequence life, little is known about the exact mechanisms and time scales. The publications reprinted in the previous chapters present new data which enable a detailed investigation of the transition. The first two papers build the basis for the latter two studies on NGC 3532 which probe the transition from fast to slow rotation directly through rotation periods and indirectly through stellar activity.

In this chapter, I review the results from the individual publications in the light of the overarching research question. Firstly, I focus on individual findings from the four studies on the two open clusters NGC 2516 and NGC 3532. I start with the former and summarize the three works on the latter in a combined manner. Finally, I discuss the conclusions drawn from the comparison of those two open clusters and focus particularly on the evolution of the fast rotators.

6.1 Stellar rotation at 150 Myr–New insights from NGC 2516

NGC 2516 is a well studied open cluster, yet rotation periods for its solar-like members were previously not published. In Fritzewski et al. (2020), we provide 308 new rotation periods for solar-type stars. In combination with data from Irwin et al. (2007), photometric rotation periods for 555 members of NGC 2516 were used in this work[1]. In contrast to other open clusters, NGC 2516 turns out to be the ideal open cluster to measure rotation periods from ground-based photometry because it is relatively young (hence its stars have large variability amplitudes), well-populated, and close-by but yet distant enough for its core[2] to be locally concentrated on the sky. Hence, the large sample of 555 stars with measured rotation periods in one open cluster is nearly unprecedented in ground-based studies which are often limited by observational time constraints, sky coverage, and detection limits of the variability. The full sample of rotators in NGC 2516 (including Healy & McCullough 2020) is shown in the CPD in Fig. 6.1.

The large number of rotation periods enables a direct comparison to the similarly-aged Pleiades for which Rebull et al. (2016) measured the rotation periods of 759 members from space-based K2 photometry. The analysis in Fritzewski et al. (2020) leads to the conclusion that both open clusters host an overall identical distribution of rotation periods with only minor (expected) variations. A further comparison to the other, nearly coeval, open clusters M 35, M 50, and Blanco 1 from the literature gives confidence that stellar rotation is universal at the zero-age main sequence and does not depend on the individual open cluster or its environment.

This fact has previously been assumed as a requirement (e.g. Soderblom et al. 1993) to explain the angular momentum evolution. Yet, it was not shown as clearly as in this work that the rotation period distributions of coeval open clusters are indeed identical.

Despite the general similarities, cluster-to-cluster variations can still be found at the level of detail. In the particular case of NGC 2516 and the Pleiades, we find a group of stars with intermediate rotation (in the rotational gap) which is present in NGC 2516 but not in

[1] Shortly after Fritzewski et al. (2020), Healy & McCullough (2020) published 120 additional photometric rotation periods for late-F and G-type stars from TESS data. Hence, 675 rotation periods for stars in NGC 2516 are now measured.

[2] Apparently, NGC 2516 is elongated and its "corona" covers a large area on the sky (Meingast et al. 2020).

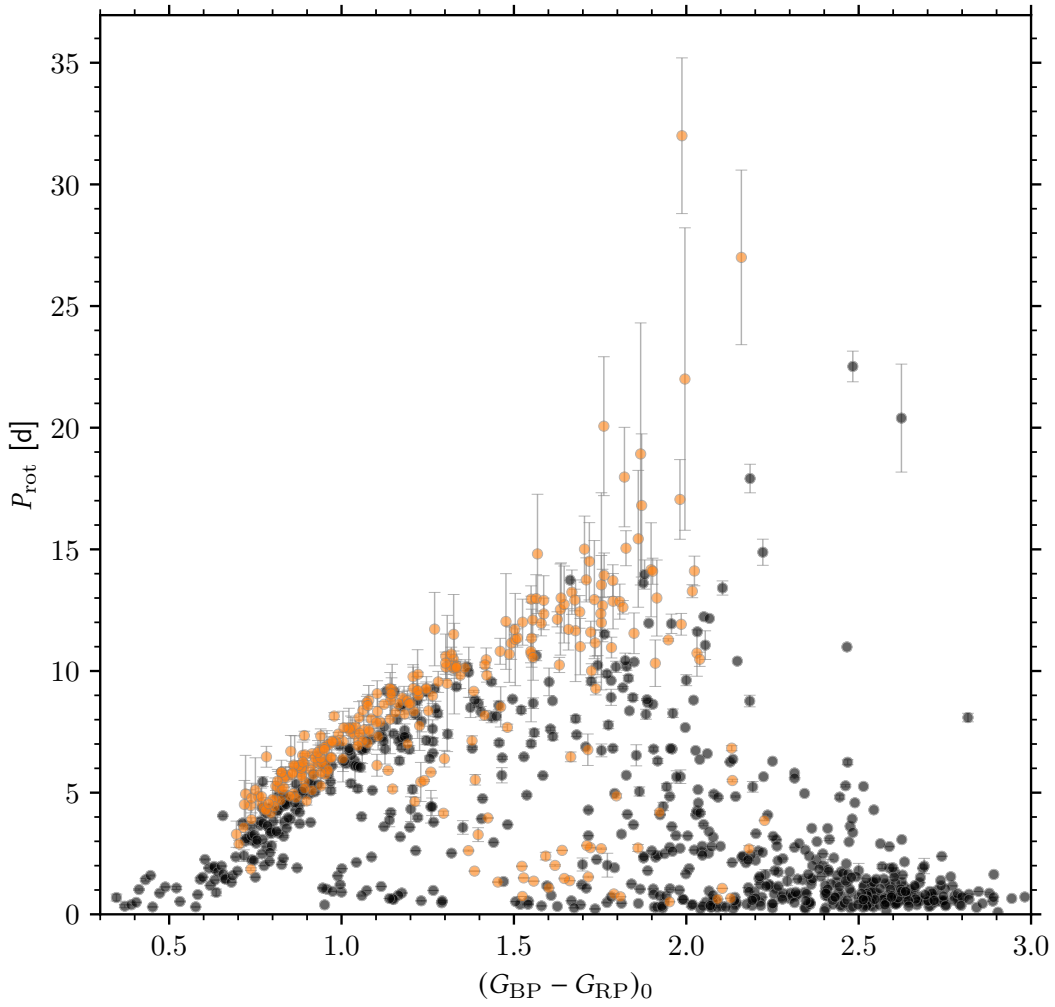

Figure 6.1: Colour-period diagrams (CPD) for NGC 2516 (black) and NGC 3532 (orange). Both clusters host well populated slow rotator sequences which span the CPD diagonally. In NGC 3532 this sequence has moved upwards to longer rotation periods compared to NGC 2516. For the first time, we also proof the existence of its continuation into the M dwarf regime: Both open clusters host an "extended slow rotator sequence" ($P_{\mathrm{rot}} > 15$ d). They also show distinct fast rotator sequences, but in the older NGC 3532, the higher-mass fast rotators already evolved towards longer periods which is expressed by the absence of fast rotators in NGC 3532 for stars with $(G_{\mathrm{BP}} - G_{\mathrm{RP}})_0 < 1.5$. Notably is also that the slow rotator sequence is the upper boundary for the rotation periods, without any outliers above. For NGC 2516, the colour-period diagram combines the rotation periods from Irwin et al. (2007), Fritzewski et al. (2020), and Healy & McCullough (2020). The NGC 3532 data are from Fritzewski et al. (2021b).

the Pleiades. Due to the small number of stars at that particular mass (despite the overall large sample) one cannot be certain whether this feature has a physical meaning.

The identical rotation period distributions of the NGC 2516 and the Pleiades are not limited to the well-known fast and slow rotators sequences. Beyond, we observed the extension of the slow rotator sequence into the M dwarf regime. This sequence is connected to the traditional slow rotator sequence for the higher-mass stars and opens a second rotational gap among the M dwarfs. It was discovered in the Pleiades but due to the unusually slow rotation Rebull et al. (2016) were unsure about the membership of those slowly rotating stars, although most criteria make them genuine members. We are able to confirm that this sequence is indeed real and occurs in NGC 2516 (and NGC 3532), too. However, with it being observed to date only in three young open clusters, it raises the question whether those stars are the young counterparts of slowly rotating (field) M dwarfs (Newton et al. 2016), or a completely different type of rotators.

The key result of Fritzewski et al. (2020) strengthens the basis of gyrochronology because it shows that the evolution of stellar angular momentum is independent of the birth environment. However, gyrochronology is also footed on angular momentum models which describe the evolution of the rotation periods with time and hence allow the age determination from the rotation periods. Despite improvements over the past years, we find that most of the current stellar angular momentum models do not describe the rotation periods well enough. The models by Barnes (2010), Matt et al. (2015), and Amard et al. (2019) share some underlying ideas and hence all overestimate the rotation periods at the age of NGC 2516. Consequently, one would estimate a younger age from gyrochronology than from isochrones. Only the two-zone model by Spada & Lanzafame (2020) is able to predict the position of the slow rotator sequence in the CPD. For the fast rotators, we find no model to describe the slightly evolved sequence of NGC 2516. Yet, the uplift for the warmer stars is visible in the models but certainly not strong enough. This issue is addressed in greater detail below in the context of the evolution of the fast rotator sequence (Sect. 6.3).

The observed discrepancies between the observations and angular momentum models need to be addressed to facilitate the aim of gyrochronology which is to determine the stellar age based on the rotation period and mass. As a consequence and due to the good match between the observations of the five young open clusters, we advocate in Fritzewski et al. (2020) to use for now the observations themselves as the 150 Myr rotational isochrone.

6.2 NGC 3532 as an open cluster and stellar rotation at 300 Myr

6.2.1 Cluster membership for NGC 3532

The second open cluster studied for this thesis, NGC 3532, is not only a very rich open cluster and therefore ideal to study stellar rotation, it is also the only major open cluster of its age within 500 pc of the Sun. However, as stressed in the introduction (Chapter 1), a clean membership of the open cluster is crucial to obtain a rotation period distribution of a truly coeval population without contamination. With the first paper (Fritzewski et al. 2019, Chapter 2), we provide such a clean and comprehensive membership and laid the important groundwork upon which further studies of NGC 3532 can build.

For the cluster membership, we obtained multi-object spectra from the Anglo-Australian Telescope for ~1 000 stars in the central field of NGC 3532. Additional, previously unpub-

lished, radial velocity observations obtained at the CTIO and data from the literature, as well as from spectroscopic surveys complement the data set. This large sample of spectra and the measured radial velocities form the first large-scale study of low-mass stars in NGC 3532. In particular, we obtained spectra for late-K and early-M dwarfs which are not covered in spectroscopic surveys due to their faintness. In combination with proper motions from *Gaia* DR2, we found 660 exclusive cluster members. This number includes the few higher-mass main sequence and evolved stars observed by Gieseking (1980, 1981) and González & Lapasset (2002).

Despite the already impressive number of cluster members among the surveyed candidates, NGC 3532 hosts certainly many more stars. Firstly, due to the restricted observation time, we only observed half of the candidates and hence NGC 3532 may have at least 1 000 true cluster members within our surveyed area[3] (~1 sq. degree). Secondly, the open cluster extends out to several degrees from the cluster centre and one could possible find many additional cluster members in this area. In combination, these estimates place NGC 3532 easily among the most populous open clusters within 500 pc. Even with the currently incomplete cluster membership, NGC 3532 can serve as a benchmark open cluster in between the ages of the Pleiades (and other ZAMS open clusters, ~150 Myr) and the Hyades and Praesepe (600 – 700 Myr). With the membership, we provided the crucial stepping stone for more advanced studies such as the detailed analysis of stellar rotation (Fritzewski et al. 2021b, Chapter 4) and stellar activity (Fritzewski et al. 2021a, Chapter 5).

Beyond the cluster membership, we probed for the first time the metallicity of the main sequence stars in NGC 3532 spectroscopically. Previous studies (e.g. Claria & Lapasset 1988, Cayrel de Strobel et al. 2001) focused on the brighter evolved stars or estimated the metallicity from photometry. With both methods metallicities ranging from [Fe/H]= −0.1 to [Fe/H]= 0.1 were obtained by the different authors (for details see Fritzewski et al. 2019). In contrast to these previous works, our sample contains 139 dwarf members. From this significantly larger main sequence set, we find the metallicity to be slightly sub-solar ([Fe/H]= -0.07 ± 0.1). Our value was shortly after confirmed with independent data by Kovalev et al. (2019) ($[\mathrm{Fe/H}]_{\mathrm{NLTE}} = 0.10 \pm 0.02$). The divergence between the metallicity of giant and dwarf stars shows the importance of spectroscopic studies of main sequence stars in open clusters beyond radial velocity measurements to fully characterize the stellar populations of open clusters.

This initial work on NGC 3532 provides a solid basis upon which further studies of NGC 3532 can build. It provides not only a homogeneous membership but also the metallicity which is crucial given the metallicity-dependent spin-down (Amard & Matt 2020).

6.2.2 Stellar rotation and chromospheric activity in NGC 3532

With the well defined cluster membership at hand, further detailed studies of this open cluster are possible. In Fritzewski et al. (2021b), we present the first stellar rotation periods for NGC 3532 (after the rotation periods in the PhD thesis of Barnes (1997) which were only published in a figure in Barnes (2003)) and fill a critical gap still present in the age-ranked succession of open clusters. The colour-period diagram with these periods is shown in Fig. 6.1.

The periods presented in this work are all photometric rotation periods, yet they were obtained in two different ways. Firstly, the "normal" analysis of the light curves as for NGC 2516 and secondly their reanalysis in the light of the chromospheric activity

[3] Cantat-Gaudin et al. (2018) find 1889 cluster members ($G \leq 18$) from *Gaia* DR2, with about half of them in the inner 1° (diameter).

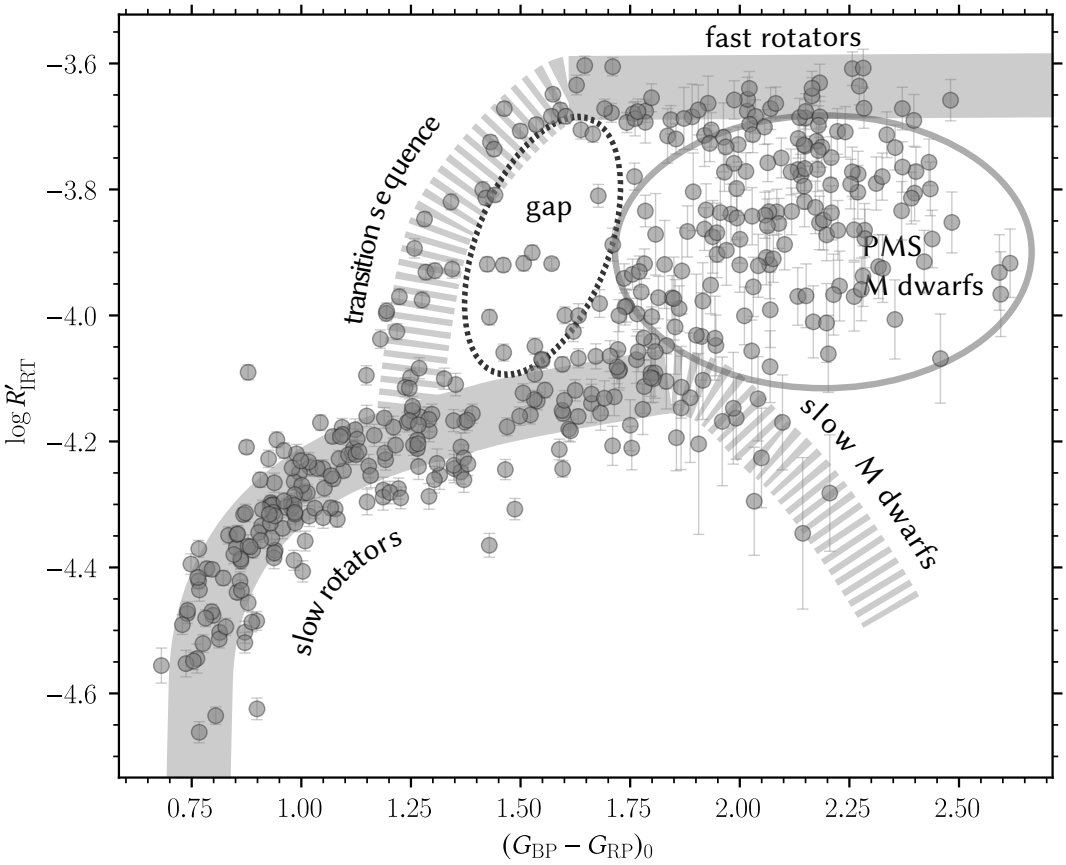

Figure 6.2: Colour-activity diagrams for NGC 3532 based on the chromospheric activity proxy $\log R'_{\mathrm{IRT}}$. In this figure, I marked the main features with their corresponding names from the colour-period diagram to highlight their connection (c.f. Fig. 1.2). The slow rotators span nearly the whole colour range in the unsaturated regime. The slowly rotating M dwarfs continue this sequence and constitute the extended slow rotator sequence. For NGC 3532 this sequence was first observed through their unusually low chromospheric activity and later confirmed with the photometric time series. Above this sequence, the pre-main sequence M dwarfs show a wide spread in activity, as they do in the colour-period space, too. The saturated fast rotators can only be found among late-K and M dwarfs. Earlier type stars follow the transition sequence of desaturated/spun-down stars. Bluewards of this transition sequence no stars are observed, confirming that theses stars have all evolved into slow rotators. See Fritzewski et al. (2021a) for an in-depth discussion of the features and their shapes.

measurements. This two step process yields 176 photometric and 103 activity-informed[4] rotation periods.

The interconnection between stellar rotation and activity does not only help us in determining additional rotation periods but supports our understanding of stellar rotation in NGC 3532 from a different vantage point. For the chromospheric activity, we measured the excess flux in the Ca II infra-read triplet (IRT) lines. Already from the colour activity diagram (CAD, Fig. 6.2) without any knowledge on the rotation periods, we gain insight

[4] Photometric rotation periods which are derived from the light curves with additional prior information on the approximate rotation period.

into the rotational state of all spectroscopically observed members (rather than the subset of rotators). The CAD turns out to be a near-mirror image of the CPD and one can easily read-off to which group in the CPD a star belongs. From the CAD, it becomes evident that the absence of rotators faster than the evolved fast rotator sequence is not observational (e.g. due to small variability amplitudes) but astrophysical. Even in the CAD, in which fast rotators are easily identified due to their higher activity, this region is unpopulated. In consequence, all fast rotators of this region moved to a lower activity regime, meaning they became slow rotators.

Together with the already known purely photometric rotation periods, we are able to construct a rotation-activity diagram and, following Noyes et al. (1984), to calculate approximate rotation periods for all stars in the unsaturated regime. Due to the intrinsic scattering of the rotation-activity correlation, these periods are less accurate than the photometric rotation periods.

However, we possess light curves for most spectroscopically observed stars and can therefore make use of the synergies of a joint analysis. The main reasons for a failed period determination from the light curves are noisy time series and strong alias signals in the periodogram. In particular the latter are efficiently suppressed when using the calculated period as a prior information because the main alias signal is present near one day, but stars in the unsaturated regime rotate slower ($P_{\mathrm{rot}} \gtrsim 4\,\mathrm{d}$). Additionally, the stellar activity narrows down the possible range of rotation periods and hence enables the detection of rotation in noisier light curves.

With this approach, we are able to identify a large number of additional (activity-informed) photometric rotation periods. In particular, we can unambiguously identify the extended slow rotator sequence for NGC 3532. In total, we find 276 rotation periods among the members of NGC 3532, enabling the detailed investigations of various parts of the CPD, including the transition from fast to slow rotation.

As in other main sequence open clusters, NGC 3532 hosts a slow rotator sequence which runs diagonally in the CPD (Fig. 6.1) from higher-mass stars, with short periods, to low-mass stars and longer rotation periods. For NGC 3532 this sequence is well populated. In addition, we find an evolved fast rotator sequence (transition sequence) on which the higher-mass stars have longer rotation periods and connect to the slow rotator sequence. Shorter periods are observed at its low-mass end where it joins the fast rotator sequence. This evolved sequence is key to understand the transition from fast to slow rotation. The fast rotator sequence can only be observed for even lower-mass stars and is sparsely populated due to the limited membership among the least massive stars. In addition to the limited membership, the smaller variability amplitudes compared to stars in NGC 2516 hinder the determination of more rotation periods in this regime. Because these rotators are mostly in the saturated regime, we were unable to derive activity-informed rotation periods for them. Yet, we can conclude that they exist, based on their abundance in the CAD.

A curious feature in the CPD is a bifurcation of the slow rotator sequence, for G stars. Among these stars the slow rotator sequence consists of two groups with slightly different rotation periods. As shown in Fritzewski et al. (2021b), the faster rotating group contains a significantly larger fraction of photometric binaries and the bifurcation could be related to this fact. Yet, further investigations of other open clusters are needed to identify the true cause.

6.3 The transition from fast to slow rotation

Some features eminent in the period distribution of NGC 3532 are not observable at earlier stages of the transition from fast to slow rotation. In younger open clusters such as M 34 the strongly mass-dependent transition has just begun and the transition sequence is not as distict as in NGC 3532. Hence, the unique rotation data of NGC 3532 can provide new insights into the transition which was previously studied either theoretically (Brown 2014) or in the slightly younger open cluster M 34 (Meibom et al. 2011). Other works simply interpolated the angular momentum evolution between the ages of the Pleiades and the Hyades (e.g. Matt et al. 2015) and were not able to account for the details of the evolution.

As already seen for NGC 2516, angular momentum models over-predict the rotation periods for stars on the slow rotator sequence in young open clusters. The same can also be observed for NGC 3532. Most models suggest a younger age than estimated from isochrones. The very same models under-predict the rotation periods for stars in transition from fast to slow rotation. Hence, they would require an older age to describe the observed sequence. This tension cannot be solved within the current framework and clearly shows our lack of understanding of the transition. The observations of NGC 3532 can help to better constrain it.

6.3.1 Comparison of the transition sequence to angular momentum models

In order to improve upon the current theoretical predictions, one has to understand how and why they differ from the observations. Hence, the comparison of isochrones in the colour-period space (gyrochrones) to the rotation period distribution might not be sufficient. Therefore, we evolved the observed distribution of NGC 2516 with angular momentum models (Fritzewski et al. 2021b). With this approach, we are independent of age constraints because we are mainly interested in whether the model can evolve one distribution into the other and not at which age. The general methodology is validated by the findings in Fritzewski et al. (2020) which clearly shows that one can assume the bulk properties of all open clusters at a certain age to be equal. Hence, we can evolve them in time and obtain the distribution of rotation periods at a different time, assuming the model used for the evolution is valid. Here, we invert this argument and test angular momentum models with the knowledge of two observed rotation period distributions.

At the age of NGC 2516 (150 Myr), fast rotators can be found from late-G to early-M stars, where the distinct fast rotator sequence vanishes due to a transition region with a wide spread of rotation periods. The earliest-type stars on the fast-rotator sequence already evolve towards slow rotators which manifests itself in the slight uplift of the sequence relative to the later-type stars (Fritzewski et al. 2020, see also Fig. 6.1).

More prominent is the evolution of the fast rotator sequence in the CPD of NGC 3532. Here, at 300 Myr, late-G type and early K-type stars evolved from their initial fast rotation into a transitional stage while earlier-type stars became exclusively slow rotators with rotation periods of up to 7 d. When studying the transition from fast to slow rotation, the boundaries of the evolved sequence, as well as its shape and slope in the CPD are important parameters which should be represented by angular momentum evolution models.

In Fritzewski et al. (2021b), we show that the forward evolution of the NGC 2516 period distribution with current models does not result in the observed distribution of NGC 3532. In particular, the models are not able to reproduce the spin-down through the rotational

gap. Given the current lack of understanding of this topic it is not surprising, otherwise the research question of this thesis would be a different one.

Strikingly, the angular momentum models predict both the evolution of the slow and fast rotators correctly but fall short in describing the transition from fast to slow rotation. In this regime, stars cross the rotational gap with a much stronger spin-down. Hence at any given time, only a small fraction of the stars along the mass-sequence is in transition. And yet, a clean sequence is observed which indicates that the transition is highly mass-sensitive.

6.3.2 Consequences for angular momentum models

Certainly, an important result of the study of stellar rotation in NGC 3532 is the strong disagreement between the observations and angular momentum models. In particular, the spin-down timescales of the slow and fast rotators are not coherently described by any of the angular momentum models. This clearly indicates that the evolution of the fast rotators is the unknown in angular momentum modelling.

The reason for the shorter time-scales is the stronger mass-dependence of the desaturation compared to current models. In NGC 3532, this effect can be seen in the evolved fast rotator sequence which is populated by stars with $0.8 \gtrsim M_\star/M_\odot \gtrsim 0.7$ and spans rotation periods between $1\,\mathrm{d} < P_{\mathrm{rot}} < 7\,\mathrm{d}$. In comparison, stars of the same mass-range on the slow rotator sequence span the period range $7\,\mathrm{d} < P_{\mathrm{rot}} < 11.5\,\mathrm{d}$. The large period spread over the small mass range in the evolved sequence shows that fast rotators spin down rapidly once they "desaturate" (i.e. leave the fast rotator phase) because even within the sequence the period gradient with mass ("$\mathrm{d}P/\mathrm{d}M$") is large. Hence, the desaturation is happening on very short time scales with a sharp transition from fast rotation into the gap region with its strong spin-down.

The comparison to the angular momentum models also shows that the transition is happening earlier in the stellar main sequence life than expected. In all models for the age of NGC 3532, the onset of the transition is placed at higher masses than observed which means that NGC 3532 is rotationally further evolved than predicted by the models. In additional, we were not able to find a single model that predicts both the position of the slow rotator sequence and one end point of the transition sequence indicating that this conclusion only applies to the fast rotators.

According to current theories the spin-down through the rotational gap is either a symmetric combination between both spin-down regimes (Barnes 2010) or determined by the period in the unsaturated regime (Matt et al. 2015). Hence, one would have to increase the spin-down in one of the regimes. However, in the Barnes (2010) case we find that both the slow rotators and the fast rotators are accurately described (within the limits of the theory) by the current formalism and one cannot simply change the spin-down efficiency of one of them. The same problem arises with the Matt et al. (2015) spin-down. Increasing the spin-down or changing other parameters simultaneously increases the efficiency among the slow rotators (whose deceleration is already over-estimated).

Although the lower edge of the transition sequence is well defined, several stars populate the rotational gap between the fast and slow rotator sequence. Hence, the transition from fast to slow rotation is not exclusively mass-dependent but stars with certain conditions can cross into the rotational gap at earlier ages. In NGC 3532, their number is much lower than the number of stars that stay on the (fast rotator and transition) sequence. Which means the transition from fast to slow rotation is mostly mass-dependent and deterministic rather than probabilistic as proposed by Brown (2014). Even the few stars, which leave the fast rotator sequence earlier might do so in a deterministic way. They could have

slightly different initial conditions like a lower angular momentum content and reach the desaturation boundary earlier.

The new rotation periods for NGC 3532, in combination with the additional work on this open cluster provides not only unique and crucial insights into stellar rotation at 300 Myr but also sheds light on novel, unexpected aspects of the stellar angular momentum evolution like the bifurcation of the slow rotator sequence and the extended slow rotator sequence among early-M dwarfs.

7

Conclusion and Outlook

The evolution from fast to slow rotation in young solar-like stars is a dramatic and quick change during the stellar main sequence evolution. In this thesis, I provide observational constraints on the transition time-scale and give insights into this event with the observations of NGC 3532.

A significant fraction of the work for this thesis is not dedicated to the main topic but provides the essential foundation for the study of the rotational evolution of young stars. Firstly, I established a membership for the open cluster NGC 3532. Without it, I would not have been able to construct a clean colour-period diagram. Secondly, the rotation periods of the young open cluster NGC 2516 are an important stepping stone, because we can only observe stellar evolution by comparing stars of different ages.

Those two studies provide not only the groundwork of the later studies but contain additional scientific results. In Fritzewski et al. (2019), we show that NGC 3532 is one of the richest open clusters in the Solar neighbourhood and measured for the first time the spectroscopic metallicity of its dwarf members. Among the M dwarfs in NGC 2516, we find slowly rotating stars which have previously only been seen in the Pleiades (Rebull et al. 2016). With this discovery, we can confirm their true membership status and question at the same time the current understanding of angular momentum evolution of young M dwarfs. In addition, we show the similarities between the distributions of rotation periods in several open clusters of the age of NGC 2516 and the Pleiades. This result strengthens the foundations of gyrochronology because it shows the independence of the rotational evolution from the cluster environment.

For the older NGC 3532, we probe the transition from fast to slow rotation not only through the stellar rotation (Fritzewski et al. 2021b) but also through chromospheric activity (Fritzewski et al. 2021a). Both observables provide valuable insights into the transition from different vantage points. The rotation periods trace the transition in the colour-period space very accurately, while the stellar activity allows to prove the absence of fast rotators among the higher-mass stars. Beyond, the combination of both data sets provides additional rotation periods including for stars on the "extended slow rotator sequence" while simultaneously verifying their slow rotation with their low chromospheric activity.

Further insight into the transition from fast to slow rotation–the main topic of this thesis–was gained from the comparison to angular momentum evolution models. Since we showed the universality of stellar rotation at the age of NGC 2516, it is possible to test angular momentum models with real rotation periods. The evolution of NGC 2516 forward to the age of NGC 3532 reveals a strong discrepancy to the observed stars in transition. These stars rotate much slower than proposed by the tested models. Yet, the most important result is that the transition from fast to slow rotation is very mass-dependent with only a small number of stars in transition at a given time. In NGC 3532, the mass difference between the slowest and fastest rotator in the transition region is only $0.1\,M_\odot$. This means that the transition from fast to slow rotation is deterministic and its onset is determined by a sudden event or sharp threshold.

To understand the mechanism of this onset, further observations of the stellar properties exactly at the beginning of the transition are needed. Yet, these observations are challenging due to the small number of such stars in open clusters. However, secondary effects (e.g. a change in coronal temperature) caused by the "desaturation" might be observable for a longer time and therefore for more stars. The increasing number of magnetic field measurements of cool stars (e.g. Marsden et al. 2014) might also shine some light on the

transition, answering the question whether the magnetic field is saturated in fast rotators and whether its large and small scale components change. However, to answer these questions stellar rotation periods are essential to select the right targets (preferentially in open clusters). Hence, further observations of young open clusters between 200 Myr and 500 Myr are important to create the richest possible set of stars in the early phase of the transition.

Recent and upcoming surveys in astronomy will provide essential auxiliary data for many stars in open clusters and the field. Firstly, with the accurate *Gaia* astrometry open cluster members can now be identified even in the outskirts of the clusters (Meingast et al. 2020), which enlarges the number of potential targets significantly. Next to *Gaia*, radial velocities from upcoming spectroscopic surveys such as WEAVE (Dalton et al. 2012) and 4MOST (de Jong et al. 2019) can be used to improve the membership on the astrometrically selected stars and to probe spectroscopic binaries in open clusters. The latter are of particular interest to answer the questions whether and how the angular momentum evolution of binary stars is different from single stars, i.e. whether fast rotation as probed in this work is strongly associated with binarity. Furthermore, spectroscopic surveys provide a large number of homogenous elemental abundance measurements with which the metallicity-dependence of the angular momentum evolution (Amard & Matt 2020) can be probed observationally (Amard et al. 2020).

Light curves provided by the increasing number of space- and ground-based exoplanet transit (e. g. TESS (Ricker et al. 2015), NGTS (Wheatley et al. 2018)) and transient surveys (e. g. ZTF (Bellm et al. 2019), LSST (Ivezić et al. 2019)) can be exploited for stellar rotation periods. Despite not providing ideal data sets due to either sparse time sampling (e. g. LSST) or large on-sky aperture (e.g. TESS) their sky-coverage allows to measure rotation periods for previously un-probed regions, e.g. sparse open clusters or stellar streams (Curtis et al. 2019a). In particular TESS is sensitive to the warmer/brighter stars and can be used to probe the first stages of the transition from fast to slow rotation (e.g. Healy & McCullough 2020).

The combination of an improved membership and accurate metallicity information with light curves from all-sky surveys allows to probe even sparse open clusters (with ~50 – 100 members) efficiently. A comprehensive analysis of rotation periods in many open clusters will enable a more definitive conclusion on the universality of angular momentum evolution than provided in Fritzewski et al. (2020).

But not only the young open clusters are of interest. A surprising decrease in the spin-down of older main sequence stars has been observed (Curtis et al. 2019b, 2020; Gruner & Barnes 2020). Yet, rotation periods of stars in older open clusters are hard to come-by because the rotational modulations are small and few old open clusters exist (in the vicinity of the Solar system). Hence, age-dating field stars with other methods such as asteroseismology of known rotators (e.g. García et al. 2014) or stellar kinematics (Angus et al. 2020) might be important intermediate steps towards understanding the spin-down of older stars.

To understand the stellar spin-down astrophysically, angular momentum models have to advance and be able to predict rotation periods distributions and their evolution accurately. As seen for the slow rotators, the current model by Spada & Lanzafame (2020) describes these stars (and even the old slow rotators) much better than previous models. An expansion of the two-zone models to the fast rotators and the transition might be able to describe the angular momentum evolution of fast rotators accurately through their entire (pre-)main sequence life.

Both observationally and theoretically the exploration of the angular momentum

evolution has just begun and our knowledge and explanations of stellar rotation in young and old open clusters alike will be challenged many more times as more data become available, unveiling surprising and new structures in the colour-period diagrams.

Acknowledgements

After all those years at the AIP, my thesis is finally finished and I would like to thank the people who enabled it and who joined me on my journey.

The whole thesis and my research would not have been possible without Sydney. With you as an advisor, I had always someone to talk to about my work, to ask my questions, and to present my ideas to. You taught me to look at the fine details of the data and how to write good papers (and that there is no perfection but we should nevertheless aim as high as possible). The extra time spend on this work was worth it. Sydney, you are a great advisor!

I am also deeply indebted to Klaus, who was always positive about my progress although it took me so long to finally arrive here and finish my thesis.

Special thanks to Jörg for being a great office mate. It was always nice to talk to you and Sydney over a cup of tea. Thanks also to the other offices mates, whom I saw coming or going: Alessandro, David, Elizabeth, and Trey. Many thanks to everyone in our 11:30 lunch group. We all know its best to be early. I would also like to thank Kim for finding the typos in this thesis.

I am grateful to my family who supported me on my way. With our two boys, we became a real family over the last years and they show me that there is more to life than astronomy. I cannot end without thanking my Mum and Dad for supporting me on this whole journey over the past ten years throughout my university time and my time as graduate student.

References

Abney, W. D. W. 1877, MNRAS 37, 278
Alphenaar, P., & van Leeuwen, F. 1981, Information Bulletin on Variable Stars 1957, 1
Amard, L. et al. 2019, A&A 631, A77
Amard, L., & Matt, S. P. 2020, ApJ 889, 108
Amard, L., Roquette, J., & Matt, S. P. 2020, MNRAS 499, 3481
Angus, R. et al. 2020, AJ 160, 90
Babcock, H. W. 1961, ApJ 133, 572
Bailey, J. I., Mateo, M., White, R. J., Shectman, S. A., & Crane, J. D. 2018, MNRAS 475, 1609
Baliunas, S. L. et al. 1995, ApJ 438, 269
Barnes, S., & Sofia, S. 1996, ApJ 462, 746
Barnes, S., Sofia, S., & Pinsonneault, M. 2001, ApJ 548, 1071
Barnes, S. A. 2003, ApJ 586, 464
— 2010, ApJ 722, 222
Barnes, S. A., Weingrill, J., Fritzewski, D., Strassmeier, K. G., & Platais, I. 2016, ApJ 823, 16
Barnes, S. A. 1997, PhD thesis (Yale University)
Bellm, E. C. et al. 2019, PASP 131, 018002
Bouvier, J., Forestini, M., & Allain, S. 1997, A&A 326, 1023
Brown, T. M. 2014, ApJ 789, 101
Cantat-Gaudin, T. et al. 2018, A&A 618, A93
Cayrel de Strobel, G., Soubiran, C., & Ralite, N. 2001, A&A 373, 159
Chaboyer, B., Demarque, P., & Pinsonneault, M. H. 1995, ApJ 441, 865
Charbonneau, P. 2014, ARA&A 52, 251
Claria, J. J., & Lapasset, E. 1988, MNRAS 235, 1129
Clem, J. L., Landolt, A. U., Hoard, D. W., & Wachter, S. 2011, AJ 141, 115
Cranmer, S. R. et al. 2015, Philosophical Transactions of the Royal Society of London Series A 373, 20140148
Curtis, J. L., Agüeros, M. A., Mamajek, E. E., Wright, J. T., & Cummings, J. D. 2019a, AJ 158, 77
Curtis, J. L., Agüeros, M. A., Douglas, S. T., & Meibom, S. 2019b, ApJ 879, 49
Curtis, J. L. et al. 2020, ApJ 904, 140
Dalton, G. et al. 2012, in: Ground-based and Airborne Instrumentation for Astronomy IV, ed. by I. S. McLean, S. K. Ramsay, & H. Takami, vol. 8446, Society of Photo-Optical Instrumentation Engineers (SPIE) Conference Series, 84460P
de Jong, R. S. et al. 2019, The Messenger 175, 3
Eberhard, G., & Schwarzschild, K. 1913, ApJ 38, 292
Edwards, S., & Snell, R. L. 1982, ApJ 261, 151
Eggen, O. J. 1981, ApJ 246, 817
Fernandez, J. A., & Salgado, C. W. 1980, A&AS 39, 11
Folsom, C. P. et al. 2016, MNRAS 457, 580
Fritzewski, D. J., Barnes, S. A., James, D. J., Järvinen, S. P., & Strassmeier, K. G. 2021a, A&A 656, A103
Fritzewski, D. J., Barnes, S. A., James, D. J., & Strassmeier, K. G. 2020, A&A 641, A51
— 2021b, A&A 652, A60
Fritzewski, D. J. et al. 2019, A&A 622, A110
García, R. A. et al. 2014, A&A 572, A34
Garraffo, C. et al. 2018, ApJ 862, 90
Gieseking, F. 1980, A&AS 41, 245
— 1981, A&A 99, 155
González, J. F., & Lapasset, E. 2002, AJ 123, 3318
Gruner, D., & Barnes, S. A. 2020, A&A 644, A16
Güdel, M. 2004, A&A Rev. 12, 71
Hale, G. E. 1892, Memorie della Societa Degli Spettroscopisti Italiani 20, 154
Healy, B. F., & McCullough, P. R. 2020, ApJ 903, 99
Hubrig, S. et al. 2008, A&A 490, 793

Irwin, J. et al. 2007, MNRAS 377, 741
Ivezić, Ž. et al. 2019, ApJ 873, 111
Jao, W.-C., Henry, T. J., Gies, D. R., & Hambly, N. C. 2018, ApJ 861, L11
Jeffries, R. D., Thurston, M. R., & Pye, J. P. 1997, MNRAS 287, 350
Kawaler, S. D. 1988, ApJ 333, 236
Koenigl, A. 1991, ApJ 370, L39
Kovalev, M., Bergemann, M., Ting, Y.-S., & Rix, H.-W. 2019, A&A 628, A54
Kraft, R. P. 1967, ApJ 150, 551
Kron, G. E. 1947, PASP 59, 261
Leighton, R. B. 1969, ApJ 156, 1
MacGregor, K. B., & Brenner, M. 1991, ApJ 376, 204
Mamajek, E. E., & Hillenbrand, L. A. 2008, ApJ 687, 1264
Marsden, S. C. et al. 2014, MNRAS 444, 3517
Matt, S. P., Brun, A. S., Baraffe, I., Bouvier, J., & Chabrier, G. 2015, ApJ 799, L23
Meibom, S., Mathieu, R. D., Stassun, K. G., Liebesny, P., & Saar, S. H. 2011, ApJ 733, 115
Meibom, S., Mathieu, R. D., & Stassun, K. G. 2009, ApJ 695, 679
Meibom, S. et al. 2015, Nature 517, 589
Meingast, S., Alves, J., & Rottensteiner, A. 2020, arXiv e-prints, arXiv:2010.06591
Mestel, L. 1965, QJRAS 6, 161
— 1984, in: Cool Stars, Stellar Systems, and the Sun, ed. by S. L. Baliunas, & L. Hartmann, vol. 193, 49
Miles, R. 2007, Journal of the British Astronomical Association 117, 172
Newton, E. R. et al. 2016, ApJ 821, 93
Newton, E. R. et al. 2017, ApJ 834, 85
Noyes, R. W., Weiss, N. O., & Vaughan, A. H. 1984, ApJ 287, 769
Orcajo, S., Cieza, L. A., Gamen, R., & Peterson, D. 2019, MNRAS 487, 2937
Ossendrijver, M. 2003, A&A Rev. 11, 287
Osterbrock, D. E. 1961, ApJ 134, 347
Parker, E. N. 1958, ApJ 128, 664
— 1988, ApJ 330, 474
Parker, E. N. 1955a, ApJ 122, 293
— 1955b, ApJ 121, 491
Patten, B. M., & Simon, T. 1996, ApJS 106, 489
Pizzolato, N., Maggio, A., Micela, G., Sciortino, S., & Ventura, P. 2003, A&A 397, 147
Prosser, C. F., Schild, R. E., Stauffer, J. R., & Jones, B. F. 1993, PASP 105, 269
Rebull, L. M. et al. 2016, AJ 152, 113
Rebull, L. M. et al. 2017, ApJ 839, 92
Ricker, G. R. et al. 2015, Journal of Astronomical Telescopes, Instruments, and Systems 1, 014003
Schatzman, E. 1962, Annales d'Astrophysique 25, 18
See, V. et al. 2019a, ApJ 886, 120
See, V. et al. 2019b, ApJ 876, 118
Shajn, G., & Struve, O. 1929, MNRAS 89, 222
Shultz, M. E. et al. 2019, MNRAS 490, 274
Skumanich, A. 1972, ApJ 171, 565
Soderblom, D. R., Stauffer, J. R., MacGregor, K. B., & Jones, B. F. 1993, ApJ 409, 624
Spada, F., & Lanzafame, A. C. 2020, A&A 636, A76
Stauffer, J. R., & Hartmann, L. W. 1987, ApJ 318, 337
Steenbeck, M., & Krause, F. 1969, Astronomische Nachrichten 291, 49
Strassmeier, K. G. 2009, A&A Rev. 17, 251
Sung, H., Bessell, M. S., Lee, B.-W., & Lee, S.-G. 2002, AJ 123, 290
Terndrup, D. M. et al. 2002, ApJ 576, 950
van Leeuwen, F., & Alphenaar, P. 1982, The Messenger 28, 15
van Leeuwen, F., Alphenaar, P., & Meys, J. J. M. 1987, A&AS 67, 483
Weber, E. J., & Davis Jr., L. 1967, ApJ 148, 217
Wheatley, P. J. et al. 2018, MNRAS 475, 4476

Wilson, O. C. 1978, ApJ 226, 379
Wright, N. J., & Drake, J. J. 2016, Nature 535, 526
Wright, N. J., Drake, J. J., Mamajek, E. E., & Henry, G. W. 2011, ApJ 743, 48
Young, C. A. 1872, Nature 7, 28